

**THE 7TH INTERNATIONAL CONFERENCE ON
INTEGRATED MODELING AND ANALYSIS IN
APPLIED CONTROL AND AUTOMATION**

*SEPTEMBER 25-27 2013
ATHENS, GREECE*

**IMAACA
2013**

**EDITED BY
AGOSTINO BRUZZONE
GENEVIÈVE DAUPHIN-TANGUY
SERGIO JUNCO
YURI MERKURYEV**

PRINTED IN RENDE (CS), ITALY, SEPTEMBER 2013

**ISBN 978-88-97999-19-5 (Paperback)
ISBN 978-88-97999-25-6 (PDF)**

© 2013 DIME UNIVERSITÀ DI GENOVA

RESPONSIBILITY FOR THE ACCURACY OF ALL STATEMENTS IN EACH PAPER RESTS SOLELY WITH THE AUTHOR(S). STATEMENTS ARE NOT NECESSARILY REPRESENTATIVE OF NOR ENDORSED BY THE DIME, UNIVERSITY OF GENOVA. PERMISSION IS GRANTED TO PHOTOCOPY PORTIONS OF THE PUBLICATION FOR PERSONAL USE AND FOR THE USE OF STUDENTS PROVIDING CREDIT IS GIVEN TO THE CONFERENCES AND PUBLICATION. PERMISSION DOES NOT EXTEND TO OTHER TYPES OF REPRODUCTION NOR TO COPYING FOR INCORPORATION INTO COMMERCIAL ADVERTISING NOR FOR ANY OTHER PROFIT - MAKING PURPOSE. OTHER PUBLICATIONS ARE ENCOURAGED TO INCLUDE 300 TO 500 WORD ABSTRACTS OR EXCERPTS FROM ANY PAPER CONTAINED IN THIS BOOK, PROVIDED CREDITS ARE GIVEN TO THE AUTHOR(S) AND THE CONFERENCE.

FOR PERMISSION TO PUBLISH A COMPLETE PAPER WRITE TO: DIME UNIVERSITY OF GENOVA, PROF. AGOSTINO BRUZZONE, VIA OPERA PIA 15, 16145 GENOVA, ITALY. ADDITIONAL COPIES OF THE PROCEEDINGS OF THE *IMAACA* ARE AVAILABLE FROM DIME UNIVERSITY OF GENOVA, PROF. AGOSTINO BRUZZONE, VIA OPERA PIA 15, 16145 GENOVA, ITALY.

ISBN 978-88-97999-19-5 (Paperback)

ISBN 978-88-97999-25-6 (PDF)

**THE 7TH INTERNATIONAL CONFERENCE ON INTEGRATED MODELING
AND ANALYSIS IN APPLIED CONTROL AND AUTOMATION
SEPTEMBER 25-27 2013, ATHENS, GREECE**

ORGANIZED BY



DIME - UNIVERSITY OF GENOA



LIOPHANT SIMULATION



SIMULATION TEAM



IMCS - INTERNATIONAL MEDITERRANEAN & LATIN AMERICAN COUNCIL OF
SIMULATION



DIMEG, UNIVERSITY OF CALABRIA



MSC-LES, MODELING & SIMULATION CENTER, LABORATORY OF ENTERPRISE
SOLUTIONS



MODELING AND SIMULATION CENTER OF EXCELLENCE (MSCOE)



LATVIAN SIMULATION CENTER - RIGA TECHNICAL UNIVERSITY



LOGISIM



LSIS - LABORATOIRE DES SCIENCES DE L'INFORMATION ET DES SYSTEMES



MIMOS - MOVIMENTO ITALIANO MODELLAZIONE E SIMULAZIONE



MITIM PERUGIA CENTER - UNIVERSITY OF PERUGIA



BRASILIAN SIMULATION CENTER, LAMCE-COPPE-UFRJ



MITIM - MCLEOD INSTITUTE OF TECHNOLOGY AND INTEROPERABLE MODELING AND
SIMULATION - GENOA CENTER



M&SNET - MCLEOD MODELING AND SIMULATION NETWORK



LATVIAN SIMULATION SOCIETY



ECOLE SUPERIEURE D'INGENIERIE EN SCIENCES APPLIQUEES



UNIVERSITY OF LA LAGUNA



CIFASIS: CONICET-UNR-UPCAM



INSTICC - INSTITUTE FOR SYSTEMS AND TECHNOLOGIES OF INFORMATION, CONTROL AND COMMUNICATION



NATIONAL RUSSIAN SIMULATION SOCIETY



CEA - IFAC



AFCEA, HELLENIC CHAPTER

TECHNICALLY CO-SPONSORED



IEEE - CENTRAL AND SOUTH ITALY SECTION CHAPTER

I3M 2013 INDUSTRIAL SPONSORS



CAL-TEK SRL



LIOTECH LTD



MAST SRL



SIM-4-FUTURE

I3M 2013 MEDIA PARTNERS



INDERSCIENCE PUBLISHERS - INTERNATIONAL JOURNAL OF SIMULATION AND PROCESS MODELING



INDERSCIENCE PUBLISHERS - INTERNATIONAL JOURNAL OF CRITICAL INFRASTRUCTURES



INDERSCIENCE PUBLISHERS – INTERNATIONAL JOURNAL OF ENGINEERING SYSTEMS
MODELLING AND SIMULATION



INDERSCIENCE PUBLISHERS – INTERNATIONAL JOURNAL OF SERVICE AND
COMPUTING ORIENTED MANUFACTURING



IGI GLOBAL – INTERNATIONAL JOURNAL OF PRIVACY AND HEALTH
INFORMATION MANAGEMENT



HALLDALE MEDIA GROUP: MILITARY SIMULATION AND TRAINING MAGAZINE



HALLDALE MEDIA GROUP: THE JOURNAL FOR HEALTHCARE EDUCATION,
SIMULATION AND TRAINING



EUROMERCI

EDITORS

AGOSTINO BRUZZONE

MITIM-DIME, UNIVERSITY OF GENOA, ITALY
agostino@itim.unige.it

GENEVIÈVE DAUPHIN-TANGUY

ECOLE CENTRALE DE LILLE, FRANCE
genevieve.dauphin-tanguy@ec-lille.fr

SERGIO JUNCO

UNIVERSIDAD NACIONAL DE ROSARIO, ARGENTINA
sjunco@fceia.unr.edu.ar

YURI MERKURYEV

RIGA TECHNICAL UNIVERSITY, LATVIA
merkur@itl.rtu.lv

**INTERNATIONAL MULTIDISCIPLINARY MODELING & SIMULATION
MULTICONFERENCE, I3M 2013**

GENERAL CO-CHAIRS

*AGOSTINO BRUZZONE, MITIM DIME, UNIVERSITY OF GENOA, ITALY
YURI MERKURYEV, RIGA TECHNICAL UNIVERSITY, LATVIA*

PROGRAM CHAIR

FRANCESCO LONGO, DIMEG, UNIVERSITY OF CALABRIA, ITALY

**THE 7TH INTERNATIONAL CONFERENCE ON INTEGRATED MODELING AND
ANALYSIS IN APPLIED CONTROL AND AUTOMATION, IMAACA 2013**

CONFERENCE CHAIRS

*SERGIO JUNCO, UNIVERSIDAD NACIONAL DE ROSARIO, ARGENTINA
GENEVIÈVE DAUPHIN-TANGUY, ECOLE CENTRALE DE LILLE, FRANCE*

IMAACA 2013 INTERNATIONAL PROGRAM COMMITTEE

Jorge Baliño, *Univ. of São Paulo, Brazil*
Wolfgang Borutzky, *BRS-Univ. Applied Sciences,
Sankt Augustin, Germany.*

Belkacem Ould Bouamama, *USTL, France*

Jean-Yves Dieulot, *Polytech'Lille, France*

Alejandro Donaire, *The University of
Newcastle, Australia*

Tulga Ersal, *University of Michigan, USA*

Gianluca Gatti, *University of Calabria, Italy*
Julien Gomand, *ENSAM, Aix-en-Provence,
France*

Zhi Han, *The Matworks, USA*

Adrian Ilinca, *Université du Québec à Rimouski,
Canada*

Fabrizio Leonardi, *FEI, São Bernardo do Campo,
Brazil*

Francesco Longo, *University of Calabria, Italy*
Loucas S. Louca, *University of Cyprus, School
of Engineering, Cyprus*

Jacinto Marchetti, *INTEC, Santa Fe, Argentina*

Norberto Nigro, *CIMEC, Santa Fe, Argentina*

Oscar Ortiz, *Univ. Nac. De San Jaun, Argentina*

P. M. Pathak, *IIT, Roorkee, India*

Ricardo Pérez, *PUC, Chile*

Xavier Roboam, *INPT-LAPLACE, France*

Christophe Sueur, *École Centrale Lille, France*

Kazuhiro Tanaka, *Kyushu Institute of
Technology, Fukuoka, Japan*

Anand Vaz, *NITJ, Jalandhar, India*

Daniel Viassolo, *Halliburton, Houston, TX, USA*

Costas Tzafestas, *NTUA, Greece*

Rafic Younes, *Lebanese University, Beirut,
Lebanon*

Anibal Zanini, *Univ. De Buenos Aires, Argentina*

Katsuya Suzuki, *Aichi Sci & Technol. Found,
Japan*

TRACKS AND WORKSHOP CHAIRS

RENEWABLE ENERGY SYSTEMS. MODELING, SIMULATION AND CONTROL

CHAIRS: RAFIC YOUNES, LEBANESE UNIVERSITY, BEIRUT,
LEBANON ; ADRIAN ILINCA, LREE, UNIVERSITÉ DU
QUÉBEC À RIMOUSKI, CANADA.

MODELLING AND CONTROL OF MECHATRONIC SYSTEMS

CHAIRS: KAZUHIRO TANAKA, KYUSHU INSTITUTE OF
TECHNOLOGY, FUKUOKA, JAPAN; KATSUYA SUZUKI, AICHI
SCI & TECHNOL. FOUND, JAPAN.

SUPERVISION SYSTEM DESIGN IN INDUSTRIAL PROCESSES

CHAIR: BELKACEM OULD BOUAMAMA, ECOLE
POLYTECHNIQUE DE LILLE, FRANCE.

OBSERVER DESIGN FOR DYNAMICAL SYSTEMS: APPLICATION TO ROBUST FAULT AND DISTURBANCE RECONSTRUCTION

CHAIR: CHRISTOPHE SUEUR, LAGIS, ECOLE CENTRALE
DE LILLE, FRANCE.

MODELING, SIMULATION AND CONTROL OF NONLINEAR OSCILLATING SYSTEMS

CHAIR: GIANLUCA GATTI, DEPT. MECHANICAL ENG.,
UNIVERSITY OF CALABRIA, ARCAVACATA DI RENDE, ITALY.

MODELING AND IDENTIFICATION FOR CONTROL APPLICATIONS

CHAIR: VIKAS RASTOGI, DELHI TECHNOLOGICAL
UNIVERSITY, DELHI, INDIA.

CONFERENCE CHAIRS' MESSAGE

WELCOME TO IMAACA 2013!

Athens counts among the cities with the highest historical and cultural heritage in the world, as it was at the heart of ancient Greece, unanimously recognized as the cradle of modern western civilization. Particularly relevant to us, even antique automation devices have been traced back to the early times of this city. Therefore Athens is the perfect place to locate IMAACA 2013. This year we have a lesser number of papers than in previous editions due to a combination of diverse factors: less submissions, higher rejection rate (around 50%) and a non negligible number of withdrawals of accepted papers originated in lack of financing experienced by some authors. Nevertheless, continuing the conference tradition of providing a forum to present high-quality research, IMAACA 2013 offers a blend of interesting topics where different mathematical modeling formalisms and simulation tools, as well as diverse control-theoretic approaches, are applied to problems in vehicle dynamics, vibration control, process control, mechatronic systems and supervision and diagnosis, among other domains. Being this year again part of I3M, the International Multidisciplinary Modeling and Simulation Multiconference – currently co-locating 7 thematic international conferences on Modeling & Simulation - IMAACA 2013 provides researchers, scientists, simulationists and practitioners with an ideal framework for sharing knowledge about innovative concepts, establishing new collaborations and research projects, and identifying new relevant research areas, also as combination of multiple disciplines that share the common Simulation denominator. As already happened in the past IMAACA experiences, the key of the IMAACA success is the invaluable contribution of its authors as well as the continuous work of the international program committee that together with the help of external reviewers has guaranteed the high scientific quality of the selected papers. Therefore, we would like to thank each author and each member of the IPC for their inputs, which keep contributing to the quality and thus to the future of our conference. Finally, before we close we would like to wish to all the attendees a fruitful and enjoyable IMAACA 2013 in Athens.



Sergio Junco,
Universidad Nacional
de Rosario, Argentina



Geneviève Dauphin-Tanguy,
Ecole Centrale de Lille, France

ACKNOWLEDGEMENTS

The IMAACA 2013 International Program Committee (IPC) has selected the papers for the Conference among many submissions; therefore, based on this effort, a very successful event is expected. The IMAACA 2013 IPC would like to thank all the authors as well as the reviewers for their invaluable work.

A special thank goes to all the organizations, institutions and societies that have supported and technically sponsored the event.

LOCAL ORGANIZATION COMMITTEE

AGOSTINO G. BRUZZONE, *DIME, UNIVERSITY OF GENOA, ITALY*
MATTEO AGRESTA, *SIMULATION TEAM, ITALY*
CHRISTIAN BARTOLUCCI, *SIMULATION TEAM, ITALY*
ALESSANDRO CHIURCO, *DIMEG, UNIVERSITY OF CALABRIA, ITALY*
MARGHERITA DALLORTO, *SIMULATION TEAM, ITALY*
LUCIANO DATO, *SIMULATION TEAM, ITALY*
ANGELO FERRANDO, *SIMULATION TEAM, ITALY*
FRANCESCO LONGO, *DIMEG, UNIVERSITY OF CALABRIA, ITALY*
MARINA MASSEI, *LIOPHANT SIMULATION, ITALY*
LETIZIA NICOLETTI, *CAL-TEK SRL*
FRANCISCO SPADAFORA, *CAL-TEK SRL*
ALBERTO TREMORI, *SIMULATION TEAM, ITALY*



This International Workshop is part of the I3M Multiconference: the Congress leading Simulation around the World and Along the Years



Index

Battery system modeling and identification for electric propulsion vehicle with fault simulation KyuHong Han	1
Nonlinear hybrid sliding mode control of an electrohydraulic active suspension Bassel Shaer, Jean-Pierre Kenné, Claude Kaddissi, Vladimir Polotski	6
Dynamic modeling and control of off-road truck using bond graphs Ashish Gupta, Vikas Rastogi	15
H-infinity control with time domain specifications applied to a heat exchanger network Fábio Delatore, Fabrizio Leonardi, Luís Novazzi, José Da Cruz	22
Bondgraphs modeling and simulation on dynamic characteristics of cavitating pump system Kazuhiro Tanaka, Toshiyuki Sato, Hiroshi Tsukamoto, Takehisa Kohda, Katsuya Suzuki	28
State and unknown input observer: analysis and design Eugene Tarasov, Ibtiseme Gahlouz, Christophe Sueur, Belkacem Ould Bouamama	37
Modeling and simulation of an automated manual transmission system Hua Huang, Sebastian Nowoisky, René Knoblich, Clemens Gühmann	44
Bond graph proportional-integral observer-based robust fault detection Ghada Saoudi, Rafika EL Harabi, Geneviève Dauphin-Tanguy, Belkacem Ould Bouamama, Mohamed Naceur Abdelkrim	52
3D computational model including topographic data for the prediction of dire wind regimes and vortex shedding in an attempt to improve tall building reliability Drishtysingh Ramdenee, Pierre Luc Paradis, Hussein Ibrahim, Hemraj Joyram, Adrian Ilinca	61
Three-dimensional multi-body bond graph model for vibration control of long shafts - application to oil well drilling Geoff Rideout, Farid Arvani, Stephen Butt, Ehsan Fallahi	70
Tuning the position of a fuzzy cognitive map attractor using back propagation through time Michal Gregor, Peter Groumpos	78
Bond-graph based controller design of a two-input two-output four-tank system Matías Nacusse, Sergio Junco	87
Observer-based actuator and sensor fault estimation Christophe Sueur	97
Author's Index	103

BATTERY SYSTEM MODELING AND IDENTIFICATION FOR ELECTRIC PROPULSION VEHICLE WITH FAULT SIMULATION

Kyuhong Han

Automotive PMO, Agency for Defense Development, Republic of Korea

clickcow@gmail.com

ABSTRACT

This paper describes development process and results of a battery system model with fault simulation for electric propulsion vehicles. The developed battery system model can be used to verify control and fault diagnosis strategies of a supervisory controller in the electric propulsion vehicle. To develop this battery system model, three sub-models, including a battery model, a relay assembly model, and a BMS (Battery Management System) model, are connected together similarly to the target real battery system. Comparison results between the real battery system hardware and the battery system model show similar tendency and values. And fault injection test of the model shows real system situation. It is possible for the model to emulate battery characteristics and fault situation if it is used in the development process of the BMS or the supervisory control strategies for electric propulsion systems.

Keywords: battery, electric vehicle, fault simulation, real time model

1. INTRODUCTION

Since problems such as shortage of fossil fuels (Campbell and Laherrere 1998), global warming, and environmental pollution have been illuminated as global issues worldwide, development and usage of environmentally friendly electric propulsion systems have been increasing in automotive, marine and aircraft fields regardless of the distinction between civilian and military. Particularly in the automotive field, vehicles using hybrid or electric propulsion systems have been developed actively (Pisu, Serrao, Cantemir, and Rizzoni 2006; Hashimoto, Yamaguchi, Matsubara, Yaguchi, and Takaoka 2010). These electric propulsion systems use electric power to drive vehicles, so that energy storage devices such as batteries have an essential role in the systems.

Because a vehicle is a platform for people to be on board directly, reliability of the platform and safety of the passengers should be taken in the development phase of the system. Besides, electric propulsion vehicles require a large number of high electric power components and controllers compared to engine-based vehicles. And electric motors and high voltage batteries are necessary in the system. So, the configuration of the

system has been complex and the safety of passengers for the high voltage has been more significant. Therefore, it is needed to assess the suitability of the distributed systems included in the entire system before the distributed systems are integrated in the development phase of the complex system. Suitability assessment of a sub-distributed system means to judge whether the system is properly operating in the entire system. The suitability assessment of the sub-system includes analysis to give effect to the other connected systems and analysis of operation in fault situation. Especially, the high voltage battery system is a core component in the electric propulsion system. So, the suitability assessment of the battery system is important in the development process. However, it is difficult to induce the fault to the battery system. Therefore, the test environment to assess suitability of the battery system is needed.

Control strategies of a controller are typically verified through the simulation test before applying it to the actual target system. In the case of the battery system that it is difficult to be made trouble actually, if the simulation environment is used in the suitability assessment, then it is possible to enhance efficiency of validation. There are commercial models about batteries like the CRUISE (Xie and Ding 2008; Chunhua, Jigao, and Fenglai 2011), the ADVISOR (Johnson 2002) and the AUTONOMIE (Aziz, Shafqat, Qureshi, and Ahmad 2011). And a variety of battery models, electrochemical models (Doyle, Fuller, and Newman 1993), analytical models (Linden and Reddy 2001), and electrical circuit models (Ehsani, Gao, and Emadi 2009; Jang and Yoo 2008; Kim 2012), have been consistently studied. However, these battery models are just performance models to see the operating behavior of the battery. So, additional tasks are required to connect with the BMS or the supervisory control models. Besides, it is hard to add fault models to the commercial battery models.

In this paper, a battery system model of the electric propulsion systems having similar configuration with a real battery system hardware including the battery, the relay assembly, and the BMS has been developed and it is possible to simulate fault situations in physical phenomena point of view.

The model has been developed using a complementary modeling tool, the MATLAB/Simulink,

and it has a real-time character for the HILS(Hardware-In-the-Loop Simulation) environment. If this developed battery system model is used in the development process of the integrated system like electric propulsion systems, then mutual effectiveness among the sub-systems of the entire system can be discerned effectively. In order to validate accuracy of the developed model, the results for the specific power scenario are confirmed. In addition, arbitrary faults are injected through the model to evaluate the characteristics of fault simulation.

2. BATTERY SYSTEM

Target battery system in this study is a real high voltage battery system of a series hybrid electric propulsion vehicle. Nominal voltage of the one battery pack is 340V, and its capacity is at about 15Ah level. And the target system uses 4 battery packs which are configured to 2 series and 2 parallel type. So, the entire battery system has 680V nominal voltage and 30Ah capacity.

2.1. Configuration of the Battery System

Target battery system consists of a battery, a relay assembly adjusting connection between the battery and DC link, and a BMS (Battery Management System) monitoring the battery status. Figure 1 shows this configuration of the battery system.

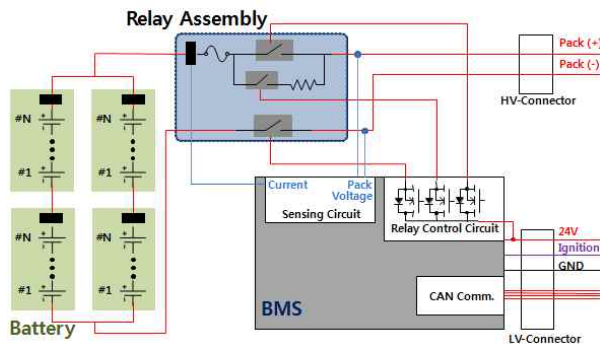


Figure 1: Configuration of the battery system

A battery module is made up of multiple unit battery cells, and the battery modules are packed in series or in parallel to make a battery pack. This package configuration of the battery pack is concluded to adjust required battery voltage. The relay assembly consists of a plus relay, a minus relay, a pre-charge relay and a pre-charge resistor. When the DC link voltage becomes the same as the battery terminal voltage, the pre-charge resistor works to give the DC link pre-charging effect. The BMS controls the three relays in the relay assembly and measures voltage and current of the battery terminal and temperature of battery cells. Also the BMS communicates with the supervisory controller to inform these values and get its command.

2.2. Modeling Requirement

In this study, the modeling of the battery system is performed to evaluate the supervisory control strategies including fault diagnosis strategies of the entire system. Therefore, three sub-model, a battery model, a relay assembly model, and a BMS model, is required to be similar with the real battery system. So, requirements of each sub-model have been derived.

First, battery cell characteristics should be shown in the battery sub-model. The main characteristic of the battery cell is the SOC (State-of-Charge) of the battery cell derived from battery cell capacity and current. And the battery sub-model should calculate loss current of the battery cell derived from heating effect. In addition, the sub-model must show change of the battery terminal voltage derived from internal resistance, internal reactance, double layer effect, and diffusion effect. From the battery package point of view, the change of voltage and current according to series or parallel connection should be shown. Change of the battery pack temperature according to the battery specification and current flow of the terminal should also be shown. Using this model to evaluate control strategies of the supervisory controller, the battery terminal through the DC-Link is connected to other electric propulsion components. Because characteristics of electrical connection are interested in the entire operation, simulating the actual battery voltage is more important than others.

Second, the requirements of the relay assembly sub-model are to have opening and closing properties of the relay itself and pre-charge resistor character. Then loss current characteristics should be shown because relay terminal is a DC link terminal.

Table 1: Battery system fault list

Fault	Detect Condition	Release Condition	BMS Behavior
Under voltage warning	$V < 550V$	Returns normal condition	Only alarm
Under voltage fault	$V < 530V$	No release	Alarm, Relay open
Over voltage warning	$V > 750V$	Returns normal condition	Only alarm
Over voltage fault	$V > 770V$	No release	Alarm, Relay open

Third, the BMS sub-model should communicate with the supervisory controller in the HILS environment. So, the communication protocol must be matched with the real hardware. Because the BMS model give various information to the supervisory controller, the application software such as SOC estimation, physical signal conditioning should be included in the BMS sub-model. And the BMS sub-model has to detect and simulate some faults like table 1. To verify these faults,

fault simulation environment should also be developed in this sub-model. Using this environment, physical value variation can be induced.

3. BATTERY SYSTEM MODELING

To develop this battery system model, three sub-models, including a battery model, a relay assembly model and a BMS model, are connected together similarly as the real battery system.

3.1. Battery Model

Main function of the battery model is calculating the variation of SOC, voltage and temperature for the target battery. To develop the battery model, a RLC equivalent circuit for the battery cell (Ehsani, Gao, and Emadi 2009; Jang and Yoo 2008; Kim 2012) is used as shown below in figure 2.

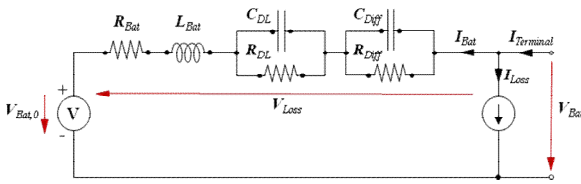


Figure 2: Battery equivalent circuit

In the battery model, SOC is first calculated using charge and discharge current of the battery cell. Because the SOC is a ratio of present energy capacity to original total capacity, the SOC is calculated using integration method which adds continuously charge and discharge current with present energy capacity based on initial SOC value as shown below in (1).

$$SOC = SOC_0 + \frac{1}{K_N} \int (I_{Terminal} - I_{Loss}) \quad (1)$$

where K_N : nominal capacity of a battery (Ah)

After calculating the SOC, battery terminal voltage is generated from the OCV (Open Circuit Voltage) data. From this voltage value, the final terminal voltage of the battery is calculated from subtracting the loss voltages such as internal resistance (2), internal inductance (3), double layer effect (4), and diffusion effect (5).

$$I_{Bat} R_{Bat} (SOC, I_{Bat}, T_{Bat}) \quad (2)$$

$$\frac{dI_{Bat}}{dt} L_{Bat} \quad (3)$$

$$\frac{1}{C_{DL}} \int \left(I_{Bat} - \frac{V_{DL}}{R_{DL}} \right) \quad (4)$$

$$\frac{1}{C_{Diff}} \int \left(I_{Bat} - \frac{V_{Diff}}{R_{Diff}} \right) \quad (5)$$

And the parameters of the battery model are tuned in order for the characteristics to match with the real system results. Figure 3 shows the results of nominal capacity test of the one battery pack.

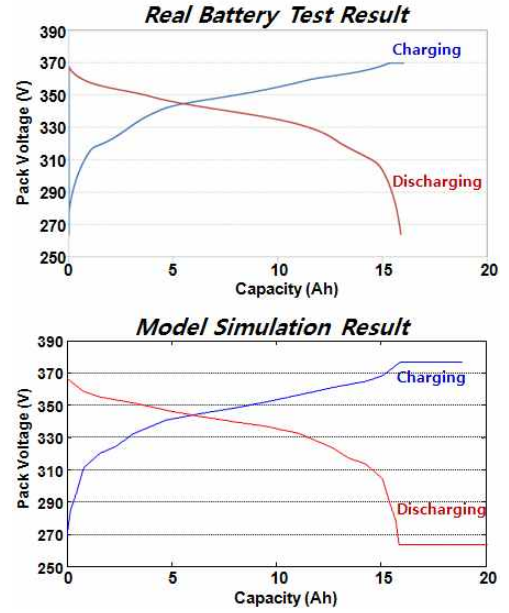


Figure 3: Battery model identification

Tested target is one of the four battery modules. As shown in figure 3, comparison results between the real battery system and the battery model show similar tendency and values.

3.2. Relay Assembly Model

The relay assembly model has a function delivering the battery terminal voltage to the DC link connected to other electric components. Because the relay assembly is designed to connect or disconnect from the battery to the DC link, the relay assembly model should be simulated as a function of connection and transient property at relay closing. The relay assembly model has been developed through rotating three sub-models using different equivalent models as below.

- Open circuit model at the relay open
- Pre-charging circuit model at the relay closing
- Short circuit model at the relay close

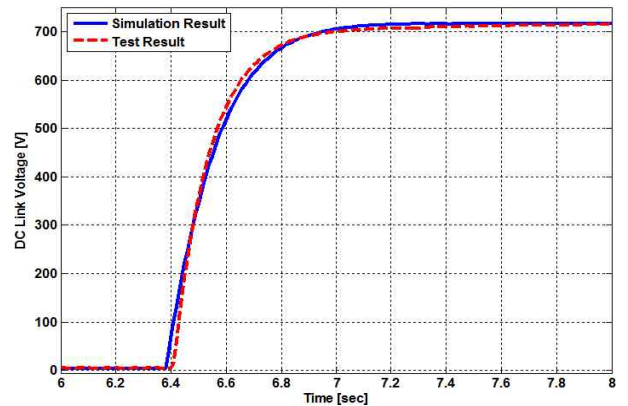


Figure 4: Relay assembly model identification

Figure 4 shows pre-charging process when the relays are closing. At the 6.4 seconds, the pre-charge and the minus relay have been closed, and then the plus relay have been also closed at about 7 seconds. As the figure 4, comparison results between the real battery system and the battery model show similar tendency and values.

3.3. BMS Model

The BMS communicates with other controllers and controls the relays in the relay assembly according to commands from the supervisory controller. And various information such as measured voltage, current, and temperature are gathered to deliver them to the supervisory controller. The developed BMS model can emulate same signals just like the real system including the control signals and the fault diagnosis signals shown in table 1.

4. PERFORMANCE EVALUATION

In order to confirm the performance of the battery system model developed in this study, a part of the characteristics of the model was confirmed based on the test results of the actual propulsion system. Then, to simulate the situation of fault occurs, fault injection simulation was performed.

4.1. System Characteristics Evaluation

In this study, to confirm the characteristics of the model, a test result of a real system's power load during the FTP-75 cycle, which has been commonly used for fuel economy test, is inserted as charged or discharged electric power to the battery system model. The FTP-75 cycle has fast and slow speed sets that is appropriate to show the loading of highly transient power, and includes resting for about 10 minutes to see the relay operation during the relay opening or closing.

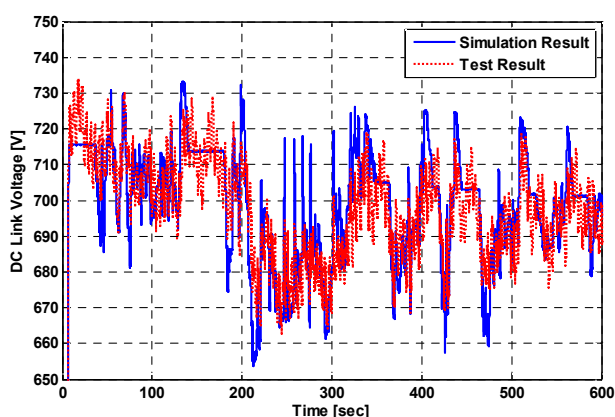


Figure 5: Battery characteristics evaluation result

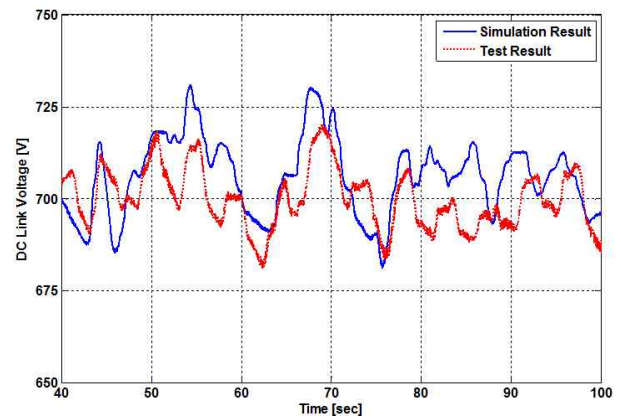


Figure 6: Battery characteristics evaluation result (part)

To confirm the battery system model, the current load has been input to the DC link terminal. And supervisory control commands such as a relay command have been input to the BMS model. In comparison with test data, the actual terminal voltage of the battery and the simulation value is generated like figure 5. And there is some part of the test data in figure 6.

The FTP-75 cycle has low and high speed region, so that battery current critically fluctuates during the cycle. Comparison results between the real battery system and the battery model show similar tendency and values. Considering the high voltage range around 700V, the result shows less than 2 percent error.

4.2. Fault Simulation

The test scenario of fault simulation that was used to confirm the performance for the fault situation is battery voltage variation for 100 seconds. The power load is applied during simulation, and the arbitrary voltage was forced at the moment of 30 seconds. With this condition, the BMS performed its own operations for fault diagnosis. Figure 7 shows the situation and results of this fault simulation.

There is a command of the supervisory controller to connect the relay at a second section, and the BMS controls the relay assembly to match this command. Therefore, it can be seen that the DC link voltage is equal to the battery voltage at this time. From the moment 30 seconds, the voltage of the battery is increased gradually. Then, a warning and a fault alarm are occurred at each conditions. Regardless to the instruction of the supervisory controller by the operation of the own behavior of the BMS, it can be seen that the relay was opened and the current flow through the battery was stopped. When a fault occurs, the DC link voltage decreases gradually, but it is possible to confirm that the battery was separated from the DC link. Through fault simulation like this, system developer can figure out how failure of a battery system can effect to other components on an electric propulsion system, and how the supervisory controller will have to go with the fault diagnosis strategy and control strategies based on the simulation results.

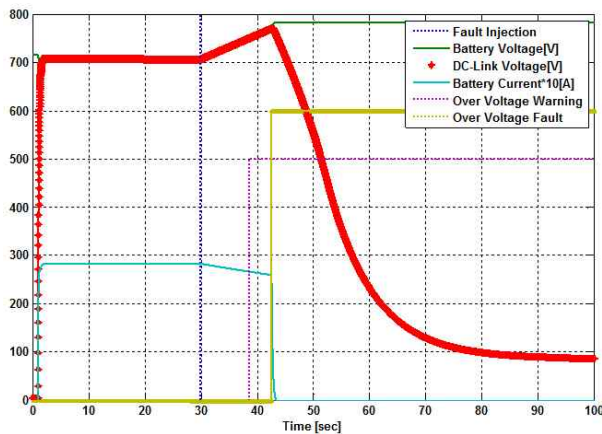


Figure 76: Fault simulation result

5. CONCLUSION

A battery system model with real-time property to evaluate control and fault diagnosis strategies has been developed. In the development process of a supervisory controller for the electric propulsion system, the developed model can be used effectively. Conclusions in this paper are as follows.

1. A detailed battery system model based on the specification and the configuration of the battery system for the electric propulsion systems with real-time properties has been implemented. Some parts in the model related to the specification of the system such as the capacity of the relay assembly element and the battery capacity have been treated with parameters for developer to change the battery system specification easily.
2. A part of the battery system model is a fault simulation model to force the physical values discretionally. Further, it has been configured to be able to accept own fault diagnosis of the BMS to behave as the actual BMS. It is possible to confirm that the fault simulation of the battery system effects the other components in the configuration of the electric propulsion system. It has purpose to reflect the design of the control strategy to the BMS or the supervisory controller.

REFERENCES

- Campbell, C.J. and Laherrere, J.H., 1998. The End of Cheap Oil, *Scientific American*, March, p. 78-83.
- Pisu, P., Serrao, L., Cantemir, C., and Rizzoni, G., 2006. Hybrid-Electric Powertrain Design Evaluation for Future Tactical Truck Vehicle Systems. *ASME 2006 International Mechanical Engineering Congress and Exposition*, pp. 271-278. November 5-10, Chicago (Illinois, USA).
- Hashimoto, T., Yamaguchi, K., Matsubara, T., Yaguchi, H., and Takaoka, T., 2010. Development of New Hybrid System for Compact Class Vehicles.

Transactions of Society of Automotive Engineers of Japan, 41 (1), 43-47.

- Xie, H. and Ding, Y., 2008. The Study of Plug-In Hybrid Electric Vehicle Power Management Strategy Simulation. *VPPC 2008 Vehicle Power and Propulsion Conference*, pp. 1-3. September 3-5, Harbin (China).
- Chunhua, X., Jigao, N., and Fenglai, P., 2011. Design and Simulation of the Power-train System for an Electric Vehicle. *AIMSEC 2011 2nd International Conference on Artificial Intelligence, Management Science and Electronic Commerce*, pp. 3868-3871. August 8-10, Zhengzhou (China).
- Johnson, V.H., 2002. Battery Performance Models in ADVISOR. *Journal of Power Sources*, 110 (2), 321-329.
- Aziz, A., Shafqat, M.S., Qureshi, M.A., and Ahmad, I., 2011. Performance Analysis of Power Split Hybrid Electric Vehicles using AUTONOMIE. *SCORED 2011 IEEE Student Conference on Research and Development*, pp. 144-147. December 19-20, Putrajaya (Malaysia).
- Doyle, M., Fuller, T.F., and Newman, J., 1993. Modeling of Galvanostatic Charge and Discharge of the Lithium/Polymer/Insertion Cell. *Journal of the Electrochemical Society*, 140 (6), 1526-1533.
- Linden, D. and Reddy, T., 2001. *Handbook of Batteries*. 3rd ed. USA: McGraw-Hill.
- Ehsani, M., Gao, I., and Emadi, A., 2009. *Modern Electric, Hybrid Electric, and Fuel Cell Vehicles: Fundamentals, Theory, and Design*. 2nd ed. USA: CRC Press.
- Jang, J.H. and Yoo, J.Y., 2008. Impedance-Based and Circuit-Parameter-Based Battery Models for HEV Power Systems. *International Journal of Automotive Technology*, 9 (5), 615-623.
- Kim, T., 2012. *A Hybrid Battery Model Capable of Capturing Dynamic Circuit Characteristics and Nonlinear Capacity Effects*. Thesis (MD). University of Nebraska.

AUTHORS BIOGRAPHY

Kyuhong Han received his BS and MS in electrical engineering (major in modeling and control of automotive propulsion systems) in 2008 and 2010, respectively, all from Hanyang University, Seoul, Korea. He joined the High Mobility Hybrid Electric Propulsion System Research Project and the Open System Integration Laboratory Project for Electric Propulsion System at Agency for Defense Development in 2010 as a research associate. Since then, he has been working in these projects on research and development of electric and hybrid electric vehicles.

NONLINEAR HYBRID SLIDING MODE CONTROL OF AN ELECTROHYDRAULIC ACTIVE SUSPENSION

Shaer, Bassel^(a), Kenné, Jean-Pierre^(b), Kaddissi, Claude^(c), Polotski, Vladimir^(d)

^(a) ^(b) ^(c) ^(d) Mechanical Engineering Department, Laboratory of Integrated Production Technologies, Université du Québec, École de Technologie Supérieure, 1100, Notre Dame Street West, Montreal QC H3C 1K3, Canada
Tel. +1-514-396-8800, FAX +1-514-396 8530,

^(a)bassel.shaer.1@ens.etsmtl.ca, ^(b)jean-pierre.kenne@etsmtl.ca, ^(c)claudio.kaddissi@etsmtl.ca,
^(d)Vladimir.Polotski@etsmtl.ca

ABSTRACT

This paper introduces the multi-objective control and modeling of a nonlinear electrohydraulic active suspension. By using a hybrid control algorithm, the objective of tracking a desired force and position was optimized to reach a satisfactory performance. When designing such a controller, a compromise needed to be made between the ride quality and the road handling. The controller structure was built in three stages, in which the sliding mode approach was used to produce the proper control signal that satisfies the requested control objective. The simulation results for position control showed that the controller was able to isolate the passengers from the road irregularities, but with significant transmitted force. In order to reduce the transmitted force to passengers, a force sliding mode controller was developed, but the passengers' vertical motion was unsatisfactory. A hybrid control algorithm was developed to track a desired vertical position and to reduce the transmitted force to the passengers at the same time. The two controllers have been added by two low pass filters with a variable gain to give priority to the force controller to react in the case of high transmitted force. These filters delay the control signals in order to prevent the singularity in simulation. The simulation results show that hybrid sliding mode control achieved a very good compromise between the two objectives without involving complex control strategies.

Keywords: hybrid control, sliding mode, position control, force control, active suspension system

1. INTRODUCTION

Recent research in electrohydraulic systems (EHS), which is very popular due to its high force-to-weight ratio and fast response, concentrates on the control of position and force separately. Most applications in industry, like robots and production machines, require accuracy in position control with some considerations to produced force.

Some applications require force tracking, but with some position limitations. From this perspective, researchers concentrated on the position control (Choi, Tafazoli et al 1998, Avila et al 2004, Indrawanto et al 2011, Rahmat et al 2011).

Many control strategies have been used to track the position of an electrohydraulic system. One of the most interesting theories is the variable structure control, or sliding mode control (SMC). The sliding mode control is known for its robustness against uncertainties, and is applicable to linear systems as well as nonlinear systems (Hashemipour et al 2009). Since the position control often leads to an undesired force magnitude in an electrohydraulic active suspension system, it is necessary to control the force magnitude by different control strategies. In (Chantranuwathana and Peng 1999), the problem of force tracking has been divided into two parts: the first part is considered as a main loop for producing the desired force by an LQ controller, and the second part is an adaptive robust controller to track the desired force under uncertainties in the system parameters.

In electrohydraulic systems, system performance at high frequencies can be deteriorated due to unmodeled dynamics. This was improved in the work of (Chantranuwathana and Peng 2000), who considered the effect of unmodeled dynamics of servo valve and the delay of the applied control signal in their algorithm. On the other side, estimation of parameters with feedback linearization has a significant effect on the position control. In (Angue-Mintsa et al 2011), an adaptive feedback linearization is applied in order to feedback estimated parameters to improve the control operation. The principle of linking two loops has been used by (Sam and Hudha 2006). An outer loop was used to calculate the force reference and an inner loop was used to ensure a small tracking error. A similar concept was used in (Shi and Liu 2011), where a double loop in auto disturbance rejection control is designed to ensure position control and

force control at the same time. As mentioned previously, when the attention was more focused on position control, the transmitted force was not acceptable. Therefore, the researchers started to express the problem differently, as in (Nguyen et al 2000), where a hybrid force/position control with sliding mode was proposed. The experimental results that were obtained showed good performance, but the desired force was chosen as a classical function of the position error by means of constant gains. This means that, if the tracking position error is a little high, the desired force will exceed the permitted limit. This is clear in the performance: they have a high tracking force error with position errors measuring many millimeters. Therefore, the position should be tracked by a robust controller rather than by a direct relation between force error and position error. A more complicated design was used by (Priyandoko et al 2009): four loops to accomplish hybrid control of position and force by applying a novel skyhook and adaptive neuro-active force control technique. They used a neural network with an adaptive algorithm to approximate the mass estimation and inverse dynamic of the actuator.

The technique produced good results for force tracking, but the position error was still high. In addition, the nonlinearity in the actuator was not modeled when designing the force controller. Another concept for controlling position and force was accomplished by (Assadsangabi et al 2009) using two references as the ideal skyhook model and ground skyhook model, with the condition of having knowledge of road perturbations. The two control signals were added linearly to form a final control signal. The performance was good in terms of achieving its objectives, but controlling both the position and acceleration of two masses was considerably weak. Trying to accomplish good acceleration/position tracking by controlling the movement of two masses is useless because of the high nonlinearity in the pressure dynamic equation.

In addition, the damping coefficient error of the selected references was not compensated, which yields to degradation in the performance.

This paper is organized as follows: the first section introduces the problem and describes the state of the art. The second section presents the modeling of the electrohydraulic active suspension system. The third section describes the position SMC controller. The fourth section shows the force SMC controller. Section 5 is dedicated to the main contribution of this paper, namely the hybrid force-position controller. A comparison between a classical PID and a hybrid SMC controller is presented in section 6. The last section presents a conclusion and a recap of our work.

2. ELECTROHYDRAULIC ACTIVE SUSPENSION MODELING

Figure 1 shows a quarter-car model of an electrohydraulic active suspension. The control cylinder is placed between the car mass and the tire mass in order to isolate the car body from road irregularities transmitted via the car tire.

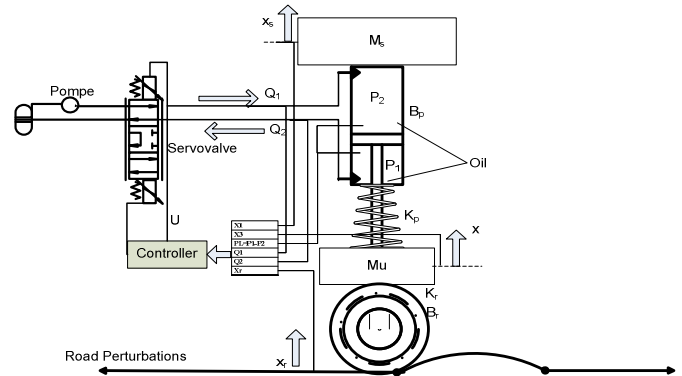


Figure 1: Active Suspension Bench

The active suspension mathematical model is derived from the mathematical model of an electrohydraulic system added to passive suspension.

The flow rate from and to the servo valve through the valve orifices, assuming symmetric and matched orifices with a small leakage, is given by (Merritt 1967):

$$Q_1 = Q_2 = C_d x_v \sqrt{\frac{P_s - \text{sign}(x_v) * P_L}{\rho}} \quad (1)$$

The sign function, which expresses the change of the fluid flow direction, can be replaced by a differentiable function for numerical simulations, as suggested in (Kaddissi et al 2009). The compressibility equation that represents the load pressure dynamics is as follows:

$$\dot{P}_L = \frac{2\beta}{V_0} \left\{ C_d x_v \sqrt{\frac{P_s - P_L * \text{sign}(x_v)}{\rho}} - L * P_L - A(\dot{x}_s - \dot{x}) \right\} \quad (2)$$

The sigm function is defined as:

$$\text{sigm}(x_v) = \frac{1 - e^{-a x_v}}{1 + e^{-a x_v}}$$

We therefore have:

$$\text{sigm}(ax) = \begin{cases} 1 & \text{if } ax \rightarrow \infty \\ 0 & \text{if } ax \rightarrow 0 \\ -1 & \text{if } ax \rightarrow -\infty \end{cases}$$

$$\text{and } \frac{d(\text{sigm}(a x_v))}{dt} = \frac{2 a e^{-a x_v}}{(1 + e^{-a x_v})^2}$$

We now proceed to identify the car dynamics, using Newton's second law:

$$M_s \dot{x}_s = -k_p(x_s - x) - B_p(\dot{x}_s - \dot{x}) + A P_L \quad (3)$$

$$M_u \dot{x} = k_p(x_s - x) + B_p(\dot{x}_s - \dot{x}) - k_r(x - x_r) - B_r(\dot{x} - \dot{x}_r) - A P_L \quad (4)$$

Rewriting equations (2), (3) and (4) in terms of chosen variables $x_i; i = 1 \dots 6$, we obtain a model as in (Kaddissi et al 2009). We propose another change of variables in order to include the suspension deflection, which is the difference between the car body position and the tire position. The control objective is to prevent this variable from hitting the imposed limits. The new state variables are:

$$y_1 = x_1, y_2 = x_2, y_3 = x_1 - x_3, y_4 = x_2 - x_4, y_5 = x_5, \\ y_6 = x_6$$

The model can be rewritten as follows:

$$\left. \begin{cases} \dot{y}_1 = y_2 \\ \dot{y}_2 = -a_0 y_3 - b_0 y_4 + a_1 y_5 \\ \dot{y}_3 = y_4 \\ \dot{y}_4 = -A_1 y_3 - A_2 y_4 + A_3 y_5 + b_1 \dot{y}_r + h_1 y_r \\ \dot{y}_5 = \frac{J_1}{f(\cdot)} (-A y_4 - L y_5 + C_d y_6 g(\cdot)) \\ \dot{y}_6 = \frac{1}{\tau} (-y_6 + k u) \end{cases} \right\} \quad (5)$$

Where:

$$A_1 = a_0 + d_0, A_2 = b_0 + d_1$$

$$A_3 = C_{10} + a_1, A_4 = J_1 * A$$

$$A_5 = J_1 * L, A_6 = J_1 * C_d$$

$$f(\cdot) = V_0^2 - A^2 y_3^2$$

$$g(\cdot) = \sqrt{\frac{P_s - \text{sigm}(y_6) y_5}{\rho}}$$

3. POSITION TRACKING CONTROL

The sliding mode is a nonlinear control strategy in which there is an invariant set that attracts every trajectory at the phase plan. Therefore, it is determined that $S = 0$ is a positive invariant set to attract the error trajectories. The control problem then reduces to (i) driving the system to this surface and (ii) ensuring that the system remains on this surface. We will calculate the command with the original coefficient of the system model. We first choose the surface S as:

$$S = c_1 y_1 + c_2 \dot{y}_1 + c_3 \ddot{y}_1 + c_4 \dddot{y}_1 \quad (6)$$

We then calculate the derivative of y_1 (7) to use it in equation (6)

$$\left. \begin{cases} \dot{y}_1 = y_2 \\ \ddot{y}_1 = \dot{y}_2 = -a_0 y_3 - b_0 y_4 + a_1 y_5 \\ \dddot{y}_1 = \ddot{y}_2 = -a_0 \dot{y}_3 - b_0 \dot{y}_4 + a_1 \dot{y}_5 \\ \quad = -a_0 y_4 - b_0 (-A_1 y_3 - A_2 y_4 + A_3 y_5 + b_1 \dot{y}_r + h_1 y_r) \\ \quad + a_1 (J_1 (-A y_4 - L y_5 + C_d y_6 g(\cdot))) \\ \quad = -b_0 A_1 y_3 - (a_0 - b_0 A_2 + a_1 J_1 A) y_4 + (-A_3 b_0 - a_1 L J_1) y_5 \\ \quad + a_1 C_d J_1 g(\cdot) y_6 - b_0 b_1 \dot{y}_r - b_0 h_1 y_r \end{cases} \right\} \quad (7)$$

Replacing (7) in (6) yields:

$$\left. \begin{cases} S = c_1 y_1 + c_2 y_2 + (-a_0 c_3 + c_3 b_0 A_1) y_3 \\ \quad - (-c_4 a_0 + c_3 b_0 - c_4 b_0 A_2 + c_4 a_1 J_1 A_2) y_4 \\ \quad - (A_3 b_0 c_4 - c_3 a_1 - c_4 a_1 J_1 L) y_5 \\ \quad + c_4 a_1 C_d J_1 g(\cdot) y_6 - c_4 b_0 b_1 \dot{y}_r \\ \quad - c_4 b_0 h_1 y_r \end{cases} \right\} \quad (8)$$

Now we take the derivative of S to realize the reaching condition (Fallaha et al 2011):

$$\dot{S} = -K_{sw} * \text{sign}(S) \quad (9)$$

$$\left. \begin{cases} \dot{S} = c_1 \dot{y}_1 + c_2 \dot{y}_2 + (-a_0 c_3 + c_3 b_0 A_1) \dot{y}_3 \\ \quad - (-c_4 a_0 + c_3 b_0 - c_4 b_0 A_2 + c_4 a_1 J_1 A_2) \dot{y}_4 \\ \quad - (A_3 b_0 c_4 - c_3 a_1 - c_4 a_1 J_1 L) \dot{y}_5 \\ \quad + c_4 a_1 C_d J_1 g(\cdot) \dot{y}_6 + c_4 a_1 C_d J_1 \dot{g}(\cdot) y_6 \\ \quad - c_4 b_0 b_1 \ddot{y}_r - c_4 b_0 h_1 \dot{y}_r \\ \quad = -K_{sw} * \text{sign}(S) \end{cases} \right\} \quad (10)$$

We calculate the derivative of $g(\cdot)$ and replace it in equation (10):

$$\left. \begin{cases} \dot{g}(\cdot) = \frac{1}{\sqrt{\rho}} * \frac{-[\text{sigm}(y_6) * y_5 + \text{sigm}(y_6) \dot{y}_5]}{2\sqrt{P_s - \text{sigm}(y_6) y_5}} \\ \quad = \frac{1}{\sqrt{\rho}} * \frac{-\left[\frac{2a_2 e^{-ay_6}}{(1 + e^{-ay_6})^2} * y_5 + \text{sigm}(y_6) \dot{y}_5\right]}{2\sqrt{P_s - \text{sigm}(y_6) y_5}} \end{cases} \right\} \quad (11)$$

To simplify the obtained expression, we choose:

$$\left. \begin{cases} A_{41} = -c_4 a_0 + c_3 b_0 - c_4 b_0 A_2 + c_4 a_1 J_1 A \\ A_{42} = A_3 b_0 c_4 - c_3 a_1 - c_4 a_1 J_1 L \end{cases} \right\} \quad (13)$$

We replace equation (13) in (12) to obtain:

$$\left\{ \begin{array}{l} \dot{S} = c_1 y_2 + [-c_2 a_0 + A_1 * A_{41}] y_3 \\ + [-b_0 c_2 - a_0 c_3 + b_0 c_4 A_1 + A_1 * A_{41} + J_1 A_1 A] y_4 \\ + [-c_2 a_1 - A_3 A_{41} + L A_{42} J_1] y_5 - \frac{c_4 a_1 C_d J_1 g(\cdot)}{\tau} y_6 \\ + c_4 a_1 C_d J_1 \dot{g}(\cdot) y_6 - A_{42} h_1 y_r - A_{42} \dot{h}_1 y_r \\ - c_4 b_0 b_1 \ddot{y}_r - c_4 b_0 h_1 \ddot{y}_r + \frac{c_4 a_1 C_d J_1 g(\cdot) K}{\tau} U_{P_{SMC}} \\ = -K_{sw} * \text{sign}(S) \end{array} \right\} \quad (14)$$

We extract the control signal $U_{P_{SMC}}$ to become:

$$\left\{ \begin{array}{l} U_{P_{SMC}} = \frac{\tau}{c_4 a_1 C_d J_1 g(\cdot) K} * \\ \left[\begin{array}{l} -c_1 y_2 - [-c_2 a_0 + A_1 * A_{41}] y_3 \\ - [-b_0 c_2 - a_0 c_3 + b_0 c_4 A_1 + A_1 * A_{41} + J_1 A_1 A] y_4 \\ - [-c_2 a_1 - A_3 A_{41} + L A_{42} J_1] y_5 + \frac{c_4 a_1 C_d J_1 g(\cdot)}{\tau} y_6 \\ - c_4 a_1 C_d J_1 \dot{g}(\cdot) y_6 + A_{42} h_1 y_r + A_{42} \dot{h}_1 y_r \\ + c_4 b_0 b_1 \ddot{y}_r + c_4 b_0 h_1 \ddot{y}_r - K_{sw} * \text{sign}(S) \end{array} \right] \end{array} \right\} \quad (15)$$

Therefore, the total control signal for the position control is:

$$U_{P_{SMC}} = U_{P_{equ}} + U_{P_{sw}} \quad (16)$$

We can write \dot{S} in the following form:

$$\dot{S} = h(y) + O(y) U_{P_{sw}} \quad (17)$$

Suppose that $h(y), O(y)$ satisfies the inequality for some known function $\rho(y)$:

$$\frac{h(y)}{O(y)} \leq \rho(y) \quad \forall y \in R^2 \quad (18)$$

Where: $O(y) \geq O_0 \geq 0$

To prove the convergence of the sliding mode, we consider the derivative of the distance of the point from the sliding mode:

$$\left\{ \begin{array}{l} V = \frac{1}{2} S^2 \\ \dot{V} = S * \dot{S} = S * (h(y) + o(y) * U_{P_{smc}}) \\ \leq O(y) * |S| * \rho(y) + O(y) * S * U_{P_{smc}} \end{array} \right\} \quad (19)$$

Taking:

$$U_{P_{smc}} = -\beta(y) * \text{sgn}(S) \quad (20)$$

$\beta(y) \geq \rho(y) + \beta_0$ Where $\beta_0 > 0$,

$$\text{sgn}(S) = \begin{cases} 1 & \text{if } S > 0 \\ 0 & \text{if } S = 0 \\ -1 & \text{if } S < 0 \end{cases}$$

This yields:

$$\left\{ \begin{array}{l} \dot{V} = O(y) |S| \rho(y) \\ - O(y) S (\rho(y) + \beta_0) \text{sign}(S) \\ = -O(y) \beta_0 |S| \leq -O_0 \beta_0 |S| \end{array} \right\} \quad (21)$$

Therefore, the trajectory reaches the manifold $S = 0$ in finite time, and once on the manifold, it cannot leave it, as seen from the inequality $\dot{V} \leq -O_0 \beta_0 |S|$.

3.1. Position SMC control results:

We built our mathematical model in Matlab. The simulation was done with a small sampling time (0.0001 sec). In Figure 2, the perturbation signal is 10 cm, and the passenger seat position is deviated to 3 cm. This shows that the SMC controller exhibits a good performance. However, the force transmitted to the passengers is approximately 3400 N, which is too high (Figure 3). The control signal is well shaped, with no significant chattering.

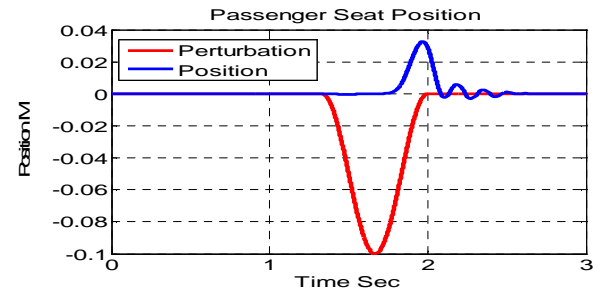


Figure 2: Sprung Mass Position.

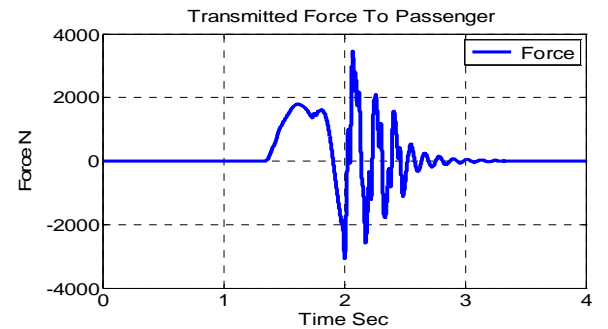


Figure 3: Force Transmitted To Passenger.

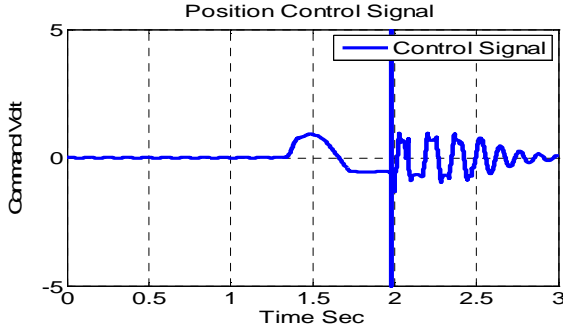


Figure 4: Control Signal

4. TRANSMITTED FORCE CONTROL

The force tracking is also accomplished by using the sliding mode controller. The surface of SMC is chosen as:

$$S = C_1(F - F_{des}) = C_1A(y_5 - y_{5des}) \quad (22)$$

The desired force has been chosen as follows (Sohl and Bobrow 1999):

$$F_{des} = M_v * ACC_{des} - K_v (\dot{y}_1 - \dot{y}_{1des}) - K_p (y_1 - y_{des}) \quad (23)$$

Where: $F_{des} = A * y_{5des}$, this equation is derived from the car dynamics equations. When the error tracking position is zero, we will have $F_{des} = M_v * ACC_{des}$. This equation means that, when we track a desired position, the force being generated represents the desired force to be tracked. We derive S as mentioned above in equation (9) to obtain the following control signal:

$$\left. \begin{aligned} \dot{S} &= C_1A(\dot{y}_5 - \dot{y}_{5des}) \\ &= C_1A \left[\frac{J_1}{f(\cdot)} (-Ay_4 - Ly_5 + C_d y_6 g(\cdot)) - y_{5des} \right] \\ &= -K_{sw} * \text{sign}(S) \end{aligned} \right\} (24)$$

From equation (5), we have $\dot{y}_6 = \frac{1}{\tau} (-y_6 + k U_{Fsmc})$

This yields:

$$y_6 = -\tau \dot{y}_6 + k U_{Fsmc} \quad (25)$$

Replacing (20) in (19), we obtain:

$$\begin{aligned} \dot{S} &= C_1A \left[\frac{J_1}{f(\cdot)} (-Ay_4 - Ly_5 + C_d g(\cdot)) \right. \\ &\quad \left. * (-\tau \dot{y}_6 + k U_{Fsmc}) - y_{5des} \right] \\ &= \frac{C_1AJ_1}{f(\cdot)} (-Ay_4 - Ly_5 - C_d g(\cdot) \tau \dot{y}_6) \\ &\quad + C_d g(\cdot) k U_{Fsmc} - C_1A y_{5des} \\ &= -K_{sw} * \text{sign}(S) \end{aligned} \quad (26)$$

Therefore, the equivalent control can be written as:

$$U_{fequ} = - \frac{\frac{C_1AJ_1}{f(\cdot)} (-Ay_4 - Ly_5 - C_d g(\cdot) \tau \dot{y}_6) - C_1A y_{5des}}{\frac{C_1AJ_1 C_d g(\cdot) k}{f(\cdot)}} \quad (27)$$

The switching control:

$$U_{fsw} = - \frac{f(\cdot)}{C_1AJ_1 C_d g(\cdot) k} * k_{sw} * \text{sgn}(S) \quad (28)$$

The total control signal for force tracking U_{Fsmc} :

$$U_{Fsmc} = U_{fequ} + U_{fsw} \quad (29)$$

In simulation, the force controller demonstrated a significant force reduction, and the amplitude of the force transmitted to the passenger was reduced to 1200 N (Figure 5). In comparison with the position controller, the passenger force is reduced by 64%, which is a good index of controller efficiency. In terms of the position of the passenger's seat, there is no significant improvement or deterioration (Figure 6). Figure 7 shows the corresponding control signal with a maximum of 0.5 volt.

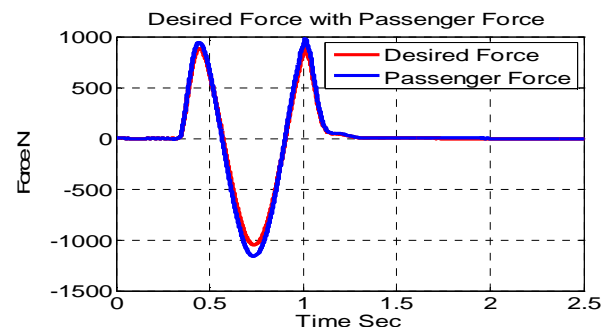


Figure 5: Force Tracking with SMC.

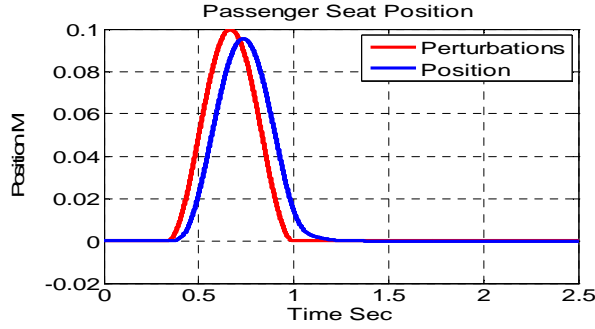


Figure 6: Sprung Mass Position

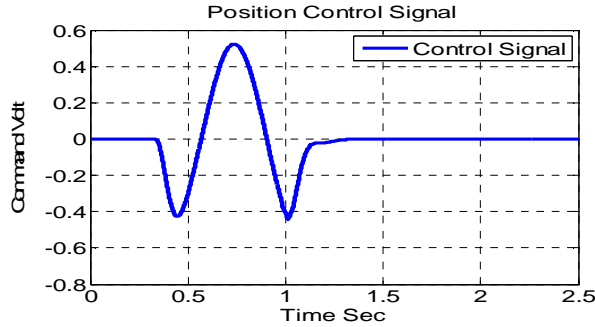


Figure 7: Control Signal

5. HYBRID POSITION-FORCE CONTROL

This section describes the main contribution of this paper, which proposes the hybrid multi-objective controller that is designed to achieve both a reduction of the passengers' vertical motion and a reduction of the force transmitted to them at the same time. The control signal is given by:

$$U_{tot} = \frac{\alpha_1}{s + \alpha_2} U_{P_{SMC}} + K1 \frac{\alpha_3}{s + \alpha_4} U_{F_{SMC}} \quad (30)$$

Where:

$$K1 = \frac{F_{passenger}}{\text{force threshold}} = \frac{M_s * \ddot{x}_s}{\text{force threshold}}$$

K1: is a variable gain that is used to give a priority to the control force when the force transmitted to the passenger $F_{passenger}$ increases. Therefore, the priority is to control the force by increasing the control signal of the force controller. The force controller responds directly to the force change and reacts to keep the forces within their limits. The force threshold is chosen in such a way as to keep the transmitted force, the position of sprung mass and the control signal within acceptable limits.

Increasing the threshold generates an increase in the position of sprung mass and the transmitted force.

Using high values for the threshold yields an unstable oscillatory performance.

We use two pass filters $\frac{\alpha_1}{s + \alpha_2}$ $\frac{\alpha_3}{s + \alpha_4}$ in order to

accomplish a smooth merging of two controllers and to prevent the singularity that can occur in such highly nonlinear systems.

α_1, α_3 are gains of the low pass filter that give priority to the corresponding filter.

α_2, α_4 are designed to select the bandwidth.

Increasing these parameters to high values could generate instability in the system response.

The bandwidth of the filters should be also greater than the bandwidth of the active suspension system in order to accomplish full control of a wide range of the system's bandwidth (Wright 1983).

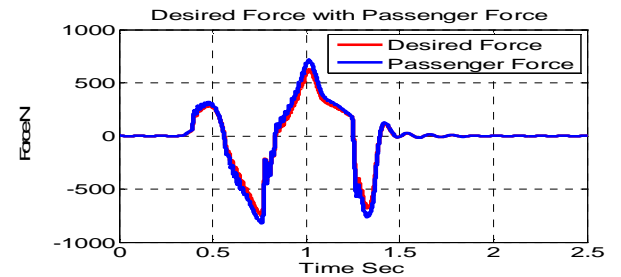


Figure 8: Force Tracking.

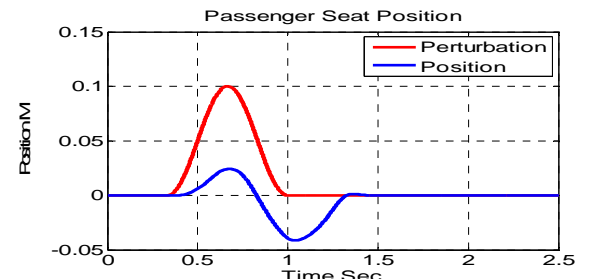


Figure 9: Sprung Mass Position.

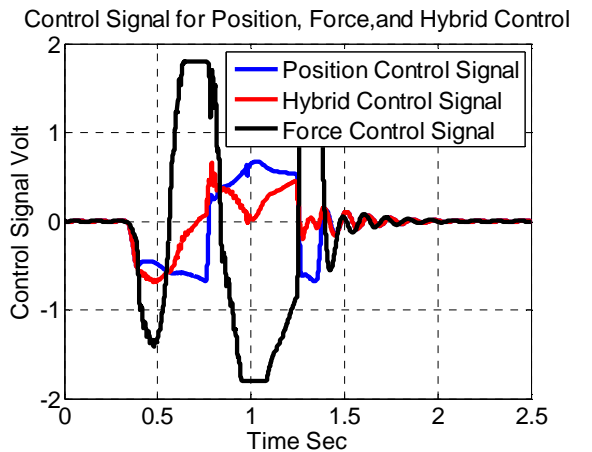


Figure 10: Control Signal

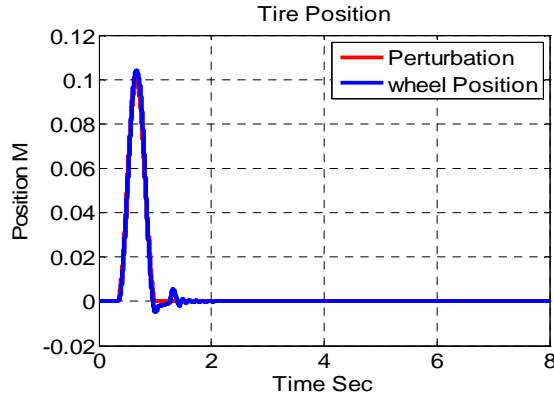


Figure 11: Unsprung Position

Figure 8 shows that the force transmitted to the passenger is limited to 717 N, with a small tracking error. The hybrid control also reduced the perturbation from 10 cm to 4.5 cm, which is another good index of controller robustness and performance as illustrated in Figure 9.

The control signal reaches a maximum of 0.6 volts, as seen in Figure 10. The road holding is proven to be good, as seen in Figure 11, in which the tire is attached to the road along with the perturbations.

6. COMPARISON OF THE CONVENTIONAL PID CONTROLLER WITH THE HYBRID SMC CONTROLLER

We will use a conventional PID for controlling the position of the sprung mass, and compare it with our proposed hybrid SMC. We chose the PID control because it is the most popular controller in the industry. The simulation results show that our proposed hybrid SMC exceeds the performance of the PID by a significant margin. The PID was designed using NCD Toolbox Simulink to produce optimal gains. We began by linearizing the nonlinear model, which gives us:

$$A = \begin{pmatrix} 0 & 1 & 0 & 0 & 0 & 0 \\ -a_0 & -b_0 & a_0 & b_0 & a_1 & 0 \\ 0 & 0 & 0 & 1 & 0 & 0 \\ d_0 & d_1 & -d_0 - h_1 & -d_1 - b_1 & -c_1 & 0 \\ 0 & -J_1 A & 0 & J_1 A & -J_1 L & -J_1 c_d (P_s/\rho)^{1/2} \\ 0 & 0 & 0 & 0 & 0 & -1/\tau \end{pmatrix},$$

$$B = \begin{pmatrix} 0 \\ 0 \\ 0 \\ 0 \\ 0 \\ K_v/\tau \end{pmatrix}, C = [1 \ 0 \ 0 \ 0 \ 0 \ 0], D = [0].$$

The PID gains are then applied to the nonlinear model. The results of the simulation show that the passenger's vertical motion has been reduced to zero faster and with smaller amplitude by the hybrid SMC controller than the PID (Figure 12). The transmitted force to a passenger with the PID has a longer settling time than with the SMC, and that is not very comfortable (Figure 13). In terms of the force

amplitude, the hybrid SMC produces a smaller controlled force in comparison with the PID due to the force controller, which acts on behalf of the position at that stage.

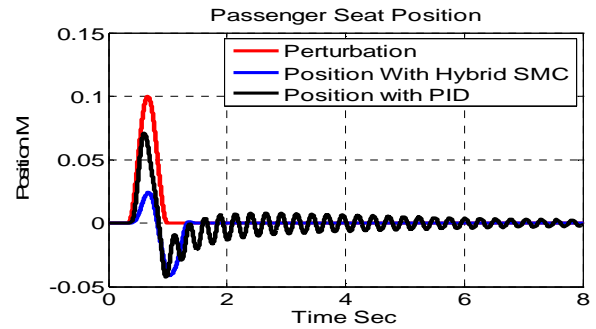


Figure 12: Sprung Mass Position

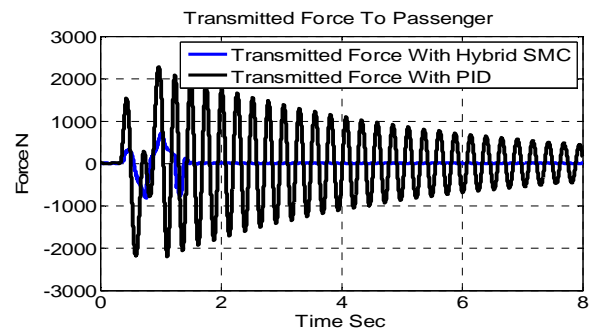


Figure 13: Transmitted Force to Passenger

7. CONCLUSION

This paper presents a force/position control for an active suspension system. Position control was achieved using the SMC controller, and the perturbations were reduced enough, but the force transmitted to the passenger was not acceptable. The resulting control signal has a slight chattering in simulation, but it is still within the acceptable limit. For reducing the transmitted force to the passenger, a force controller was developed to achieve good force tracking, but it did not produce a significant improvement with respect to the passenger seat position. In terms of force tracking, the desired force was derived from a desired acceleration. The hybrid force/position controller was developed and applied. Good force tracking was achieved with an attenuation of the vertical seat perturbations. Using this hybrid controller, the passenger seat was isolated from road irregularities with good road holding. The control signal that was produced has a combined form in order to fit the requirements. In this project, two objectives were achieved with a hybrid controller by integrating the advantages of each controller (position, force) and applying them to the system. In a future project, an application of our integrated controller in real time will be tested and applied to the active suspension bench in order to verify the validity of the proposed controller.

APPENDIX

A. Active suspension parameters

P_1, P_2	Pressure at cylinder's chambers	$P_s = P_1 + P_2$
β	Effective bulk modulus	7.995e8 N/m ²
L	Coefficient of total leakage due to pressure	9.047e-13 m ⁵ /Ns
A	Piston area	3.35e-4 m ²
P_L	Load pressure	$P_2 - P_1$
P_s	Supply pressure	103.4e5 N/m ²
ρ	Hydraulic fluid density	867kg/m ³
V_0	Actuator volume in one actuator chamber	135.4e-6 m ³
C_d	Flow discharge coefficient	0.63
M_u	Unsprung mass	59 kg
M_s	Actuator mass	290 kg
k_r	Tire spring stiffness	190,000 N/m
k_p	Load spring stiffness	16,812 N/m
B_r	Tire viscous damping	800 Ns/m
B_p	Load viscous damping	800 Ns/m
τ	Servo-valve time constant	0.01s

B. Controllers Parameters.

Position Control Parameters		
C_1	Gains sliding surface	125000
C_2	Gains sliding surface	7500
C_3	Gains sliding surface	150
C_4	Gains sliding surface	1
a	Sigmoid function	2000
K_{sw}	Switching gain	330000
Force Control Parameters		
C_1	Gains sliding surface	10000
PID Control Parameters		
K_p	Proportional gain	5
K_i	Integral gain	0.4
K_d	Derivative gain	0.1

C. Systems variables

x_r	External unknown perturbation
\dot{x}_r	Speed of perturbation signal
$x_1 = x_s$	Vertical position of the car body
\dot{x}_s	Piston speed
$x_2 = \dot{x}_1$	Vertical speed of the car body
$x_3 = x_u$	Vertical position of the car wheel
$x_4 = \dot{x}_3$	Vertical speed of the car wheel
$x_5 = P_L$	Pressure difference in the circuit
$x_6 = x_v$	Area of the servo valve orifice
U	Control signal

REFERENCES

- Angue-Mintsa, H., Venugopal, R., et Kenne, J. P., and Belleau, C. 2011. Adaptive Position Control of an Electrohydraulic Servo System with Load Disturbance Rejection and Friction Compensation. *Journal of Dynamic Systems, Measurement, and Control* 133(6), 064506-1 - 064506-8
- Assadsangabi, B., Eghtesad, M., Daneshmand, F., and Vahdati, N., 2009. Hybrid sliding mode control of semi-active suspension systems. *Smart Materials and Structures* 18(12), 1-10.
- Avila, M. A., Loukianov, A. G., and Peter D.L., 2004. Electro-hydraulic actuator trajectory tracking. *Proceedings of the American Control Conference*, pp.2603-2608, June 2004, Boston, USA.
- Chantranuwathana, S. and Peng, H. 1999. Force tracking control for active suspensions – theory and experiments. *Proceedings of the IEEE International Conference on Control Applications*, pp. 442-447. August 22-27, Hawai’I, USA.
- Chantranuwathana, S. and Peng, H, 2000. Practical adaptive robust controllers for active suspensions. *Proceedings of the 2000 ASME International Congress and Exposition*, Orlando, Florida, USA.
- Choi, J. 2011 .Robust control of hydraulic actuator using back-stepping sliding mode controller. *Proceedings of the 28th ISARC*, pp. 1261-1266, Jun 29- Jul 2, Seoul, Korea.
- Fallaha, C. J., Saad, M., Kanaan, H. Y., and Al-Haddad, K. 2011.Sliding-mode robot control with exponential reaching law. *IEEE Transactions on Industrial Electronics* 2011, 58(2), 600-610.
- Hashemipour, H., Amiri, M. Mirzaei, M., and Maghoul, A., 2009. Nonlinear control of vehicle active suspension considering actuator dynamics. *Second International Conference on Computer and Electrical Engineering*, pp. 362-366. December 28-30. Dubai, UAE.
- Indrawanto, T., Nurprasetio, P., Bagiasna, K., Suharto, D., Tjahjowidodo, T., Nik,W,W., Ahmad,A., Sulaiman,O., Syahrullail,S., 2011.Sliding Mode Control of a Single Rigid Hydraulically Actuated Manipulator. *International Journal of Mechanical and Mechatronics Engineering*, 11(5), 19-25.
- Kaddissi, C., Saad, M., Kenne, Jean-Pierre., 2009. Interlaced backstepping and integrator forwarding for nonlinear control of an electrohydraulic active suspension. *Journal of Vibration and Control* 15(1), 101-131.
- Merritt, H. E. 1967. Hydraulic control systems, Wiley, New York.
- Nguyen, H. Q., Ha, Q. P., Rye, D. C.,Durrant-whytel, H. F., 2000. Force/position tracking for electrohydraulic systems of a robotic excavator. *Decision and Control, 2000. Proceedings of the 39th IEEE Conference*, pp. 5224-5229.December Sydney, Australia
- Priyandoko, G., Mailah, M., and Jamaluddin, H., 2009. Vehicle active suspension system using skyhook adaptive neuro active force control. *Mechanical Systems and Signal Processing*, 23(3), 855-868.
- Rahmat, M,F., Zulfatman, A,R., and Husain, K. I., Sam, Y. M., Ghazali, R., and Rozali, S. M., 2011. Modeling and controller design of an industrial hydraulic actuator system in the presence of friction and internal leakage. *International Journal of the Physical Sciences*, 6(14), 3502-3517.
- Sam, Y. M. and Hudha, K., 2006. Modelling and force tracking control of hydraulic actuator for an active suspension system. *First IEEE Conference on Industrial Electronics and Applications*, pp.24-26 May 2006, Piscataway, NJ, USA.
- Shi, M., Liu, X., and Shi, y.,2011. Research on enhanced ADRC algorithm for hydraulic active suspension. *Proceedings of the International IEEE Conference on Transportation, Mechanical, and Electrical Engineering*, pp. 1539-1543. December 16-18, Changchun, China.
- Sohl, G. A., Bobrow, J. E. 1999. Experiments and simulations on the nonlinear control of a hydraulic servosystem. *IEEE Transactions on Control Systems Technology*, 7(2), 238-247.
- Tafazoli, S., Clarence, S., and Peter, L., 1998. Tracking control of an electrohydraulic manipulator in the presence of friction. *IEEE Transactions on Control Systems Technology*, 6(3), 401-411.
- Wright, P. G., 1983. The influence of aerodynamics on the design of Formula One racing cars. *International Journal of Vehicle Design*, 3(4), 383-397.

DYNAMIC MODELING AND CONTROL OF OFF-ROAD TRUCK USING BOND GRAPHS

Ashish Gupta¹, Vikas Rastogi²

¹ Assistant professor in Mechanical Engineering department

² Professor in Mechanical Engineering department

¹Krishna Engineering College, Mohan Nagar, Ghaziabad

²Delhi Technical University, New Delhi

ashish.j001@gmail.com, rastogivikas@yahoo.com

ABSTRACT

The truck vibration problems have increase in recent years due to the rapid industrlization and demand for the modern machines and product to transfer from one place to the other. Vibration in modern off-road road trucks can affect driver comfort, cargo safety, equipment wear and productivity. This work presents the modeling of off road truck using bond graphs. The vehicle system is comprised of cab, cargo, base frame, suspension system and pneumatic tires. In this work, dynamic behavior of the truck has been presented using bond graphs, which include the wheel/tires, axle/suspension and frame of the vehicle. The vehicle is modeled with the integration of rigid bodies that are allowed to move the dimensional space subject to forces and moments. This works also incorporating Proportional Integrated Derivative (PID) control in the suspension system of truck. These controllers are frequently designed in the frequency domain, and on the hypothesis of linearity. These control systems reduce the deflection of suspension system and increase comfort level of driver.

Keywords: bond graph modeling, ride comfort, proportional control.

1. INTRODUCTION

Modeling and simulation has an increasing importance in the development of complex, large mechanical systems. In areas like road vehicles (Demic and Lukic 2002; Filippini 2004; Pacejka 1975), rail vehicles, high speed mechanisms, industrial robots and machine tools (Paul 1975), simulation is an inexpensive way to experiment with the system and to design an appropriate control system. Generally, modeling is an expensive way to experiment with different system design concepts and to aid the design development of an appropriate control system. There are different approaches to model a vehicle. 1) Ignoring body flexibility by using a lumped mass model, 2) Modeling the frame as a regular free-free beam and calculating, estimating or measuring modal masses and stiffness's, and 3) Modeling the entire vehicle using the finite element method (Ibrahim 1996; Goodarzi and Jalali 2006; Yi 2000; Cao 2005). As in most other dynamic systems, the analyst is faced with a spectrum of possible model complexity. Traditionally, linear models have been used, based on the well-known partial

differential equation for transverse vibration $w(x, t)$ of a free-free beam subject to separation of variables (Karnopp 2006). Bond graph models of a bus and tractor-trailer were created in ref. (Margolis and Edeal 1989), in which small vertical vibration motions were assumed.

Vibration in modern over-the-road trucks can affect driver comfort, cargo safety, equipment wear, productivity etc. Among all the problems, vibration may have a number of different sources and its effective solution due to various causes should be accurately determined. The truck vibration problems have increased in recent years due to the rapid industrialization and demand for the modern machines and product to transfer from one place to the other. The dynamic behavior of truck also depends on load on cargo-body and the mechanical system such as springs, dampers etc, which interact with the wheels/tires, the truck base, cab and cargo. Ride Comfort evaluation is one of the most critical factors to evaluate the vehicle performance and has been an interesting topic for researchers for many years. Generally, two methods are prevalent to investigate the ride comforts. The first method is the use of computer simulation, and the second is the road experiment. Generally, the road experiment found to be very costly and complex process finding out the results. This paper deals with the multi-rigid body theory through the bond graph technique (Ronald 2003; Albert 1986; Inhee and Changsoo 1998; Erial, Stein and Louca 2004; Cellier) for modeling of a complex off-road truck. Primarily, bond graphs (BG) represent elementary energy-related phenomena (generation, storage, dissipation, power exchange) using a small set of ideal elements that can be coupled together through external ports representing power flow. With the aid of bondgraphs, hierarchical modeling becomes possible through coupling of component or subsystems models through their connecting ports. Besides these physical features capturing energy exchange phenomena, it is also possible to code on the graph the mathematical structure of the physical system to show the causal relationships (in a computational sense) among its signals (Ronald 2003). The conjunction of all these features make the bond graphs techniques a physically based, object oriented, graphical language, which is most suitable for dynamic modeling, analysis and

simulation of complex engineering systems involving mixed physical and technical domains in their constitution (Cellier).

This paper also incorporates the PID control system (which is combined form of proportional, integrated and derivative controller) to the vehicle suspension system with an objective to reduce vehicle jerks and increase comfort level for the driver. This controller determines the value of controlled variable, compares the desired value, determines the deviation and produces a control signal that will reduce the deviation to zero or to a smallest possible value.

2. DETAILED DESCRIPTION OF THE ELEMENTS OF THE OFF-ROAD TRUCKS

Truck structure can be disassembled into the following parts, a) Cab b) Cargo c) Base frame, d) Suspension system e) Pneumatic tires. The schematic view of whole truck structure is shown in Fig.1. A structure of the vehicle is composed of components such base frame, suspension system, cab, cargo and so-forth. When dynamic system is connected to these components, one must interconnect rotating and translating inertial elements with axial and rotational spring and dampers and also appropriately account for the system structure. Bond graphs are well suited for this task. The next section consists of modeling of different sub system of a truck-car vehicle. In deriving the bond graph models, the vehicle velocities in upward direction are assumed to be positive and springs and dampers are all assumed positive in compression. The base frame is modeled as a rigid body, which is allowed to move for pitching and rolling. The various elements of off-road trucks are presented in the following subsections.

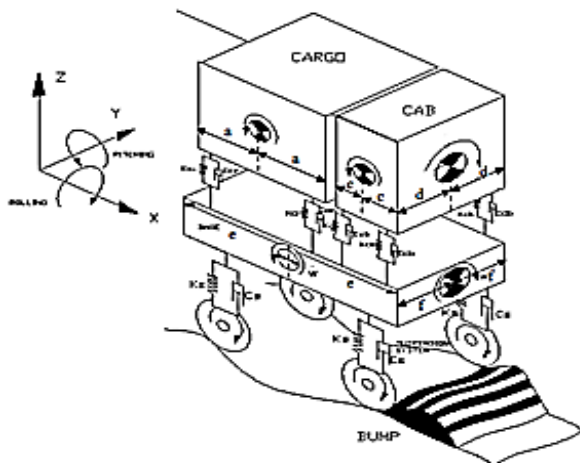


Figure 1: Physical system

2.1 Vehicle Base

The vehicle base is modeled as a rigid body with a local coordinate reference frame (x, y) attached to the center of mass and aligned with the inertia principal axes as is shown in Fig.1. It has mass m_b , and the following principal inertia moments: roll (J_{bx}) respect to the body

x-axis, pitch (J_{by}) respect to the body y-axis. It is also connected with suspension system.

2.2 Cab body

The cab body is also designed as a rigid body. In this part of vehicle, have a driver seat and the other space of sitting. It has mass m_{cb} , and the rolling inertia J_{cbx} respect to the X-axis or (J_{cby}) pitching inertia moments respect to the axis. It has a four spring-damper systems which connected the cab-body to the base. The cab-body is also shown in Fig.1.

2.3 Cargo mass

The cargo mass is designed as a rigid body. These masses are lifted by the base frame. The cargo is assembled with truck for carrying a mass from one place to another. This mass also includes the mass of frame structure of the truck.

2.4 Suspension system

Suspension is the term given to the system of springs, shock absorbers and linkages that connects a vehicle to its wheels. This assembly is used to support weight, absorb and damped road shock, which helps to maintain the tire contact as well as proper wheel-to-base relationship. Without being a restriction for future extensions of the overall vehicle model, only static suspension systems are considered in this research work, which may or may not have non-linearly.

2.5 PID control system

A structure of PID control is shown in fig.2, where it can be seen that in a PID controller, the error signal $e(t)$ is used to generate the proportional, integral and derivative actions, with the resulting signal weighting and summed to control signal $u(t)$ applied to a plant model. A mathematical description of the PID controller is,

$$u(t) = K_p e(t) + \frac{1}{G_i} \int_0^t e(t) + G_d \frac{de(t)}{d(t)}$$

Where, $u(t)$ is the input signal to the plant model, the error signal $e(t)$ is defined,

$$e(t) = r(t) - y(t)$$

A proportional controller (G_p) will have the effect of reducing the rise time and will reduce, but never eliminate, the steady-state error. An integral control (G_i) will have the effect of eliminating the steady-state error, but it may make the transient response worse. A derivative control (μ) will have the effect of increasing the stability of the system, reducing the overshoot, and improving the transient response. The combination of proportional, integral, and derivative control is called PID control system. In the fig 2, G_p presents proportional gain, G_i presents integrated gain and μ presents derivative gain.

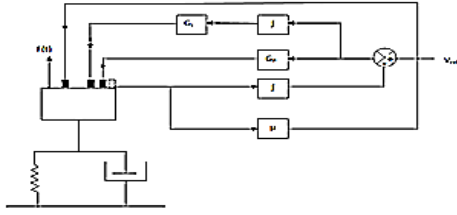


Figure 2: Proportional control

3. BOND GRAPH MODELING

This section will elucidate the bond graph modeling of various elements and the integrated bond graph model of off-road truck.

3.1 Cab body

The cab body modeled as a rigid body with centre of mass located at distance 'c' from the front and rear spring damper & at a distance 'd' from the left and right spring damper system. The cab body is characterized by the centre of mass velocity and angular velocity, so I elements for the mass, M_{cb} and moment of inertia, J_{cbx} and J_{cby} , are attached to the appropriate 1-junctions. The weight of the body is an effort source attached to the centre of mass velocity. Positive power is directed into the source owing to the velocity convention (positive upward).

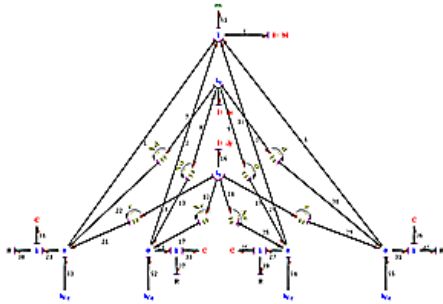


Figure 3: Bond graph model of cab-body

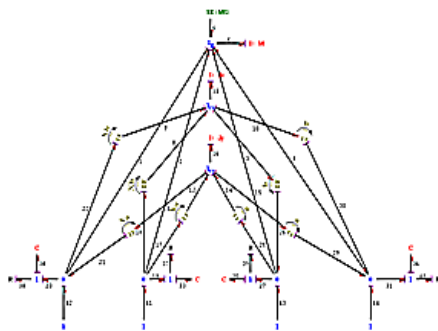


Figure 4: Bond graph model of cargo-body

Kinematic constraints must be enforced correctly for constructing the correct model. Kinematic constraints are always having relationship among the flow variables. To add the flow according to the constraints, 0-junctions are used. The transformers are used to convert the angular velocity (ω) into velocity components $\omega \times c$ and $\omega \times d$. On the transformer the moduli are appended according to the definition of the

transformer. In Fig. 3, the constraints of Eq. (1) to Eq. (8) are summed up using 0- junctions.

$$V_{cb1} = V_{Gcb} + \omega_{ycb} \times c \quad (1)$$

$$V_{cb3} = V_{Gcb} - \omega_{ycb} \times c \quad (2)$$

$$V_{cb2} = V_{Gcb} + \omega_{ycb} \times c \quad (3)$$

$$V_{cb4} = V_{Gcb} - \omega_{ycb} \times c \quad (4)$$

$$V_{cb1} = V_{Gcb} + \omega_{xcb} \times d \quad (5)$$

$$V_{cb2} = V_{Gcb} - \omega_{xcb} \times d \quad (6)$$

$$V_{cb3} = V_{Gcb} + \omega_{xcb} \times d \quad (7)$$

$$V_{cb4} = V_{Gcb} - \omega_{xcb} \times d \quad (8)$$

3.2 Cargo Body

The cargo body is also modeled as a rigid body with center of mass located at distance of 'a' from the front and rear spring damper system 'b' from the left and right spring-damper system. The cargo body is characterized by the centre of mass, velocity and angular velocity, so I-elements for the mass M_{cr} and moments of inertia, J_{crx} and J_{cry} are attached to the appropriate 1-junction. The weight of the body is an effort source attached to the center of mass velocity. Positive power is directed in to the source owing to the velocity convention (positive upward).

On the transformer the moduli are appended. 0-junctions are used again to add the flow to the kinematic constraints. In Fig 4, the constraints of Eq (9-16) are summed up using 0 junctions.

$$V_{cr1} = V_{Gcr} + \omega_{ycr} \times a \quad (9)$$

$$V_{cr3} = V_{Gcr} - \omega_{ycr} \times a \quad (10)$$

$$V_{cr2} = V_{Gcr} + \omega_{ycr} \times a \quad (11)$$

$$V_{cr4} = V_{Gcr} - \omega_{ycr} \times a \quad (12)$$

$$V_{cr1} = V_{Gcr} + \omega_{xcr} \times b \quad (13)$$

$$V_{cr2} = V_{Gcr} - \omega_{xcr} \times b \quad (14)$$

$$V_{cr3} = V_{Gcr} + \omega_{xcr} \times b \quad (15)$$

$$V_{cr4} = V_{Gcr} - \omega_{xcr} \times b \quad (16)$$

3.3 Base frame

The Base frame also modeled as a rigid body with center of mass located at distance of 'e' from the front and rear spring damper system and 'f' from the left and right spring-damper system. The cargo body is characterized by the centre of mass, velocity and angular velocity, so I-elements for the mass, M_{bs} and moments of inertia J_{bsx} and J_{bsy} are attached to the appropriate 1-junction. The weight of the body is an effort source attached to the center of mass velocity. Positive power is directed in to the source owing to the velocity convention (positive upward). One may obtain the similar equations presented in Eqs (17-24) are summed up using 0 junctions. However, due to page

limitation, the base frame model is shown in the integrated model.

$$V_{bs1} = V_{Gbs} + \omega_{ybs} \times e \quad (17)$$

$$V_{bs2} = V_{Gbs} + \omega_{ybs} \times e \quad (18)$$

$$V_{bs3} = V_{Gbs} - \omega_{ybs} \times e \quad (19)$$

$$V_{bs4} = V_{Gbs} - \omega_{ybs} \times e \quad (20)$$

$$V_{bs1} = V_{Gbs} + \omega_{xbs} \times f \quad (21)$$

$$V_{bs2} = V_{Gbs} - \omega_{xbs} \times f \quad (22)$$

$$V_{bs3} = V_{Gbs} + \omega_{xbs} \times f \quad (23)$$

$$V_{bs4} = V_{Gbs} - \omega_{ybs} \times f \quad (24)$$

3.4 Suspension System

The spring damper in general reacts to the relative velocity across them. To properly add the velocity component at each end of these elements, the spring and damper are assumed to be positive in compression. The modeling of suspension system and pneumatic tire has been presented in the integrated bond graph model of the system.

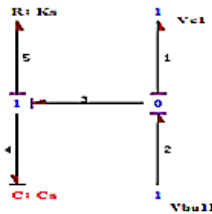


Figure 5: Bond graph model of Suspension system

3.5 PID control system

The bond graph model of PID control system is shown in Fig 6. A system is applying on a quarter suspension system. In the present model, 'mu' is representing a derivative gain, G_p is proportional gain which modulated on a Transfer Function (TF) and G_i is an integral gain.

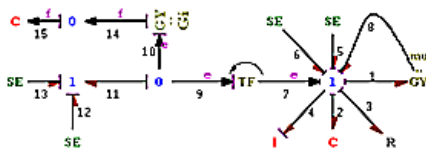


Figure 6. Bond graph model of PID control system

3. 6 Integrated Bond Graph model of complete off-road truck without control system

The bond graph model of road-truck is constructed by adding the models of different components of vehicle as shown in Fig. 6.

4. SIMULATION STUDIES

The bond graph model of the vehicle is simulated for 10 sec to obtain different output responses. Total 1024 records are used in the simulation and error of the order

of 5.0×10^{-4} is considered. Symbols shakti software is used to carried out for simulation work. Fifth-order Runge-Kutta method, is used in simulation work.

The dynamic wheel loads generated by a moving vehicle are mainly due to various wheel/road imperfections. These imperfections are considered as the primary source of dynamic track input to the road vehicles. In actual practice different type of periodic, periodic or random road irregularities may exist on the track. However, but in the present study bump type of irregularity is considered as shown in Fig.8 (Mukherjee and Karmakar 2000). For simplicity, the shape of irregularity is assumed to be of same nature on left and right wheel. However different shape of irregularity may be attempted in near future. Velocity inputs at different wheels are calculated by using equations from Eq. (25) and Eq. (26).

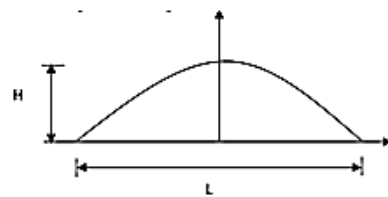


Figure 8: Bump type surface irregularities

The bump excitation of the front wheels is,

$$V = H \sin\left(\pi \frac{V}{L} t\right) \quad \text{For} \quad 0 \leq t \leq \frac{L}{V}$$

$$V = 0 \quad \text{For} \quad t \geq \frac{L}{V}$$

The bump excitation of the rear wheels is,

$$V = H \sin\left(\pi \frac{V}{L} \left(t - \frac{A}{V}\right)\right) \quad \text{For} \quad \frac{A}{V} \leq t \leq \frac{A+L}{V}$$

$$V = 0 \quad \text{For} \quad t \geq \frac{A+L}{V}$$

In the present study H is taken as 0.03 m and L is taken as 1m.

Following output parameters are obtained in the simulation of the bond graph model of the complete truck model:

- Suspension displacement with PID and proportional control system for quarter car model
- Vertical effort on suspension system

(a) Suspension displacement with PID and proportional control system for quarter car model

In a quarter truck model, PID control system incorporates in left rear suspension system and Proportional control system incorporates in right rear system therefore front suspensions are not connected by

these systems. The deflection of suspension at various speeds is shown in Figs. The effect of PID and proportional control systems in suspensions of both rear wheels are shown in Figs 8-12. Since irregularities on both the wheel are assume to be same shape, therefore the deflection of suspension springs of both rear suspension will not be same, which is also apparent from all the above simulated curves.

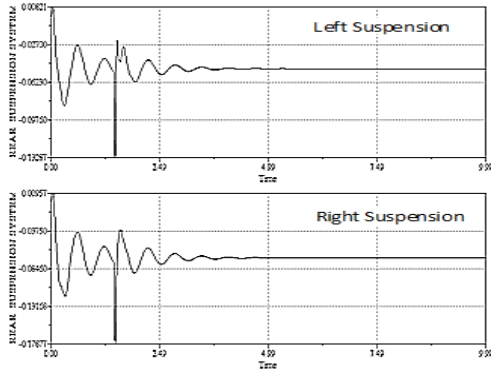


Figure 8: Deflection of suspension at 20 km/hr

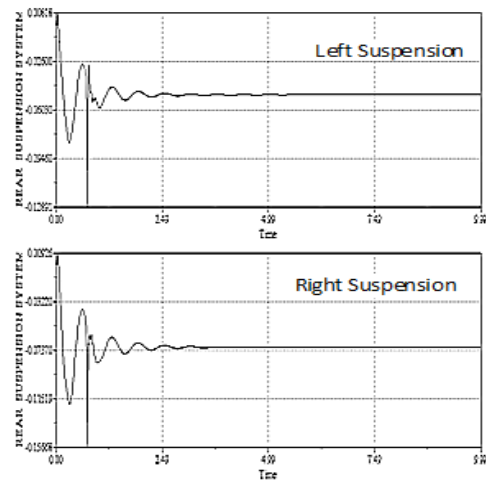


Figure 9: Deflection of suspension at 40 km/hr

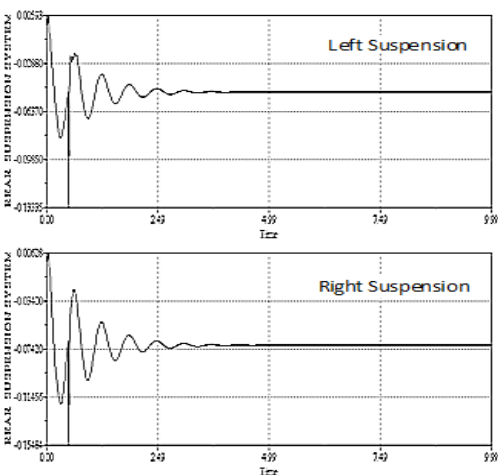


Figure 10: Deflection of suspension at 60 km/hr

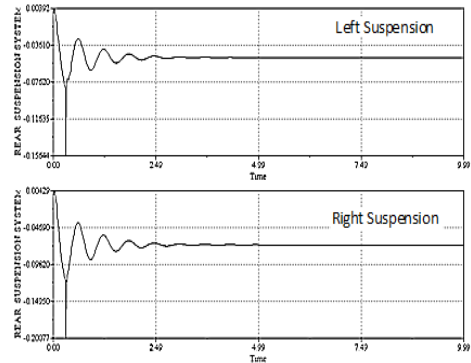


Figure 12: Deflection of suspension at 100 km/hr

b) Vertical effort on suspension system

The vertical effort on left rear suspension with respect to time are presented in Figs 13-17, whether suspension system is incorporates with Proportional Integrated Derivative control system.

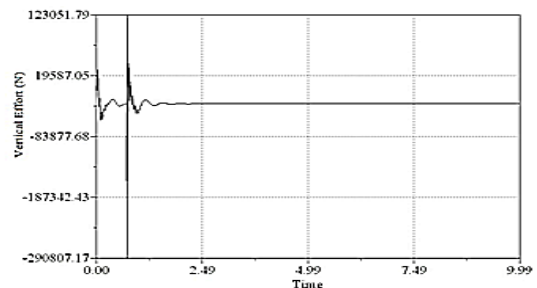


Figure 13: Vertical Effort on Suspension system at 20 Km/hr

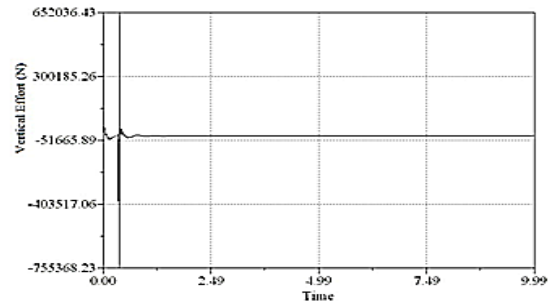


Figure 16: Vertical Effort on Suspension system at 80 Km/hr

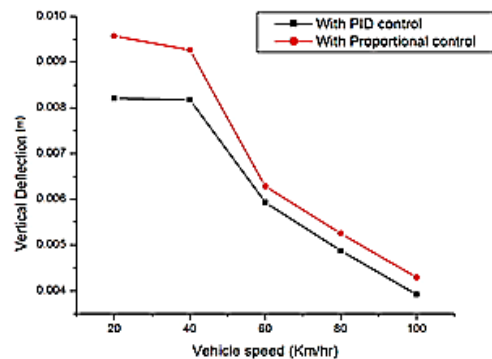


Figure 18: Suspension deflection of truck model at various speeds

It is evident from Fig.18 that the magnitude of displacement of suspension is comparatively lower, when connected by PID control system. At speed 60 km/hr, PID control connected suspension gives lower magnitude, whereas when the suspension is connected with proportional controller gives comparatively higher magnitude of amplitude of vibration.

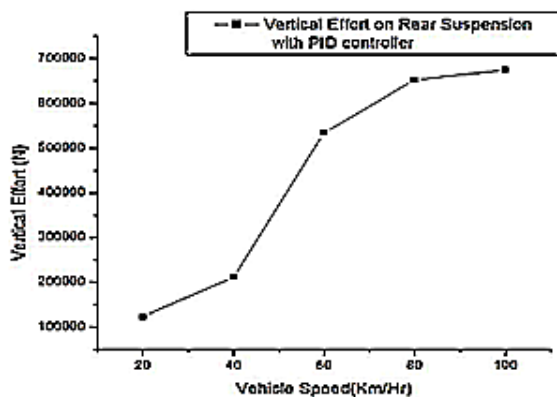


Figure 19: Vertical effort on suspension system

Fig.19 shows a vertical effort of rear suspension system, when connected by a Proportional Integrated Controller. It is evident from plot, that a value of vertical effort is continuously increased with the vehicle speed. It is resulted from both figures that PID control system gives satisfactory result at speed limit 40-60 km/hr.

5. CONCLUSIONS

The dynamic model of off-road truck of cab/cargo/base had been constructed through bond graph technique. Vertical dynamics has been carried out for off-road truck model. A 6-degree of freedom model is used for the analysis. Velocity input at the entire tire has been given by considering same shape bump irregularity at both right and left tire. The PID control system is attached to a suspension system, which provides a good analysis to analyze the vibration of the system.

REFERENCES

- Demic, M., Lukic, J., 2002. Some aspects of the investigation of random vibration influence on ride comfort, *Journal of Sound Vibration*. 253 (1), 109–129.
- Filippini, G., 2004, *Nigro. N. and Junco.S.*, Dinámica Vehicular mediante bond graphs. Proyecto final de carrera de grado. Escuela de Ingeniería Mecánica, Universidad Nacional de Rosario.
- Pacejka, H. B., 1975. Principles of plane motion of automobiles, *IUTAM symposium on the dynamics of automobiles*, Delft Univ. of Tech. pp. 33- 59.
- Paul, B., 1975. Analytical dynamics of mechanisms-a computer oriented overview, *Mechanism and Machine Theory*, vol 10, pp. 481-507, 1975.

- Ibrahim, I.M., 1996. Effect of Frame Flexibility on the Ride, *Vibration of Heavy Trucks*, 58(4), pp. 709-713. Elsevier Science Ltd.
- Goodarzi, A., and Jalali, A., 2006. An Investigation of Body Flexibility Effects on the Ride Comfort of Long Vehicles. Proc. CSME *Canadian Congress of Applied Mechanics*, (CANCAM 2006).
- Yi, T.Y., 2000. Vehicle Dynamic Simulations Based on Flexible and Rigid Multi-body Models, SAE Paper 2000-01-0114. *Society of Automotive Engineers*, Warrendale, PA.
- Cao, C., 2005. Approaches to Reduce Truck Beaming, SAE Paper 2005-01-0829. *Society of Automotive Engineers*, Warrendale, PA.
- Margolis, D. and Edeal, D., Modeling and Control of Large Flexible Frame Vehicles Using Bond Graphs SAE Paper 892488. *Society of Automotive Engineers*, Warrendale, PA, 1989.
- Karnopp, D. et al., 2006. System Dynamics – Modeling and Simulation of Mechatronic Systems (4th ed.) *John Wiley and Sons, Inc.*
- Rosenberg, R.C., Margolis, R.L., Karnopp, D.C., 2003. Modeling and Simulation of Mechatronic Systems, *A Wiley-Interscience Publication*, New York.
- Albert M. Bos, 1986. *Modeling Multibody Systems in terms of Multi-bond Graphs, with application to a motorcycle*, PhD thesis at Twente Univ.
- Jang, I., Changsoo H Edeal , 1998. Proposition of a Modeling Method for Constrained Mechanical Systems Based on the Vector Bond Graph, *Journal of the Franklin Institute*. Vol. 335B, No 3, pp. 451 469..
- Erial,T., Stein, J., Louca, L., 2004. A Bond Graphs Based Modular Modeling Approach towards an Automated Modeling Environment for Reconfigurable Machine Tools. *IMAACA 2004*.
- Cellier, F., Hierachical non-linear bond graph: A unified methodology for modelling complex physical systems, *Simulation*, Vol 58, No. 4, pp. 230-248.
- Mukherjee, A., and Karmakar, R., Modelling and Simulation of engineering System through Bond Graph, *Narosa publishing House*, New Delhi, reprinted by CRC press for North America and by Alpha Science for Europe, 2000.
- Mukherjee, A., and Samantaray, A. K., *SYMBOLS-Shakti User's Manual*, High-Tech Consultants, STEP Indian Institute of Technology, Kharagpur, India, 2006.

Authors Biography

First author of this paper, is working as an Assistant Professor in Mechanical Engineering Department in Krishna Engineering College, India. He has completed his Master degree from Sant Longowal Institute of Engineering & Technology, Estd by Govt. of India. His interested areas of research are system dynamics, rotor dynamics and vehicle dynamics.

second author of the paper is working as Professor in Mechanical Engineering Department in Delhi

Technological University. He got his doctor of philosophy from Indian Institute of Technology, Kharagpur. His main areas of research are rotor dynamics, vehicle dynamics, bio-mechanics and bond graph modeling.

APPENDIX

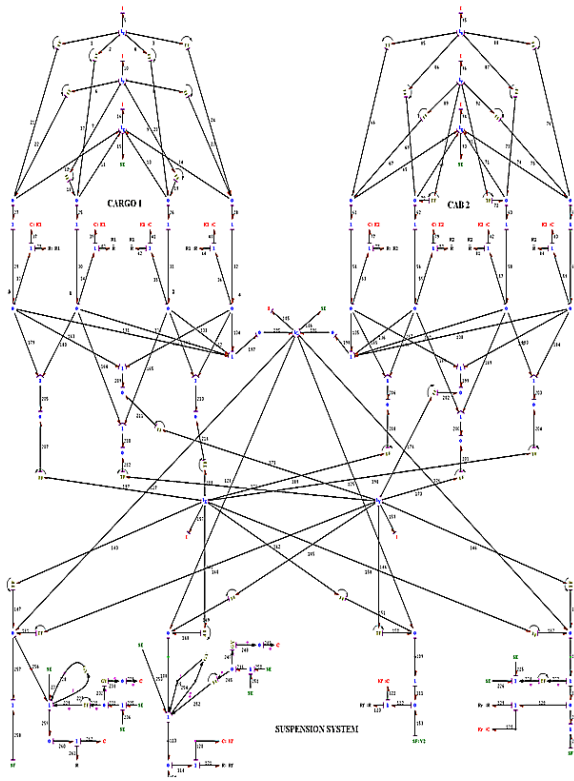


Figure 7: Bond graph model of integrated system

Table 1: Main data

Cab/Engine Mass m	2500 kg
Cargo	10,000 kg
Base mass	4250 kg
Mass of tire	500 Kg
Front_suspension_stiff	$2.67e+006 \text{Ns/m}^2$
Rear_suspension_stiff	$1.15e+006 \text{Ns/m}^2$
Front_suspension_resistance	31895 Ns/m
Rear_suspension_resistance	33884 Ns/m
Length of ground excitation	0.3m
Distance_between_suspension	8m
Base_angular_inertia_X-direction	24000Kg-m^2
Base_angular_inertia_Y-direction	24000Kg-m^2
Cab_angular_inertia_X-direction	2000Kg-m^2
Cab_angular_inertia_Y-direction	2000Kg-m^2
Cargo_angular_inertia_X-direction	4500Kg-m^2
Cargo_angular_inertia_Y-direction	4500Kg-m^2
Cargo_front_stiffness	$1.67e+07 \text{Ns/m}^2$
Cargo_rear_stiffness	$1.67e+07 \text{Ns/m}^2$
Cargo_rear_resistance	8124 Ns/m
Cargo_front_resistance	8124 Ns/m
Cab_front_stiffness	$1e+08 \text{Ns/m}^2$
Cab_rear_stiffness	$1e+08 \text{Ns/m}^2$
Cab_rear_resistance	$1e+06 \text{Ns/m}$
Cab_front_resistance	$1e+06 \text{Ns/m}$
Left/Right suspension distance to the centre of the base	2.28
Left/Right spring-damper system distance to the centre of the cargo	2.28
Front /Rear spring-damper distance to the centre of cargo	3
Front /Rear spring-damper distance to the centre of base	4

H_{∞} CONTROL WITH TIME DOMAIN SPECIFICATIONS APPLIED TO A HEAT EXCHANGER NETWORK

Fabio Delatore^(a), Fabrizio Leonardi^(b), Luís Fernando Novazzi^(b), José Jaime da Cruz^(c)

^(a) FATEC Santo André

^(b) Centro Universitário da FEI

^(c) Universidade de São Paulo

^(a) fabio.delatore@fatec.sp.gov.br, ^(b) fabrizio@fei.edu.br, ^(c) lnovazzi@fei.edu.br, ^(d) jaime@lac.usp.br

ABSTRACT

Multivariable control techniques have been applied to chemical plants, ranging from multi-loop control up to predictive controls. This work intends to present a study developed using a control solution based on the H_{∞} design with time domains specifications applied on a heat exchanger network (HEN) with bypasses. The HEN is frequently used in chemical processes to promote energy transfer between hot/cold streams, reducing the utility consumption as its main objective. The H_{∞} control is used here to ensure a prescribed time domain response by means of a solution of model matching problem so that the closed loop dynamics are approximately the same as the ones of the reference model. The simulations results have demonstrated that the proposed control leads to a good performance with process variables decoupled, null offset and output responses with the prescribed dynamics.

Keywords: heat exchanger, heat exchanger network, H_{∞} control, process control

1. INTRODUCTION

The heat exchanger (HE) is an important equipment widely used in chemical plants in order to promote an suitable energy exchange between hot/cold streams, minimizing the utilities consumption (cold water and high pressure steam) necessities for the manufacturing processes. The reducing on utilities consumption are always desirable because it reflects directly on the industries expenditure, minimizing the usage of electrical and fuel (gas, oil) energies to cool / heat the process streams.

This reduction is achieved by using some HE's, where this arrangement is named as heat exchanger network (HEN) that is an indispensable equipment to achieve the reducing on utilities consumption. The HEN is responsible to promote the energy integration of the chemical plant by interchanging some hot and cold streams (Hewitt *et al.*, 1993)

The major problem faced by the process engineers on this energy integration is to choose which streams (hot/cold) will perform the energy integration. One of the current techniques to develop this study that helps

engineers to achieve the desirable integration on the industries is the Pinch technology (Hewitt *et al.*, 1993).

Nowadays, the most of the industrial HEN applications uses the shell and tube HE. Independently of the HE model used, is very important that the stream outlet temperatures are in a specified range (Hewitt *et al.*, 1993). This specified range of temperatures could be achieved by using an efficient control system.

There are some different control techniques that could be used in industrial processes. Normally, the methodologies that are such complex demands a high engineered design but they present a superior performance. On the other hand, there are methodologies that are easy to design but normally not capable to lead to a desirable performance. As an example, the PID is the most common controller due to its simple design procedure (such as the heuristic tuning methods) and implementation, widely used on chemical plants.

However, on chemical process that presents several inputs/outputs, the PID designs will demand an additional engineering effort to tune and design the controllers. In this situation, the DMC Predictive controller may be considered a suitable control strategy to be used. It may deals with many inputs/outputs, complex dynamics, dead time or inverse output response (Hu and Sun, 2002), but its drawback is that it needs much engineering contribution to be designed (Gonzalez *et al.*, 2006).

Based on the literature, the most common applied control techniques to perform the closed loop control on a HEN are the predictive control, the neural network and the feed forward PID (Ogunnaiké, 1994). In the range of suitable controllers to be applied on a HEN, one may include the H_{∞} control. The H_{∞} design is typically performed on frequency domain and it is quite powerful in the sense that it allows a clear way of dealing with wide spectrum tradeoffs of the project. Nevertheless, its design usually requires a deeper engineering background and the time domains specifications must be first converted to equivalent frequency domain specifications.

The H_{∞} control problem can be expressed as an optimization problem in which a controller must be

found to satisfy the requirements of robustness, performance and control effort. The most common way to design the H_∞ is the so called mixed sensitivity formulation that involves the use of weighting matrices, responsible for adjusting the performance, control effort and stability robustness. To take the most of this technique and also allowing time domain specifications, this work proposes a control solution for a HEN based on a H_∞ model matching control, where the time domain specifications are converted in a reference model. In order to perform this requirement, the H_∞ mixed sensitivity formulation is adapted to solve the model matching and the H_∞ controller found is capable to force the transfer matrix of the closed loop system to be close to the reference matrix with a prescribed precision (Leonardi, 2002). Note that H_∞ control applied to the HEN is not commonly found on the scientific literature (Delatore *et al.*, 2009).

2. THE HE MATHEMATICAL MODEL AND HEN ARRANGEMENT

Before presenting the studies about the control design and its performance applied on a HEN, it is important to define a physical arrangement of the exchangers, determining the manipulated, the controllable and the disturbances variables of the HEN. The shell and tube HE, as mentioned before, is the most common one used in chemical plants, mainly due to its low cost, uncomplicated repairing/maintenance and it can also be built with a lot of different exchanger area, in order to be suitable to almost all chemical processes. For this reason, the shell and tube HE were chosen to be used on this work.

The configured HEN was obtained by interconnecting adequately the inputs and the outputs of the HE model (Novazzi, 2006), which results on a HEN with two hot streams and one cold stream, two output controllable variables and two manipulated variables. Figure 1 shows the arrangement adopted of the HEN considered on this work.

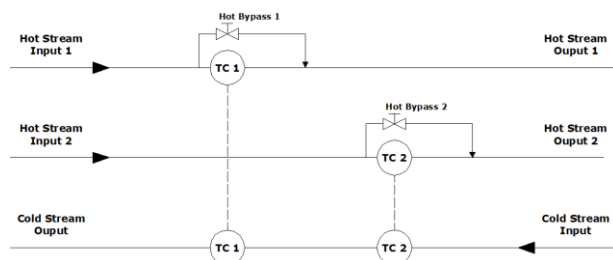


Figure 1. The HEN structure.

The variables related to the HEN are:

- Controllable variables: $TH_{OUT 1}$ (hot stream 1 output) and $TH_{OUT 2}$ (hot stream 2 output);
- Manipulated variables: fh_{11} (bypass valve position, hot stream 1) and fh_{12} (bypass valve position, hot stream 2);

- Disturbance variables: $TH_{IN 1}$ (hot stream 1 input), $TH_{IN 2}$ (hot stream 2 input) and TC_{IN} (cold stream input).

The mathematical model of the HE used to obtain the HEN arrangement proposed on Figure 1 was obtained through stream energy balance, as represented in Equations (1), (2), (3) and (4) (Novazzi, 2006):

$$\frac{dT_{H,i}}{dt} = (a_1 - a_2)T_{H,i-1} - (a_1 + a_2)T_{H,i} + a_2T_{C,n-i} + a_2T_{C,n-i+1} \quad (1)$$

$$\frac{dT_{C,n-i+1}}{dt} = a_4T_{H,i-1} + a_4T_{H,i} + (a_3 - a_4)T_{C,n-i} - (a_3 + a_4)T_{C,n-i+1} \quad (2)$$

$$\frac{dT_{Hby,i}}{dt} = a_5T_{Hby,i-1} - a_5T_{Hby,i} \quad (3)$$

$$\frac{dT_{Cby,n-i+1}}{dt} = a_6T_{Cby,n-i} - a_6T_{Cby,n-i+1} \quad (4)$$

where T is the stream temperature, m is the mass flow rate, ρ is the density, v is the relationship between volume and length of the exchanger, t is the time, z is the axial position, A is the heat transfer area, CP is the specific heat, V is the volume and U is the global heat transfer coefficient. The indices c and h refers to the variables related to the *cold* and to the *hot* stream. The indices *by* refers to the bypass and the parameters a_1 up to a_6 equals to

$$\begin{aligned} a_1 &= nm_H(1-f_H)/(\rho_H V_H), & a_2 &= UA/(2\rho_H V_H C_{p,H}), \\ a_3 &= nm_C(1-f_C)/(\rho_C V_C), & a_4 &= UA/(2\rho_C V_C C_{p,C}), \\ a_5 &= nm_H f_H /(\rho_H V_{Hby}), & a_6 &= nm_C f_C /(\rho_C V_{Cby}), \end{aligned}$$

Equations (2) up to (5) were discretized and solved by finite difference method, in Matlab (Novazzi, 2006). Note that the HE model is nonlinear due to the product between the a_3 parameter and T_C on Equation 2. The bypasses positions f_H and f_C are the manipulated variables that affect the controlled variables TH_{OUT} and TC_{OUT} . The simulations developed by using the HE equations demonstrated that the dynamics involved can be basically represented by first-order transfer functions with variable loop interaction. At least, the nominal variables, the physical dimensions of the HEN and the fluid characteristics are described in Table 1.

Table 1. Nominal values of the HEN

Variable	Description	Value
ρ	Fluid Density	Cold, Hot streams: 1000 kg.m ⁻³
CP	Specific Heat	Cold, Hot streams: 1000 J.kg ⁻¹ .°C ⁻¹
T	Input temperature	Cold stream: $TC_{IN 1} = 24$ °C Cold stream: $TC_{IN 2} = 28$ °C Hot stream: $TH_{IN 1} = 55$ °C Hot stream: $TH_{IN 2} = 55$ °C
U	Global coefficient of Heat Exchanger	$U = 190$ W.m ⁻² .°C ⁻¹
A	Heat Exchanger area	$A = 0.1$ m ²
n	Number of cells	$n=20$

3. THE H_∞ CONTROLLER

During the development of a control system, the engineer aims to primarily stabilize the plant. Besides, it is also supposed to obtain a particular transient response, ensure the rejection of measurement noise, the improvement in the steady-state error and the robustness to variations in parameters of the plant model (Doyle and Stein, 1981).

For the development of these designs, one can apply classical control techniques which generally involve the study of plants with single input and single output (SISO), using analytical methods (Laplace transform, Routh criteria, etc.) and graphics (Nyquist, Bode, etc.). However, when the system has multiple inputs and multiple outputs (MIMO), the designer may find it difficult to apply classical control techniques (Doyle and Stein, 1981).

Several of the current techniques for multivariable linear control systems uses a plant model representation in state space and one of the most powerful of these techniques is the H_∞ control. It allows dealing explicitly with robustness issues and the design specifications are usually presented in the frequency domain (Williams, 1991). The technique most commonly used for designing H_∞ controllers is the so-called mixed sensitivity problem in which a sub-optimal problem is solved.

In this work the H_∞ compensator is designed using the mixed sensitivity technique and the performance specifications refer to force the output temperature to follow set-point step changes with null steady state errors with a dynamic approximately to a first order system with a predetermined time constant and also that the closed loop system becomes approximately uncoupled. Note that, since the performance specifications are given in the time domain, they must be converted to equivalent specifications in the frequency domain. This work shows that a convenient way of doing this is solving a model matching problem using the mixed sensitivity technique.

The H_∞ control problem can be expressed as an optimization problem in which the controller must be able to meet the requirements of robustness, performance and control effort. In the mixed sensitivity procedure this is done by molding the loop gain. Figure 2 show a typical open loop shape that was molded by means of the matrices $W_1(s)$ and $W_3(s)$ that are part of the formulation of the optimization problem.

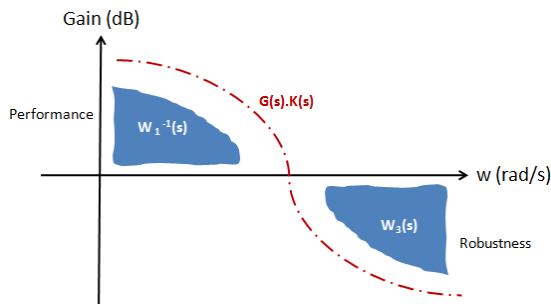


Figure 2. H_∞ loop shaping.

The H_∞ mixed sensitivity problem can be schematized by Figure 3 where $G(s)$ represents the plant and $K(s)$ the controller which stabilizes the plant and has the same number of states of it.

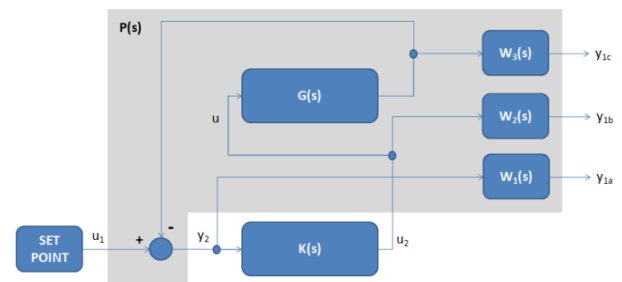


Figure 3. H_∞ control with the $W_1(s)$, $W_2(s)$ and $W_3(s)$.

The augmented plant is obtained by inserting the requirements of robustness, performance and control effort by means of the weighting functions $W_1(s)$, $W_2(s)$ and $W_3(s)$, which penalize the error $E(s)$, the control effort $U(s)$ and the output $Y(s)$, respectively, where

$$Y(s) = \begin{bmatrix} Y_{1a}(s) \\ Y_{1b}(s) \\ Y_{1c}(s) \end{bmatrix}$$

With the specifications previously defined, the design will find a H_∞ controller $K(s)$ satisfying the inequality

$$\left\| \begin{bmatrix} W_1(s)S(s) \\ W_2(s)R(s) \\ W_3(s)T(s) \end{bmatrix} \right\|_\infty < 1, \quad (5)$$

where $T(s)$ matrix is the complementary sensitivity function between the outputs and the input, $S(s)$ is the sensitivity function, and $R(s)$ is a function related to the control effort.

In addition to this traditional design in which the performance specifications are expressed indirectly by the matrix $W_1(s)$, it is possible that the controller $K(s)$ is obtained by a more direct performance specification. Figure 4 shows how to adapt the H_∞ problem for this purpose through the matrix $G_{REF}(s)$ which is a reference matrix containing the expected dynamics for the closed loop. The control structure of Figure 4 is known as model matching (LEONARDI, 2002).

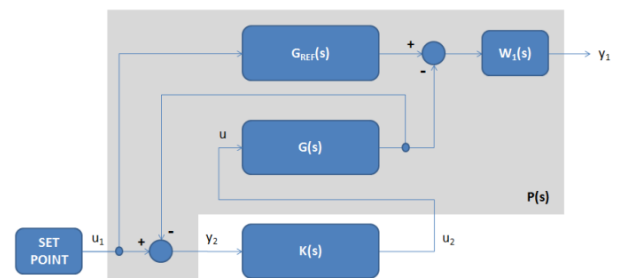


Figure 4. H_∞ model matching.

The $W_1(s)$ matrix, in this case, is the penalty of the difference between the signals $Y_{REF}(s)$ and $Y(s)$, and because of the nature of $G_{REF}(s)$, the matrix $W_1(s)$ is often chosen as a merely constant matrix. The solution of the H^∞ problem given by (6) solves the problem of determining the model matching controller $K(s)$ capable of making $T(s)$ close to $G_{REF}(s)$ with an accuracy given by the $W_1(s)$ matrix.

$$\|W_1(s)T(s)\|_\infty < 1. \quad (6)$$

4. METHODOLOGY

This work, as pointed out before, intends to present a H^∞ control solution for a HEN using a time domain specifications for the control design. The model matching problem ensures that the H^∞ controller imposes approximately the same dynamics present on the reference model (Deshpande, 1989). If necessary, the control design can be improved by adding the $W_2(s)$ and $W_3(s)$ matrices to deal with control effort issues and robustness.

Then it is shown how the methodology was applied to control the HEN. The H^∞ model matching design begins by defining the reference matrix

$$G_{REF}(s) = \begin{bmatrix} \frac{1}{110s+1} & 0 \\ 0 & \frac{1}{110s+1} \end{bmatrix}. \quad (7)$$

$G_{REF}(s)$ represents the desirable closed loop dynamics, using a suitable time constant (110 seconds) for this experiment. The null values on $G_{REF}(s)$ matrix represent the desired decoupling between the two channels and the unity gains came from the null steady state error in tracking reference step signals. On the controller implementation, an anti-windup architecture (Aström *et al.*, 1988) was also used, resulting on the control structure shown in Figure 5.

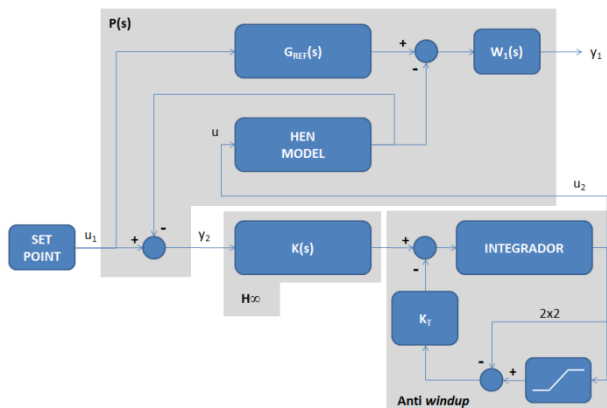


Figure 5. H^∞ model matching with Anti-windup.

The HEN model $G(s)$ on Figure 4, was defined by linearizing the model proposed on section 2. The linearization was performed by using the Matlab, resulting on a 50th order model. A reduction order was applied, resulting on a 15th order model. The weighting

matrix $W_1(s) = 50$, constant over the entire frequency band, representing a 2% matching error and the $K(s)$ matrix obtained on the H^∞ design is presented as follows, using the Matlab as support.

$$A_K = \begin{bmatrix} -0.603 & -16.620 & -0.714 & -4.870E^{-4} & 0 & 0 \\ 16.620 & -0.649 & -2.832E^{-3} & 0.646 & 0 & 0 \\ 0.714 & -2.836E^{-3} & -0.600 & -15.210 & 0 & 0 \\ 1.812E^{-4} & -0.646 & 15.210 & -0.651 & 0 & 0 \\ 0 & 0 & 0 & 0 & 0 & 0 \\ 0 & 0 & 0 & 0 & 0 & 0 \end{bmatrix}$$

$$B_K = \begin{bmatrix} -1.173 & -2.633 \\ 1.050 & 2.682 \\ 2.572 & -0.993 \\ -2.517 & 1.121 \\ 0.897 & 0.467 \\ 0.465 & -0.896 \end{bmatrix}$$

$$C_K = \begin{bmatrix} -7.840E^{-3} & 0.125 & -2.754 & -2.756 & 0 & 0 \\ 2.882 & 2.878 & 0.132 & -6.697E^{-3} & 0 & 0 \end{bmatrix}$$

$$D_K = \begin{bmatrix} 0 & 0 \\ 0 & 0 \end{bmatrix}$$

5. METHODOLOGY

The following results were obtained by numerical simulation and show the controller performance in view of performance specifications.

5.1. Cold mass flow (mc) disturbance rejection

On this first simulation, the disturbance was applied on the HEN at $t = 500$ sec. by a modification on the nominal cold mass flow (m_C) to $m_C = 0,135\text{kg}\cdot\text{s}^{-1}$. The simulation time was 1500 sec. Figure 6 show the TC_{OUT1} and TC_{OUT2} plots and Figure 7 show the control effort demanded.

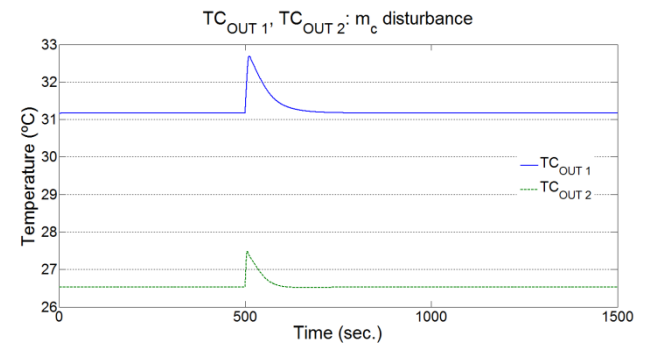


Figure 6. TC_{OUT1} e TC_{OUT2} : m_C disturbance.

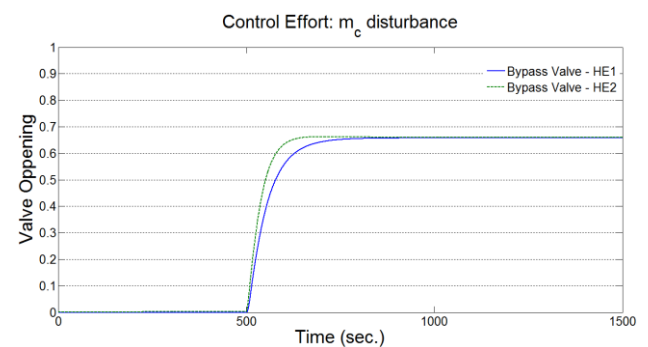


Figure 7. Control effort: m_C disturbance.

Analyzing the Figures 6 and 7, some conclusions could be attended about the HEN performance with the H^∞ controller on cold flow mass disturbance:

- It is possible to notice that the controller rejected the disturbance in a suitable time, returning the output temperatures values TC_{OUT1} and TC_{OUT2} to its original setpoint value;
- To keep unchanged the cold output temperatures values, the bypass valves open diverting more cold fluid to the HE outlet, while a smaller fraction continues to flow internally to the exchanger.

5.2. Hot input temperature (THIN) disturbance rejection

The second simulation verified the controller performance on reject the TH_{IN} disturbance, by modifying the nominal (+4% step variation) values of the heat streams. The disturbance happened on the instants $t = 500$ sec. and $t = 1500$ sec. and the simulation time was adjusted to 2500 sec. Figure 8 show the TC_{OUT1} and TC_{OUT2} plots and Figure 9 show the control effort demanded.

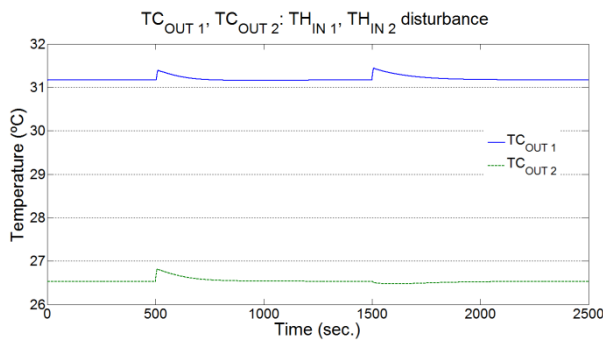


Figure 8. TC_{OUT1} e TC_{OUT2} : TH_{IN} disturbance.

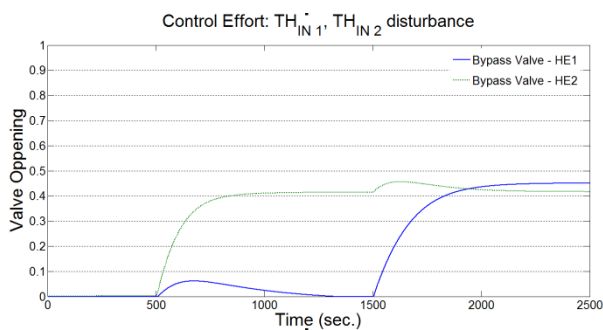


Figure 9. Control effort: TH_{IN} disturbance.

Analyzing the Figures 8 and 9, some conclusions could be attended about the HEN performance with the H^∞ controller on hot input temperature disturbance:

- It is possible to notice that the controller rejected the disturbance in a suitable time, returning the output temperatures values TC_{OUT1} and TC_{OUT2} to its original setpoint value;
- To keep unchanged the cold output temperatures values, the bypass valves open diverting more cold fluid to the HE outlet, while a smaller fraction continues to flow internally to the exchanger.

5.3. Setpoint change

The third and last simulation demonstrated the controller performance on setpoint variation. The setpoint was changed on the instant $t = 500$ sec. and the simulation time was 1500 sec. The TC_{OUT} setpoints were adjusted to 31,3°C and 26,8°C to TC_{OUT1} and to TC_{OUT2} , respectively. Figure 10 show the TC_{OUT1} and TC_{OUT2} plots and Figure 11 show the control effort demanded.

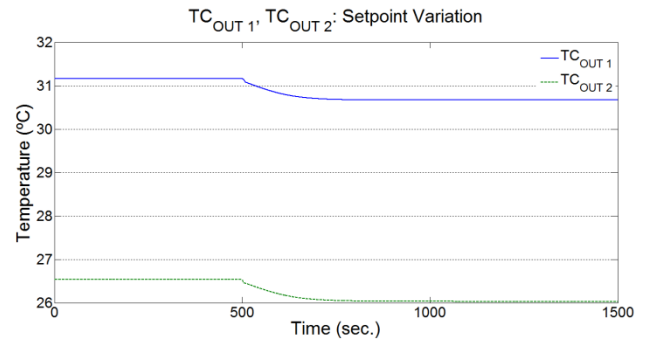


Figure 10. TC_{OUT1} e TC_{OUT2} : setpoint variation.

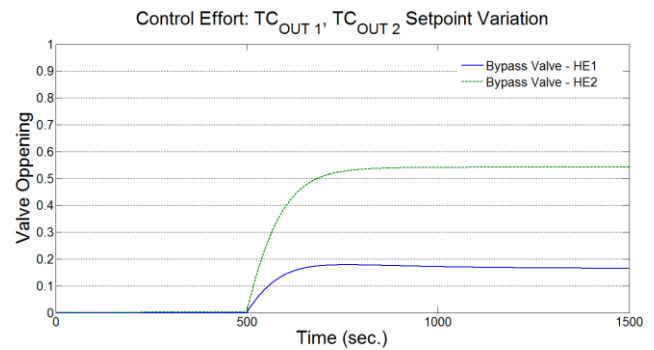


Figure 11. Control effort: setpoint variation.

Analyzing the Figures 10 and 11, some conclusions could be attended about the HEN performance with the H^∞ controller on setpoint variation:

- The new requested setpoint values designed to TC_{OUT1} and to TC_{OUT2} were successfully achieved;
- The bypasses valves kept between its maximum and minimum values. No saturation was noticed.

6. CONCLUSIONS

In this work we have studied the use of H^∞ control to provide a specified time domain performance for a heat exchanger network.

It was shown here how time domain specifications can be converted into an equivalent reference model and how the H^∞ mixed sensitivity control technique can be adapted for the controller design.

Observing the H^∞ model matching closed loop simulations responses applied to the HEN (Figures 6 up to 11), the following conclusions can be pointed out:

- The H^∞ design was developed by using a non-traditional method. Normally, the specifications

and the requirements for the traditional H_∞ project are expressed on a frequency domain. The model matching technique, adopted on this paper, gives the possibility to design the H_∞ controller by indirectly using time domain specifications;

- The H_∞ model matching controller obtained to implement the closed loop control for the HEN presents a small order since we previously reduced the plant model order;
- In spite of H_∞ not being a new control methodology, the results obtained suggested that it can be an interesting alternative when compared to other traditional techniques, such as PID. The H_∞ presented an accurate performance to decouple the variables, associated with a short time to establish the outputs, as notice on Figures 6 up to 11;
- New studies with the HEN will be performed by including robustness issues on the H_∞ design.

7. REFERENCES

- Aguirre, L.A., 2007. *Enciclopédia de Automática Controle e Automação*, Vol 1, Blucher.
- Aström, K. J., Hägglund, T., 1988. Automatic Tuning of PID Controllers – Instrument Society of America.
- Delatore, F., Cruz, J.J., Leonardi, F., Novazzi, L.F., 2009. Multivariable Control of a Heat Exchanger with Bypasses, *Proceedings of the 11th IASTED International Conference on Control and Applications*, Cambridge, UK.
- Deshpande, P.B., 1989. *Multivariable Process Control*, Instrument Society of America.
- Doyle, J.C., Stein, G., 1981. Multivariable Feedback Design: Concepts for a Classical/Modern Synthesis. *IEEE Transactions on Automatic Control*, 26, 4-16.
- Gonzalez, A. H., Odloak, D., Marchetti, J.L., 2006. Predictive control applied to heat-exchanger networks, *Chemical Engineering and Processing*, 45.
- Hewitt, G.F., Shires, G.L., Bott, T.R., 1993. *Process Heat Transfer*, CRC Press Inc.
- Hu, G.L.; Sun, Y.X., 2002. Study and application of dynamic matrix control in refinery processes, *Proceedings of IEEE Technical Conference on Computers, Communications, Control and Power Engineering*, China, 1667-1671.
- Leonardi, F., 2002. *Multivariable robust control systems with time specifications* Thesis (PhD). Universidade de São Paulo (in Portuguese).
- Novazzi, L.F., 2006. *Dynamics and control of heat exchanger networks*. Thesis (PhD). Universidade Estadual de Campinas (in Portuguese).
- Ogunnaike, B.A., 1994. *Process, dynamics, modeling and control*, Oxford University Press.
- Williams, J.S., 1991. H-Infinity for the Layman, *Measurement and Control*, v.24, p. 18-21, 1991

BONDGRAPHS MODELING AND SIMULATION ON DYNAMIC CHARACTERISTICS OF CAVITATING PUMP SYSTEM

Kazuhiro TANAKA^(a), Toshiyuki SATO^(b), Hiroshi TSUKAMOTO^(c), Takehisa KOHDA^(d), Katsuya SUZUKI^(e)

^{(a)(e)}Dept. of Mech. Information Science and Technology, Kyushu Institute of Technology, Iizuka 820-8502, Japan

^(b)Hitachi Ltd., Infrastructure Systems Company, Tsuchiura 300-0013, Japan

^(c)Kitakyushu National College of Japan, Kitakyushu 802-0985, Japan

^(b) Dept. of Aeronautics and Astronautics, Kyoto University, Kyoto 606-8501, Japan

^(a)kazuhiro@mse.kyutech.ac.jp, ^(b)toshiyuki.sato.bh@hitachi.com, ^(e)htsuka@kct.ac.jp,

^(d)kohda.takehisa.5m@kyoto-u.ac.jp, ^(e)kachandesu2002@yahoo.co.jp

ABSTRACT

Internal flows including cavitation phenomena in a pump can be analyzed by CFD commercial codes and system performances are traditionally obtained by experimental tests. However, they cannot correctly analyze the dynamic characteristics of the system especially when the transients are very fast or the system sometimes becomes complicated according to cavitation phenomena. It is important to predict dynamic behaviors of the pump system in the development stage. 3D-CFD numerical calculation is so time-consuming to analyze total flow field in the system that it is useful to develop 1D-mathematical models to express the dynamic characteristics of the system. The mathematical models of a pump system already have been developed by Bondgraphs without cavitation phenomena. In this study, the numerical result of cavitating flow is considered into the system Bondgraphs.

Keywords: pump system dynamics, Bondgraphs, CFD result, cavitating flow

NOMENCLATURE

B: flow passage width in the impeller
 c: radial velocity of fluid in velocity triangle
 C_{cav} : element representing cavitation
 C_p : cavitation compliance
 D: diameter
 d: pipe diameter
 f_0 : cavitation surging frequency
 H_{sv} : net positive suction head
 I : inertia of rotational parts of pump, $I = I_m + I_s + I_l$
 I_l : rotational inertia of liquid within the impeller
 I_q : fluid inertia of liquid in the pipe
 I_{q1} : fluid inertia in suction pipe
 I_w : through flow inertia of liquid within the impeller
 K: bulk modulus
 L: length of flow passage of whole system
 M_b : mass flow gain factor
 P, ΔP : pressure, pressure difference
 Q: flow rate, discharge
 Q_0 : rated flow rate

R: impeller radius
 R_c : contraction loss in Rc element
 R_e : expansion loss in Re element
 R_g : power gyrating parameter in MGY element
 R_l : leakage loss in Rl element
 R_{pf} : pipe friction parameter
 R_{if}, R_{is} : losses in an impeller in Rif and Ris elements
 R_s : flow resistance in suction pipe
 R_v : hydraulic loss parameter in a valve, in Rv element
 R_{vf}, R_{vs} : losses in a volute in Rvf and Rvs elements
 R_w : disk loss parameter in R ω element
 T, ΔT : torque, torque loss
 t: time
 U: fluid velocity
 u: peripheral velocity of an impeller
 V: absolute velocity
 v: absolute velocity of an impeller in velocity triangle
 V_c : cavitation volume
 W: relative velocity of fluid within the impeller in velocity triangle
 Z: number of blades of the impeller
 α : angle between u and c in the velocity triangle, void fraction
 β_2 : flow angle with the slip factor at the impeller outlet
 β_{b2} : blade angle at the impeller outlet
 φ : flow coefficient = $\overline{Q_2} / (B_2 u_2)$
 ρ : density
 σ : cavitation number = $H_{sv} / (u_1^2 / 2g)$
 τ : shear stress
 ω : rotational speed

Subscript:

0: rated value
 1: inlet of impeller, suction side
 2: outlet of impeller, delivery side
 I, i: impeller
 m: motor
 s: shaft
 $\bar{\quad}$: mean value
 θ : peripheral component

1. INTRODUCTION

Researches on system dynamics of a pump system have been performed (Barrand Ghelic and Caignaert 1993; Nguyen Kaenel and Danguy 1993; Rong Tanaka Tsukamoto and Tanaka 1996; Tsukamoto and Ohashi 1982; Rong Tanaka and Tsukamoto 1997). To analyze dynamic behaviors of a system equipped with fluid machinery, it is necessary to study dynamic characteristics especially in cavitating flow. These characteristics are traditionally obtained by performance tests. However, they cannot correctly represent the dynamic characteristics of turbomachinery, because:

1) The dynamic characteristics of turbomachinery systems are very complicated since these systems consist of mechanical, hydraulic and the other sub-systems. Especially the nonlinear characteristics are serious in a fluid sub-system. The sub-systems affect each other in a dynamic process;

2) As the behaviors of a turbomachinery system are combined with all sub-systems, it is difficult to distinguish the influence of them one by one.

Therefore, it is very useful to develop a mathematical model to express the dynamic characteristics of the fluid machinery, both in steady state and dynamic modes.

Bondgraphs method (Karnopp and Rosenberg 1990) has been used to solve the above problems recently (Paynter 1972; Rong Tanaka and Tsukamoto 1996). This is a method of analyzing system dynamics based on the conservation of energy flow within these systems. As this method modeling these systems is unified it is easy to derive the mathematical model of dynamic behaviors of the whole system including pump.

The mathematical model representing the dynamic behaviors of pump systems can predict the unsteady characteristics of the system. When the system operating point moves far from the design point as well as when cavitating flow occurs, the non-linear characteristics become more serious. Even in these cases, the Bondgraphs model can still represent the system dynamics correctly.

2. BONDGRAPHS OF THE PUMP SYSTEM

The schematic figure of a pump system in a closed circuit is illustrated in Fig. 1. In this paper, only the mechanical and hydraulic systems are considered to study the dynamic behaviors of the pump system. The power flow in this system is as follows;

The power from the motor is transferred to the pump shaft. A part of the shaft power is consumed through the mechanical and disk friction loss and the other are stored as the rotational inertia. The rest flows into the impeller, in which the mechanical power is converted into hydraulic power. In the process of conversion, there exist shock loss, friction loss and leakage loss. And also, in the dynamic mode, some of the power will be stored in the system acceleration as the liquid inertia in the impeller.

Then, the power flows into the volute casing where some of the kinetic energy will be converted into the pressure energy. In the process of conversion there also

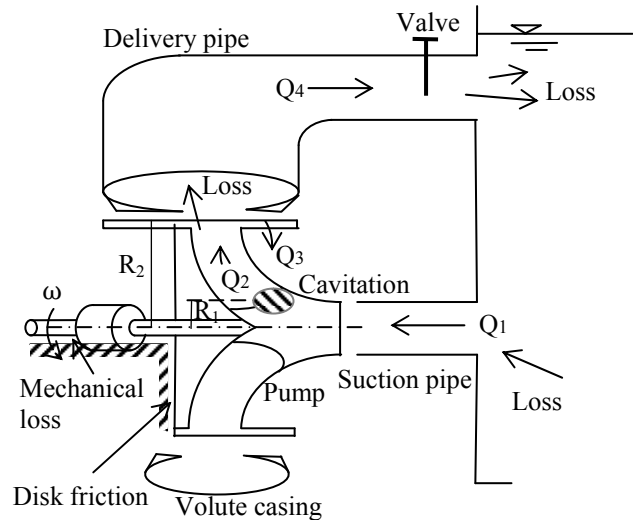


Figure 1: Pump system

exist shock loss and friction loss.

Then the power flows into the piping system, where there is friction loss. In the dynamic process, some of the power is stored due to the longitudinal acceleration of the liquid. The remaining power flows into the valve, some of which is consumed there.

Then the power flows into the tank with the expansion loss. Also when the power flows into the suction pipe from the tank, a part of the power will be consumed as the contraction loss as well as the friction loss. The remains flow into the pump. Here the power circulation closes in the pump system. The above power flow can be represented by using Bondgraphs, as shown in Fig. 2.

2.1. System Bondgraphs

In system Bondgraphs (Fig. 2), SE represents Torque input to the pump system through the rotating shaft of the motor system. The power input is $(T_0 \times \omega)$.

Before flowing into the impeller system, the power is divided into four components; the first is the power storing element I, $(\Delta T_I \times \omega)$ as the rotational inertia, the second is the power consuming element R_m , $(\Delta T_m \times \omega)$ as the mechanical loss and the third is the disk friction loss R_o , $(\Delta T_f \times \omega)$, and the last is transferred to the impeller.

In Bondgraphs, turbomachinery is represented as MGY element (Painter 1972). The mechanical power given to the impeller $[(T_0 - \Delta T_I - \Delta T_m - \Delta T_f) \times \omega]$ is converted to the fluid power $(P \times Q_2)$ by the test pump. The gyrating function of the MGY element is given as R_g (Rong Tanaka Tsukamoto and Tanaka 1996).

The power generated in the impeller $(P \times Q_2)$ separates into several components. The first of which is an element indicating fluid inertia in the impeller I_w , $(\Delta P_w \times Q_2)$. The second of which is R_{is} , $(\Delta P_{is} \times Q_2)$ element indicating hydraulic shock loss in the inlet of the impeller. The third of which is R_{if} , $(\Delta P_{if} \times Q_2)$ element indicating hydraulic loss in the impeller. And before the power flows into the volute casing, some power is consumed as leakage loss R_l , $\{(P_2 - P_1) \times Q_3\}$ because of the pressure difference between impeller inlet and outlet.

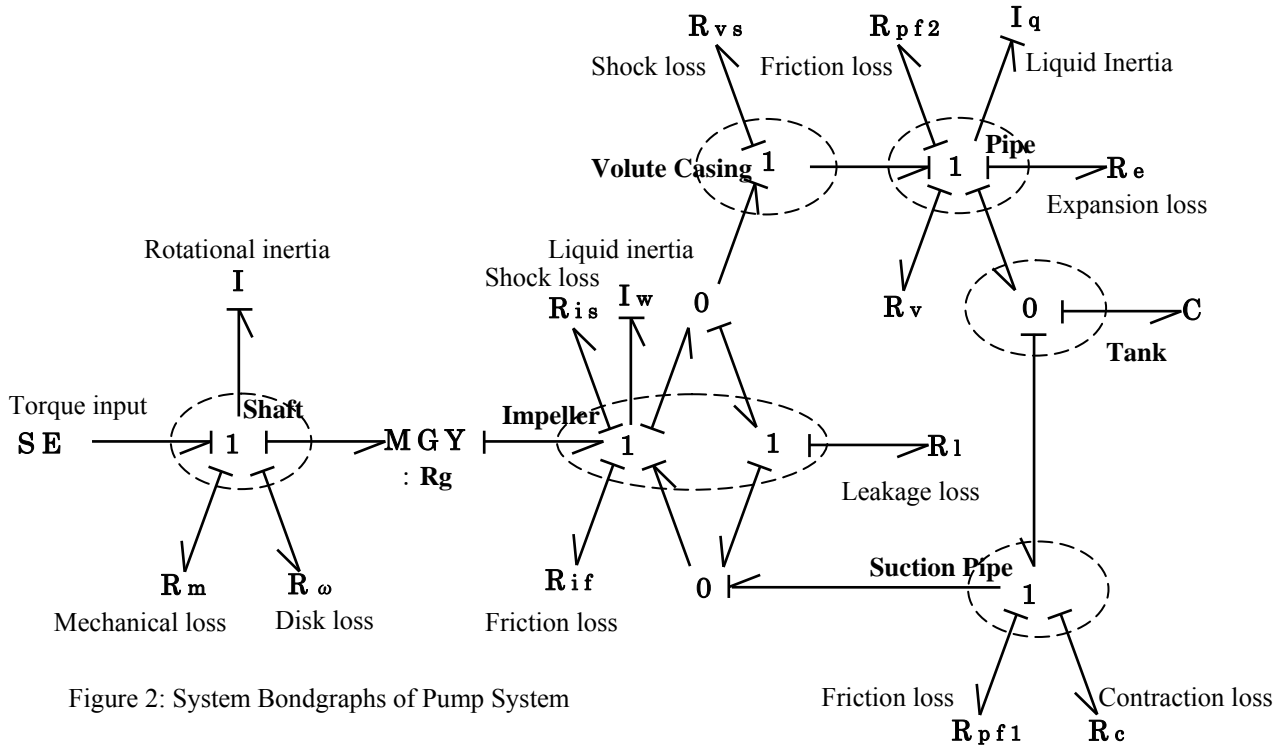


Figure 2: System Bondgraphs of Pump System

In the volute casing the hydraulic loss and shock loss are expressed as R_{vs} , $(\Delta P_{vs} \times Q_4)$ and R_{vf} , $(\Delta P_{vf} \times Q_4)$ elements respectively.

According to the modeling in a pipe and $P_4 = P_2 - \Delta P_{vs} - \Delta P_{vf}$, the power flows into the pipe $P_4 \times Q_4$ is divided into several power elements: hydraulic loss element R_{pf2} , $(\Delta P_{pf2} \times Q_4)$; energy storing element I_{q_1} , $(\Delta P_{Iq} \times Q_4)$ because of liquid inertia in the pipe and valve loss R_{vs} , $(\Delta P_v \times Q_4)$; The remaining power $(P_4 - \Delta P_{pf2} - \Delta P_{Iq} - \Delta P_v) \times Q_4$ flows into the tank. Then power flows through the tank into the pipe only with losses. These are expansion loss R_e , $(\Delta P_e \times Q_4)$ and contraction loss R_c , $(\Delta P_c \times Q_4)$.

In case that the transients are very fast, the flow rate is much smaller than the water volume inside the tank, and even if cavitation phenomena are considered, the water level in the tank can be considered to be constant within the transients.

Then the power flows from the tank into the suction pipe. In the pipe, the power are divided into hydraulic loss R_{pf1} , $(\Delta P_{pf1} \times Q_1)$, inertia storing elements. And the remaining power flows into the impeller, $(P_1 \times Q_1)$. When cavitating flow happens at the impeller inlet, the phenomenon is represented by C_{cav} element. Then $Q_1 \neq Q_4$ because cavitation bubble occurs and its volume fluctuates. In non-cavitating flow, $Q_1 = Q_4$.

In the Bondgraphs, if an element is considered necessary or useful to represent the dynamic behaviors of a system, it can be added to the system Bondgraphs easily. On the other hand, if an element is considered to be negligible, it can be removed from the Bondgraphs. These corrections do not affect the computer program.

2.2. Mathematical Functions of Power Transfer Element in an Impeller

An impeller transfers rotational mechanical power to

hydraulic power. This power transformation can be represented as the following equation without losses.

$$T \cdot \omega = \rho [(uv_\theta)_2 - (uv_\theta)_1] Q_2 + (I_m + I_s + I_i) \frac{d\omega^2}{dt} + I_1 \frac{d\omega^2}{dt} - I_w \frac{dQ^2}{dt} \quad (1)$$

$$= \rho [(uv_\theta)_2 - (uv_\theta)_1] Q_2 + \Delta T_i \cdot \omega + \Delta T_i \cdot \omega - \Delta P \cdot Q_2$$

In this equation, T_0 is the input torque of the pump shaft. When $d\omega^2/dt=0$ and $dQ^2/dt=0$ in the steady mode, the equation becomes Euler equation of turbomachinery.

2.3. Losses in the system

There exist many losses in the process of power flow in the system. The main losses are shown as R elements in Fig. 2. The mathematical expressions of their representative losses are as follows according to JSME standard (1989).

2.3.1. Disk Friction Loss

Disk friction loss can be expressed in the following equation.

$$\Delta E_\omega = C_{M_D} D_2^5 N^3 \quad (2)$$

$$C_M = C_{M_D} + \sum C_{M_C} \quad (3)$$

ΔE_ω is energy loss in the disk friction loss and N is rotational speed of an impeller. The whole friction coefficient of an impeller is represented by Eq. (3), where C_{M_D} is coefficient on the disk, while C_{M_C} is friction coefficient on the peripheral area. C_{M_D} and C_{M_C}

can be calculated using the equations verified through experiments.

2.3.2. Friction loss in an impeller

The pressure loss based on the friction loss in an impeller can be expressed as

$$\Delta P_{I_f} = \xi_{I_f} (W_2^{*2} + W_1^{*2}) / 4 \quad (4)$$

W^* means relative velocity in case that slip factor is considered at the impeller outlet. ξ_{I_f} is a friction coefficient, which can be calculated using basic theory of fluid dynamics.

2.3.3. Shock Loss in an impeller

In general, the shock loss can be expressed as the following equation.

$$\Delta P_{I_s} = \xi_{I_s} (W_{u1} - W_{u1}^*)^2 / 2 \quad (5)$$

But this equation is effective only in the case of the rated operating point. When the system is operating in the other area or in the transient mode, this loss should be considered in detail.

The other losses such as leakage loss in the impeller, hydraulic and shock loss in the volute casing can be expressed using the same method. It should be noted here, in some cases of high speed transients cavitation will happen. This may affect the characteristics greatly. But in this research, the influence of cavitation to the dynamic behaviors are not considered

3. STATE SPACE EQUATION OF PUMP SYSTEM

Considering the system bondgraphs shown in Fig. 2, only one C element and three I elements, I , I_w and I_q , are time-dependent and the others are not. The following differential equations representing the dynamic behaviors of a pump system are obtained by eliminating all variables except the variable ω , Q_1 and Q_2 , from the characteristic functions of all elements derived in this paper and the algebraic equations for the conservation law at all junctions.

$$I' \frac{d\omega}{dt} = -R_m - R_\omega \omega^2 - R_g Q_2 + T_0$$

$$I' = I_s + I_i + I_m + I_l$$

$$I\omega \frac{dQ_2}{dt} = R_g \omega - (R_{i_s} R_{i_f}) Q_2^2 - R_l (Q_2 - Q_1)^2$$

$$I_{q1} \frac{dQ_1}{dt} + I_{q4} \frac{dQ_4}{dt} = R_l (Q_2 - Q_1)^2 \quad (6)$$

$$-(R_{v_s} + R_{v_f} + R_v + R_e + R_{pf2}) Q_4^2 - (R_{pf1} + R_c) Q_1^2$$

$$R_g = \rho ((R_2^2 - R_1^2) \omega - \frac{Q_2}{2\pi} (\frac{1}{B_2 \tan \beta_2} - \frac{1}{B_1 \tan \beta_1})) \quad (7)$$

$$\beta_2 = \arctan \left(\frac{2\pi R_2^2 B_2 \omega \sqrt{\sin \beta_{b2}}}{Z^{0.7} Q_2} + \frac{1}{\tan \beta_{b2}} \right)^{-1} \quad (8)$$

Table 1: Parameters of Pump and Impeller (imp.)

Specific speed	$N_s \approx 130$ [rpm, m ³ /min, m]
Rated rotational speed	$N_r = 3455$ [rpm]
Rated head of pump	$H_r = 31.5$ [m]
Rated flow rate	$Q_r = 0.25$ [m ³ /min]
Rated efficiency	$\eta_r = 0.6$
Rated torque	$T_r = 5.925$ [N-m]
Rated input power	$P_r = 2.173$ [kW]
Imp. outlet diameter	$D_2 = 0.137$ [m]
Width in imp. outlet	$B_2 = 0.0093$ [m]
Thickness of blade at imp. inlet and outlet	$S_1 = 0.005$ [m] * $S_2 = 0.007$ [m] *
Blade angle at outlet	$\beta_{b2} = 20$ [°]
Diameter in imp. inlet	$D_1 = 0.07$ [m] *
Width in imp. inlet	$B_1 = 0.01$ [m] *
Blade angle at inlet	$\beta_{b1} = 15$ [°] *
Number of blades	7
Momentum	$0.012 + 0.0005$ [kg-m ²] *
	* Means estimated value

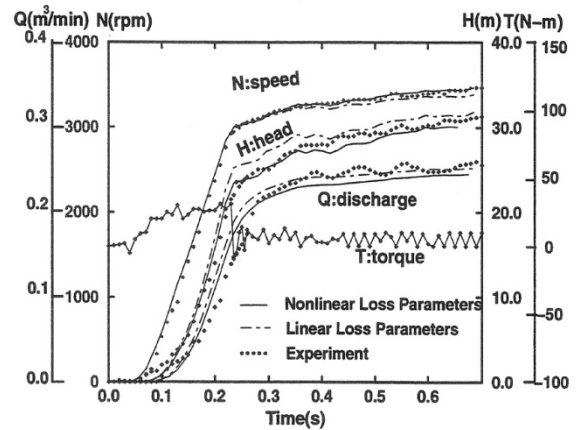


Figure 3: Dynamic behaviors of Pump Starting. Effects of Hydraulic Losses to Dynamics of Pump System

The system dynamic behaviors are decided by its own attributes, such as impeller diameter, blade angle and losses etc. In the cases with power input, the dynamic behaviors are decided by both system attributes and input T_0 .

4. SIMULATION RESULTS BASED ON SYSTEM BONDGRAPH

In the high speed starting modes of the test pump system, the total length of the pipes is $L_p = 5.1$ [m], while the diameter is $d_p = 0.05$ [m]. The other parameters of the system are listed in Table 1. In the high speed starting mode, the pump system is accelerated from stationary state to the rated state quickly. The results are shown in Fig. 3. In the simulation, the experimental data of torque was input to the system according to the experimental results.

In Fig. 3, we compare the simulation results with the experimental results. Even in the very fast starting mode, they agree very well. This means that system Bondgraphs shown in Fig. 2 and their mathematical model can represent the dynamic behaviors of systems equipped with turbomachinery.

From this comparison, we know that the losses have relatively little influence to the dynamic behaviors when the transients are very fast. In the case of constant loss parameters, parameters are calculated from the rated operating point. They are smaller than that in the nonlinear loss expressions. Because of this, the starting up in this case is a little faster than that in the case of nonlinear loss parameters. These results also affect the dynamic behaviors immediately after the starting up. However in the end of the process, the results of the two models will be the same, since in the steady state mode, their loss parameters are the same. From this comparison, Bondgraphs method is a useful method to represent the system.

5. CFD STUDY ON PUMP CAVITATING FLOW

5.1. Cavitation Analysis Method

Commercial CFD codes enable to analyze cavitation phenomena with good precision of numerical calculation recently (Philippe and Okamura 2002; Sato Nagahara Suzuki Tanaka Fuchiwaki, and Nishi 2009; Sato Nagahara Tanaka Fuchiwaki Shimizu and Inoue 2011). As solution methods for bubble flows, there are a VOF method of two-phase flow (Volume-of-Fluid Method), a cavity bubble tracking method and a method that solves the motion equation of Rayleigh-Plesset (Brennen 1995; Tamura Sugiyama and Matsumoto 2001; Tamura Fukaya and Matsumoto 2002) coupling it with flow equations to obtain fluid density mixed with water and bubbles. A method with the motion equation of Rayleigh-Plesset is used in this study. Its outline is shown below.

Usually, Eq. (9) of Rayleigh-Plesset for spherical bubbles is solved.

$$R \frac{d^2 R}{dt^2} + 3 \left(\frac{dR}{dt} \right)^2 = \frac{1}{\rho} \left(p_g - p - \frac{4\mu}{R} \frac{dR}{dt} - \frac{2\sigma}{R} \right) \quad (9)$$

Here, R indicates a radius of bubble, ρ liquid density, p_g gas pressure inside the bubble, p pressure of the liquid phase, μ viscosity coefficient of liquid phase and σ surface tension of liquid.

It is difficult to solve with multi-purpose software the detail of second order derivative term for approximation of the condition that bubbles repeat to grow and collapse with p_{in} , where vapour and air mixed. Therefore, it is common to solve the equations below. Equation (9) is simplified to Eq. (10) so that time variations of R are obtained.

< 1 > $p_g = p_v$; Bubbles are filled with saturated vapour continuously,

< 2 > Second order derivative term, surface tension term and viscous term are abbreviated.

$$\frac{dR}{dt} = \sqrt{\frac{2}{3} \frac{p_v - p}{\rho}} \quad (10)$$

In addition, when expressing void fractions α with R as a bubble radius and n_0 as number density per a unit volume of liquid,

$$\alpha = \frac{n_0 \frac{4}{3} \pi R^3}{1 + n_0 \frac{4}{3} \pi R^3} \quad (11)$$

Equation (12) is used as a transport equation of void fractions.

$$\frac{\partial \alpha}{\partial t} + \frac{\partial}{\partial x_j} (\alpha U_j) = \left(\frac{n_0}{1 + n_0 \frac{4}{3} \pi R^3} \right) \frac{d}{dt} \left(\frac{4}{3} \pi R^3 \right) \quad (12)$$

The equations mentioned above and the following conservation equation of mass and momentum (Navier-Stokes equation) are coupled and solved.

$$\frac{\partial \rho}{\partial t} + \frac{\partial}{\partial x_j} (\rho U_j) = 0 \quad (13)$$

$$\frac{\partial}{\partial t} (\rho U_j) + \frac{\partial}{\partial t} (\rho U_j U_i) = - \frac{\partial p}{\partial x_j} - \frac{\partial \tau_{ij}}{\partial x_j} + \rho f_j \quad (14)$$

5.2. Turbulence Model and Calculating Conditions

In prediction of pump oscillation in a test pump, cavitation occurrence with turbulence at the suction part is expected. Therefore, it is necessary to predict precisely the flow field at the suction part and the vortex occurrence caused by flow separation in particular. Transient rotor stator interface is used for the boundary between rotating part and stationary part. For a digitizing scheme, a second order upwind windward finite difference scheme is used for both convection and diffusion terms (Barth and Jespersen 1989). Simple method is used for an algorithm and inner iteration is assumed 50 iterations for each step. For boundary conditions, a pressure boundary and velocity integral boundary are used for the inlet and outlet, respectively.

Precision and reliability of capturing the sudden pressure rise after cavitation bubble collapse are compared among the results using a standard k- ϵ model, SST model and LES model in case that the number of grids is 5,200,000 elements. Overall features are almost the same in all cases though LES captures finer vortex structures such as the vorticity distributions at the location corresponding to the impeller inlet in each model. As a result, cavitating flow analyses have been performed with SST turbulence model from viewpoint of calculating conditions such as the number of grids, non-dimensional wall distance y^+ , and calculating time, as shown in Table 2. The calculation was performed every

Table 2: Calculating conditions

Details of elements	Number of elements	Maximum aspect ratio
Suction domain	437000 at $1.0 Q_0$ 548000 at $0.6 Q_0$	316.0
Impeller domain	557000	34.8
Volute domain	352000	309.3
Overall view	About 1400000	
N = 1800 rpm	z = 6 blades	y+ = 4 -150
$\Delta T = 9.26 \times 10^{-5}$ sec (for Impeller revolution by 1.0 degree)		SST turbulence model

time step correspondent to the impeller rotation by 1.0 degree, for 6 revolutions of the impeller.

5.3. Confirmation of Cavitation Occurrence

Figure 4 shows streamlines from the baffle plate to the rotational impeller. Rotational flow is generated near the baffle plate and the flow reaches the rotating impeller. There is a sign that the cavitation occurs from the baffle plate when there is strong rotation in the suction passage. In addition, there is one more sign that another cavitation occurs in the shroud side of the impeller. As a characteristic, this cavitation occurs from a low pressure region generated by leakage flow from the suction passage and mixed with main stream.

Figure 5 shows the iso-surface of $\alpha = 0.5$ of the vortex cavitation. The existence of the vortex cavitation from the baffle plate can be confirmed clearly in this figure. It can be seen that the vortex cavitation is generated near the baffle plate and reaches the rotating impeller. Hereafter, the impeller rotational angle shown in this figure becomes a norm, θ_0 .

5.4. Calculation of cavity volume

The commercial code can calculate the volume of cavities in each calculating domain. As there is a distribution of void fraction inside a cavity, air volume in the cavity is calculated from the product of volume-averaged void fraction in some calculating domain and the volume of the domain. Consequently, it becomes possible to calculate the air volume in each domain even when different type of cavitation occurs simultaneously in the different location.

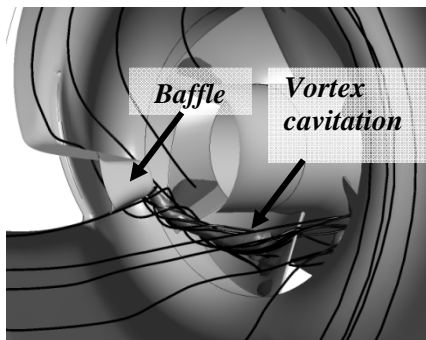


Figure 4: Stream lines and vortex cavitation from baffle plate (Simulation result, $\varphi=0.11$, $\sigma=0.30$)

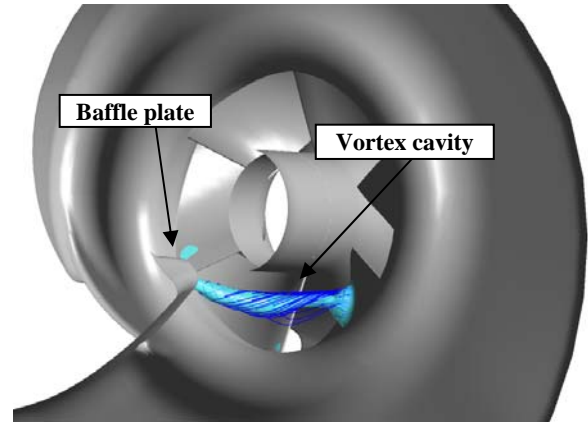


Figure 5: Iso-surface of $\alpha = 0.5$

6. SYSTEM MODEL OF CAVITATING FLOW

Cavitating flow raises many troubles, one of which is cavitation surge (Tsuji moto 2006; Yamamoto and Tsujimoto 2009). This is an important dynamic behavior of a pump system. Cavitation surge is considered as a complicated self oscillation phenomenon brought by total characteristics of the pump system. However, the surging frequency can easily be considered as the natural frequency of the pump system. Studies on the cavitation surge in a centrifugal pump have been performed under consideration that the phenomenon is supposed as quasi-linear self oscillation.

Here, basic characteristics of the surging frequency are analyzed one-dimensionally under quasi-steady response model using the CFD results on the cavitation surge in a centrifugal pump. In the field of pump cavitating flow, the characteristic parameters, cavitation compliance and mass flow gain factor, are generally used. Here, how to determine the value of the parameters is described.

6.1. Lumped parameter model of cavitation (C_p, M_b)

Assuming the quasi-steady response can be permitted in cavitating flows, cavitation volume can be represented by use of cavitation compliance C_p and mass flow gain factor M_b .

$$C_p = \frac{\partial V_c}{\partial P_1} \quad (15)$$

$$M_b = \frac{\partial V_c}{\partial Q_1} \quad (16)$$

$$\dot{V}_c = C_p \dot{P}_1 + M_b \dot{Q}_1 \quad (17)$$

Equation (17) can easily be replaced with an equation of spring-damper system in a mechanical system. Equation (17) is changed as follows.

$$P_1 = \frac{1}{C_p} \int \dot{V}_c dt - \frac{M_b}{C_p} Q_1 \quad (18)$$

Equation of continuity in Fig. 7,

$$\dot{V}_c = Q_1 + Q_3 - Q_2 = \Delta Q \quad (19)$$

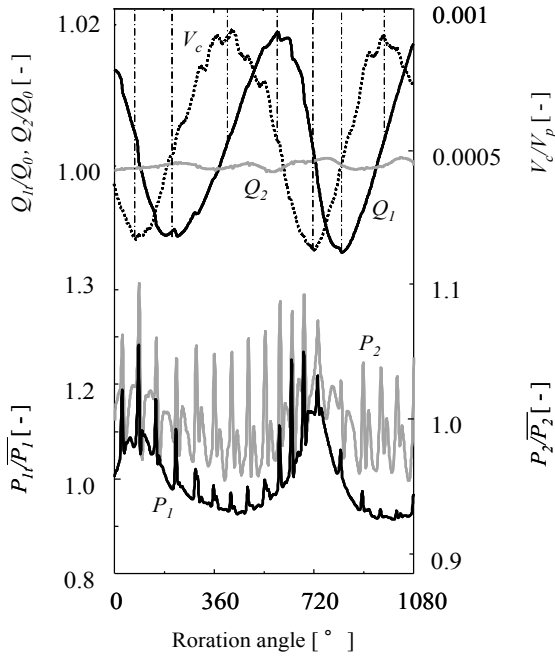


Figure 6: V_c - Q - P simulated by LES model ($\varphi=0.11$, $\sigma=0.30$)

From the above Eq. (17) and (18),

$$P_1 = \frac{1}{C_p} \int \Delta Q dt - \frac{M_b}{C_p} Q_1 \quad (20)$$

This is the characteristic equation of the cavitation element C_{cav} in Fig. 7.

This equation means that cavitating flow can be represented as spring-damper system. The spring coefficient is $1/C_p$ and damper coefficient is $-M_b/C_p$. In other words, a spring coefficient is defined as $-K/V_c$ in a lumped parameter system as follows.

$$\frac{1}{C_p} = -\frac{K}{V_c} = -\frac{\left(\frac{dp}{-dV_c/V_c}\right)}{V_c} = \frac{1}{dV_c/dp} \quad (21)$$

Because Eq. (21) is similar to Eq. (15), $1/C_p$ of Eq. (18) means the spring coefficient. Moreover, $-M_b/C_p$ of Eq. (18) is changed to the next equation.

$$-\frac{M_b}{C_p} = -\frac{\partial V_c / \partial Q}{\partial V_c / \partial P} = -\frac{\partial P}{\partial Q} \quad (22)$$

Because the last term means the gradient of pump performance curve, $-M_b/C_p$ indicates flow resistance coefficient of the pump system.

Figure 6 shows characteristics of cavitation compliance and mass flow gain factor. The phase of cavitation volume is quite opposite to suction pressure in the result. Therefore, the cavitation compliance is always negative from Eq. (15) and fluctuates according to the cavitation volume change from Eq. (21). Due to the phase difference between cavitation volume and suction flow rate, mass flow gain factor repeats positive and

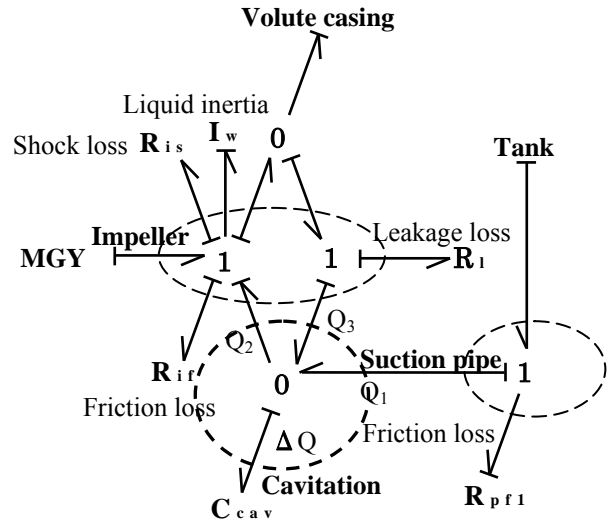


Figure 7: Bondgraphs Model of Cavitating Flow

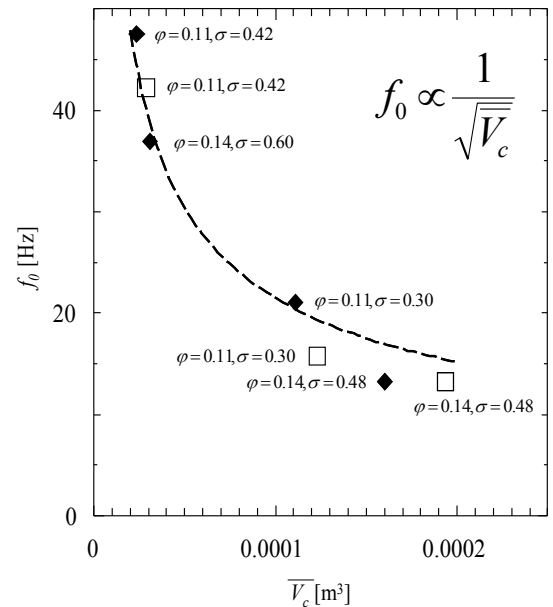


Figure 8: f_0 - \bar{V}_c simulated by SST model (\square), and by LES model (\blacklozenge), Approximate curve: $f_0 = 0.21/\sqrt{\bar{V}_c}$

negative values across the border indicated as the dashed line in Fig. 6 according to Eq. (16). When mass flow gain factor is negative, the pump system has negative resistance from Eq. (22). This means that pump performance has positive slope, which is clearly characteristic for negative damping of the system. These results show that cavitating flow system has two kind of self oscillation modes based on coefficient fluctuation and negative damping based on positive/negative fluctuation of flow resistance.

As stated above, cavitating flow in a pump can be represented by C element in Bondgraphs model as shown in Fig. 7 and the coefficient can be calculated by the cavity volume through CFD analysis. In the next section, the value of coefficient is validated by estimating natural frequency.

6.2. Natural frequency of pump system

Cavitation surge in a pump system can be modeled by considering a suction pipe and cavitation phenomenon. Here, the suction pipe is modeled by mass-damper system as represented in Eq. (19) and the cavitation phenomenon is modeled by spring-damper system as represented in Eq. (18). As a result, the pump system dynamics is represented by the following equations.

$$P_1 = -I_{q1} \dot{Q}_1 - R_1 Q_1 \quad (23)$$

$$I_{q1} \ddot{Q}_1 + \left(R_1 - \frac{M_b}{C_p} \right) \dot{Q}_1 - \frac{1}{C_p} Q_1 = \frac{-1}{C_p} Q_2 \quad (24)$$

From this equation, the natural frequency of pump system can be represented by the first and third terms.

$$f_0 = \frac{1}{2\pi} \sqrt{\frac{1}{-I_{q1} C_p}} \quad (25)$$

From Eq. (21) and Eq. (25),

$$f_0 = \frac{1}{2\pi} \sqrt{\frac{K}{I_{q1} V_c}} \quad (26)$$

In the above equation, $\overline{V_c}$ which is the mean value of V_c , can be replaced with V_c in Eq. (26) when cavitation volume V_c fluctuates.

$$f_0 = \frac{1}{2\pi} \sqrt{\frac{K}{I_{q1} V_c}} \quad (27)$$

CFD results on the cavitating flow are expressed by Eq. (27). Figure 8 shows the relationship between f_0 and $\sqrt{\overline{V_c}}$ and the approximate equation. This fact means that Bulk modulus can be assumed constant in the cavitation approximately.

Form the approximate equation in the Fig. 8, Bulk modulus is derived as follows.

$$\frac{1}{2\pi} \sqrt{\frac{K}{I_{q1}}} = 0.21 \quad \therefore K = 3.20 \times 10^4 [Pa] \quad (28)$$

Considering that Bulk modulus is $1.33 \times 10^5 [Pa]$ under normal condition, this value seems to be a little bit smaller.

However, if the vaporous pressure would be defined as $p = 3171 [Pa]$, the bulk modulus of pure vapor is calculated as the following, $K_{vapor} = \kappa p = 4.22 \times 10^3 [Pa]$.

The bulk modulus of water is $K_{water} = 2.06 \times 10^9 [Pa]$. The apparent bulk modulus of cavitation including water and pure vapor is defined as follows,

$$K_{cavi} = \frac{K_{water} K_{vapor}}{K_{vapor} + x(K_{water} - K_{vapor})} \quad (29)$$

where x means mixing ratio of water and vapor in a cavitating flow. The each value of K_{vapor} , K_{water} and K_{cavi} , that is given as $K = 3.20 \times 10^4 [Pa]$ in Eq. (28), is substituted into Eq. (29), the mixing ratio is calculated as $x = 13.2\%$. This value is considered as reasonable.

7. CONCLUSIONS

In this study, the Bondgraphs model representing the dynamic characteristics of a pump system has been used to perform modeling and simulation of the cavitating flow. As a result, the following conclusions are obtained.

- 1) Cavitating flow can be modeled by C element in Bondgraphs model.
- 2) The value of coefficient of the C element for cavitating flow can be calculated by CFD analysis.
- 3) Finally The system Bondgraphs of a pump system including cavitating flow has been established.

REFERENCES

- Barrand, J.P., Ghelici, N., and Caignaert, G., 1993. Unsteady flow during the fast start-up of a centrifugal pump, *ASME, FED-Vol. 154, Pumping Machine*, 143-150.
- Barth, T. J. and Jespersen, D. C., 1989. The Design and Application of Upwind Schemes on Unstructured Meshes, *AIAA Paper*, 89-0366.
- Brennen, C. E., 1995. *Cavitation and bubble dynamics*, Oxford University Press.
- Karnopp, D., Rosenberg, R., 1975. *SYSTEM DYNAMICS: A UNIFIED APPROACH*, John Wiley & Sons, Inc.
- JSME STANDARD, 1989. *Performance Conversion Method for Hydraulic Turbines and Pumps*.
- Nguyen Duc., J.M., Von Kaenel, A., and Danguy, F., 1993. Transient behaviors of liquid hydrogen pumps during start-up and shutdown of rocket engines, *ASME, FED-Vol. 154, Pumping Machinery*, 159-170.
- Painter, H.M., 1972. The Dynamics and Control of Eulerian Turbomachines, *Trans. ASME, Journal of Dynamic Systems, Measurement, and Control*, 198-205.
- Philippe, D. and Okamura, T., 2002. Cavitating Flow Calculations in Industry, *Proceedings of the 9th of International Symposium on Transport Phenomena and Dynamics of Rotating Machinery*, FD-146.
- Rong, W.H., Tanaka, K., Tsukamoto, H., Tanaka, H., 1996. Dynamic Behaviors Analysis of Pump System by Bond Graphs Method, *Proceeding of ASME FED-Vol. 237*, 805-812.
- Rong, W.H., Tanaka, K., Tsukamoto, H., 1997. Unsteady Characteristics and Transfer Matrix of Pump System based on Bondgraphs, *Proceeding of ASME FEDSM97-3368*, 1-7

- Sato, T., Nagahara, T., Suzuki, S., Tanaka, K., Fuchiwaki, M., and Nishi, M., 2009. Cavitation Analysis on Double-Suction Volute Pump, *Proceeding of 3rd IAHR International Meeting of the Workgroup on Cavitation and Dynamic Problems in hydraulic Machinery and Systems*, D1, 185-193.
- Sato, T., Nagahara, T., Tanaka, K., Fuchiwaki, M., Shimizu, F., and Inoue, A., 2011. Vortex Cavitation from Baffle Plate and Pump Vibration in a Double-Suction Volute Pump, *Int. Journal of Fluid Machinery and systems*, Vol. 4, No. 1, 76-83.
- Tsukamoto, H. and Ohashi, H., 1982. Transient Characteristics of a Centrifugal Pump During Starting Period, *Trans. ASME Journal of Fluids Engineering*, Vol. 104, 6-14.
- Tamura, Y., Fukaya, M., and Matsumoto, Y., 2002. Numerical Method for Cavitating Flow Simulations and Its Application to Axial Flow Pumps, *Proceedings of the 9th of International Symposium on Transport Phenomena and Dynamics of Rotating Machinery*, FD-129.
- Tamura, Y., Sugiyama, K., and Matsumoto, Y., 2001. Physical Modeling and Solution Algorithm for Cavitation Flow Simulations, *15th AIAA Computational Fluid Dynamics Conference*, AIAA2001-2652.
- Tsujimoto, Y., 2006. Flow Instabilities in Cavitating and Non-Cavitating Pumps, Design and Analysis of High Speed Pumps, RTO-EN-AVT-143, Paper 7, 7-1-7-24.
- Yamamoto, K. and Tsujimoto, Y., 2009. Backflow Vortex Cavitation and Its Effects on Cavitation Instabilities, *Int. Journal of Fluid Machinery and systems*, Vol. 2, No. 1, 40-54.

AUTHORS BIOGRAPHY

KAZUHIRO TANAKA,

He graduated from the University of Tokyo, obtained the first job as an assistant professor in Sophia University, and he moved back to the University of Tokyo. After then, he moved again to Kyushu Inst. of Tech. and is a professor. He has interests in CFD analyses on flow patterns inside components and systems as well as in analyses of dynamic characteristics for turbomachinery systems as well as oil-hydraulic systems.

TOSHIYUKI SATO

He graduated from Kyushu Inst. of Tech. as Ph.D student supervised by Prof. Tanaka. He is a high class engineer in Hitachi Ltd. for CFD analysis and design of turbomachinery including steady as well as unsteady flow. He has much interest in fishing.

HIROSHI TSUKAMOTO

He graduated from the University of Tokyo and moved to Kyushu Inst. of Tech. He retired as a professor of KIT and now the president of Kitakyushu National College of Japan. He has interests in transient characteristics of pump systems.

TAKEHISA KOHDA

He graduated from Kyoto University, obtained the first job in National Institute of Advanced Industrial Science and Technology, and moved back to Kyoto University. He is an associate professor. He developed BGSP, BondGraph Simulation Program, in Japan.

KATSUYA SUZUKI

He retired from Toyota Motor Corp., where he was a manager of Drive Train Division. He obtained Ph.D. degree in Nagoya University. He is now a visiting professor in Kyushu Inst. of Tech. and enjoys a lively discussion of Bondgraphs with Prof. Tanaka. He is a member of a chorus group singing the Ninth Symphony.

STATE AND UNKNOWN INPUT OBSERVER: ANALYSIS AND DESIGN

E. Tarasov⁽¹⁾, I. Gahlouz⁽²⁾, C. Sueur⁽³⁾ and B. Ould Bouamama⁽⁴⁾

⁽¹⁾⁽³⁾Ecole Centrale de Lille, LAGIS CNRS UMR 8219, BP 48, 59651, Villeneuve d'Ascq cedex, France

⁽²⁾⁽⁴⁾Polytech Lille, LAGIS CNRS UMR 8219, 59655, Villeneuve d'Ascq cedex, France

christophe.sueur@ec-lille.fr, belkacem.ouldbouamama@polytech-lille.fr

ABSTRACT

This paper presents a structural approach for the state and unknown input estimations of linear systems when the classical matching condition is not verified. At the analysis step, the finite and infinite structures of the model are studied from the bond graph representation. At the synthesis level, the observer is directly implemented from the initial model with some additives terms and can be represented by a bond graph model. An illustrative example which considers a real system is included.

keyword: Unknown Input Observer, bond graph, linear models, structural approach

1. INTRODUCTION

Consider a linear perturbed system described by a state space equation defined in (1), where $x \in \mathfrak{R}^n$ is the state vector, $z \in \mathfrak{R}^p$ is the vector set of measured variables (also output variables to be controlled in this paper). The input variables are divided into two sets $u \in \mathfrak{R}^m$ and $d(t) \in \mathfrak{R}^q$ which represent known and unknown input variables respectively.

$$\begin{cases} \dot{x}(t) = Ax(t) + Bu(t) + Fd(t) \\ z(t) = Hx(t) \end{cases} \quad (1)$$

Generally, the state vector $x(t)$ cannot be entirely measured and the system is often subject to unknown inputs $d(t)$ (disturbance or failure...) which must be estimated. The unknown input and state observability problem (UIO) is a well known problem. Different approaches give solvability conditions and constructive solutions for this problem.

At the analysis step, before design, most of the approaches require the analysis of the structural invariants of the model which play a fundamental role in this problem. The infinite structure of the model is also often related to solvability conditions. They have been extensively studied in many papers and books [2], [24], [26], [18], [14], [19]. The knowledge of zeros is an important issue because zeros are directly related to stability conditions of the observer and of the controlled system.

For LTI models, constructive solutions with reduced order observers are first proposed with the geometric approach [15], [3], [2]. Constructive solutions based on generalized inverse matrices are given in [22] and then in [23] and [17]. Full order observers are then proposed in a similar way (based on generalized inverse matrices) in [8] and [7], but with some restriction on the infinite structure of the model

(known as observer matching condition), which is a rather restrictive condition.

The algebraic approach is proposed in [29] and in [5] for continuous and discrete time systems, without restriction on the infinite structure of the model. When this condition (matching condition) is not satisfied [13] proposed unknown input sliding mode observers after implementing a procedure to get a canonical observable form of the model. New output variables are defined with some derivatives. In this approach, sliding mode observers combined with a high-gain approach are often proposed [20]. New developments are now proposed with an observer based approach for some classes of nonlinear systems with a fuzzy approach [30], fuzzy systems with time delays [28] or with uncertain systems [4].

This work makes the following contributions: extension of a previous work [31] when the classical matching condition is not verified and simple synthesis of an UIO with output variables' derivatives. In section 2, the previous UIO design is recalled with the different steps for design and synthesis. An extension without the matching condition is proposed in section 3. In that case, the UIO is a bond graph model, close to the bond graph model of the physical system. At the analysis step, a graphical approach is proposed and as for many estimation and control problems, the invariant zeros are of great interest in the analysis. An illustrative example which considers a real system is included in section 4, and we conclude in section 5.

2. UIO WITH MATCHING CONDITION

In the literature, the different proposed approaches consider first the finite structure of $\Sigma(H,A,F)$ and then its infinite structure. The finite structure gives some stability conditions on the UIO and the infinite structure some conditions on the existence of the UIO.

2.1. Finite and infinite structures of $\Sigma(H,A,F)$

The concepts of strong detectability, strong* detectability and strong observability have been proposed in [16] for systems with unknown inputs $d(t)$. The strong detectability of system with only the unknown input vector $d(t)$ corresponds to the minimum-phase condition, directly related to the zeros of system $\Sigma(H,A,F)$ (finite structure). The system $\Sigma(H,A,F)$ in (1) is strongly detectable if and only if all its zeros s satisfy $Re(s) < 0$.

The infinite structure of multivariable linear models is characterized by different integer sets. $\{n'_i\}$ is the set of infinite zero orders of the global model $\Sigma(H, A, B)$ and $\{n_i\}$ is the set of row infinite zero orders of the row sub-systems $\Sigma(h_i, A, B)$. The infinite structure is well defined in case of LTI models [9] with a transfer matrix representation or with a graphical representation (structured approach), [10].

The row infinite zero order n_i verifies condition $n_i = \min \{k | h_i A^{(k-1)} B \neq 0\}$. n_i is equal to the number of derivations of the output variable $z_i(t)$ necessary for at least one of the input variables to appear explicitly. The global infinite zero orders [12] are equal to the minimal number of derivations of each output variable necessary so that the input variables appear explicitly and independently in the equations.

In order to solve the UIO problem for systems in (1), a necessary condition called *observer matching condition* for the existence of observers is often required (see [22]; [8]): $\text{rank}[HF] = \text{rank}[F]$. For a SISO model, the infinite zero order of model $\Sigma(H, A, F)$ is equal to 1. When this condition is not satisfied [13] proposed unknown input sliding mode observers after implementing a procedure to get a canonical observable form of the model. This method can also be extended in the nonlinear case. Necessary and sufficient conditions are that system $\Sigma(H, A, F)$ is left invertible and minimum phase.

2.2. Bond graph models

In a bond graph model [21] and [25], causality and causal paths are useful for the study of properties, such as controllability, observability and systems poles/zeros. State space and transfer representations can be directly written from a bond graph model, thus properties of these mathematical representations can be derived before any calculus with a causal analysis. Bond graph models with integral causality assignment (BGI) can be used to determine reachability conditions and the number of invariant zeros by studying the infinite structure. The rank of the controllability matrix is derived from bond graph models with derivative causality (BGD).

A LTI bond graph model is controllable iff the two following conditions are verified [27]: first there is a causal path between each dynamical element and one of the input sources and secondly each dynamical element can have a derivative causality assignment in the bond graph model with a preferential derivative causality assignment (with a possible duality of input sources). The observability property can be studied in a similar way, but with output detectors. Systems invariant zeros are poles of inverse systems. Inverse systems can be constructed by bond graph models with bicausality (BGB) which are thus useful for the determination of invariant zeros.

The concept of causal path is used for the study of the infinite structure of the model. The causal path length between an input source and an output detector in the bond graph model is equal to the number of dynamical elements met in the path. Two paths are different if they have no dynamical element in common. The order of the infinite zero

for the row sub-system $\Sigma(h_i, A, B)$ is equal to the length of the shortest causal path between the i^{th} output detector z_i and the set of input sources. The global infinite structure is defined with the concepts of different causal paths. The orders of the infinite zeros of a global invertible linear bond graph model are calculated according to equation (2), where L_k is the smallest sum of the lengths of the k different input-output causal paths.

$$\begin{cases} n'_1 = L_1 \\ n'_k = L_k - L_{k-1} \end{cases} \quad (2)$$

The number of invariant zeros is determined by the infinite structure of the BGI model. The number of invariant zeros associated to a controllable, observable, invertible and square bond graph model is equal to $n - \sum n'_i$.

2.3. UIO synthesis

The model $\Sigma(H, A, F)$ is supposed to be a SISO model in order to simplify the presentation. It can be easily extended to MIMO models using for example the same procedure as for the input-output decoupling problem with the concept of row and global infinite structures from a structural point of view in the analysis step. If a somewhat physical approach is proposed, some assumptions are also possible for the state space model deduced for example from a bond graph representation.

Asumption 1. It is supposed that the SISO system $\Sigma(H, A, F)$ defined in (1) is controllable/observable and that the state matrix A is invertible.

With Asumption 1, a derivative causality assignment is possible for bond graph models (physical model without null pole). The extension to models with non invertible state matrix is straight for bond graph models, because a graphical approach can be proposed in that case. It is not proposed in this paper.

The state equation (1) is now rewritten as (3).

$$\begin{cases} \dot{x}(t) = A^{-1}\dot{x}(t) - A^{-1}Bu(t) - A^{-1}Fd(t) \\ z(t) = HA^{-1}\dot{x}(t) - HA^{-1}Bu(t) - HA^{-1}Fd(t) \end{cases} \quad (3)$$

If matrix $HA^{-1}F$ is invertible (Model $\Sigma(H, A, F)$ has no null invariant zero), the disturbance variable can be written in equation (4) and then the estimation of the disturbance variable can be written in equation (5). The extension to models with $HA^{-1}F = 0$ is straight and not proposed in this paper.

$$d(t) = -(HA^{-1}F)^{-1}[z(t) - HA^{-1}\dot{x}(t) + HA^{-1}Bu(t)] \quad (4)$$

$$\hat{d}(t) = -(HA^{-1}F)^{-1}[z(t) - HA^{-1}\hat{x}(t) + HA^{-1}Bu(t)] \quad (5)$$

From the state equation (3), estimation for the state vector is defined in equation (6), which can also be written as (7), which is similar to a classical estimation, but with a difference in the last term. It needs the derivation of the measured variable. Matrix K is used for pole placement.

$$\dot{x}(t) = A^{-1}\dot{\hat{x}}(t) - A^{-1}Bu(t) - A^{-1}F\hat{d}(t) + K(\dot{z}(t) - \dot{\hat{z}}(t)) \quad (6)$$

$$\dot{x}^{\wedge}(t) = Ax^{\wedge}(t) + Bu(t) + F\hat{d}(t) - AK(z^{\wedge}(t) - \hat{z}^{\wedge}(t)) \quad (7)$$

In this approach [31], the state equations for the model and the observer are the same, with only an extra term for the observer. This observer is simple and take into account the control inputs, which is not always true in the literature.

The convergence of the disturbance variable can be verified with equation (8), obtained from (4) and (5).

$$d(t) - \hat{d}(t) = (HA^{-1}F)^{-1}HA^{-1}(\dot{x}(t) - \dot{\hat{x}}(t)) \quad (8)$$

The estimation of the disturbance variable converges to the disturbance variable only if $(\dot{x}(t) - \dot{\hat{x}}(t))$ converges asymptotically. Convergence of the state estimation must be proved with the study of the observer fixed poles.

Matrices N_{BO} and N_{BF} are introduced in (9), in order to simplify notations.

$$\begin{cases} N_{BO} = A^{-1} - A^{-1}F(HA^{-1}F)^{-1}HA^{-1} \\ N_{BF} = A^{-1} - A^{-1}F(HA^{-1}F)^{-1}HA^{-1} - KH \end{cases} \quad (9)$$

From previous equations, with $e(t) = x(t) - \hat{x}(t)$ it comes (10).

$$e(t) = N_{BF}\dot{e}(t) \quad (10)$$

This observer requires the matching condition defined in some well known approaches [16], [7] and in that case, fixed poles of the estimation error are all the invariant zeros of system $\Sigma(H,A,F)$ [31], which means that this system must be strong* detectable .

3. UIO EXTENSION

For many physical systems modeled by (1), the observer matching condition is not satisfied. To overcome the restriction imposed by this condition, an observer has been proposed in [13] using the infinite structure of model $\Sigma(H,A,F)$, and the derivatives of input and output variables.

An extension of the state and unknown input estimations is proposed in this paper without the observer matching condition in the SISO case. It can be easily extended to the MIMO case using the global infinite structure of model $\Sigma(H,A,F)$. Only some derivatives of the output variables are needed for this new observer.

3.1. UIO synthesis

Let r be the infinite zero order of the SISO model $\Sigma(H,A,F)$. It is the smallest positive integer such that $HA^{r-1}F \neq 0$.

The estimation of the disturbance variable is still written as in equation (5) and the estimation of the state vector is now written as (11). This new observer is very close to

the previous one, with a matrix K used for pole placement multiplied by the r^{th} output variable derivative.

$$\dot{x}^{\wedge}(t) = Ax^{\wedge}(t) + Bu(t) + F\hat{d}(t) - AK(z^{\wedge}(t) - \hat{z}^{\wedge}(t)) \quad (11)$$

From (3) and (11), the state error estimation equation $e(t) = x(t) - \hat{x}(t)$ is given by (12), where N_{BF_r} is defined in (13) (Proof in Appendix).

$$e(t) = N_{BF_r}\dot{e}(t) \quad (12)$$

$$N_{BF_r} = A^{-1} - A^{-1}F(HA^{-1}F)^{-1}HA^{-1} - KHA^{r-1} \quad (13)$$

Matrix N_{BF_r} can be written in an easy way (obtained from $x(t) - \hat{x}(t)$). The difference between matrix N_{BF} defined in equation (9) and matrix N_{BF_r} defined in equation (13) is due to the output derivative and is just associated to the extra matrix A^{r-1} .

If the state equation (1) is written from a bond graph model, it is possible to draw a bond graph model for the state estimation defined in (11) because equation (11) is very close to the initial state equation. Some signal bonds must be added for the disturbance equation defined in (5). The structure of the observer is proposed in Fig. 1, with BGI for the bond graph model and BGO for the observer bond graph model.

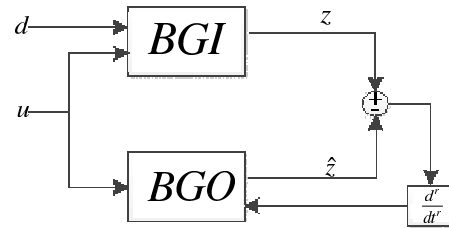


Figure 1: Structure of the observer based on bond graph model

With Fig. 1, it is possible to estimate unknown variables (disturbance inputs or actuators faults) in an easy way.

3.2. Properties of the observer

In equation (12), conditions for pole placement are studied. If matrix N_{BF_r} is invertible, a classical pole placement is studied, and the error variable $e(t) = x(t) - \hat{x}(t)$ does not depend on the disturbance variable. The conditions for (12) to be an asymptotic state observer of $x(t)$ is that N_{BF_r} must be an Hurwitz matrix, i.e., has all its eigenvalues in the left-hand side of the complex plane. Properties of the observer are studied.

A necessary condition for the existence of the state estimator is proposed in Proposition 1.

Proposition 1: A necessary condition for matrix N_{BF_r} defined in (13) to be invertible is that $HA^{r-1}F \neq 0$.

Proof In Proposition 1, matrix $N_{BF_r}F$ is equal to $[A^{-1} - A^{-1}F(HA^{-1}F)^{-1}HA^{-1} - KHA^{r-1}]F$, thus it can be rewritten as $N_{BF_r}F = A^{-1}F - A^{-1}F(HA^{-1}F)^{-1}HA^{-1}F - KHA^{r-1}F =$

$KHA^{r-1}F$. If condition $HA^{r-1}F \neq 0$ is not satisfied, the Kernel of matrix N_{BF_r} is not empty, which means that matrix N_{BF_r} is not invertible and that this matrix contains at least one null mode, thus pole placement is not possible (all its eigenvalues are not in the left-hand side of the complex plane).□

Condition defined in proposition 1 is an extension of the well-known matching condition defined in [16] and [7]. It means that the infinite zero order between the disturbance variable $d(t)$ and the measured variable $z(t)$ can be greatest than 1, equal to r with this observer.

It is now supposed that $HA^{r-1}F \neq 0$ is satisfied. Two properties are proved. First, it is proved that for matrix N_{BF_r} , r poles can be assigned and that the other poles (fixed poles) are the inverse of the invariant zeros of system $\Sigma(H, A, F)$.

Proposition 2: In matrix N_{BF_r} defined in (13), r poles can be chosen with matrix K .

Pole placement for matrix N_{BF_r} is equivalent to pole placement for system $\Sigma(HA^{r-1}, N_{BO})$. The observability property of this system must be studied, and particularly the rank of the observability matrix which is equal to the number of poles which can be assigned.

The n rows of the observability matrix of system $\Sigma(HA^{r-1}, N_{BO})$ are $HA^{r-1}, HA^{r-1}.N_{BO}, \dots, HA^{r-1}.N_{BO}^{n-1}$. Each row is calculated.

$$\left\{ \begin{array}{l} HA^{r-1} \\ HA^{r-1}.N_{BO} = HA^{r-1}.(A^{-1} - A^{-1}F(HA^{-1}F)^{-1}HA^{-1}) \\ \quad = HA^{r-2} \\ HA^{r-1}.(N_{BO})^2 = HA^{r-3} \\ \vdots \\ HA^{r-1}.(N_{BO})^{r-2} = HA \\ HA^{r-1}.(N_{BO})^{r-1} = H \\ HA^{r-1}.(N_{BO})^r = 0 \\ \vdots \\ HA^{r-1}.(N_{BO})^{n-1} = 0 \end{array} \right. \quad (14)$$

The rank of this observability matrix is r because model $\Sigma(H, A)$ is observable and the non null rows calculated in (14) are thus linearly independent. This proved that r poles can be assigned in equation (12) and that the observer has $n - r$ fixed poles.□

Now it is proved that the fixed poles are the inverse of the invariant zeros of system $\Sigma(H, A, F)$.

Proposition 3: The eigenvalues of matrix N_{BO} defined in (9) are the inverse of the invariant zeros of system $\Sigma(H, A, F)$ ($n - r$ modes) plus r eigenvalues equal to 0.

Proof: Appendix□

Proposition 4: The fixed poles of the estimation error defined in (12) are the invariant zeros of system $\Sigma(H, A, F)$.

Proof: From Proposition 3, the eigenvalues of matrix N_{BO} are the inverse of the invariant zeros of system $\Sigma(H, A, F)$ with r eigenvalues equal to 0, and since N_{BF} is invertible and only r poles can be chosen, all the fixed poles are the non null eigenvalues.□

4. EXAMPLE

The previous procedures are applied on a real hydraulic system modeled by bond graph. At the analysis step, proposed methods on bond graph models do not require the knowledge of the value of parameters, because intrinsic solvability conditions can be given and a formal calculus can be proposed at the synthesis level.

4.1. Bond graph model

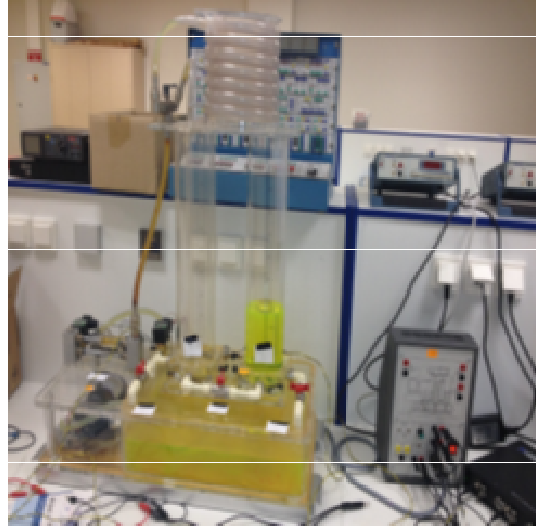


Figure 2: Hydraulic system with two tanks

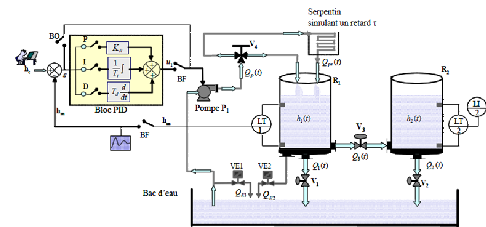


Figure 3: Process diagram to study

Consider for illustration the two coupled tanks depicted in figure 2 and 3. The aim of the two tanks is to provide a continuous water flow to a consumer via the valve V2. The process consists of two tanks R1 and R2 connected by a valve V3. The connection pipe between the tanks is placed at the bottom of the tanks. T1 is filled by a controlled pump P1 modeled as source of flow Q_p to keep water level constant. The pressures (image of levels) at the bottom of each tank are measured by sensors $P1_m$ and $P2_m$ respectively. The electro valves VE_1 and VE_2 can be used to simulate a leakage (as a disturbances). In the faultless mode VE_1 and VE_2 are closed. The three ways valve V_4 is used to connect inlet flow through the coil (to introduce a time delay) or directly to the tank R_1 in Fig. 2. The BGI model of the system with a disturbance signal is given in Fig. 4, and the state-space equations are presented in (15), with $(x_1, x_2)^T$ the state vector. It corresponds to the volume in the tanks.

$u = Q_p$ is the control input variable (flow) and $z_1 = h_2$ is the output vector. It corresponds to the height of liquid in second tank. In order to use classical bond graph rules, a parameter k is added before the output detector, Fig. 4, with $k = 0.0102m^2s^2kg^{-1}$. d is the disturbance input variable (if the second valve V_2 is closed, $R_2 = \infty$. d is an unknown input if tap valve R_2 is open). The input $u(t)$ is a step function, i.e. $u(t) = 4.36 \cdot 10^{-4}m^3s^{-1}$.

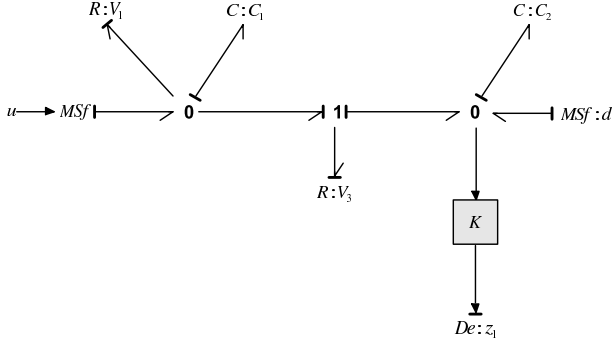


Figure 4: BGI model of the hydraulic system with the disturbance

$$\begin{cases} \dot{x}_1 = -\left(\frac{1}{C_1R_3} + \frac{1}{C_1R_1}\right)x_1 + \frac{1}{C_2R_3}x_2 + u \\ \dot{x}_2 = \frac{1}{C_1R_3}x_1 - \frac{1}{C_2R_3}x_2 + d \\ z_1 = \frac{k}{C_2}x_2 \end{cases} \quad (15)$$

The bond graph model is controllable and observable (a derivative causality can be assigned). The numerical values of system parameters are shown in Table I. Simulations and control of this system are implemented with MATLAB® Simulink.

Table 1: Numerical values of system parameters

C_1	C_2	R_1	R_3
$7.78 \times 10^{-7} \frac{m^2 \cdot s^2}{kg}$	$8.01 \times 10^{-7} \frac{m^2 \cdot s^2}{kg}$	$4.21 \times 10^7 \frac{pa \cdot s}{m^3}$	$5.78 \times 10^7 \frac{pa \cdot s}{m^3}$

The valve V_2 is opened with start time 300s and end time 330s. Then the disturbance variable d and its estimate \hat{d} and the estimation errors for the state variables are drawn.

4.2. Observer with matching condition

The design of the observer proposed in the previous section can thus be redesigned from a bond graph approach.

The causal path length between the output detector $De : z_1$ and the disturbance input $Sf : d$ is equal to 1, path $De : z_1 \rightarrow C : C_2 \rightarrow Sf : d$, thus the matching condition is verified, and there is an invariant zero in the system $\Sigma(H, A, F)$. After calculation, the invariant zero is $s = -\frac{1}{C_1} \left(\frac{1}{R_3} + \frac{1}{R_1} \right)$ which verifies the minimum phase condition. The bond graph representation of the observer is drawn in Fig. 5 in a general form without values for parameters.

For the considered hydraulic system, the two poles of the second order model are approximatively equal to -0.064 and -0.0103 . In the state estimation equation defined in (10), matrix $K = (k_1, k_2)^t$ is used for pole placement. The first

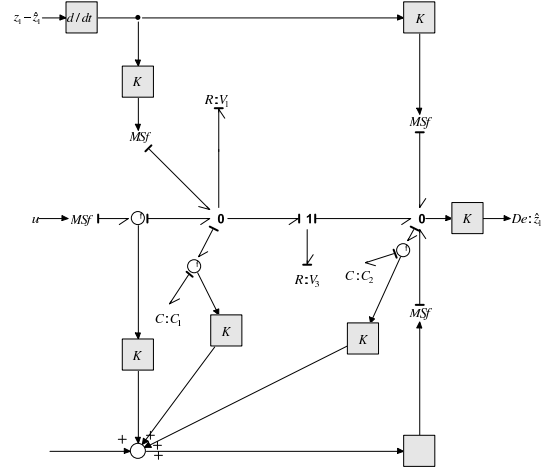


Figure 5: Observer with the bond graph representation

one is a fixed pole equal to $s_1 = -0.0527$. The second one is chosen at $s_2 = -0.6$, thus $k_2 = 1.3 \times 10^{-6}$ because with some formal calculus, the second poles of matrix N_{BF}^{-1} defined in the state estimation error equation is $s = -\frac{C_2}{k_2}$.

The two estimated variables \hat{h}_2 and \hat{d} are very close to the real variables, Fig. 6 and Fig. 7. The different figures prove the accuracy of this UIO.

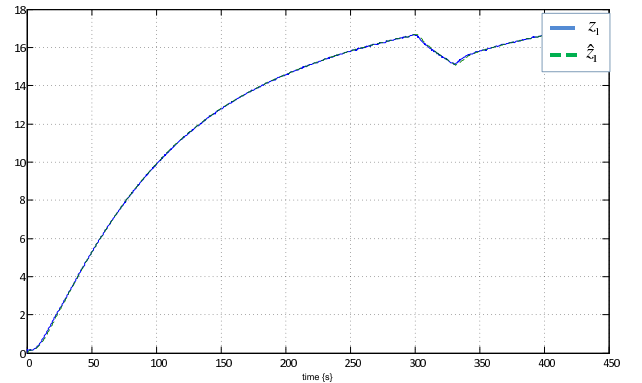


Figure 6: Water level in the second tank h_2 and its estimate \hat{h}_2

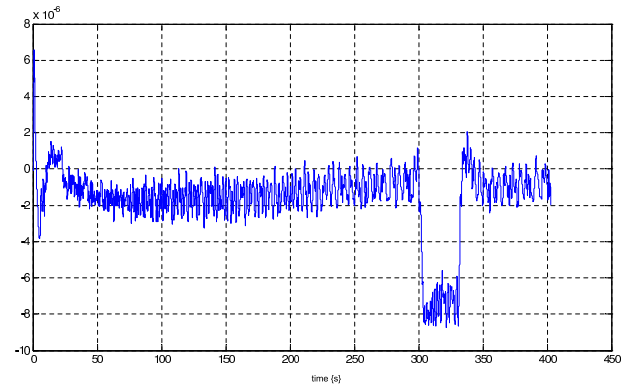


Figure 7: The disturbance variable estimate \hat{d}

4.3. Observer without matching condition

In a second step, a new sensor z_2 is used to estimate the disturbance variable, as shown in Fig. 8. The state-space equations are presented in (16).

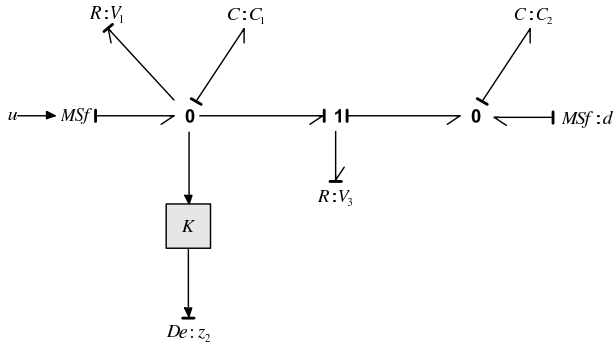


Figure 8: BGI model of the hydraulic system with the disturbance

$$\begin{cases} \dot{x}_1 = -\left(\frac{1}{C_1 R_3} + \frac{1}{C_1 R_1}\right)x_1 + \frac{1}{C_2 R_3}x_2 + u \\ \dot{x}_2 = \frac{1}{C_1 R_3}x_1 - \frac{1}{C_2 R_3}x_2 + d \\ z_2 = \frac{k}{C_1}x_1 \end{cases} \quad (16)$$

In this case, the same parameters of the hydraulic system are used. The unknown input is a perturbation (opening of the valve R_2 with start time 720s and end time 750s). The causal path length between the output detector $De : z_2$ and the disturbance input $Sf : d$ is equal to $r=2$, the infinite zero order (path $De : z_2 \rightarrow C : C_1 \rightarrow R : R_3 \rightarrow C : C_2 \rightarrow Sf : d$). The classical matching condition is not verified. The extended observer is used, equation (17)

$$\dot{\hat{x}}(t) = A\hat{x}(t) + Bu(t) + F\hat{d}(t) - AK(\hat{z}(t) - \ddot{z}(t)) \quad (17)$$

The model order is equal to 2, thus there is not any invariant zero and all poles can be assigned in the error estimation equation. The state error estimation is given by (10) with $N_{BF_2} = A^{-1} - A^{-1}F(HA^{-1}F)^{-1}HA^{-1} - KHA$. The two poles are chosen at $s_1 = -0.5$ and $s_2 = -0.6$, thus the observer gains in matrix $K = [k_1, k_2]^t$ are $k_1 = 3.44 \cdot 10^{-6}$ and $k_2 = 3.44 \cdot 10^{-6}$.

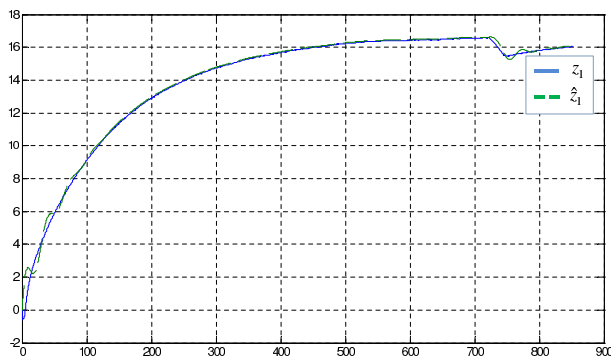


Figure 9: The water level in the first tank h_1 and its estimate \hat{h}_1

Experimental results (fig. 9 - 10) show that the observer reproduces closely the output value of the water level in the

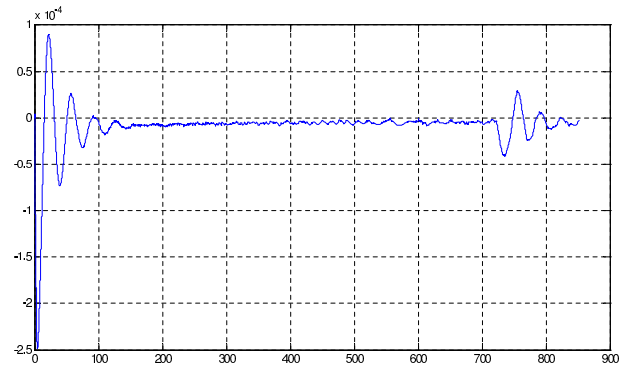


Figure 10: The disturbance variable estimate \hat{d}

tank $y = h_1$ and the unknown input. In this experimental system, the unknown input is not only a perturbation (opening of the valve R_2) but also noise, mostly at the beginning of the experiment, which can be pointed out at the beginning of the estimation, Fig. 10.

Numerical differentiation of a signal is an old problem in automation and many problems have been solved (estimation, control...) with approximation of derivatives. Different approaches use an interpolation technique [11]. In other works, the authors apply a cubic spline interpolant method, [1] and [6].

In this case study, simulations are performed using the software Matlab-Simulink. For numerical differentiation of the real signal, a block "Discrete Derivative" is used. From the simulation results and experimental results presented in this paper, it should be noted that these differentiations are possible in this experiment.

5. CONCLUSION

In this paper, an extension of an unknown input observer is proposed when the classical matching condition is not verified. The necessary condition to obtain a stable solution is that invariant zeros belong to the left half complex plan (Hurwitz condition). A bond graph approach with classical graphical conditions is used. The approach is proposed for a real hydraulic linear system. Experiments have shown that the proposed observer is accurate. In the future this method will be extended to nonlinear systems.

REFERENCES

1. M.A. Al-Alaoui. Novel digital integrator and differentiator. *Electronics Letters*, 29(4):376378, 1993.
2. G. Basile and G. Marro. A new characterization of some structural properties of linear systems: Unknown-input observability, invertibility and functional controllability. *International Journal of Control*, 17(5):931943, 1973.
3. S.P. Bhattacharyya. Observer design for linear systems with unknown inputs. *IEEE Transactions on Automatic Control*, 23:1483-484, 1978.
4. W. Chen, A.Q. Khan, M. Abid, and S.X. Ding. Integrated design of observer based fault detection for a class of uncertain nonlinear systems. *Int. J. Appl. Math. Comput. Sci.*, 21(3):423430, 2007.
5. J. Daafouz, M. Fliess, and G. Millerioux. Une approche intrinsèque des observateurs linéaires à entrées inconnues. *CIFA 2006, Bordeaux*, 2006.
6. A. Dabroom and H.K. Khalil. Numerical differentiation using highgain observers. *Proceedings of the 36th IEEE Conference on Decision and Control*, 5:47904795, 1997.

7. M. Darouach. Complements to full order observer design for linear systems with unknown inputs. *Applied Mathematics Letters*, 22:1107–1111, 2009.
8. M. Darouach, M. Zasadzinski, and S.J. Xu. Full-order observers for linear systems with unknown inputs. *IEEE Transactions on Automatic Control*, 39:606–609, 1994.
9. J. M. Dion and C. Commault. Smith-mcmillan factorizations at infinity of rational matrix functions and their control interpretation. *System & Control Letters*, 1:312–320, 1982.
10. J. M. Dion and C. Commault. Feedback decoupling of structured systems. *IEEE Transactions on Automatic Control*, 38:1132–1135, 1993.
11. S. Diop, J.W. Grizzle, P.E. Moraal, and A. Stefanopoulou. Interpolation and numerical differentiation for observer design. In *American Control Conference*, 2:13291333, 1994.
12. P. L. Falb and W. A. Wolovich. On the decoupling of multivariable systems. *Preprints JACC, Philadelphia*, pages 791–796, 1967.
13. T. Floquet and J.P. Barbot. *Advances in variable structure and sliding mode control*, chapter A canonical form for the design of unknown input sliding mode observers, pages 271–292. Springer, 2006.
14. E. G. Gilbert. The decoupling of multivariable systems by state feedback. *SIAM Journal of Control and Optimization*, 7:50–63, 1969.
15. R. Guidorzi and G. Marro. On wonham stabilizability condition in the synthesis of observers for unknown-input systems. *IEEE Trans. Automat. Control*, 16:499–500, 1971.
16. M. L. J. Hautus. Strong detectability and observers. *Linear Algebra and its Applications*, 50:353–368, 1983.
17. M. Hou and P.C. Muller. Design of observers for linear systems with unknown inputs. *IEEE Trans. Automat. Control*, 37:871–875, 1992.
18. T. Kailath. *Linear Systems*. Prentice Hall, Englewood-Cliff, N.J., 1980.
19. R. E. Kalman, P. L. Falb, and M. A. Arbib. *Topics in Mathematical System Theory*. McGraw-Hill, New York, 1969.
20. K. Kalsi, J. Lian, S. Hui, and S. Zak. Sliding-mode observers for systems with unknown inputs: A high-gain approach. *Automatica*, 46:347–353, 2010.
21. D. Karnopp, D. Margolis, and R. Rosenberg. *System dynamics: a unified approach*. John Wiley & Sons, 1975.
22. P. Kudva, N. Viswanadham, and A. Ramakrishna. Observers for linear systems with unknown inputs. *IEEE Trans. Automat. Control*, 25:113–115, 1980.
23. B.J. Miller and R. Mukunden. On designing reduced-order observers for linear time-invariant systems subject to unknown inputs. *Internat. J. Control*, 35:183–188, 1982.
24. A. S. Morse. Structural invariants of linear multivariable systems. *SIAM J. Control*, 11:446–465, 1973.
25. R. Rosenberg and D. Karnopp. *Introduction to physical system dynamics*. McGraw Hill, 1983.
26. H.H. Rosenbrock. *State space and multivariable theory*. Nelson, London, England, 1970.
27. C. Sueur and G. Dauphin-Tanguy. Bond-graph approach for structural analysis of mimo linear systems. *Journal of the Franklin Institute*, 328:55–70, 1991.
28. S. Tong, G. Yang, and W. Zhang. Observer-based fault-tolerant control against sensor failures for fuzzy systems with time delays. *International Journal of Applied Mathematics and Computer Science*, 21(4):617627, 2011.
29. H. L. Trentelman, A. A. Stoorvogel, and M. Hautus. *Control theory for linear systems*. London, UK: Springer, 2001.
30. D. Xu, B. Jiang, and P. Shi. Nonlinear actuator fault estimation observer: an inverse system approach via a t-s fuzzy model. *Int. J. Appl. Math. Comput. Sci.*, 22(1):183196, 2012.
31. D. Yang and C. Sueur. Unknown input observer: a physical approach. *IMAACA 2012, September 19-21, Vienna, Austria*, 2012.

APPENDIX

Proof of equations (12) and (13)

Equations (12) and (13) are proved for $r = 2$. The extension for any integer r is simple are straight.

First, write $z = Hx$. A first order derivative is $\dot{z} = H\dot{x} = H(Ax + Bu + Fd) = HAx + HBu$ with $HFd = 0$. Thus $\ddot{z} = H\ddot{x} = H\dot{A}\dot{x} + H\dot{B}\dot{u}$. The same equation is written for \hat{z} , thus

$\dot{\tilde{z}} = H\dot{\tilde{x}} = H\dot{A}\hat{x} + H\dot{B}\dot{u}$. From these two expressions, a new one is written: $\ddot{z} - \ddot{\hat{z}} = H\dot{A}\dot{x} + H\dot{B}\dot{u} - (H\dot{A}\hat{x} + H\dot{B}\dot{u}) = H\dot{A}(\dot{x} - \hat{x})$.

With an easy extension, it is proved that $z^{(r)} - \hat{z}^{(r)} = HA^{r-1}(\dot{x} - \hat{x})$, which proves equations (12) and (13).

Proof proposition 3

First, the observability property of model $\Sigma(HA^{r-1}, N_{BO})$ is studied. The non observable poles are the roots of the invariant polynomials obtained from the Smith form of matrix $N(s)$ defined in (18). With matrix HA^{r-1} , only r modes of matrix N_{BO} can be assigned, because the rank of the observability matrix of system $\Sigma(HA^{r-1}, N_{BO})$ is equal to r . Structurally, with $s = 0$, the rank of matrix (18) degenerates. The non observable modes are all the null modes.

$$N(s) = \begin{pmatrix} sI - N_{BO} \\ HA^{r-1} \end{pmatrix} \quad (18)$$

The fixed poles of the state estimation error defined in (10) are thus the r null non observable poles of model $\Sigma(HA^{r-1}, N_{BO})$. Now, some equivalent transformations are proposed for the Smith matrix $S(s)$ of system $\Sigma(H, A, F)$ defined in (19).

$$S(s) = \begin{pmatrix} sI - A & -F \\ H & 0 \end{pmatrix} \quad (19)$$

$$S(s) \sim \begin{pmatrix} sA^{-1} - I & -A^{-1}F \\ H & 0 \end{pmatrix} \sim \quad (20)$$

$$\begin{pmatrix} sA^{-1} - I & -A^{-1}F \\ H + sHA^{-1} - H & -HA^{-1}F \end{pmatrix} \sim \begin{pmatrix} sA^{-1} - I & A^{-1}F(HA^{-1}F)^{-1} \\ sHA^{-1} & I \end{pmatrix} \quad (21)$$

$$\sim \begin{pmatrix} sA^{-1} - I - A^{-1}F(HA^{-1}F)^{-1}(-sHA^{-1}) & 0 \\ sHA^{-1} & I \end{pmatrix} \quad (22)$$

$$\sim \begin{pmatrix} sN_{BO} - I & 0 \\ 0 & I \end{pmatrix} \quad (23)$$

Since $\det(pI - N_{BO}) = p^n \det(I - N_{BO}/p)$, with $s = 1/p$ it comes $\det(pI - N_{BO}) = (-1)^n s^{-n} \det(sN_{BO} - I)$ which is a polynomial of degree n with variable p and of degree $-n$ with variable s . But, $\det S(s)$ is a polynomial of degree $n - r$, thus from a simple mathematical analysis it is proved that the polynomial $\det(pI - N_{BO})$ has r null roots and that the roots of the polynomial $\det(sN_{BO} - I)$ are the inverse of the non null roots of polynomial $\det(pI - N_{BO})$ since $(p = 1/s)$. In that case the non null poles of matrix N_{BO} are the inverses of the invariant zeros of model $\Sigma(H, A, F)$.

The non observable modes of system $\Sigma(HA^{r-1}, N_{BO})$ are thus all the inverse of the invariant zeros of system $\Sigma(H, A, F)$. They are the fixed modes of the state estimation error equation.

MODELING AND SIMULATION OF AN AUTOMATED MANUAL TRANSMISSION SYSTEM

Hua Huang, Sebastian Nowoisky, René Knoblich, Clemens Gühmann

Technische Universität Berlin
Department of Energy and Automation Technology
Chair of Electronic Measurement and Diagnostic Technology
Berlin 10587, Germany

{[hua.huang@campus.](mailto:hua.huang@campus.tu-berlin.de), [sebastian.nowoisky@](mailto:sebastian.nowoisky@tu-berlin.de), [r.knoblich@](mailto:r.knoblich@tu-berlin.de), [clemens.guehmann@](mailto:clemens.guehmann@tu-berlin.de)}tu-berlin.de

ABSTRACT

With the continuous growth in the emission requirements and higher riding comfort demand, the shift quality takes more and more an important role in automated transmission control algorithms. In order to effectively optimize the corresponding control parameters and functions in the transmission control units (TCU), the model-based calibration is a suitable method. For this purpose a detailed dynamic model which can provide a virtual platform for shift quality optimization is imperative and necessary. In this paper a 5-speed automated manual transmission (AMT) is used as a research object and a detailed Modelica® based hydro-mechanical dynamic model is presented. Finally, model simulations are compared with the measurements from a test bench. Testing results show the dynamic model can describe detailed gear shifting phenomena.

Keywords: automated transmission, hydraulic, dynamic modeling

1. INTRODUCTION

With the continuous growth in the stricter emission requirements and higher riding comfort demand, the shift quality takes more and more an important role in automated transmission control algorithms. With the traditional software development process, these requirements rapidly increase the manpower and finance resources, especially the optimization period during real vehicle calibration. In order to effectively optimize the corresponding control parameters and functions in the transmission control units (TCU), the model-based calibration is a suitable method. The general process is shown in figure 1. Firstly, a formula expression based transmission model is built. By means of measurements from a test bench or a real vehicle, the draft model is detailed and improved till it reaches corresponding requirements. Afterwards, this model is taken as a virtual platform to optimize the shift quality. Finally, the optimized control parameters are verified on the test bench or in the real vehicle, the operation maps are generated and stored into the TCU.

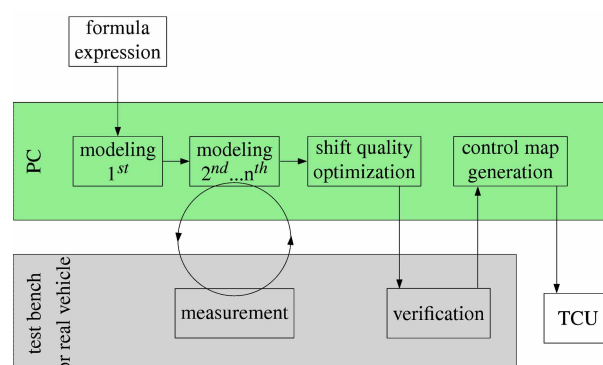


Figure 1: Model-based Optimization Process

Traditionally the shift quality is assessed subjectively by the driver's feeling. For the model-based development the shift quality objective evaluation is a critical step. This requires that the automated transmission model has a detailed performance such as speed oscillation and the longitudinal acceleration variations during a gear shifting. Only the detailed dynamic transmission model can reproduce these behaviors. Moreover, an AMT is designed and improved on the basis of a manual transmission (MT), it inherits the MT features such as lower weight, high efficiency and convenient maintenance. With the help of improved electronic technology and optimized control algorithms, AMT also offers its own advantages, such as improved driving convenience, reduction of life-cycle costs and enabled low fuel consumption.

In this paper a 5-speed AMT with dry clutch is chosen as the research object (see Figure 2). A Modelica® based nonlinear dynamic hydro-mechanical AMT model for the future model-based shift quality development is presented. The model is relatively simple, yet it visually describes AMT system detailed structures as “what you see is what you get” and predicts the important dynamic gear shifting behaviors quite well, such as 5 stages synchronization (pre-sync, locking, unlocking, turning hub and engagement), magnetic valve fluid pressure fluctuation under different currents and the driveline oscillation during transmitted torque changes.

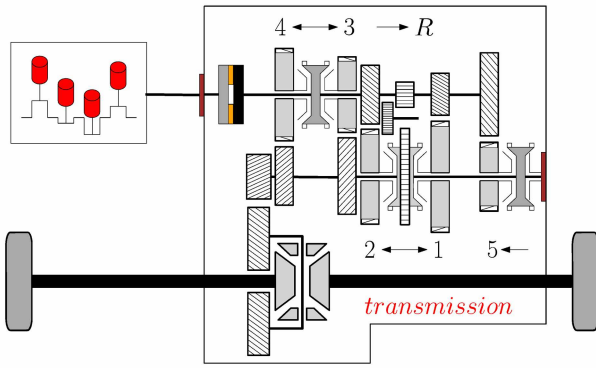


Figure 2: Schematic Diagram of the 5-speed AMT

The structure of this paper is: Section 2 gives an introduction of the hydro-mechanical components and detailed description of the corresponding working principles. Section 3 presents the simulation results and the results are also compared with measurements from an AMT equipped test bench. Finally, a summary and further research outlook is concluded.

2. MODELING

This section mainly introduces the AMT modeling process and implementation method. Each part separately presents its hydro-mechanical elements working principles. Then the dynamic processes are expressed through Bernoulli's theory and Newton's laws. The corresponding Modelica[®] modules are also described. Finally, in order to compose a nonlinear AMT system, the dynamic shafts are used to flexibly connect with the engine, clutch and gearbox.

2.1. Gearbox Model

A gearbox is used to transmit power from the engine to the driving wheels, satisfy the rotate speed and torque requirement to the vehicle driving condition. The gearbox is divided into two parts: hydraulic part (magnetic valves and cylinders) and mechanical part

(synchronization system).

As figure 3 shows, the hydraulic fluid is first pumped by a bang-bang controller from the tank to the pressure accumulator where it is stored under high pressure. Then the fluid is transmitted through magnetic valves to different branches.

2.1.1. Hydraulic Components

In order to realize a shift actuation, there are mainly two types of magnetic valves: Pressure control valves (PCV1 and PCV2 in figure 3) and switch valves (SV1 and SV2 in figure 3). The two pressure control valves are used to control the rotation of a piston rocker, which is connected with a gear shifting lever. The other two switch valves are connected to another piston rocker, which is used to select the gate position (Volkswagen AG 1999). Since the process of gate selection has a tiny influence on the gear shift quality, only the gear selection and the pressure control valves modeling are described.

The pressure control valve shown in figure 4 has three ports: supply port, release port and output port. The output port is connected with an integrated sensing chamber, which gives a feedback force to the plunger. The magnitude of this force depends on the output port pressure and the effective area of the sensing chamber.

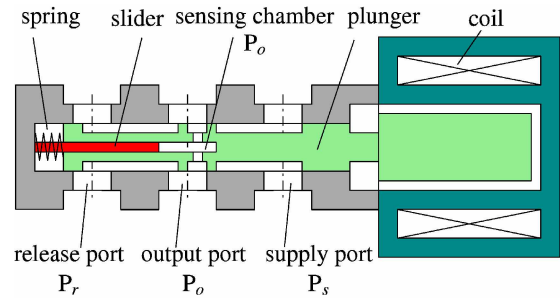


Figure 4: Schematic Diagram of the Pressure Control Valve

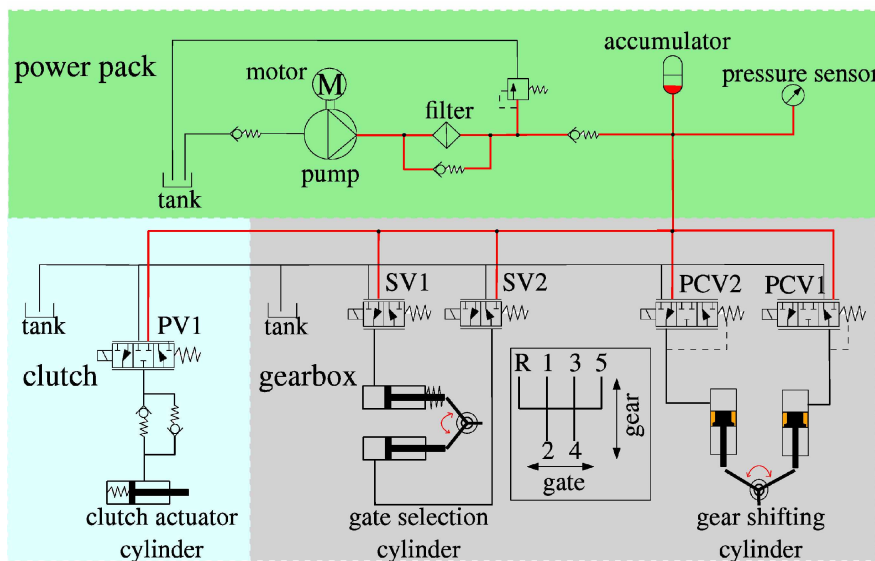


Figure 3: Hydraulic System Plan

The hydraulic fluid follows through the supply port, generates a force and moves the plunger to the left till the spring force is equal to the supply pressure. This stable state is called middle position. The steady-state equation is expressed in equation 1, where A_s , A_r are the effective areas of supply port and release port chambers, P_s , P_r are the supply port and release port hydraulic pressures, $F_{spring0}$ denotes the initial spring preload force.

$$F_{spring0} = P_s A_s - P_r A_r \quad (1)$$

When this magnetic valve is actuated by a current i , the coil induces an electromagnetic force $F_{magnetic}$ (see equation 2), which gives the plunger an impulse to move to the left side. During the plunger movement process, the orifice area of the supply port to output port increases and output pressure grows. Since the output port is connected with the sensing chamber, a pressured fluid is accumulated and reacts against the plunger. Besides the reaction of pressure force, the plunger is also affected by the spring force and friction. These forces take the plunger a back and forth spring-damping movement till it stops at the middle position again. Equation 2 describes the transient response,

$$\begin{aligned} \dot{x}_{plunger} &= v_{plunger} \\ m_{plunger} \dot{v}_{plunger} &= F_{magnetic} + P_s A_s - P_0 A_0 \\ &\quad - P_r A_r - P_0 A_{slider} - F_{spring} \\ &\quad - F_{spring0} - F_{friction} \\ F_{friction} &= \text{sign}(v_{plunger})(F_{coulomb} \\ &\quad + F_{prop} + F_{stribeck}) \\ F_{magnetic} &= \frac{1}{2} i^2 \frac{dL}{dx_{plunger}} + ci \end{aligned} \quad (2)$$

where $x_{plunger}$, $v_{plunger}$ and $m_{plunger}$ is plunger position, speed and mass, A_{slider} is the effective area of sensing chamber, $F_{magnetic}$ is the magnetic force induced by current i , coil inductance L and converter constant c (depends on the structure parameters such as flux density and wire length) (Modelon 2009), $F_{friction}$ is the resistance friction including constant coulomb friction $F_{coulomb}$, speed proportional friction force F_{prop} and stribeck friction $F_{stribeck}$, F_{spring} is spring force by stiffness k . If a dither signal is added into the magnetic valve control, $F_{stribeck}$ can be taken as zero.

The final steady-state is given by equation 3. In this state the plunger stops at the middle position, its velocity and acceleration are zero. The spring returns to the initial position and takes a force as large as the preload force $F_{spring0}$.

$$\begin{aligned} 0 &= F_{magnetic} + P_s A_s - P_0 A_0 \\ &\quad - P_r A_r - P_0 A_{slider} - F_{spring0} \end{aligned} \quad (3)$$

With equation 1 and equation 3 the relationship between magnetic force and sensing chamber reaction force can be expressed in equation 4. For a detailed magnetic valve the physical geometrical parameters are fixed, so the conclusion that pressure control valve command current has a linear relationship with output pressure can be accepted. This relation is described in equation 5, where m is the slope, n is the offset and i_0 denotes the initial current which is used to overcome the friction from static condition (Nowoisky 2012a).

$$F_{magnetic} = P_0 A_{slider} + P_0 A_0 = P_0 (A_{slider} + A_0) \quad (4)$$

$$P_0 = \begin{cases} 0 & i < i_0 \\ m(i - i_0) + n & i \geq i_0 \end{cases} \quad (5)$$

Fluid flow q during this process can be expressed by Bernoulli's equation (see equation 6), γ is the discharge coefficient and ρ is the density of fluid. When the plunger moves from the middle to the left position, the output port is connected to the supply port, fluid flow and its pressure level increase. When the plunger moves to the right side from the middle position, the output port is connected to the release port. This causes fluid flows to the tank. When the plunger is in the middle position, there is no flow rate except leakage, the output port pressure keeps a stable value (Merritt 1967).

$$q = \begin{cases} \gamma \sqrt{\frac{2(P_s - P_0)}{\rho}} A_s(x_{plunger}) & \text{left} \\ 0 & \text{middle} \\ -\gamma \sqrt{\frac{2(P_0 - P_r)}{\rho}} A_s(x_{plunger}) & \text{right} \end{cases} \quad (6)$$

Based on the above description, a Modelica[®] based module can be built as figure 5 shows. Its components are modeled based on the Modelica Standard Library (MSL) and hydraulic library HyLib[®] (Modelcia Association 2008, Modelon 2009). The geometrical parameters are identified through measurements, the others are fixed through experiments and calculation from theoretical and physical laws.

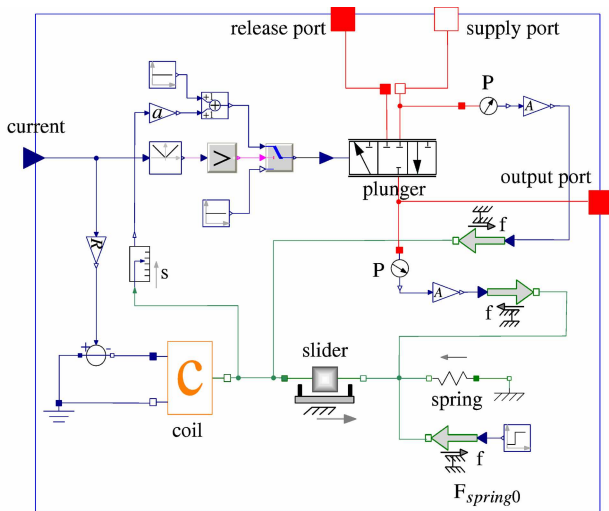


Figure 5: Dynamic Module of Pressure Control Valve

2.1.2. Mechanical Components

Synchronizers are important components in the transmission. It uses friction and locking elements to synchronize the occurring speed difference during gear shifting. As shown in figure 6, the gear shifting process can be divided into 5 stages according to the gearshift position and the difference speeds (Kiencke 2005). This division is defined under the assumption that the gearshift sleeve is at the beginning in the neutral position:

Stage 1: Gearshift force F_S causes an axial movement of the gearshift sleeve and triggers the gear shifting process. The movement stops when the synchronizer ring blocks the gearshift sleeve.

Stage 2: The axial force is transmitted from the gearshift sleeve to the synchronizer ring, resulting in a friction torque T_R , which is much larger than the gearing torque T_Z . At this stage the speed difference ΔS between the idler gear and transmission shaft is reduced to zero.

Stage 3: When the speed difference ΔS is close to zero, the friction torque T_R vanishes. At this moment the synchronizer ring turns back to release the gearshift sleeve.

Stage 4: The gearshift sleeve begins to move until it encounters the synchronizer hub external gearing. The speed difference ΔS increases again as the synchronizing torque diminishes.

Stage 5: The whole synchronization process is completed as soon as the gearshift sleeve tothing engages the synchronizer hub gearing. The power flow

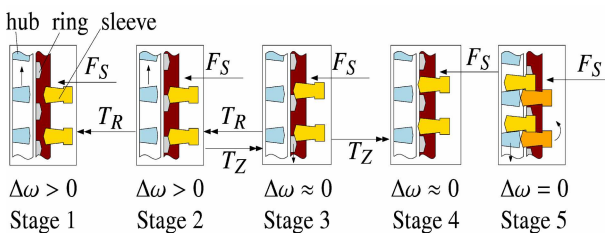


Figure 6: Synchronizing Process

is transmitted from the transmission shaft to the gear.

The torque detailed values are changed according to the synchronization stages: The friction torque T_R given by equation 7 (applied to stages 1 and 2) is calculated through the gearshift force F_S , the number of friction surfaces j and some other geometric values. The gearing torque T_Z expressed as equation 8 (used in stages 2 and 3) is calculated by gearshift force F_S , clutch diameter d_{KS} , teeth angle and friction μ_{lt} between gearshift sleeve and synchronization ring (INA 2007, Kirchner 2007). The Modelica® based synchronizer module is shown in figure 7. It is modeled based on MSL library and some new created Modelica® based blocks (such as *SynStatusCheck* block and *RingandHub* block). Detailed description and modeling process are in Huang (Huang 2012).

$$T_R = jF_S \frac{d_{ms}}{2} \frac{\sim_{ft}}{\sin \gamma} \quad (7)$$

$$T_Z = \frac{F_S d_{ks}}{2} \left(\frac{\cos \frac{S}{2} - \sim_{lt} \sin \frac{S}{2}}{\sin \frac{S}{2} + \sim_{lt} \cos \frac{S}{2}} \right) \quad (8)$$

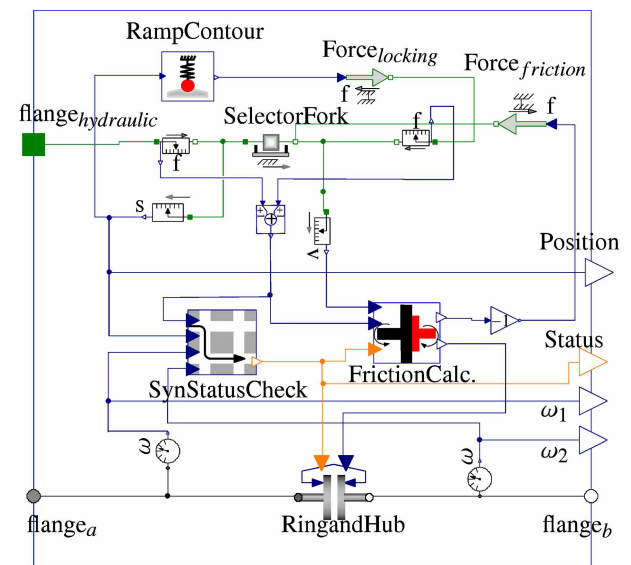


Figure 7: Dynamic Module of Synchronizer

In order to improve the dynamic behavior during gear shifting, the simplified dynamic shaft with viscous and elastic effect is necessary. The transmission shafts (crankshaft, main shaft and secondary shaft) are considered as spring-damper elements connected with inertias. The whole driveline schematic diagram is expressed in figure 8. The necessary friction losses are also added. They are modeled with lookup-tables based on experiment data.

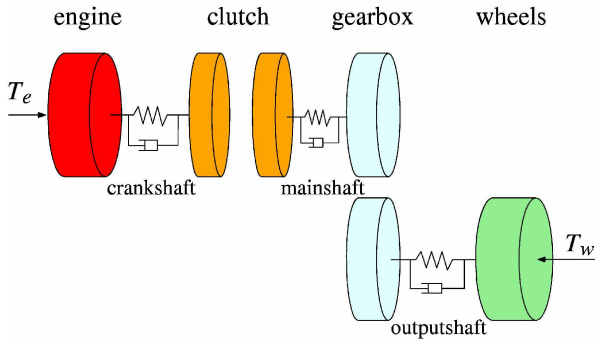


Figure 8: Schematic Diagram of Driveline

2.2. Clutch Model

Figure 9 depicts the push-type single-plate dry clutch used in the researched AMT system.

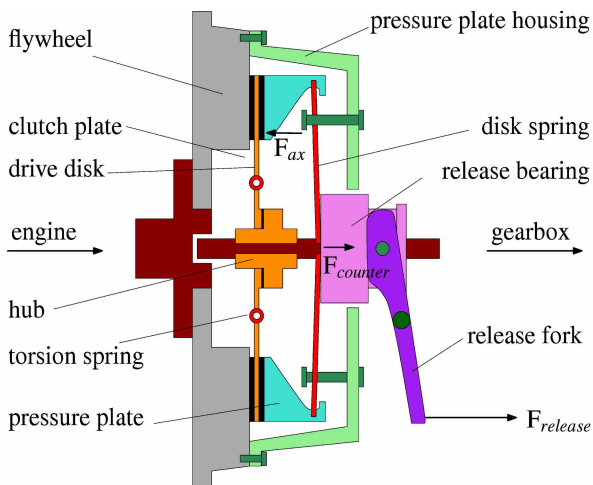


Figure 9: Schematic Diagram of Clutch

The release fork and the disk spring are used to gain an axial pressure to the release bearing and the pressure plate. The release force $F_{release}$ causes an increased normal force on the clutch plate (consists of drive disk, torsion spring, hub and etc.), the engine and the gearbox are then separated. When the force $F_{release}$ releases, the pressure plate comes close to the clutch plate, and the engine torque can be transmitted from flywheel to the gearbox through drive disk and torsion spring. Disk spring and the torsion spring are two important elements in clutch components for the gearshift quality research.

2.2.1. Hydraulic Components

A proportional valve (PVI in figure 3) is used to control the clutch cylinder movement. This dynamic process is described in equation 9. The movement depends on the mass of the cylinder piston m_{piston} , acceleration a_{piston} , piston area A_{piston} , pressure P , the friction force $F_{friction}$ (mentioned in equation 2) and the counterforce $F(s)$ from the mechanical clutch component.

$$m_{piston} a_{piston} = PA_{piston} - F_{friction} - F(s) \quad (9)$$

The derivation of piston pressure is calculated through equation 10, where K is compressibility modulus and V_0 is the offset volume due to hydraulic feed line.

$$\dot{P} = \frac{K}{V_0 + A_{piston} x_{piston}} (q - A_{piston} v_{piston}) \quad (10)$$

The proportional valve has the feature that the opening area A_{pv} has a linear response to the input current i . The causing volume flow q expression is similar to equation 6 (the valve opening area is controlled by the electric current i rather than plunger position $x_{plunger}$).

2.2.2. Mechanical Components

The clutch capacity describes the characteristic of the torque transmitted over the clutch while the sliding stage. It is expressed in equation 11,

$$T_c \approx F_{ax} \sim z \frac{2(r_0^3 - r_i^3)}{3(r_0^2 - r_i^2)} \quad (11)$$

with axial force F_{ax} on the friction lining, speed depended friction coefficient μ , friction surfaces plates number z , outer and inner friction surface radius r_0 and r_i . It is worth noting that during the clutch slipping phase, the clutch transmitted torque equals to the clutch capacity. When the clutch engages (becomes a coupling system), the torque equals to the engine torque minus engine friction losses. For simplification, the release bearing axial displacement is used as module input for the calculation of clutch capacity, and the relationship between clutch transmitted torque and release bearing axial displacement is depicted by a lookup-table generated through experiment (Nowoisky 2013). The release bearing axial counterforce $F_{counter}$ is a resultant force of disk and coat springs. It can be obtained from axial force F_{ax} under the assumption that the disk spring is a stiff lever. But actually the disk spring has a variable stiffness depends on the compressed clutch position. A lookup-table, which avoids the stiff lever transformation problem, is used to describe this counterforce when releasing bearing has an axial displacement.

The clutch torsion damping system is used to reduce rotational irregularities induced by internal combustion engines (Luk 2012). This element is significant for the dynamic model in the purpose of shift comfort calibration. The clutch torsion damping system is modeled with a spring-damping system (multiple compression springs and a damper). Figure 10 depicts the torsion spring characteristic. When the relative angle Δ_n begins from zero, the smaller spring with stiffness k_1 is firstly compressed (this process is used for vehicle idle operations), after the relative angle reaches Δ_{n1} , the smaller spring is fully compressed, and the stiffer

spring with stiffness k_2 starts to be compressed (this process is used for vehicle driving operations). When Δ_{r_2} reaches, springs are stopped to be compressed and comes to a mechanical stop (Naunheimer 2011, Drexl 1997). The Modelica[®] based clutch module is shown in figure 11. Its mechanical components are modeled with MSL library and hydraulic components are modeled with HyLib[®] library. The corresponding parameters are fixed through measurements and test bench experiments.

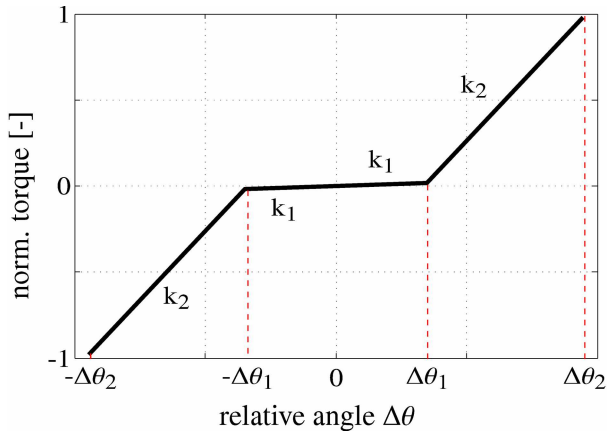


Figure 10: Torsion Spring Characteristic

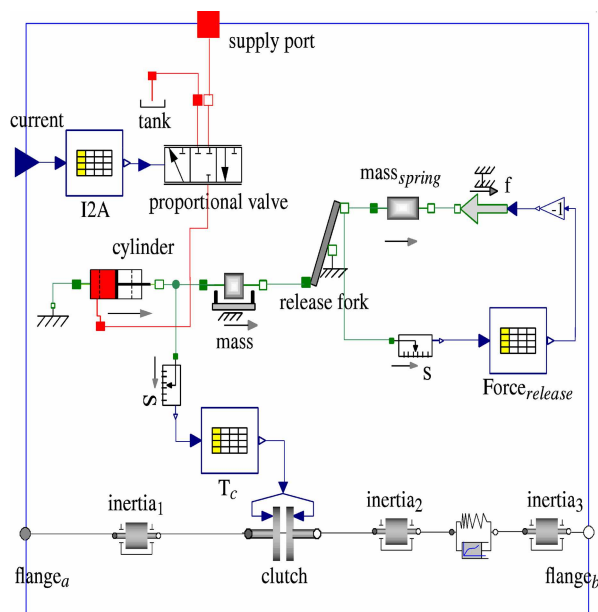


Figure 11: Dynamic Module of Clutch System

3. MODEL SIMULATION

In order to verify the rationality and effectiveness of this dynamic model, some tests are carried out. These simulations are carried out with Dymola[®] DASSEL (differential-algebraic system solver) integration Algorithm, tolerance setting is 0.0001 (Dynasim AB 2010). Detailed testing results of synchronizers can be found in Huang (Huang 2012).

Figure 12 shows the pressure control valve output pressure responses under different step currents beginning at 0.05 s. The output pressure firstly has an overshoot which is generated by current, and then the

plunger takes a back and forth spring-damping movement till it stops at middle position (see figure 4), so the output pressure takes an oscillation at the beginning and then keeps a stable value at the end. When the input command current value is less than 600 mA, the valve output pressure is zero since the impulse cannot overcome the fluid viscosity and some other friction.

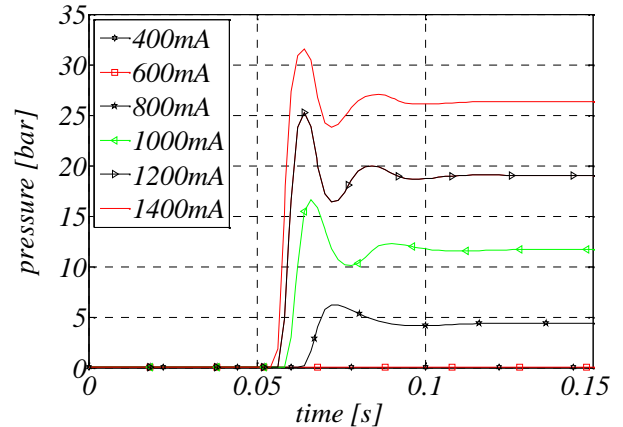


Figure 12: Simulation Result of Pressure Control Valve

Finally, the model is compared with measurement data from an AMT equipped test bench (Knoblich 2011, Nowoisky 2012b). Two three-phase asynchronous motors are used as drive and load engine. In this testing the drive engine and load engine were set in constant torque mode, 10 Nm and -20 Nm. After the system has reached the steady-state, the clutch was totally opened and gear was shifted from neutral position to 1st gear, then the clutch was closed in a ramp mode. For the simulation model the magnetic valves were triggered with the same signals as those of the test bench. The shafts of the model input and output are connected with the constant torque values of 10 Nm and -20 Nm. The comparison results are shown in figure 13. If the drive motor has a positive torque, the engine speed and gearbox input speed at the beginning have a positive value (figure 13 (a) and (b)). For the same reason the gearbox output rotates with a negative value (figure 13 (c)). At 1 s the clutch begins to open (figure 13 (e)) and subsequently the gear shifts (figure 13 (d)), the gearbox input speed decreases and synchronizes with the output speed. Afterwards, at 2 s the clutch closes in a ramp mode (figure 13 (e)), engine speed and gearbox input speed begin to engage (at 4 s). Since the torque transferred from the drive engine is larger than the one from the load torque, the input speed increases to a positive value again (figure 13 (b)). From the comparison it can be seen the model can accurately reproduce the gear shifting process and the normalized root mean square errors (NRMSE, see equation 12) are below 10%. Moreover, this model describes the important shifting behavior for the shift quality evaluation (e.g. the speed oscillation during the clutch engagement) and expresses the influences with different control variants (e.g. the change trend of the clutch

cylinder pressure), these shifting phenomena are not possible to be represented through a very simple model. The CPU-time costs 0.88 seconds for this simulation (7 seconds) under a quad-core processor.

$$e_{NRMS} = \sqrt{\frac{1}{N} \sum_{i=1}^N \left(\frac{y_{meas} - y_{sim}}{\max(y_{meas}) - \min(y_{meas})} \right)^2} \quad (12)$$

4. SUMMARY AND OUTLOOK

This paper gives a detailed introduction to AMT system working principles, presents a relative simple but effective Modelica[®] based dynamic model. The shift behaviors are also successfully verified through experimental data. This model has following features:

1. Represents a detailed AMT gear shift process, describes synchronization process with 5 stages.
2. Describes detailed hydro-mechanical actuators, represents the pressure control valve dynamic response.
3. Models torsion damping system in clutch and spring-damping system in driveline, which makes speed oscillation during torque changes possible. This improves dynamic model closer to a real one.
4. Detailed expresses the relationships between the control parameters and the shift process, this makes the model-based calibration possible.
5. Develops a multi-domain model, dynamically integrates hydraulic and mechanical systems together.
6. The model is developed based on Modelica[®], it

describes the system in a physical perspective. This makes other co-developer or user more easily to understand the physical meaning.

7. The tested AMT modules have a good modularity for other similar systems setups only through parameters changes.
8. Supplies a complete virtual AMT system platform for future mode-based shift quality calibration.

Based on the above description and comparison, this dynamic nonlinear model makes model-based shift quality calibration on automated transmissions possible.

REFERENCES

- Volkswagen AG, 1999. *Self-study Programme 221: Electronic Manual Gearbox, Design and Function*. Volkswagen AG.
- Modelon, 2009. *HyLib (2009), version 2.7*. Product help, Modelon, 2009.
- Nowoisky, S., Knoblich, R., and Gühmann, C., 2012a. Comparison of Different Model Types based on a Synchronization of an Automated Manual Transmission. *Proceedings of Simulation und Test für die Automobilelektronik IV*, 38-47. 2012, Berlin.
- Merritt, H. E., 1967. *Hydraulic Control Systems*. USA: John Wiley & Sons, Inc.
- Modelica Association, 2008. *Modelica Standard Library (2008), version 3.1*. Product help, Modelica Association.
- Kiencke, U., Nielsen, L., 2005. *Automotive Control Systems: For Engine, Driveline, and Vehicle, 2nd edition*. Germany: Springer.
- INA, 2007. *Intermediate Rings for Multi-Cone Synchronizer Systems*. Schaeffler Technologies

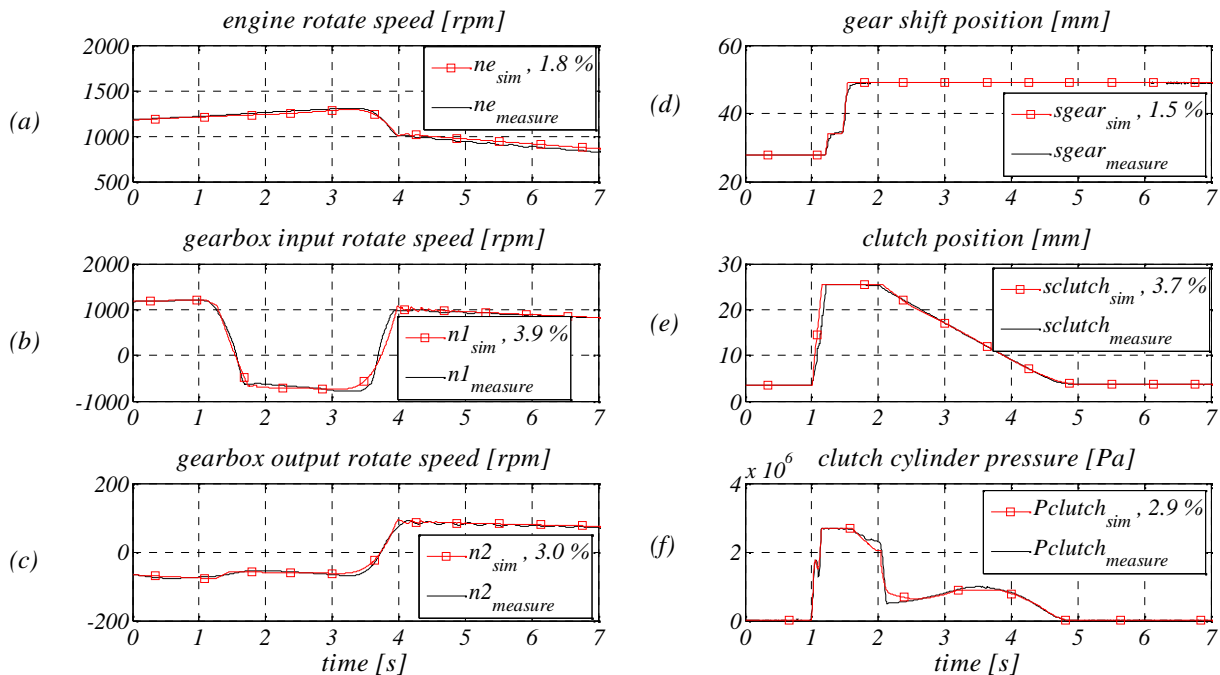


Figure 13: Comparison of Shifting Process with Measurements

AG & Co. KG.

- Kirchner, E., 2007. *Leistungsübertragung in Fahrzeuggetrieben: Grundlagen der Auslegung, Entwicklung und Validierung von Fahrzeuggetrieben und deren Komponenten* (in German). Germany: Springer.
- Huang, H., Nowoisky, S., Knoblich, R., and Gühmann, C., 2012. Modeling and Testing of the Hydro-mechanical Synchronization System for a Double Clutch Transmission. *Proceedings of the 9th International Modelica Conference*, 284-294. 2012, Germany.
- Nowoisky, S., Gühmann, C., 2013. Automated Parameter Identification for a Dry Clutch. *Proceeding of 10th International Multi-Conference on Systems, Signals & Devices (SSD)*,18-21. 2013, Tunisia.
- Luk, 2012. *Luk Clutch Course: An Introduction to Clutch Technology for Passenger Cars*. Schaeffler Automotive Aftermarket GmbH & Co. KG.
- Naunheimer, H., Bertsche, B., Ryborz, J., Novak, W., 2011. *Automotive Transmissions: Fundamentals, Selection, Design and Application, 2nd edition*. Germany: Springer.
- Drexl, H.-J., 1997. *Kraftfahrzeugkupplungen: Function und Auslegung* (in German). Germany: Moderne Industrie.
- Dynasim AB, 2010. *Dymola (2010), version 7.4*. Product help, Dynasim AB.
- Knoblich, R., Beilharz, J., and Gühmann, C., 2011. Modellbasierte Steuergeräteentwicklung für Kfz-Getriebesysteme am Prüfstand (in German). *In Tagungsband Mechatronik*, 191-196. 2011, Dresden.
- Nowoisky, S., Knoblich, R., and Gühmann, C., 2012b. Prüfstand für die Identifikation und den Funktionstest an automatisierten Schaltgetrieben (in German). *In Virtuelle Instrumente in der Praxis*, 150-156. 2012, Germany.

BOND GRAPH PROPORTIONAL-INTEGRAL OBSERVER-BASED ROBUST FAULT DETECTION

Ghada Saoudi ^(a), Rafika El Harabi ^(b), Geneviève Dauphin-Tanguy ^(c), Belkacem Ould Bouamama ^(d), Mohamed Naceur Abdelkrim ^(e)

^(a) ECOLE NATIONALE D'INGENIEURS DE GABES, TUNISIE

^(b) ECOLE NATIONALE D'INGENIEURS DE GABES, TUNISIE

^(c) ECOLE CENTRALE DE LILLE, FRANCE

^(d) POLYTECH' LILLE, FRANCE

^(e) ECOLE NATIONALE D'INGENIEURS DE GABES, TUNISIE

^(a) saoudighada90@hotmail.fr, ^(b) rafikaharabi@yahoo.fr, ^(c) genevieve.dauphin-tanguy@ec-lille.fr,

^(d) belkacem.ouldbouamama@polytech-lille.fr, ^(e) naceur.abdelkrim@enig.rnu.tn

ABSTRACT

The present paper investigates a bond graph tool to design full-order proportional-integral (PI) observers for a robust fault detection purpose. The proposed method allows the calculation of the gain matrix graphically through covering causal paths and loops based on the pole placement techniques for linear systems. The robust residuals are further generated from an uncertain bond graph model in linear fractional transformation (LFT) form so as to detect actuator faults in presence of parameter uncertainties. Simulation tests on a hydraulic system show the dynamic behavior of system variables and the robustness of the PI observers in the presence of modeling errors. The effectiveness of the proposed robust fault detection estimator is later illustrated via a DC motor.

Keywords: Bond Graph, Proportional-Integral observer, Robust fault detection, Linear fractional transformation, DC motor

1. INTRODUCTION

Bond graph approach has been developed in recent years as a powerful tool for modeling dynamical systems. It essentially focuses on the exchange of energies between the system and its environment and between different elements within the system.

Robust fault diagnosis has been the subject of several researches, due to the increase of system complexity, and the industrial requirement around the safety and the yield (Isermann 1993). In this context, due to the structural and causal properties of quantitative graphical approaches, the bond graph is more and more used for modeling and fault diagnosis. Bond graph representation can be used for monitoring ability (i.e. ability to detect and to isolate faults) and supervision system's design via the generation of formal Analytical Redundancy Relations (ARRs) in a systematic way (Djeziri, Merzouki, Ould Bouamama

and Dauphin Tanguy 2007). In his works, Djeziri dealt with the generation of fault indicators in the presence of parameter uncertainties by using a bond graph representation in linear fractional transformation (LFT) form. Since diagnosis using (ARRs) is more common in practice, in this paper we will particularly focus the attention on the design of graphical PI observers for robust fault detection issue.

For the general case of systems modeled by the bond graph tool, little has so far been achieved in the development of associated FDI graphical observers. Abderrahmène (Sallami, Zanzouri and Ksouri 2012) integrated a method of robust diagnosis based on observers for systems with parameter uncertainties modeled by the bond graph. Hence, the observer design is obtained by using graphical methods and referring to structural properties (Sueur and Dauphin Tanguy 1989).

For this reason, the main interest of the present paper is to build a robust bond graph observer (RBGO) in proportional-integral form (Pichardo-Almarza, Rahmani, Dauphin-Tanguy and Delgado 2003) for linear systems based on causal and structural properties for graphical approach (Bond Graph). It consists to generate residual signals from linear BG-LFT models to take into account the presence of parameter uncertainties in multiplicative form.

The outline of the paper is as follows: Section 2 presents the graphical PI observers design for linear systems while section 3 deals with the robust residual generation. Illustrative examples of a hydraulic system and a DC motor are developed in section 4 and show the efficiency of the proposed robust fault detection estimator.

2. DESIGN OF A GRAPHICAL PI OBSERVER

2.1. Conventional PI observer

The Luenberger observer is itself a linear dynamic system. Its input values are the values of measured

outputs from the original system, and its state vector generates missing information about the state of the original system. The observer can be regarded as a dynamic device that, when connected to the available system outputs, generates the entire state. However, the idea of a proportional integral observer, Fig.1, is to use additionally the integral of the error as follows:

$$\hat{w} = \int_0^t (y(\tau) - C\hat{x}(\tau))d\tau \quad (1)$$

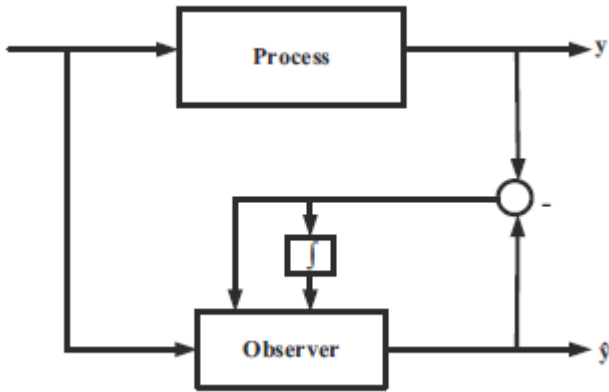


Figure 1: Proportional Integral Observer's diagram.

Then, the PI observer for the model is written using this set of equations:

$$\begin{cases} \frac{d\hat{x}}{dt} = A\hat{x} + Bu + K_p(y - C\hat{x}) + K_I\hat{w} \\ \frac{d\hat{w}}{dt} = y - C\hat{x} \end{cases} \quad (2)$$

where x in \mathcal{R}_n , y in \mathcal{R}_q , and u in \mathcal{R}_m are respectively the state, the measurement output and the control input vectors. A , B and C are constant matrices of proper dimensions. K_I and K_p are respectively the integral and proportional gains. Hence, the error equation ($e_x = \hat{x}$ and $e_w = \hat{w}$) is defined as:

$$\begin{pmatrix} \frac{de_x}{dt} \\ \frac{de_w}{dt} \end{pmatrix} = \begin{pmatrix} A - K_p C & -K_I \\ C & 0 \end{pmatrix} \begin{pmatrix} e_x \\ e_w \end{pmatrix} \quad (3)$$

2.1.1. Bond Graph PI observer

The algorithm presented in this section is dedicated to fault detection observers for linear systems, in which bond graph tool is used.

- **Step 1: Checking the existence of any redundant outputs** The existence of redundant outputs is the first condition to check for the observer construction. The interest of this step is to avoid unnecessary calculations. Indeed, the selection of the non-redundant outputs allows the computing of the gain K with minimal size. This condition can be verified by calculating the rank of the observation matrix C (difference between the number of detectors De and Df , and the detectors which cannot be dualized in the bond graph in integral causality).

- **Step 2: Checking the structural observability of the model**

Property 1: From a Bond Graph point of view proposed by Sueur and Dauphin-Tanguy (Sueur and Dauphin Tanguy 1989) a bond graph model is structurally observable if and only if the following conditions are met:

1. On the bond Graph model in integral causality, there is a causal path between all the dynamic elements I and C and a detector De or Df . Or,
2. All dynamic elements admit a derivative causality in the derivative bond graph model. If there are dynamic elements remaining in integral causality, the dualization of detectors De and Df is necessary.

- **Step 3: Construction of the Luenberger bond graph observer** The objective of this stage is to design the BGO equivalent to the conventional Luenberger observer equation defined as:

$$\begin{cases} \dot{x} = Ax + Bu + K(y - \hat{y}) \\ \hat{y} = C\hat{x} \end{cases} \quad (4)$$

The BGO is composed of the integral bond graph model to which the term $K(y - \hat{y})$ is added. Figures 2 and 3 represent the linear output injection in the dynamic components I and C , by using modulated flow sources for an element I and modulated effort sources for an element C .

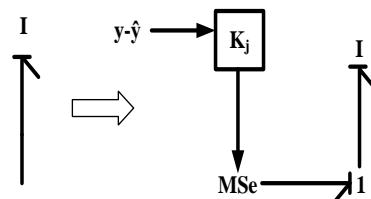


Figure 2: Linear output injection: case of an I element.

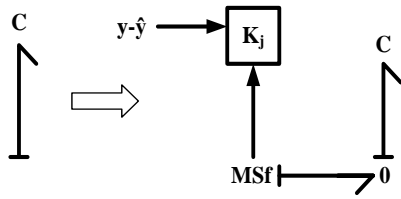


Figure 3: Linear output injection: case of a C element.

- Step 4: Construction of the bond graph PI observer** The Bond Graph model is defined with the changes described in the below figures. In the same way, modulated effort sources (respectively flow sources) are used when the state variable is associated with an I-element (respectively a C-element) to apply the integral action in the observer.

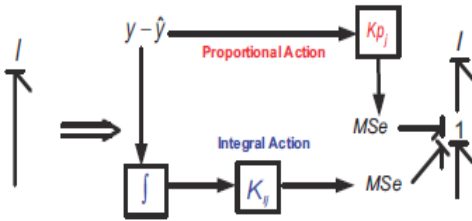


Figure 4: Linear output injection: case of an I element.

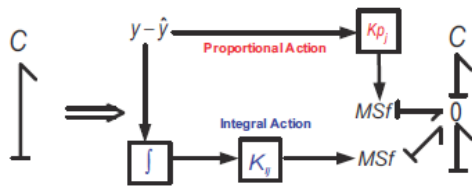


Figure 5: Linear output injection: case of a C element.

3. ROBUST RESIDUAL GENERATION

Inspired from BG-LFT representation introduced by (Dauphin and Djeziri 2006), graphical PI observers are used to generate robust residual signals by following these steps:

- Verify that the uncertain bond graph model in LFT form of the system is reachable and structurally observable;
- Construction of the BG PI observer;
- The residual signal (residual output estimation) is deduced from this equation: $r = y - \hat{y}$.

In the next section, we will illustrate the effectiveness and the performance of the developed graphical PI estimator comparing to Luenberger one (Saoudi, EL Harabi and Abdelkrim 2012; Saoudi, EL Harabi and Abdelkrim 2013) via a hydraulic system with two tanks. Robust fault residuals are tested through a DC motor with parameter uncertainties under multiplicative form.

4. SIMULATION AND DISCUSSIONS

4.1. Hydraulic System with two tanks

Consider the sketch of the studied system where its characteristic values are presented in Table 1. From the bond Graph model in integral causality (see Figure 7), the associated graphical PI observer is deduced verifying these steps:

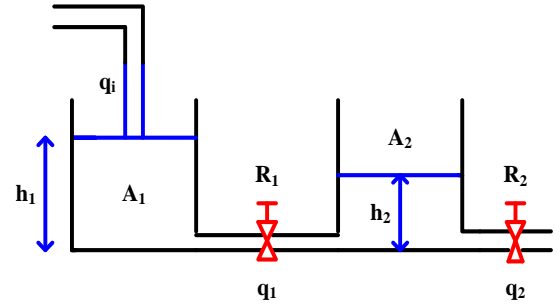


Figure 6: Hydraulic system with two tanks.

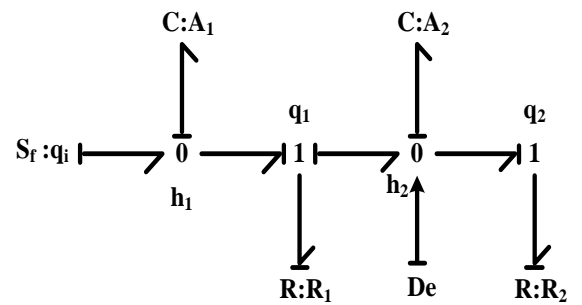


Figure 7: Bond Graph model of the system in integral causality.

Table 1: Parameter Values

Elements		
Parameter	Symbol	Value
Section Area of tank 1	A_1	1m^2
Section Area of tank 2	A_2	2m^2
Hydraulic Resistance 1	R_1	$10\text{m}(\text{m}^2\text{s}^{-1})^{-1}$
Hydraulic Resistance 2	R_2	$20\text{m}(\text{m}^2\text{s}^{-1})^{-1}$

- Step 1: Checking the existence of redundant outputs.** This step is unnecessary in this case study, since the model has only a single detector.
- Step 2: Verification of the structural observability.** As it is mentioned previously, the structural observability, can be easily obtained using structural analysis of the derivative bond graph model (DBG) (See

Figure 8). All the dynamic elements admit a derivative causality; hence, the model is structurally observable.

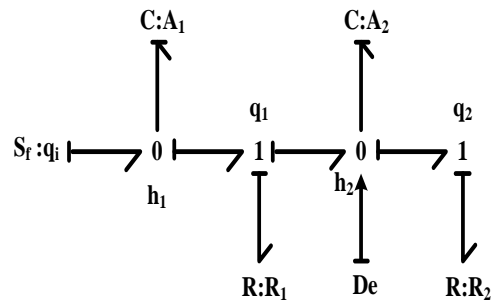


Figure 8: Bond Graph model in derivative causality.

- **Step 3: Construction of the Luenberger BG observer.** It is possible to construct a Luenberger observer from the bond graph model by using linear output injection cited above.

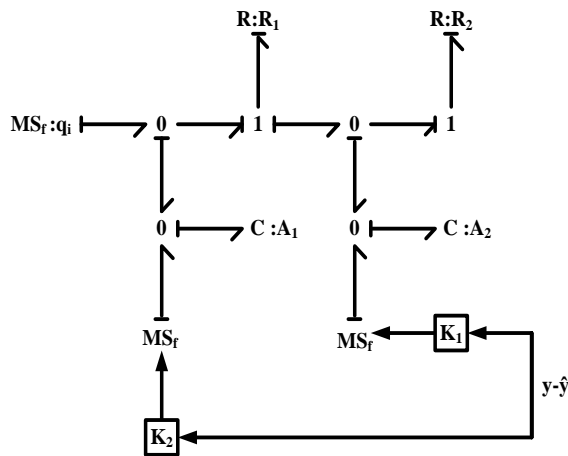


Figure 9: Bond Graph model of the Luenberger observer.

- **Step 4: Construction of the PI observer-based bond graph (BGO).** The proposed BG PI observer is described in Fig.10 after modifying the bond graph model.

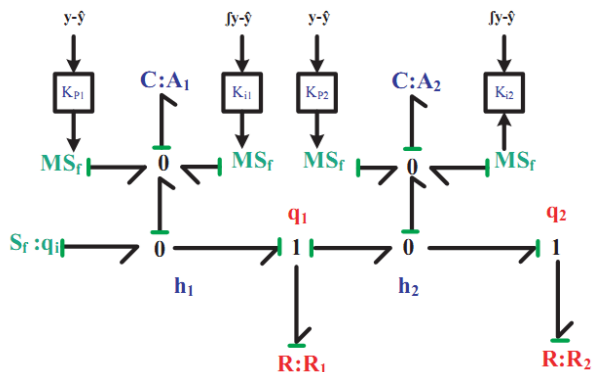


Figure 10: Bond graph model of the graphical PI observer.

- **Step 5: Gain calculation of the BG PI observer.** We calculate Kp as the gain of the Luenberger observer. We choose the poles of the observer and such that they are slightly faster than the poles of the model and non-oscillating.

$$s = \begin{bmatrix} s_1 \\ s_2 \end{bmatrix} = \begin{bmatrix} -0.318 \\ -0.032 \end{bmatrix} \quad (5)$$

This selection gives the following desired characteristic polynomial:

$$P_d(s) = s^2 + 0.35s + 0.01 \quad (6)$$

with these coefficients and after the calculation of causal cycles of order 1-2, we obtain Kp as

$$Kp = \begin{bmatrix} 2 \\ 0.15 \end{bmatrix} \quad (7)$$

Then, we can apply the same method to calculate KI using the calculated values of KP for the Luenberger observer, with the following poles selection:

$$s = \begin{bmatrix} -0.318 \\ -0.032 \\ -0.0033 \end{bmatrix} \quad (8)$$

Furthermore, the desired polynomial for the PI observer is:

$$P_d(s) = s^3 + 0.3533s^2 + 0.1115s + 0.00003 \quad (9)$$

with these coefficients, we obtain now three equations depending on the components of K1 and KP. We use the values of Kp2 calculated for the Luenberger observer and after the calculation of the family of causal cycles of order 1-3, we can calculate the new Kp1 and K1 vector that generate the coefficients of the desired polynomial.

Finally, we obtain the following gains:

$$Kp = \begin{bmatrix} Kp_1 \\ Kp_2 \end{bmatrix} = \begin{bmatrix} -0.2467 \\ 0.15 \end{bmatrix} \quad (10)$$

$$K_I = \begin{bmatrix} K_{I1} \\ K_{I2} \end{bmatrix} = \begin{bmatrix} 0.00373 \\ -0.00718 \end{bmatrix} \quad (11)$$

The initial conditions of the BG model states in integral causality are considered null. Simulation tests were implemented in 20-sim software. In this part, The performance of the Luenberger and PI observers are evaluated in presence of modeling errors. Thus, let's consider that the hydraulic resistance parameter R2 for

the OBG have a variation of -10% in comparison with the parameters of the BG model.

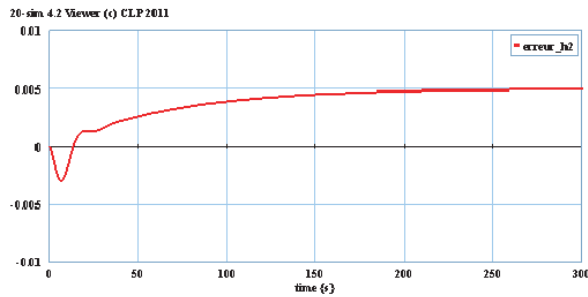


Figure 11: Estimation error via the Luenberger BG observer.

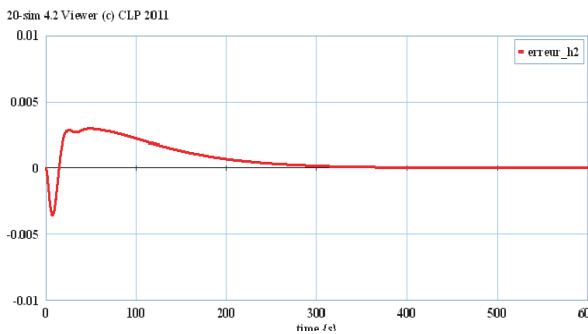


Figure 12: Estimation error via the BG PI observer.

We conclude that the estimation error converges to zero despite the presence of modeling errors in the observer's parameters unlike to the graphical Luenberger observer (see figures 11 and 12).

Now, Let's use the BG PI observer for a robust fault detection purpose.

4.2. DC motor

The DC motor is a combination of electrical and mechanical fields. The electrical part corresponds to an RL circuit. It is composed of an input voltage source U_{alim} , an electrical inductance L_a and an electromotive force feedback represented by a gyrator (GY) (with a constant k). The mechanical part is characterized by a rotor inertia J , a viscous friction parameter b and transmission axle rigidity.

The nominal characteristics and parameter values of the DC motor are defined in Tables 2 and 3.

Table 2: Nominal Operation Of The Dc Motor

DC Motor Characteristics	
Power	1KW
Velocity (w)	452tr/mn
Current (I_a)	1.8A
Voltage (U_{alim})	47.3V

Table 3: Parameter and Uncertainties Values Of The DC Motor

Parameter and Uncertainties Values			
Symbol	Parameter	Value	Uncertainty
R_a	Armature Resistance	8Ω	0
L_a	Rotor Inductance	0.129 H	$\delta_{L_a}=0.0002$
k	Constant Torque	0.07745	0
J	Constant Inertia	0.02Kg.m ²	$\delta_J=0.00035$
b	Fluid Friction	0.0218 Nm/s	0

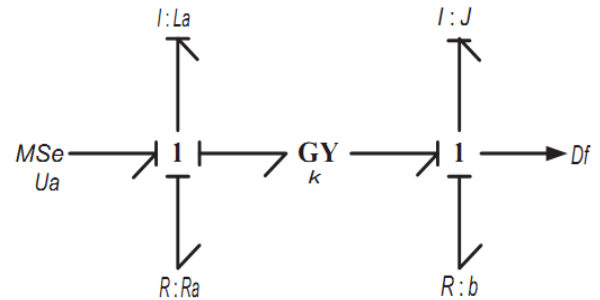


Figure 13: Bond graph model of the DC motor with permanent magnet.

To this bond graph model of the DC motor (see Fig.13), we will apply the method described in section 2 in order to design the graphical PI observer.

The bond graph model of the studied system (see Fig.14) is structurally observable (steps 1 and 2 are verified).

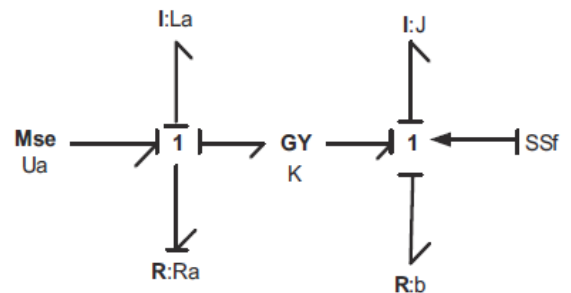


Figure 14: Bond graph model in derivative causality.

- **Step 3: Construction of the Luenberger BG observer.** The bond graph model of the proportional observer is deduced as seen in Fig.15.

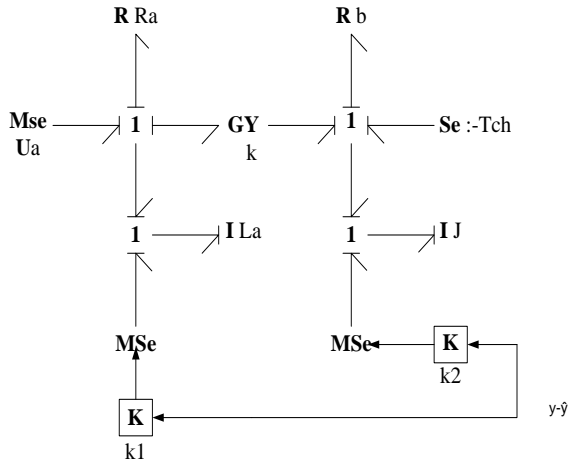


Figure 15: Bond graph model of the Luenberger observer.

- **Step 4: Construction of the BG PI observer.** PI observer deduced from BG model is presented in Fig.16.

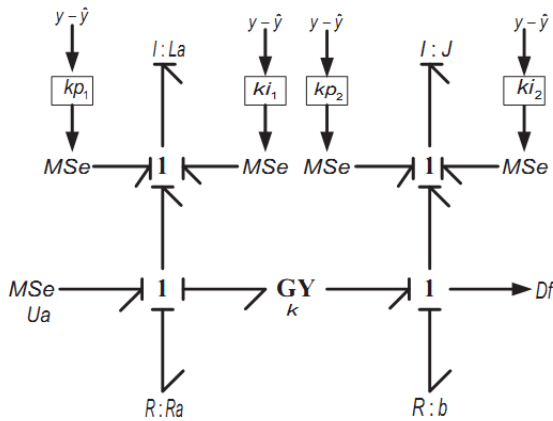


Figure 16: Bond graph model of the PI observer.

- **Step 5: Calculation of the observer gain (Kp and Ki).** It is determined using the bond graph models of the observers. Applying the same technique to calculate the gains of the previous observer, from Fig.16 we obtain the corresponding families of causal cycles (see Table 4).

a_i	Causal Cycle families	Gains
β_1	$I:L_a \leftarrow 1 \rightarrow R:Ra$	$G_a = (-1) \cdot \frac{-R_a}{L_a s}$
	$I:J \leftarrow 1 \rightarrow R:b$	$G_b = (-1) \cdot \frac{-b}{J s}$
	$J \uparrow \leftarrow 1 \leftarrow MSe \leftarrow \boxed{kp2} \leftarrow y - \hat{y}$	$G_c = (-1) \cdot \frac{-k_{p2}}{J s}$
β_2	$I:L_a \uparrow \leftarrow 1 \leftarrow GY_k \leftarrow 1 \leftarrow I:J$	$G_d = (-1) \cdot \frac{-k^2}{L_a J s}$
	$y - \hat{y} \downarrow \leftarrow \boxed{kp1} \rightarrow MSe \rightarrow 1 \leftarrow GY_k \rightarrow 1 \leftarrow J \uparrow$	$G_e = (-1) \cdot \frac{-k \cdot k_{p1}}{L_a J s^2}$
	$J \uparrow \leftarrow 1 \leftarrow MSe \leftarrow \boxed{ki2} \leftarrow y - \hat{y}$	$G_f = (-1) \cdot \frac{-k_{i2}}{J s^2}$
	$J \leftarrow 1 \rightarrow b$ $L_a \leftarrow 1 \rightarrow R_a$	$G_g = \frac{R_a \cdot b}{L_a J s^2}$
	$L_a \leftarrow 1 \rightarrow R_a$ $J \uparrow \leftarrow 1 \leftarrow MSe \leftarrow \boxed{kp2} \leftarrow y - \hat{y}$	$G_h = \frac{R_a \cdot k_{p2}}{L_a J s^2}$
	β_3	$L_a \uparrow \leftarrow 1 \leftarrow MSe \leftarrow \boxed{ki1} \leftarrow y - \hat{y}$ $1 \leftarrow GY_k \rightarrow 1 \leftarrow J \downarrow$
$L_a \leftarrow 1 \rightarrow R_a$ $J \uparrow \leftarrow 1 \leftarrow MSe \leftarrow \boxed{ki2} \leftarrow y - \hat{y}$		$G_j = \frac{k_{i2} \cdot R_a}{L_a J s^3}$

Finally, we obtain the following gains:

$$K_p = \begin{bmatrix} 2.3 \\ 0.3642 \end{bmatrix} \quad (11)$$

$$K_I = \begin{bmatrix} -5.217 \\ 10.998 \end{bmatrix}$$

The input signal U_{alim} and the load torque T_{ch} , in normal situation, are illustrated respectively in figures 18 and 19. Moreover, the estimated states $i_{a_{est}}$ and w_{est} when a PI observer is used are shown in figures 20 and 21. The observer error is near zero. In this case, it is able to estimate states. Thus, the obtained estimator can be used to generate residual signals.

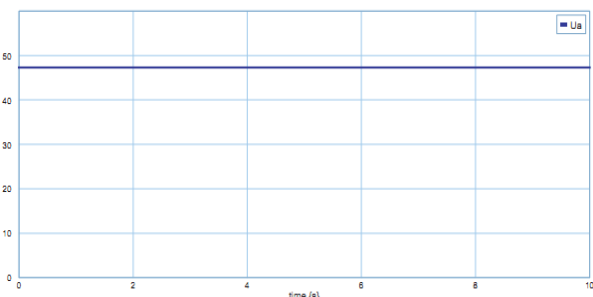


Figure 18: Input signal evolution.

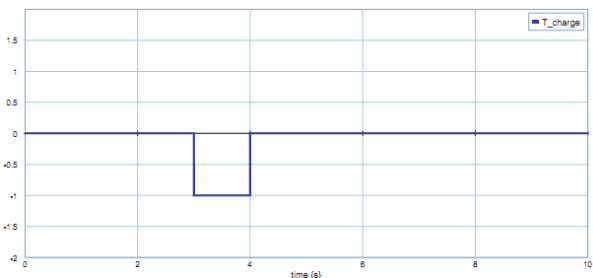


Figure 19: Load torque evolution.

The figures 20 and 21 show a clear precision of estimation of the systems state variables. We observe, also, that the pace of the estimated variables $i_{a_{est}}$ and w_{est} and the state variables i_a and w are indistinguishable.

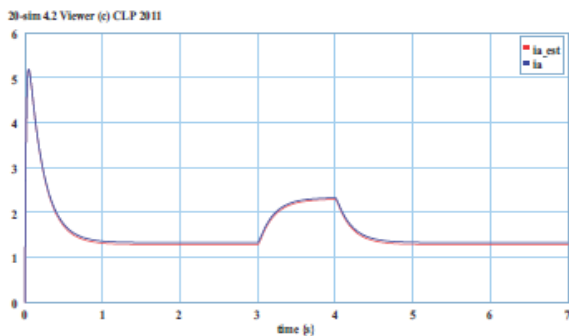


Figure 20: Estimation of the Induced current via the BG PI observer.

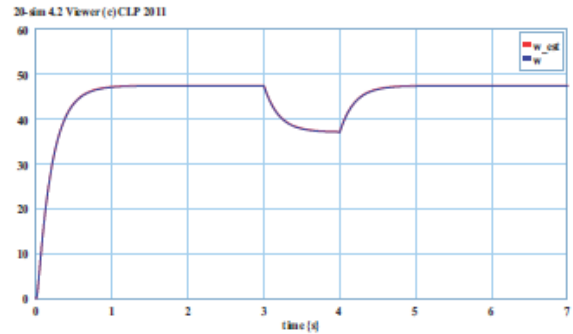


Figure 21: Estimation of the velocity via the BG PI observer.

The estimation errors are null as it is shown in figures Fig.23 and Fig.24.

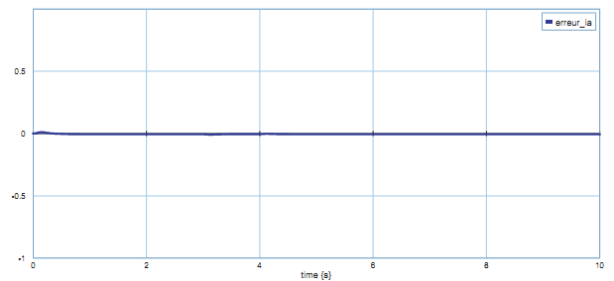


Figure 22: Estimation error of the induced current.

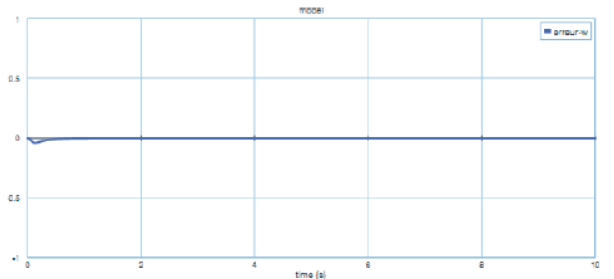


Figure 23: Estimation error of the velocity.

In LFT bond graph representation, parameters uncertainties are represented under multiplicative form at the level of bond graph component, which represent respectively, the inertia J and the rotor inductance L_a in the DC motor. The graphical linear PI observer is depicted in Fig.24. Indeed, the proportional-integral observer provides a more robust estimation against parameter uncertainties as it is shown in figures 25 and 26. The estimation errors are practically null. Thus, the robustness of the graphical PI observer against modeling errors.

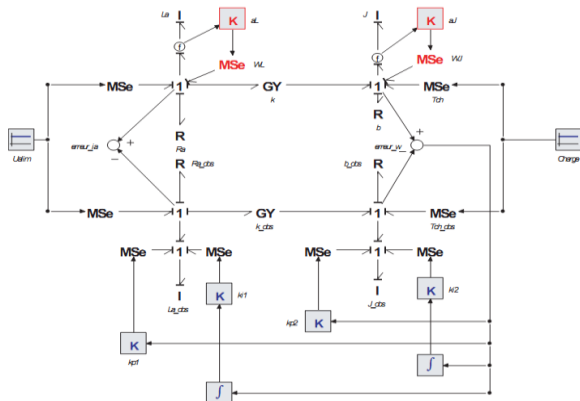


Figure 24: BG-LFT model with multiplicative uncertainties of the system and its observer.

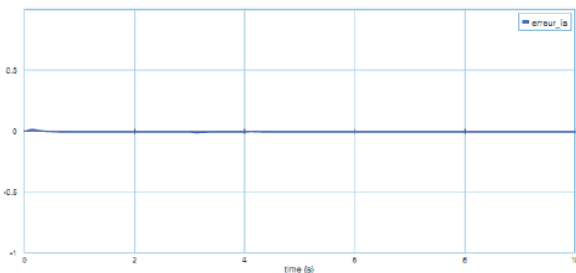


Figure 25: Estimation error of the induced current in faulty free case (in presence of parameter uncertainties).

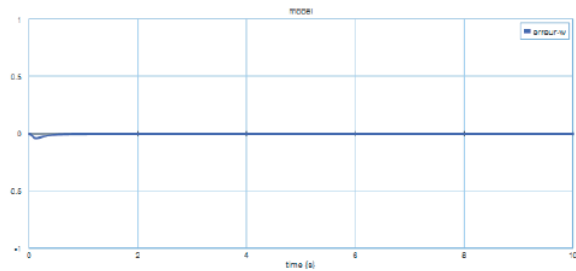


Figure 26: Estimation error of the velocity in faulty free case (in presence of parameter uncertainties).

Hence, it improves the performance and the efficiency of the bond graph PI observer. Now, it can be used to generate fault indicators.

However, DC motor failures can be classified as electrical and mechanical faults and the residues are obtained from the linear graphical PI observer.

The fault scenario considers the occurrence of the actuator fault (partial blocked rotor), with subtractive amplitude of 20 Volt between the instants 3s and 4s (abrupt failure), while the motor is operating in charge.

From figures 27 and 28, we observe that the state variables are affected by the occurrence of this default and drawn aside from their nominal values.

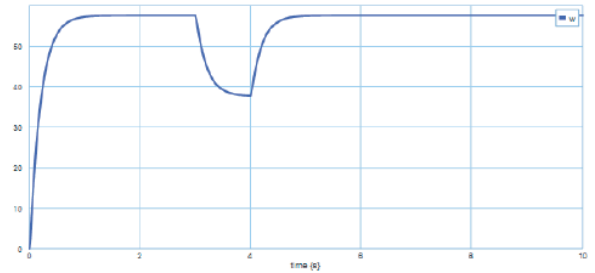


Figure 27: Velocity evolution in faulty case.

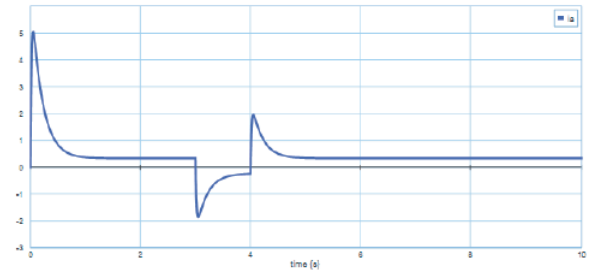


Figure 28: Induced current evolution in faulty case.

Figures 29 and 30 show that residues are different from zero during the appearance of the actuator failure. Then, the graphical PI observer able guarantee a robustness to parameter uncertainties and a sensitivity against faults.

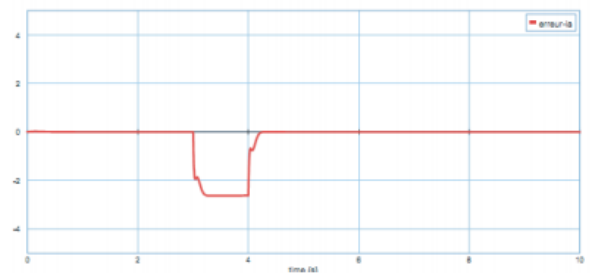


Figure 29: Residual response in abnormal situation (r_1).

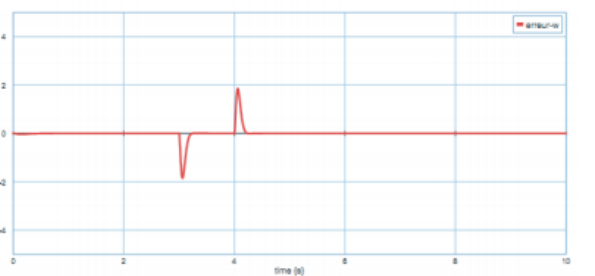


Figure 30: Residual response in abnormal situation (r_2).

5. CONCLUSION

In this paper, a robust fault detection procedure using a proportional-integral observer based on bond graph model for linear systems has been addressed. This approach is based exclusively on the causal handling operated on a bond graph representation. The

implementation of graphical PI observers improve the residual generation. In fact, the obtained fault indicators are robust to the multiplicative parameter uncertainties and the modeling errors. The major interest of this approach lies in the fact that the bond graph model has a true physical direction and gives access to many flow and effort variables. Due to graphical proportional-integral observer's limits, future works will focus on an unknown input observer design so as to ensure more robustness against disturbances.

REFERENCES

- Isermann, R., 1993. Fault diagnosis of machines via parameter estimation and knowledge processing. *Automatica*, 29 (4), 815–836.
- Djeziri, M., Merzouki, R., Ould Bouamama, B., Dauphin-Tanguy, G., 2007. Robust Fault Diagnosis by Using Bond Graph Approach. *IEEE Transactions on Mechatronics*, 12 (6).
- Luenberger, D., 1966. Observers for multivariable systems. *IEEE Transactions on Automatic Control*, 11, 190–197.
- Karnopp, D., 1979. Bond Graphs in Control: Physical State Variables and Observers. *Journal of The Franklin Institute*, 308 (3), 221–234.
- Pichardo-Almarza, C., Rahmani, A., Dauphin-Tanguy, G., Delgado, G., 2003. Bond Graph Approach to Build Reduced Order Observers in Linear Time Invariant Systems. *Proceedings of 4th MATHMOD, Fourth International Symposium on Mathematical Modeling*.
- Hajji, N., Rahmani, A., 2010. Observer for an omnidirectional mobile robot. *ICBGM*, Orlando: USA.
- Loureiro, R., BenMoussa, S., 2011. Graphical approach for state reconstruction and monitoring analysis. *The 5th International Conference on Integrated Modeling and Analysis in Applied Control and Automation IMAACA*, Rome: Italy, 259–266.
- Sallami, A., Zanzouri, N., Ksouri, M., 2012. Robust Fault Diagnosis Observer of Dynamical Systems Modelled by Bond Graph Approach. *International Journal of Computer Science and Network Security*, 12 (1).
- Sueur, C., Dauphin-Tanguy, G., 1989. Structural Controllability and Observability of linear Systems Represented by Bond Graphs. *Journal of Franklin Institute*, 326, 869–883.
- EL Harabi, R., Ould Bouamama, B., El Koni Ben Gayed, M., Abdelkrim, M., 2012. Bond graphs for diagnosis of chemical processes. *Computers & chemical engineering*, 36, 301–324.
- EL Harabi, R., Ould Bouamama, B., El Koni Ben Gayed, M., Abdelkrim, M., 2011. Bond Graph Model Based for Robust Fault Diagnosis. *Computers & chemical engineering. the 5th International Conference on Integrated Modeling and Analysis in Applied Control and Automation IMAACA*, Rome: Italy, 259–266.
- Beale, S., Shafai, B., 1989. Robust control System Design with a proportional integral observer. *International Journal of Control*, 50 (1), 97–11.
- Busawon, K., Kabore, P., 2000. On the design of integral observers and proportional integral observers. *Proceedings of the American Control Conference*, 3275–3279.
- Saoudi, G., EL Harabi, R., Abdelkrim, M., 2012. Fault Detection Based on Luenberger Observers. *CRATT*, Tunis: Tunisia.
- Saoudi, G., EL Harabi, R., Abdelkrim, M., 2013. Graphical Linear Observers For Fault Detection. *SSD*, Hammamet: Tunisia.
- El Harabi, R., 2011. *Supervision des Processus Chimiques à Base de Modeles Bond Graph*. Thesis (PhD). Gabes University.
- Rahmani, A., 1993. *Etude structurelle des systèmes linéaires par l'approche bond graph*. Thesis (PhD). Lille University.

3D COMPUTATIONAL MODEL INCLUDING TOPOGRAPHIC DATA FOR THE PREDICTION OF DIRE WIND REGIMES AND VORTEX SHEDDING IN AN ATTEMPT TO IMPROVE TALL BUILDING RELIABILITY

Drishtysingh Ramdenee⁽¹⁾, Pierre Luc Paradis⁽²⁾, Hussein Ibrahim⁽³⁾, Hemraj Joyram⁽⁴⁾, Adrian Ilinca⁽⁵⁾

⁽¹⁾Institut Technologique de la Maintenance Industrielle, Cegep de Sept Îles

⁽²⁾T3e, École Technologique supérieur, Montréal

⁽³⁾Technocentre Éolien, Gaspé, Québec

⁽⁴⁾Sir Abdool Raman Osman, Phoenix, Mauritius

⁽⁵⁾Wind Energy Research Laboratory, 300 allée des Ursulines, Rimouski. G5L3A1

drishtysingh.ramdenee@itmi.ca

ABSTRACT

A structure's wind resistance largely determines its Extended Coverage Endorsement (ECE) and is an important factor in determining total insurance costs. Insurance policies and costs are often not very representative or prejudicial to either the insurer or the policy holder due to uncertainties in the ability to predict structures' wind resistance capacities. In other words, according to International Standards (ISO 2394:1998(E)) all structures including tall buildings must abide to the criteria of serviceability. Serviceability means the ability of a structure or structural element to perform adequately under normal use, expected actions or bounded actions (actions which have a limited value which cannot be exceeded and which is exactly or approximately known). Consequently, the ISO rules stipulate that choice of structural system, design for durability and implementation of quality policy need to be accordingly set up as to appropriate degree of reliability, which, in turn should be judged with due regard to the possible consequences of failure. In the case of tall buildings, mostly as to what concerns claddings, it is becoming more and more important to define proper reliability framework to increase

certainty and render insurance policies more tailor made and unbiased. When it comes to static or quasi-permanent value solicitations on buildings such as known winds, collisions, etc, a high level of certainty exists in the calculations and models predicting failure and damage. However, when it comes to loads with high variability, the reliability index becomes very low. In many countries, skyscrapers are rapidly growing in restrained areas such that the formed corridors accelerate the winds and increase formation of vortices. Furthermore, in cases of rapidly changing gusts, the wind loads can be quite dangerous and cause damage and even failure to the buildings. Unfortunately, limited work enables very precise prediction of such loads such that insurance policies are accordingly unspecific. In this paper, work conducted at the Wind Energy Research Laboratory (WERL) to model pressure and velocity fields around buildings in a test area is presented. In most studies, proposed results are only for one building only and the wind regime do not account for the topography around. This present article, wishes to propose a full scale 3D simulation of the pressure, turbulence and velocity regimes around multiple buildings in the

same city whilst accounting for topography and canopy information of the region. Further to being a tool to uncertainty prediction in wind modeling, this highly complex CFD (computational Fluid dynamics) model proposes vortex modeling in high gradient regions. These are, moreover, compared and calibrated using a Matlab model.

Keywords: Wind modeling, turbulence, tall building, simulation, insurance policy

1. INTRODUCTION

Wind is a highly complex and variable phenomenon as it interacts at all times with structures, gets modified according to different canopy and is inherent of turbulence of vortices in many cases. Modeling of the effects of gusts on structures is uncertain and hazardous due to turbulence induced rotational eddies. This turbulence nature tends to be more important in the lower atmosphere as the wind interacts with rough ground and decreases with height. Therefore, slender skyscrapers are often subjected to variable winds both in time but also in altitude. The lower parts of the buildings are subjected to slower but highly turbulent winds while the uppermost parts are subjected to higher speed but less turbulent winds. These variable characteristics of wind make it difficult to model and impose dangerous dynamic loads on the buildings. In case of significant eddies as compared to the building size, well established pressures develop in these regions whereas for small eddies (as compared to the building size), variable uncorrelated pressures develop with distance separation. These effects bring risks of occurrence of very dire aeroelastic effects like flutter. In other words, if there is a positive retroaction of the turbulent dynamic loads with the elastic response of the buildings, the latter may start to oscillate with expansive amplitude until failure. One such example is the Tacoma bridge failure in 1940 at wind speed of only 19 m/s. Bridge failure as a result of resonance was modeled by D.Ramdene et al. of the WERL team in [1]. We can, hence, clearly see that the need to properly model aeroelastic and aerodynamic effects on building is very important. The breakthrough of our work is that we make use of very precise CFD methods coupled with complete consideration of the terrain aerodynamics around to find very accurate results. The terrain aerodynamics

consideration enables us to set as realistic as possible wind regimes in the computational domain. Furthermore, Matlab support enables us to compare and calibrate the model via vortex shedding consideration. Such precise analysis can be very interesting tools to mend knowledge around reliability and serviceability of buildings so as to improve building norms and adjust the insurance policies around buildings.

2. WIND CHARACTERISTIC

Loads modeling (pressure and wind speed) on buildings require accurate modeling of approaching wind. However, such is quite difficult and in many cases require time and money costly experiments. For example, as we can see in a study by Deaves and Harris (1978) [2], the extensive full scale data and classic logarithmic law based wind model in neutral stability conditions has been the fruit of very tedious work. It will be very cumbersome as method to build a model for different places using such methods. Such models are expressed in the following equation with specific coefficients A, B, C, D and E.

$$\bar{V}_z = \frac{u^*}{A} \left[\ln \left(\frac{z}{z_0} \right) + B \left(\frac{z}{z_g} \right)^1 + C \left(\frac{z}{z_g} \right)^2 + D \left(\frac{z}{z_g} \right)^3 + E \left(\frac{z}{z_g} \right)^4 \right] \quad (1)$$

Where

\bar{V}_z is the hourly mean wind velocity at a height of z measured in ms^{-1}

u^* is the friction velocity and is given by:

$$u^* = \sqrt{\frac{\text{surface friction shear stress}}{\text{atmospheric density}}}$$

z_g is the stretch version of gradient length in m

z_0 is the average ground roughness in m

The above model allows modeling of the wind profile according to different altitudes. However, it does not take into account canopy, atmospheric thermal stratification (only significant for very tall buildings) and roughness effects which are very important. In our model, the wind profile is inherent of all these characteristics via modeling of wind profiles within buildings region from far

unperturbed boundary winds in Windmodeller [3] software. The output wind profile expressions (inherent of all the above described phenomena) are used as boundary inlet conditions in modeling the wind profile around the buildings.

3. PRESENT CONSTRUCTION FRAMEWORK AND POLICIES RELEVANT TO WIND LOADS

Studies conducted by the Division of Building Research, National Research Council of Canada, in an attempt to rationalize the calculation of wind loads on buildings are exclusively based on generalization of smooth wind tunnels experimental results. These allow us to define potential hazards and a broad range of domains where the latter might appear. However, no tools have been developed that can actually model with satisfactory precision the pressure distribution around buildings, wakes effects, interaction of multiple flows due to buildings and acceleration in corridors. In many cases, as design criteria for buildings and to evaluate failure probabilities, static analysis is made use of. This method uses the criteria of the peak pressure to calculate classic structural failure like stress, shear or torsion. The peak pressure is taken to be the product of the gust dynamic wind pressure and the mean pressure coefficients. The mean pressure coefficients are calculated in wind tunnel experiments such that the values are specific to a given context. This kind of analysis, furthermore, assumes fully correlated progression of the variations in the upwind velocity such that a peak wind speed value will automatically imply a peak value in the pressure or load on the structure. Such kind of analysis is used despite surprisingly low level of accuracy because it offers simplicity, continuity with previous practice and allows direct use of existing meteorological data on wind gusts. However, the method is not suitable for tall structures or those with significant dynamic response. Furthermore, the near quasi-steady assumption fails in many cases where the mean pressure coefficient is near zero. Also, this assumption fails in many cases of vortex shedding whereby a rapid rotational phenomenon triggers a short lived but high gradient low pressure region (disastrous for claddings) or rapidly changing wind velocities (considering magnitude and direction) which interferences in a positive retroaction with the buildings structural dynamics. The actually used models are, thus, clearly, insufficient to adequately

model and provide guarantee on the ability of building to withstand different wind regimes. Hence, the uncertainty in relevant wind induced hazards on buildings make it difficult for completely relevant insurance policies to be applied or construction framework devised. The wind association for Wind Engineering makes it clear that there is need for improvement in this field. Advancements in proper wind modeling and effects on structures will, further, enable different stakeholders to assess risks for potential projects and increase precision in cost management analysis. [3 to 9] provide further details of limitations prevailing in the framework of wind loads effects on buildings.

4. METHODOLOGY ADOPTED IN THIS WORK

In this work we wish to propose a generic tool capable of modeling wind distribution (pressure and velocity) around tall structures (in this case building). The idea behind is to propose results that can allow us to evaluate potential hazards and hence accordingly set insurance policies and construction norms. In further work, aeroelastic modeling will be performed. In this paper, the final simulation permits the definition of a tool that allows simulation of wind field distribution over a city skyline. The simulation is 3D and is transient. The reasons for modeling a whole city and in transient state (with time dependent wind) follow: the closeness of tall buildings allows us to see if the tool satisfactorily model wind acceleration in the corridors and interaction of wakes with neighboring buildings. In many present tools and studies such phenomena are not taken into consideration. Transient state modeling allows us to see the presence of vortex shedding as the wind changes its profile over the buildings. Furthermore, to these rotational phenomena, analysis of changing pressure field allows us to predict hazards for claddings or risk of positive retroaction with the buildings structural dynamics. Such study has been done through successive steps whilst calibrating and sustaining our CFD model. In a preliminary study, the domain calibration, mesh optimization and turbulence model calibration was performed using a steady flow simulation on a single building. The idea behind has been to simulate a most common flow on simple structure. This simulation will allow us to see if the domain is sufficiently large to prevent interaction of the boundary walls with the simulation (creating artificial vortices or pressure gradients), to refine

the mesh size and type until any additional change has no or very insignificant change on the results and a study of the results to choice which turbulence model better performs in such cases. In a second simulation, a transient flow modeling was performed on the same building with optimized domain, mesh and turbulence model properties. In this case, we wish to see if our model offers precise results with transient modeling. In order to validate such, we have set up a Matlab code capable of calculating the pressure changes and simulate the vortices in the rear of the buildings according to the time dependent wind. Comparison of the CFD obtained vortices and those by the Matlab code will enable us to see if the tool performs well. Once the model having been calibrated and supported, we performed a transient wind distribution simulation of wind field around buildings in a city for a given wind regime. Finally, we add the model additional precision from Windmodeller software (topography, canopy and wind profiles) to add realism to our model and propose a very accurate tool.

5. DOMAIN, MESH AND TURBULENCE MODEL CALIBRATION

The calculation domain is defined by a cuboids of length L, height H and with W. This was inspired from works from both Bhaskaran presented in the Fluent tutorial and from Nathan Logsdon [10-14]. As an objective we only vary L, H and W to see how the distance between the boundaries limits and the building influence the results. As these three parameters will vary, the number of elements will also vary. In order to define the optimum calculation domain, we created different domains linked to a preliminary arbitrary one by a homothetic transformation with respect to the centre of the cuboids. For the city a 1:400 scale was used on a city of 5 skyscrapers. The average size of the real skyscrapers is 40m by 40 m by 300m and the size of the city (horizontal plane) 1000m by 1000m. The size of the domain and other relevant sizes are illustrated in table 1 below:

Table 1: Relative sizes of real entities and CFD model in optimised domain

Entities	Real life Size (m)	CFD model size (m)
Average length of building	40	0.1

Average width of building	40	0.1
Average height of building	300	0.75
Length of city	1000	2.5
Width of city	1000	2.5
Length of domain	4000	10
Width of domain	1400	3.5
Height of domain	400	1

The working domain and buildings are shown in figure 1 below.



Figure 1: CFD model and domain of wind flow over city

For the mesh optimization, the one building steady flow simulation was run with increasingly refined meshes until the results changed only insignificantly. We, hence, made use of mesh sizes as defined in table 2.

CFX proposes several turbulence models for flow over structures resolution applications. Documentations from [15] advise the use of three models for such kind of applications namely the $k-\omega$ model, the $k-\omega$ BSL model and the $k-\omega$ SST model. The Wilcox $k-\omega$ model is reputed to be more accurate than $k-\epsilon$ model in the near wall layers. It has been successfully used for flows with moderate adverse pressure gradients, but does not succeed well for separated flows. The $k-\omega$ BSL model (Baseline) combines the advantages of the Wilcox $k-\omega$ model and the $k-\epsilon$ model but does not correctly predict the separation flow for smooth surfaces. The $k-\omega$ SST model accounts for the transport of the turbulent shear stress and overcome the problems of $k-\omega$ BSL model. The $k-\omega$ SST model has been chosen as previous works and analysis like [14] leads to us to believe that this turbulence model will better model intrinsic effects like turbulent shear stress transport along the walls of the structures.

Table 2: Table of optimized mesh size

Description	Value (m)
Size of elements along the buildings	0.001
Size of first element in the boundary layer	0.00008
Size of the elements on the boundary limits	0.3
Number of layers in the boundary layer	17
Inflation factor in the boundary layer	1.19
Inflation factors near the boundary limits	1.19

6. TRANSIENT MODEL ANALYSIS WITH ONE BUILDING

Another simulation was performed: A transient flow simulation was run over a single building using the same domain, mesh and turbulence model as in the previous case. The wind profile used only varies in time and not in space. This simulation was performed in an attempt to validate our model in transient state. As no particular experimental validations exist, we have modeled an identical transient flow simulation in Matlab. The aim has been to be able to see the same vortex shedding in the rear of the building in the two simulations thus confirming same transient pressure distribution results and velocity field. This will validate the capacity of our model to simulate transient flow over buildings. To do so, in an attempt to see the vortices very well, the domain size was reduced. The length, width and height of the CFD domain were made very close to that of the building. The simulation resembled a flow in a duct with a barrier as the building. Such was done to increase the presence of vortices (more visible) and ease the programming of a Matlab code. The size of the used domain was 4m*0.2m*1m. The building was at the centre of the domain. In the Matlab code, the Euler equations for the two dimensional inviscid flow are written in the integral form for a region Ω with the boundary $\delta\Omega$ as :

$$\begin{aligned} & \frac{\delta}{\delta t} \iint w dx dy \\ & + \oint (f dy - g dx) \\ & = 0 \end{aligned} \quad (2)$$

Where x and y are Cartesian coordinates and:

$$\begin{aligned} w &= \begin{pmatrix} \rho \\ \rho u \\ \rho v \\ \rho E \end{pmatrix}, f = \begin{pmatrix} \rho \\ \rho u^2 + p \\ \rho uv \\ \rho uH \end{pmatrix}, g \\ &= \begin{pmatrix} \rho v \\ \rho uv \\ \rho v^2 + p \\ \rho vH \end{pmatrix} \end{aligned} \quad (3)$$

p, ρ , u, V, E and H denote the pressure, density, Cartesian velocity components, total energy and total energy considered in our situation (as in the CFD modeling) as an ideal gas. The discretization procedure follows the method of lines in decoupling the approximation of the spatial and temporal terms. The domain is divided into quadrilateral cells and the system of differential Euler equations is applied to each cell separately. Each quantity, such as u_1 or ρu_1 is then evaluated as the average of the values in the cells of the two sides of the face:

$$\begin{aligned} & (\rho u)_1 \\ & = \frac{1}{2} (\rho u)_{i,j} \\ & + \frac{1}{2} (\rho u)_{i+1,j} \end{aligned} \quad (4)$$

Boundary conditions such as pressure at the velocity at the entry, free slip walls and atmospheric pressure at exit were specified. Improper treatment of the boundary conditions can lead to serious errors and perhaps instability. Fourth order Runge Kutta was used to solve the equations. The used speed was $200 \cdot \sin(30^\circ)$ ms^{-1} . This velocity has very high amplitude and variability. The used velocity (both in Matlab code and CFD modeling) were the same. The pressure in the vortices at the same position (in the wake of the highest region of the building) were compared. The results are illustrated and discussed below.

First of all, we will illustrate the vortices obtained at different time steps via Matlab code as compared to the simulation results for time $t=30$ seconds on the ANSYS-CFX code. The aim

of this is only to see the importance of the pressure discrepancies and vortex presence from a qualitative point of view.

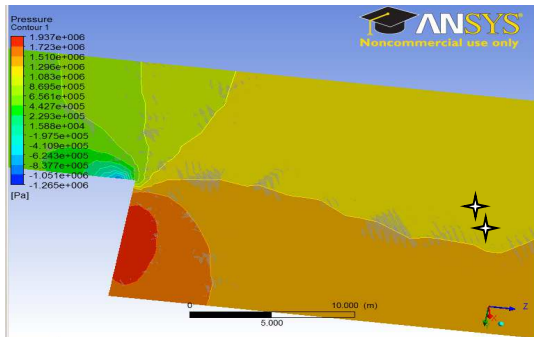


Figure 2: pressure and vortices in the wake of the building

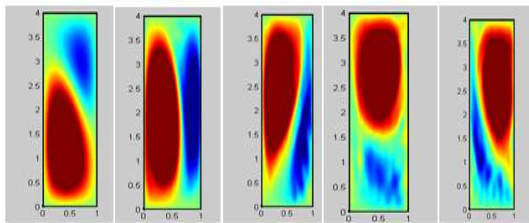


Figure 3: Presence of vortices at different time intervals using Matlab code

The pressures are measured at the two points illustrated by stars in figure 2 at different time intervals in both the CFD based and Matlab based codes. The results are illustrated in table 3.

First of all, we note that both the Matlab code pressure results and the CFD generated pressure results are very close. This is quantitatively supported by extracted results illustrated in table 3. This firmly supports the validity of our tool in transient modeling. Furthermore, we note that, on average the Matlab code generates results which are larger than those generated by our CFD tool. This was expected as our Matlab code did not cater for dissipative terms such that a slight over prediction of pressure was anticipated. The dissipative terms suppress the tendency for odd and even point decoupling and prevent the appearance of wiggles in regions containing severe pressure gradient.

Table 3: Pressure at different points by Matlab model

Time (s)	Pressure at point 1 obtained via ANSYS (Pa)	Pressure at point 1 obtained via Matlab (Pa)	Pressure at point 2 obtained via ANSYS (Pa)	Pressure at point 2 obtained via Matlab (Pa)
0	1010000	1333200	1010000	1515000
0.5	1240071,84	1785703,45	1240071,84	1612093,39
1	660434,411	911399,488	631188,675	315594,338
1.5	1311049,67	1586370,1	1311049,67	1678143,57
2	902158,002	1055524,86	893135,608	1178939
2.5	872802,857	1152099,77	872802,857	1056091,46
3	1326296,02	1685722,24	1352758,32	2029137,48
3.5	666624,617	859279,131	666624,617	791283,42
4	1215420,24	1391899,26	1232606,33	1599923,01
4.5	1041264,84	1500670,89	1041264,84	1468183,43
5	757076,719	1022053,57	735916,377	838944,67

7. TRANSIENT MODEL ANALYSIS ON THE WHOLE CITY USING WINDMODELLER IN BOUNDARY CONDITIONS DEFINITION

The previous sections of this article have pondered on the importance and relevance of making dynamic aerodynamic over large structures in an attempt to evaluate risks of aeroelastic effects and other dynamic hazards. The aim of this study is to verify the ability of CFD models to predict pressure distributions for different wind flow regimes over large structures so as to better support the implementation of reliability factors and insurance policies. A CFD tool has been developed at the WERL to predict such. The article, has till now focused on specific cases in an attempt to calibrate and validate the model. This achieved, we will now illustrate the model as such. The model can use both as input user defined winds (e.g. 5 ms^{-1}) or very accurate wind profiles defined using Windmodeller software. Windmodeller software has uses as boundary conditions velocities at different angles

defined at several particular altitudes. The software then models the velocity profile while taking into account, thermal stratification, the topography, roughness and canopy. In modeling the pressure and velocity distribution in a particular city, it is interesting to use as boundary condition, the velocity or velocities from a region of low velocity gradient and variability, for example having winds from the sea or large water systems where the velocity is quite constant. These velocities are used as boundary conditions in Windmodeller to model the wind profile in the vicinity of the city. The flow of the air is transported by the software till the city region and the output is a set of velocity profiles which can be then used in the CFD model to calculate the pressure and velocity field in the city. Figure 4 below shows the velocity input in a region of low wind variability in Windmodeller. These velocities will be transported into the inner circle as illustrated in figure 4 which represents the outskirts of the city. Therefore, the input boundary conditions of the city are, in fact, the output from Windmodeller which define high accuracy wind profiles that take into account the topography, roughness, canopy and thermal stratification.

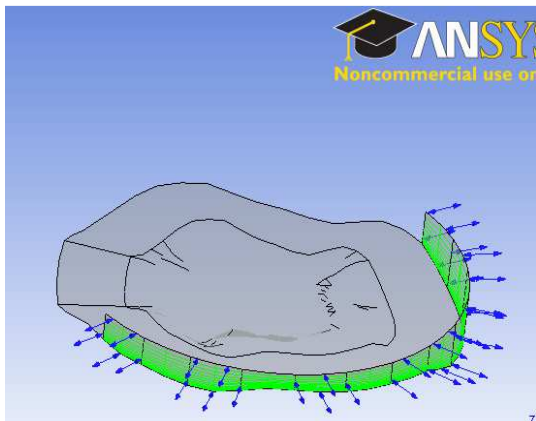


Figure 4: Boundary conditions treatment in Windmodeller

We used our model to simulate the pressure distribution around a hypothetical city comprising of 5 skyscrapers. We will present results of the modeling and discuss that intrinsic observed phenomena and improvements that need to be added to the CFD model.

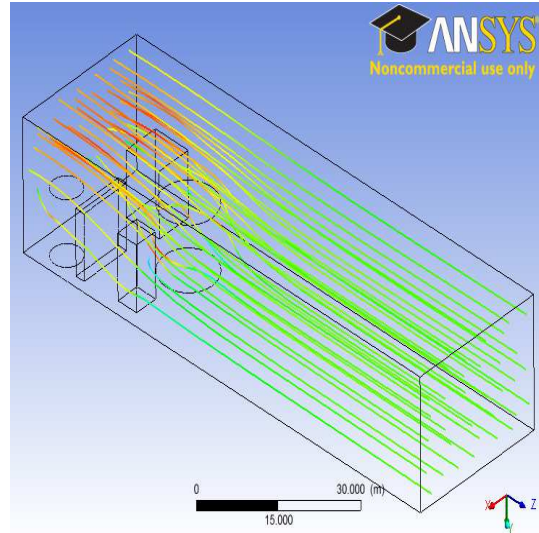


Figure 5: 3D modeling of the wind distribution over the hypothetical city

Figure 6 below shows velocity fields in different horizontal planes at different altitudes. From these illustrations, we can clearly see the variation of the velocity near the buildings, rapid retardation, general acceleration, corridor acceleration and wake phenomena.

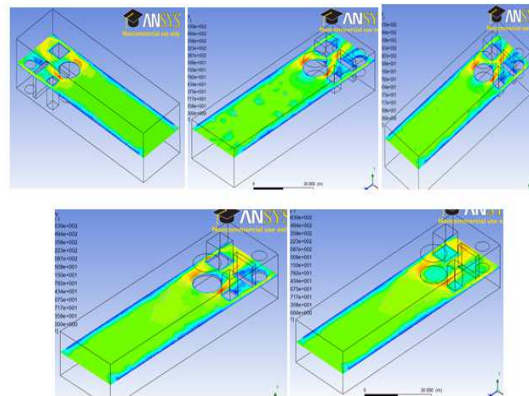


Figure 6: 3D modeling of the wind distribution over the hypothetical city at different horizontal planes

The different illustrations in figure 6 shows the wind velocity field for $t=5s$ at different altitudes. We observe that in all cases, we see acute corridor acceleration between the buildings.

These zones (red color) represent zones of low pressure and even negative pressure which can be dire for the cladding. Furthermore, we note a pressure disparity at different levels for the same horizontal coordinates. In case of intensive winds of high variability such pressure disparity may bring rapidly changing dynamic solicitations on the building and, in case of positive retroaction, cause flutter like events.

An analysis of the transient behavior of the wind was performed on a vertical plane passing through 2 skyscrapers at the same time. The idea behind was to see if there is a significant variation of the pressure distribution for a wind varying within Windmodeller boundary limits as follows: at $t=0$ s, $v=50$ kmh^{-1} , at $t=5$ s, $v=100$ kmh^{-1} and at $t=10$ s, $v=150$ kmh^{-1} . All the velocities have been entered at a reference height of 10 m and a direction along the length of the domain. The obtained pressure distribution profile is the same for the different velocities; however, the quantitative data are different. Therefore, only the pressure distribution illustration for $t=10$ s is shown in figure 7 to avoid redundancy.

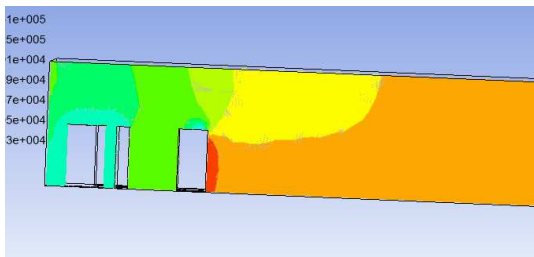


Figure 7: Pressure distribution on a vertical plane at $t=10$ s

We note from figure 7 that the pressure disparity between the front and the back of the building facing first the wind is quite important. This will create an appreciable torque on the structure. Rapidly changing wind direction, but with similar magnitude (in case of cyclones) will cause the torque to change direction very often and might lead to some positive retroaction of such movements.

8. CONCLUSION

In this article, we have proposed a CFD tool capable of simulating the pressure, velocity (and any other relevant parameters like turbulence intensity) fields. The importance of such modeling has been underlined and attributed to the need to better quantify the reliability and serviceability of structures when it comes to dynamic solicitations. This tool can be used to analyze the pressure distribution according to different winds and evaluate the loads and risks of failure or damage on cladding. In future work, we would like to extend this analysis to an aeroelastic one where the tool would be able to directly evaluate the structural response of the building according to the aerodynamic loads. Nowadays static models that use peak pressures are mostly used. This paper shows the possibility of using breakthroughs in wind modeling to better predict building serviceability and set a framework for insurance policies. However, this model only predicts the pressure distribution around the buildings but does not predict the dynamic and elastic behavior and response of the buildings when subjected to such pressure differences. In future work, the building should be designed with parameterized soil fixture, material properties and elastic nature and couple the purely fluid simulation with a structural simulated with ANSYS-CFX dual simulation.

REFERENCES

- [1] D.Ramdene et al. "Static, dynamic and spectral response of a suspended bridge under known solicitations" Processing, Performance and Failure Analysis of Engineering Materials conference, Luxor, Egypt. Nov 2011
- [2] Deaves D.M., Harris, R.I. (1978) A mathematical model of the structure of strong winds. Report No. 76. United Kingdom Construction Industry Research and Information Association.
- [3] D. Ramdenee et al. "Modeling wake effects on wind farm for inefficiency Assessment using computational fluid dynamics" ASME 2012 International Mechanical Engineering Congress & Exposition IMECE2012 November 9-15, 2012, Houston, Texas, USA
- [4] National Institute of Building Sciences (NIBS). 2006. Whole Building Design Guide.
- [5] National Weather Service (NWS). 2005. Tropical Cyclone Report for Hurricane Katrina. National Hurricane Center. December 20, 2005. 2006

- [6] FEMA. 2006. Recommended Residential Construction for the Gulf Coast: Building on Strong and Safe Foundations, FEMA 550. Publication available May .
- [7] Sachs, P., “Wind forces in engineering”. Pergamon Pres, 1978.
- [8] Saunders, J.W., and Melbourne, W.H., “Tall rectangular building response to cross-wind excitation”. Proc. 4th International Conference on Wind Effects on Buildings and Structures, Cambridge University Press, September 1975, pp. 369–379.
- [9] Saunders, J.W., and Melbourne, W.H., “Buffeting effects of upwind buildings”. 5th International Conference on Wind Engineering (Fort Collins), U.S.A. Pergamon Press, 1979.
- [10] Nathan Logsdon, Dr. Gary Solbrekken, A Procedure For Numerically Analyzing Airfoils And Wing Sections, doctoral diss., University of Missouri – Columbia, December 2006.
- [11] T. Tardif d’Hamonville, A. Ilinca Modélisation et Analyse des Phénomènes Aéroélastiques pour une pale d’Éolienne. Master s Thesis, UQAR/LREE
- [12] T. Tardif d’Hamonville, A. Ilinca. Modélisation de l’écoulement d’air autour d’un proil de pale d’éolienne, Phase 1: Domaine étude et Maillage. Rapport Technique, UQAR/LREE-05, Décembre 2008
- [13] T. Tardif d’Hamonville, A. Ilinca. Modélisation de l’écoulement d’air autour d’un proil de pale d’éolienne, Phase 2 : Modèles Turbulents. Rapport Technique, UQAR/LREE-06, Janvier 2009.
- [14] T. Tardif d’Hamonville, A. Ilinca. Dynamic stall and transitional turbulent model, Technical Report UQAR/LREE-05, Décembre 2008
- [15] ANSYS CFX, Release 11.0

THREE-DIMENSIONAL MULTI-BODY BOND GRAPH MODEL FOR VIBRATION CONTROL OF LONG SHAFTS – APPLICATION TO OILWELL DRILLING

D. Geoff Rideout^(a), Farid Arvani^(b), Stephen D. Butt^(c), Ehsan Fallahi^(d)

Advanced Drilling Group, Faculty of Engineering and Applied Science
Memorial University
St. John's, NL Canada A1B 3X5

^(a)g.rideout@mun.ca, ^(b)f.arvani@mun.ca, ^(c)sdbutt@mun.ca, ^(d)e.fallahi@mun.ca

ABSTRACT

During oilwell drilling, the long slender drillstring is susceptible to coupled lateral, axial and torsional vibrations that can reduce drilling efficiency and damage components. A bond graph model of an 80 metre drillstring collar section, subjected to bit-rock interaction boundary conditions and multiple lateral stabilizers, is created. Three-dimensional rigid lumped segments are connected by axial, torsional, shear, and bending springs. Thirty segments are sufficient to predict the lowest natural frequencies and static deflection accurately. An active lateral vibration controller is implemented, in which actuators and strain gauges are placed 90-degrees apart around the pipe walls, near the middle of the longest span. A proportional controller acting on the strain gauge output significantly attenuates vibration. The model structure allows easy reconfiguration of the drillstring geometry, boundary conditions, and actuator and sensor locations, to study the effect of any controller on coupled lateral, axial, and/or torsional vibration.

Keywords: multibody dynamics, bond graph, lumped segment, drillstring, lateral vibration control

1. INTRODUCTION

Drilling accounts for approximately 35% of all oil and gas exploration and production costs (CAPP, 2012). An estimated 2% to 10% of well drilling costs can arise from vibration-related problems, such as lost time while pulling out of hole, reduced rate of penetration (ROP), poor wellbore quality, and increased service cost because of the need for ruggedized equipment (Jardine et al., 1994). Figure 1 shows a schematic of a drillstring. The drill pipes form a long slender beam-like structure in tension. The bottom-hole assembly (BHA) consists of heavier pipes called collars, shock absorbers ("shock subs"), the bit, and possibly vibrating tools and measurement-while-drilling (MWD) tools for logging vibration levels and reporting orientation in deviated (non-vertical) wells. A "neutral point" between tension and compression is typically near the top of the BHA. Stabilizers provide low radial clearance at certain points, potentially creating multiple

spans for lateral vibration. Stabilizers are typically modeled as pinned lateral boundary conditions.

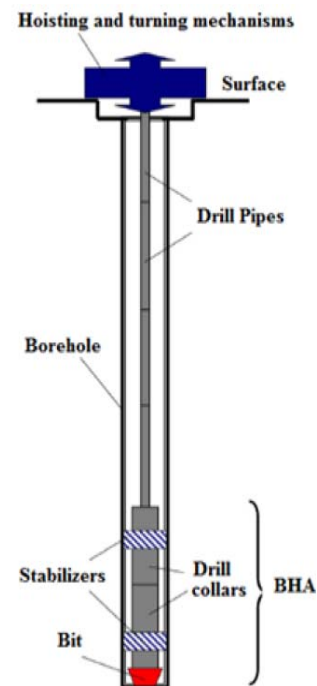


Figure 1: Drillstring Schematic (Khulief et al., 2007)

Potentially destructive vibration can occur axially, torsionally, or laterally. The most severe manifestations of these are, respectively,

- bit bounce where the bit comes off bottom despite weight on bit (WOB) from collars
- stick slip where the bit alternately stops and overspeeds
- severe lateral forward or backward whirl with wellbore contact

While many approaches to drillstring modeling have been pursued, there are few models that can capture axial, torsional and lateral vibration without prohibitively high computation time. Most models capture a subset of the three types of vibration, and may

neglect coupling. Control design is typically done on overly simple models. Verifying the performance of the controller by including sensors and actuators in a more complex finite element or modal expansion model can be difficult. This paper presents a physically intuitive multibody bond graph model that predicts three-dimensional drillstring (or any other long shaft) vibratory motion, and into which a controller and associated components can be easily added. A simple lateral vibration controller, effected by axial force actuators, is demonstrated.

2. LITERATURE REVIEW

Active control of drillstring vibration is an emerging research area. Linear quadratic regulator (LQR) control of torsional vibration has been simulated by Yigit and Christoforou (2006) and Sarker et al. (2012), with torsional control action having a positive effect on axial vibration. Lumped segment models with axial and torsional degrees of freedom, coupled through a bit-rock interaction model, were used. Stick-slip control has been simulated using robust μ -synthesis (Karkoub et al., 2010), H_∞ control (Serrarens et al., 1998), genetic algorithms (Karkoub et al., 2009), torque estimators (Pavkovic et al., 2011), and modeling error compensation-based control (Puebla and Alvarez-Ramirez, 2008). These controllers were designed using simple two-mass torsional pendulum models.

Many such controllers have practical limitations, most notably the difficulty in measuring states such as instantaneous bit speed. While measurement-while-drilling (MWD) tools exist for recording accelerations, force and torque near the bit, there is no reliable and cost-effective means for delivering this information, at a suitable sampling frequency, to a controller at the surface. A "Soft Torque Rotary System" (Jansen and Van den Steen, 1995), which has been adopted by industry, controls top drive speed to absorb torsional waves, based on torque feedback. Rotary vibration control is most common in industry because of the relative ease of detecting torque fluctuations at the surface. Active lateral and axial control is not currently done. In other applications such as bridges (Younesian et al., 2010) and cantilever beams (Ahmadabadi and Khadem, 2012), lateral vibration has been suppressed by elements such as nonlinear energy sinks; however, the structures are not rotating shafts. In drilling, lateral vibration control is done indirectly, through control of parameters such as rotary speed to avoid lateral resonance frequencies.

The rotating shaft can be modeled using simple one-dimensional decoupled lumped-segment or modal expansion approaches (Karnopp et al., 2006) for axial, torsional, and lateral motion. While axial-torsional coupling can be done through bit-rock interaction models, the coupling of lateral vibration to axial and torsional is more difficult. Energy methods (Lagrangian, Hamiltonian) have been used to analytically determine equations of motion, which have been solved with approximate methods (Yigit and

Christoforou, 1996, Ghasemloonia et al., 2012). Reconfiguring such models for different and new boundary conditions (e.g., more spans between stabilizers), and new discrete components such as vibrating tools, shock absorbers, and actuators is neither obvious nor trivial. Finite element models, for example (Ghasemloonia et al., 2013, Khulief and Al-Naser, 2005), can be more easily reconfigured, but typically exhibit high computation times and are not suited to prediction of closed-loop dynamic response.

This paper describes a bond graph model in which three-dimensional rigid lumped segments are connected by axial, torsional, shear, and bending springs. The model is demonstrated to capture coupled axial, lateral and torsional vibrations at the appropriate natural frequencies. Boundary conditions, including wellbore contact, location of stabilizers, and bit rock force or displacement can be reconfigured. The bond graph formalism and modeling approach allow straightforward inclusion of actuator or sensor submodels. Implementation of a controller directly on to the bond graph is done in commercial software. A lateral vibration suppression controller case study is presented.

3. MODEL DESCRIPTION

The drillstring is represented as a sequence of cylindrical rigid bodies joined by spherical joints with three translational and rotational compliances, as shown in Figure 2. Springs " k_{bend} " are rotary springs about the body-fixed x and y axes of body $i+1$, " k_{tors} " is a rotary spring about body-fixed z , " k_{axial} " is a translational spring in body-fixed z , and " k_{shear} " are translational springs in body-fixed x and y . The torsional and bending springs are shown separately in the right portion of the figure, and one shear spring is not shown for clarity; however, all springs exist at the joint between point B on body i and Point A on body $i+1$.

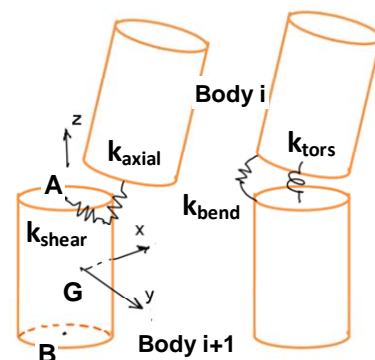


Figure 2: Successive Multibody Segments

Stiffness values are computed for a segment length $\Delta x = L/n$ of a string of length L with n segments, using basic solid mechanics theory, as follows (Karnopp et al., 2006):

$$\begin{aligned}
k_{\text{axial}} &= EA/\Delta X \\
k_{\text{torsion}} &= GJ/\Delta X \\
k_{\text{bend}} &= EI/\Delta X \\
k_{\text{shear}} &= \kappa AG/\Delta X
\end{aligned}
\quad (1-4)$$

where E is elastic modulus, A and I are cross-sectional area and area moment, G is modulus of rigidity, J is polar moment of area, and κ is a parameter accounting for non-uniform shear across a cross section.

3.1. Bond Graph of Segments and Joints

The Euler Junction Structure is used, representing the following equations governing the dynamics of bodies undergoing large motions (Karnopp et al., 2006):

$$\Sigma^0 \bar{F} = d/dt (\bar{m}^0 \bar{v}_{Gi}) = \bar{m}^0 \dot{\bar{v}}_{Gi} \quad (5-6)$$

$$\Sigma^i \bar{M} = d/dt (\bar{J}^i \bar{\omega}_i) = \bar{J}^i \dot{\bar{\omega}}_i + {}^i \bar{\omega}_i \times \bar{J}^i \bar{\omega}_i$$

where G is the mass centre, left superscript θ indicates vectors resolved into inertial frame components, and i indicates vectors (in this case, absolute velocities) resolved along body-fixed frame i . The translational equations are expressed in frame θ to facilitate application of the gravity vector. The first term on the right hand side of the rotational equation is an inertial term, and the second term gyrational. The hinge point A velocity is defined as follows (B is defined similarly):

$${}^1 \bar{v}_{Ai} = {}^1 \bar{v}_{Gi} + {}^1 \bar{v}_{Ai/Gi} \quad (7-8)$$

$${}^1 \bar{v}_{Ai/Gi} = {}^i \bar{\omega}_i \times {}^i \bar{r}_{Ai/Gi} = {}^i \tilde{r}_{Ai/Gi} {}^i \bar{\omega}_i$$

where ${}^i \bar{r}_{Ai/Gi}$ is the position vector from G to A , and ${}^i \tilde{r}_{Ai/Gi}$ is a skew-symmetric matrix containing the relative position vector components.

Figure 3 is a top-level vector bond graph (Breedveld, 1985) representation of the above equations. Note the modulated transformer representation of Eq'n (8). Cardan orientation angle (rotations ψ , θ , ϕ about body fixed z , y , x) rates are calculated, integrated, and used to create rotation matrices between body-fixed and inertial coordinate frames according to the following equations:

$$\begin{aligned}
\dot{\theta} &= \cos \phi \omega_y - \sin \phi \omega_z \\
\dot{\psi} &= \frac{\sin \phi}{\cos \theta} \omega_y + \frac{\cos \phi}{\cos \theta} \omega_z
\end{aligned}
\quad (9-11)$$

$$\dot{\phi} = \omega_x + \sin \phi \frac{\sin \theta}{\cos \theta} \omega_y + \cos \phi \frac{\sin \theta}{\cos \theta} \omega_z$$

Orthogonal rotation matrices transform vector components as follows:

$${}^0 \bar{v} = R_i^0 {}^i \bar{v}, {}^i \bar{v} = R_0^i {}^0 \bar{v}, R_0^i = [R_i^0]^T \quad (12)$$

The rotation matrix, as a function of Cardan angles, is:

$$R_i^0 = \begin{bmatrix} c_\theta c_\psi & -c_\theta s_\psi & s_\theta \\ c_\phi s_\psi + s_\phi s_\theta c_\psi & c_\phi c_\psi - s_\phi s_\theta c_\psi & -s_\phi c_\theta \\ s_\phi s_\psi - c_\phi s_\theta c_\psi & s_\phi c_\psi + c_\phi s_\theta c_\psi & c_\phi c_\theta \end{bmatrix} \quad (12)$$

where “ c ” and “ s ” represent \cos and \sin respectively.

Figure 4 shows a joint submodel in which the relative velocity between point B and A on successive bodies is calculated in the Body $i+1$ -fixed frame. The multiport C and R elements have a diagonal stiffness matrix to model the stiffnesses described in Eq'ns (1-4), and a viscous material damping matrix tuned to give a reasonable damping ratio in the first mode.

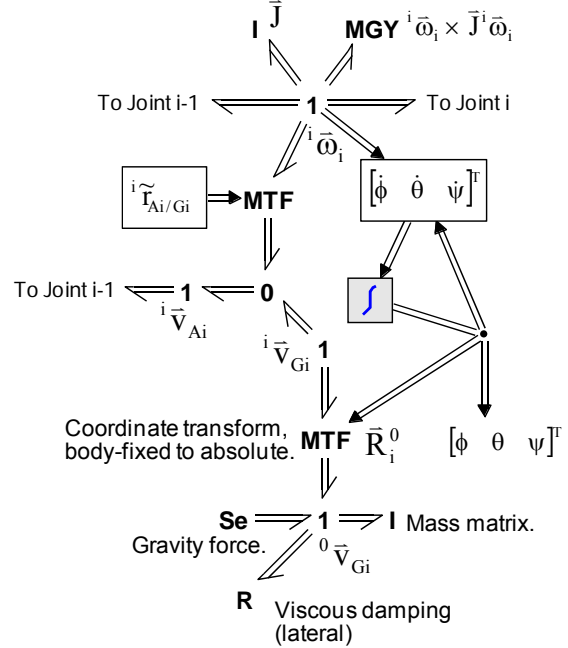


Figure 3 – Body i Bond Graph

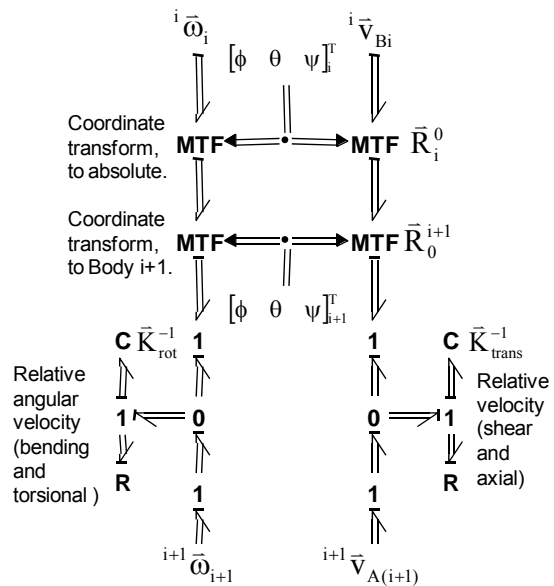


Figure 4 – Joint i Bond Graph

The 80-m collar section under study is very similar to the schematic shown in Figure 1. The top is constrained axially and laterally with stiff translational springs, and a rotational speed increasing from 0 to 20 rad/s over 1 second is prescribed. Stabilizers are modeled via stiff lateral constraint springs at the bit, and 26.67 m above the bit. A 3 mm sinusoidal axial bit displacement boundary condition is applied, at a frequency equal to rotational speed. The pipe is divided into 30 segments of equal length.

3.2. Modeling Wellbore Contact

Use of lumped segments, rather than energy methods, simplifies the inclusion of wellbore contact. Assuming a radial clearance of 2 cm between the collars and wellbore, stiff springs with discontinuous constitutive laws provide no effort until the radial deflection exceeds 2 cm at Bodies 11 and 26, which are at the middle of their respective spans and thus most likely to collide with the borehole. The velocities of points G_{11} and G_{26} are expressed in the inertial frame, and integrated to determine their position and then angle, so that the wellbore contact spring force can be directed along that angle. The spring is linear, with an arbitrary high stiffness value of 10^7 N/m. This value can be refined, given knowledge of the specific rock type for uncased wells, or using contact mechanics models of steel-on-steel for wells with a steel casing sleeve surrounding the drillstring. The contact model does not include rubbing friction. Future work will add such friction in addition to elastic restoring force, so that forward and backward whirl can be predicted. Detection of wellbore contact and computation of force and angle are done using the following equations.

$$\delta = \sqrt{X^2 + Y^2}$$

$$\phi = \tan^{-1}(Y/X) \quad (14-17)$$

$$F = k_w(\delta - \delta_0)$$

$$F_x = F \cos \phi, F_y = F \sin \phi$$

where δ is radial deflection, δ_0 is maximum wellbore clearance, X and Y are absolute coordinates of the centre of gravity, F and k_w are contact force and stiffness, and ϕ is angle between the wellbore centre and the inertial X axis. See Figure 5.

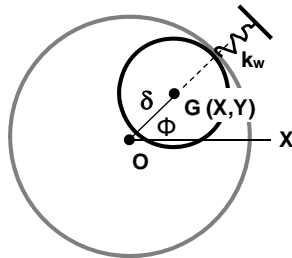


Figure 5 – Wellbore Contact Schematic

3.3. Modeling Sensors and Actuation

Strain on the outer surface of the pipe is assumed to correlate to bending stress, and is thus used as the input to the lateral vibration controller. Two pairs of actuators are modeled at the midpoints of the two spans. Figure 6 shows actuators that work as follows: positive tensile strain at point C results in the controller applying a compressive force to expand the distance between points D on adjacent bodies. An equal and opposite tensile force is applied at points C to create a moment about body-fixed y that opposes bending stress. Similarly, actuators at E and F will create a moment in response to strain at E .

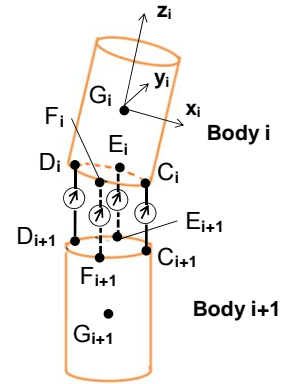


Figure 6 – Actuator Location Detail

Strain at C is assumed proportional to the state (torsional deflection) of the bending spring component in the body-fixed y direction as shown in Figure 7. Lateral vibration-induced strain is assumed to be much larger than axial deformation strain.

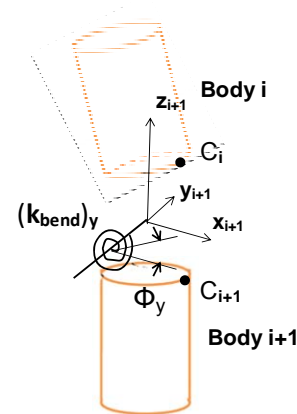


Figure 7 – Tensile Strain Computed at Points C

Combining Hooke's Law, Eq'n (3), and the relation between bending moment and beam curvature, the proportionality constant between spring state and strain is derived.

$$\varepsilon = \frac{\sigma}{E} = \frac{Mr}{EI} = \frac{r}{EI} \left(EI \frac{d\phi}{dx} \right) \quad (18)$$

4.1. Controller Performance

Actuators are placed near the midpoints of both the long and short spans. Figure 11 compares the onset of lateral vibration at the long span midpoint with and without the controller. The upper plot is uncontrolled, showing vibration peaking at 15 mm radial displacement and arriving at a steady-state level of approximately 8 ± 5 mm. The middle plot is with the high-gain proportional controller that allows each actuator to apply unlimited compressive or tensile forces. The unrestricted actuator force approaches 5000 N, with low power requirements as shown in Figure 12. A simulated actuator that could only generate compressive forces, and is restricted to 5000 N, generates the vibration shown in the lower plot of Figure 11. Figure 13 compares power output for the unrestricted and restricted actuators. The actuators must provide power equal to the magnitude of the values in Figure 13 (negative power refers to effort and velocity in opposite directions). The model indicates that restricting actuation direction and peak force significantly decreases control effect while increasing power requirements. Results for actuators *C-D* are shown, but actuators *E-F* behave similarly.

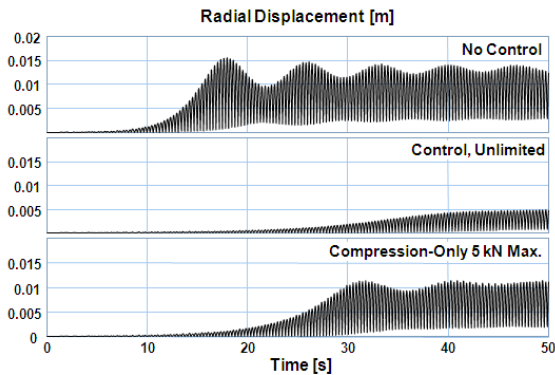


Figure 11 – Open- and Closed-Loop Vibration Levels, System Starting From Rest

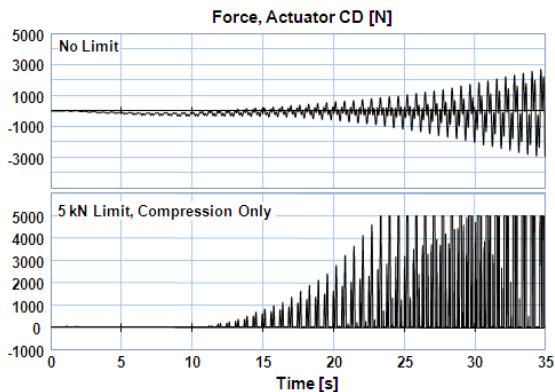


Figure 12 – Actuator Force

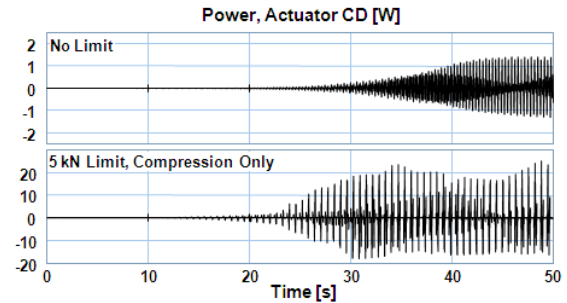


Figure 13 – Actuator Power

If the controller is switched on during steady-state uncontrolled vibration, the radial deflection of both spans is reduced as shown in Figure 14. Top span vibration is reduced, strain is dramatically reduced, actuator power peaks at a higher value of 400 W compared to when control is initiated at startup; and peak actuator force (not shown) is 26 kN. Radial deflection of the bottom span is reduced slightly, but is small even without control.

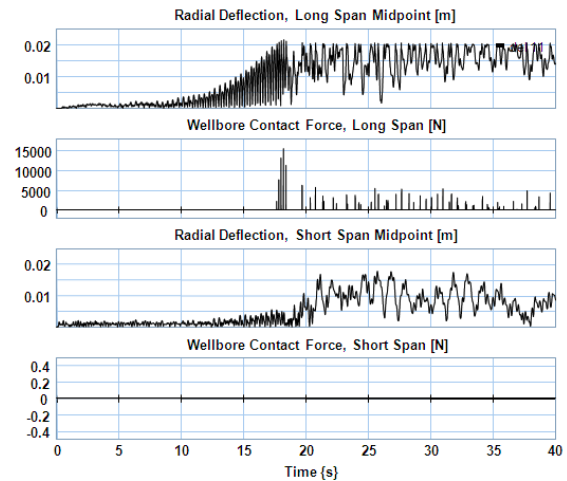


Figure 14 – Controller Switched On After 25 Seconds

4.2. Discussion

The use of only two actuators, one on each span, results in high proportional gains and very few actuation sites. While the controller is stable for the scenarios shown, it exhibits instability when actuator delays are introduced. Lowering gains to 10^6 restores stability, but control benefit is lost. Figure 14 shows that vibration is not reduced in proportion to strain near the actuator, when only one actuator per span is used. This underactuation means that it is possible to reduce strain, say at point *C* in the middle of the long top span, to zero without restoring the radial position of the cross section to the middle of the wellbore. The actuator can create a local region of zero bending in a pipe section that is pressed against the wellbore, and subjected to rubbing and repeated collision forces. Figure 15 shows such behavior when the controller is switched on during a more severe vibration than in Figure 14. Figures 15 and 16 show repeated and prolonged excursions of the pipe

to the wellbore wall for both spans, and no reduction of vibration despite reduction of strain. More actuation sites, with lower gains, are suggested by the model in order to stably control lateral motion using strain feedback.

The separate controllers for the two orthogonal lateral directions are, in this preliminary study, single input-single output. More sophisticated controller design would require a study of the coupling between the orthogonal modes and the potential benefits of a multiple-input approach to the design and tuning of each controller.

A three-dimensional model, as opposed to a planar model, is necessary for exploratory simulations of the potential of a vibration suppression system such as the strain-based proportional feedback controller. Axial and lateral vibrations could be studied in a decoupled manner by simple modal expansion or lumped segment models, and a multibody approach could be done much more simply with motion restricted to a single lateral plane, to simulate strain-feedback actuation. However, the rotation of a drillstring or similar shaft introduces centrifugal excitations and moves the actuators in and out of a given lateral plane. The model described herein is a physically intuitive and easily-reconfigured representation of a rotating beam with the required three dimensions.

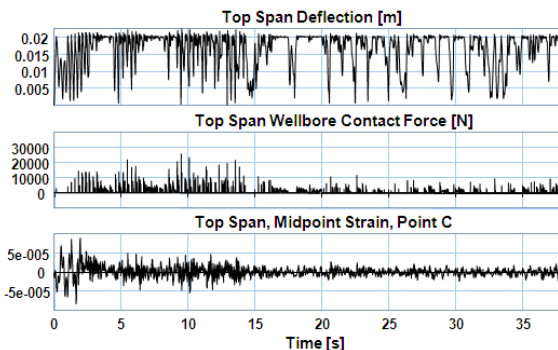


Figure 15 – Controller Pushing Pipe into Wellbore, Top Span

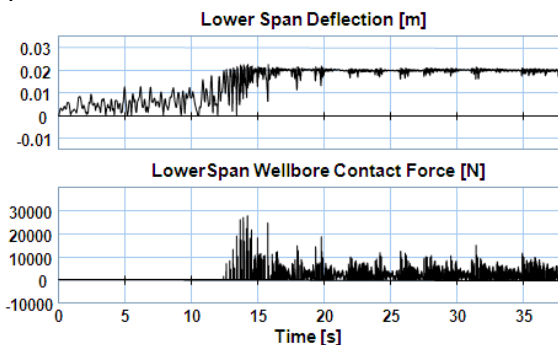


Figure 16 – Controller Pushing Pipe into Wellbore, Top Span

5. CONCLUSIONS AND FUTURE WORK

A rotating shaft, in this application an oilwell drillstring, has been modeled using a succession of rigid

bodies moving in three dimensions and constrained by shear, torsional, bending, and axial stiffness elements. Thirty segments are used to model a two-span rotating beam with a bit-rock displacement axial boundary condition, rotating unbalance, and contact with an exterior surface (wellbore) at the midpoint of each span. The model is useful not only for predicting coupled axial, torsional, and lateral vibrations due to unbalance or external excitation, but also for preliminary design and implementation of vibration controllers. Mid-span strain gauges and actuators are simulated, with high-gain proportional feedback showing potential for vibration suppression. The model indicates that more than two actuation sites are required, to prevent the actuators from locally straightening the shaft to eliminate bending strain without reducing lateral deflection. The model is easily reconfigurable to study alternate control strategies such as active unbalance masses that could apply transverse control forces more directly. Future work will be directed towards more robust control using these two approaches, as well as validating the model against finite element models and measured data from actual oil wells. Important model extensions include sliding friction from wellbore contact, fluid friction, and a bit-rock interaction submodel to predict axial displacement and reaction torque with higher fidelity.

ACKNOWLEDGEMENTS

This work was done at the Advanced Exploration Drilling Technology Laboratory at Memorial University in St. John's, Canada. Financial support was provided by Husky Energy, Suncor Energy, Newfoundland and Labrador Research and Development Corporation, and Atlantic Canada Opportunities Agency under AIF contract number 781-2636-192049.

REFERENCES

- Ahmadabadi, Z. N., and Khadem, S.E., 2012. Nonlinear vibration control of a cantilever beam by a nonlinear energy sink. *Mech. and Machine Theory*, 50, 134-149.
- Breedveld, P.C., 1985. Proposition for an unambiguous vector bond graph notation. *Journal of Dynamic Systems, Measurement and Control*. 104 (3), 267-270.
- Canadian Association of Petroleum Producers (CAPP), 2012. *Compiled Industry Statistics 1981-2011*.
- Ghasemloonia, A., Rideout, D. G., and Butt, S. D., 2012. Coupled Transverse Vibration Modeling of Drillstrings Subjected to Torque and Spatially Varying Axial Load, *Journal of Mechanical Engineering Science (IMEchE, Part C)*. 227 (5), 946-960.
- Ghasemloonia, A, Rideout D. G. and Butt, S. D., 2013. Vibration Analysis of a Drillstring in Vibration-Assisted Rotary Drilling: Finite Element Modeling With Analytical Validation. *ASME Journal of Energy Resources Technology*, 135 (3).

- Jardine, S., Malone, D., and Sheppard, M., 1994. Putting a Damper on Drilling's Bad Vibration, *Oilfield Review*, 6 (1), January.
- Jansen, J.D., and Van den Steen, L., 1995. Active Damping of Self-Excited Torsional Vibrations in Oil Well Drillstrings. *Journal of Sound and Vibration*, 179 (4), 647-668.
- Karkoub, M., Abdel-Magid, Y. L., and Balachandran, B., 2009. Drill-string Torsional Vibration Suppression Using GA Optimized Controllers. *Journal of Canadian Petroleum Technology*, 48 (12), 32-38.
- Karkoub, M., Zribi, M., Elchaar, L., and Lamont, L., 2010. Robust μ -Synthesis Controllers for Suppressing Stick-slip Induced Vibrations in Oil Well Drill Strings. *Multibody System Dynamics*, 23 (2), 191-207.
- Karnopp, D.C., Margolis, D. L., & Rosenberg, R. C., (2006). *System Dynamics; Modeling and Simulation of Mechatronics Systems*, 4th ed., New York: John Wiley & Sons, Inc.
- Khulief, Y. A., and Al-Naser, H., 2005. Finite Element Dynamic Analysis of Drillstrings. *Finite Element in Analysis and Design*, 41 (13), 1270-1288.
- Khulief, Y. A., Al-Sulaiman, F. A., and Bashmal, S., 2007. Vibration Analysis of Drillstrings with Self-excited Stick-slip Oscillations. *Journal of Sound and Vibration*, 299 (3), 540-558.
- Pavkovic, D., Deur, J., and Lisac, A., 2011. A Torque Estimator-based Control Strategy for Oil-well Drill-string Torsional Vibrations Active Damping Including an Auto-tuning Algorithm. *Control Engineering Practice*, 19 (8), 836-850.
- Sarker, M., Rideout, D.G., and Butt, S.D., 2012 "Advantages of an LQR Controller for Stick-Slip and Bit-Bounce Mitigation in an Oilwell Drillstring". *Proc. 2012 ASME International Mechanical Engineering Congress and Exposition, IMECE2012-87856*, November 9-15, Houston (Texas, USA).
- Serrarens, A. F. A., van de Molengraft, M. J. G., Kok, J. J., and van den Steen, L., 1998. H_{∞} Control for Suppressing Stick-slip in Oil Well Drillstrings. *Control Systems, IEEE*, 18 (2), 19-30.
- Yigit, A. S., and Christoforou, A. P., 1996. Coupled Axial and Transverse Vibrations of Oilwell Drillstrings. *Journal of Sound and Vibration*, 195 (4), 617-627.
- Yigit, A. S., and Christoforou, A. P., 2006. Stick-slip and Bit-bounce Interaction in Oil-well Drillstrings. *Journal of Energy Resources Technology*, 128 (4), 268-274.
- Younesian, D. et al., 2010. Application of the Nonlinear Energy Sink Systems in Vibration Suppression of Railway Bridges. *Proc. ASME 10th Biennial Conf. on Eng. Sys. Design and Analysis*, July 12-14, Istanbul (Turkey).

AUTHORS' BIOGRAPHIES

Geoff Rideout received his B.Eng. (Mechanical) from Memorial University of Newfoundland in 1993. After working in telecommunications equipment manufacturing and building systems consulting, he earned his M.A.Sc. in Mechanical Engineering from Queen's University in Kingston, Ontario and his Ph.D. in Mechanical Engineering from the University of Michigan. He has lectured at the University of Michigan and at the Humber Institute for Advanced Technology and Applied Learning in Toronto. He is currently Associate Professor at Memorial University, teaching mechanics, modeling, and design. His research areas are automated modeling, vibration-assisted drilling, vehicle dynamics and control, and modal testing for nondestructive evaluation.

Farid Arvani received his B.Sc. degree in Mechanical Engineering from University of Tabriz in 2003. He was actively involved in design and development of test facilities for condition monitoring and fatigue testing for the automotive industry for four years. He received his M.Eng degree in Mechanical Engineering from Memorial University of Newfoundland in 2009. He is currently a Ph.D. candidate and the Managing Engineer in the Advanced Drilling Project, an industry-driven research project at Memorial University focusing on the design and development of state-of-the-art technologies for the drilling industry.

Stephen D. Butt has B.Eng. and M.Sc. degrees from Memorial University of Newfoundland, a Ph.D. from Queen's University in Kingston, Canada, and is a registered Professional Engineer. From 1996 to 2006, he was a faculty member in the Faculty of Engineering at Dalhousie University, and has been a faculty member in Faculty of Engineering and Applied Science at Memorial University of Newfoundland from 2006 to the present, where he is currently Professor and Process Engineering Chair. He has held past administrative positions, including Mining Program Chair at Dalhousie University and Associate Dean at Memorial University. His research activities are in the area of drilling engineering, geomechanics and the development of geophysical imaging technology for various applications in petroleum, mining and civil engineering..

Ehsan Fallahi received his Bachelor's degree in Mechanical Engineering from Sharif University of Technology in Iran in 2010. His research interests are multibody dynamics and vibration problems in drilling. He is currently finishing his Master's degree in Oil and Gas Engineering at Memorial University.

TUNING THE POSITION OF A FUZZY COGNITIVE MAP ATTRACTOR USING BACKPROPAGATION THROUGH TIME

Michal Gregor^(a), Peter P. Groumos^(b)

^(a)Department of Control and Information Systems, Faculty of Electrical Engineering, University of Žilina

^(b)Laboratory for Automation and Robotics, Department of Electrical and Computer Engineering, University of Patras

^(a)michal@gregor.sk, ^(b)groumos@ece.upatras.gr

ABSTRACT

The paper proposes a new learning method for fuzzy cognitive maps, which makes it possible to encode an attractor into the map. The method is based on the principle of backpropagation through time known from the theory of artificial neural networks. Simulation results are presented to show how well the method performs. It is shown that the results are superior to those achieved using Hebbian learning approaches such as nonlinear Hebbian learning. Some lines for possible future research and development are given.

Keywords: fuzzy cognitive maps, learning, backpropagation.

1. INTRODUCTION

Fuzzy cognitive maps (FCMs) represent a well recognized method in the theory of soft computation. They exhibit several noticeable traits, which make them similar to artificial neural networks (ANNs). More specifically the FCM can be considered as a distinct type of a single-layer recurrent neural network with synchronous activation of units.

Some learning methods from the theory of ANNs have been introduced into the theory of FCMs before. Most notable among these approaches is a family of methods based on Hebbian learning.

The paper will present a new method for encoding an attractor state into an FCM using the principle of backpropagation through time. The theoretical background of the method will be outlined hereinafter, and results of several simulation experiments will be presented as well as their evaluation and discussion of possible future lines of research.

2. DELTA RULE AND BACKPROPAGATION

Let us in this section cover some of the basic theory of supervised error correction learning in artificial neural networks (ANNs). It will later be shown how ANNs are related to fuzzy cognitive maps (FCMs), and how this theory may find applications there.

2.1. Artificial Neuron

In order to set down how the learning method works, let us first with all due brevity give a basic definition of

what we mean by the artificial neuron, and by artificial neural networks in general.

An artificial neuron is a structure, which has (a) its set of inputs $X = \{x_1, x_2, \dots, x_n\}$, (b) a set of weights corresponding to the inputs $W = \{w_1, w_2, \dots, w_n\}$, (c) its threshold Θ , its squashing function f (which is perhaps most often the sigmoid function, or the hyperbolic tangent) (Krose and Smagt 1996). The illustration is given in Figure 1.

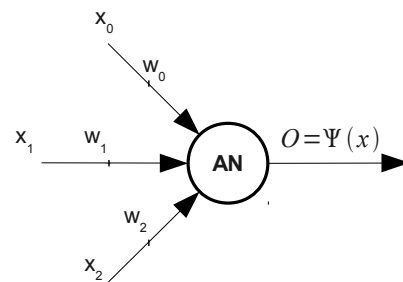


Figure 1: Unwrapping a recurrent network

The output of the neuron is determined in the following fashion (Krose and Smagt 1996):

$$O = f(u - \Theta) = f\left(\sum_{i=1}^n (w_i x_i) - \Theta\right), \quad (1)$$

where u is the inner potential of the neuron.

Furthermore, in order to simplify derivation of the learning rules, the threshold value Θ is often interpreted as a bias received from a neuron with the constant output of 1 – thus the threshold value does not have to be considered separately, and its value can be learned in the same way as the weights of the inputs.

By an artificial neural network (ANN) we simply understand a collection of mutually interconnected artificial neural networks.

2.2. The Delta Rule

The delta rule is probably the best known approach (based on error correction) to learning weights of an artificial neuron. It has been designed for supervised learning – that is to say learning from a dataset

consisting of pairs of the following form: (*input, desired output*). In other words, for every sample's input in the dataset, its corresponding desired output is specified as well.

This allows formulation of an error function (Krose and Smagt 1996):

$$E(W) = \sum_p E^p(W) = \frac{1}{2} \sum_p (D^p - O^p)^2, \quad (2)$$

where D^p and O^p denote the desired and the real output for input pattern p .

Once such error function has been formed, the idea behind delta rule is to do gradient descent minimization with respect to the weights, thus bringing the real output as close to the desired output as possible. For linear neurons (neurons with no squashing function) the following rule – known as the delta rule – has been derived (Krose and Smagt 1996):

$$\Delta_p w_j = \gamma \delta^p x_j, \quad (3)$$

where $\Delta_p w_j$ denotes the prescribed change of weight w_j due to pattern p , γ is the learning rate, and:

$$\delta^p = D^p - O^p. \quad (4)$$

The delta rule can be generalized for non-linear neurons as well, in which case it contains the derivative of the squashing function f' (Krose and Smagt 1996):

$$\delta^p = (D^p - O^p) f'(u^p), \quad (5)$$

where u^p is the inner potential of the neuron with pattern p at the input.

2.3. The Backpropagation Principle

The delta rule cannot by itself be used for learning in multi-layer networks, because only the errors of the output neurons can be computed directly using (3) or (4) – desired outputs of hidden neurons remain unspecified.

However, the delta rule can be generalized to multi-layer networks using the backpropagation principle.

In this case the error is propagated back from the output layer to hidden layers. Again, the full derivation of the rule can be found in (Krose and Smagt 1996). The rule itself can be stated as follows:

$$\delta_h^p = F'(u_h^p) \sum_{o=1}^{N_o} \delta_o^p w_{ho}, \quad (6)$$

where h refers to a neuron of the hidden layer, and o refers to neurons of the output layer. N_o is the number of neurons in the output layer. If there are several hidden layers, the principle can be applied recursively.

2.4. Backpropagation Through Time

Backpropagation through time (BPTT) is a further extension of the principle to recurrent neural networks. Recurrent neural networks (RNNs) are networks in which signals may propagate from one time step to another (as opposed to feed-forward neural networks, which only propagate inputs from the current step and have no memory).

The idea is that an RNN can be unwrapped in time into a feedforward neural network, and then trained using backpropagation.

Figure 2 shows an example of unwrapping a single-layer recurrent neural network in 3 time steps, resulting in a feedforward neural network with 3 layers.

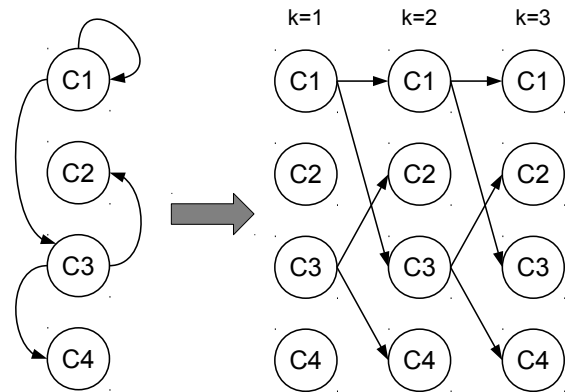


Figure 2: Unwrapping a recurrent network

For additional details and precise mathematical and algorithmic formulations the reader may refer to Werbos (1990). For the present purpose, what has already been said concerning backpropagation itself should suffice.

2.5. Vanishing/Exploding Gradients

The backpropagation principle faces significant problems when applied to deep neural networks. The same kind of problem is usually associated with RNNs using BPTT – because RNNs become deep themselves when unwrapped in time.

The problem that occurs is referred to as the vanishing/exploding gradients problem. When the errors are propagated back through the network, unlike the forward pass no squashing functions are applied. Depending on the values of the weights, the gradients tend to grow very small (*vanishing gradient*), or very large (*exploding gradient*) after they have been propagated through a number of layers (Sutskever, Martens, Hinton 2011).

However, lately some considerable advances in deep learning have been introduced through the work of Hinton, and Salakhutdinov (2006), and Bengio et al. (2007). These mainly advocate careful initialization of the weight matrix based on unsupervised pre-training.

An important breakthrough in the theory of deep learning has been marked by Martens (2010). The author has developed an application of Hessian-free optimization method to learning in deep networks. It

has later been shown that this approach can indeed be adapted for recurrent neural networks as well (Martens, and Sutskever 2011). Applications of the method have since begun to appear (Sutskever, Martens, Hinton 2011).

In consequence of these developments, the backpropagation principle has lately been experiencing a renaissance. Backpropagation coupled with Hessian-free optimization is now counted among the most promising tools for learning in both – deep neural networks and recurrent networks.

3. FUZZY COGNITIVE MAPS

Fuzzy cognitive maps (FCMs) are a symbolic representation for the description and modeling of complex systems (Groumpos 2010). They can be expressed and visualized using a weighted directed graph such as that shown in Figure 3.

The nodes of such graph represent the concepts associated with the system being modeled. The number and kind of concepts that form any particular FCM is determined by experts from the corresponding field of knowledge (Groumpos 2010). Every concepts C_i is associated with its activation value A_i . The activation values are most often taken from the interval $[0,1]$, or $[-1,1]$ (this depends on the particular squashing function used – see equation (7) for the context).

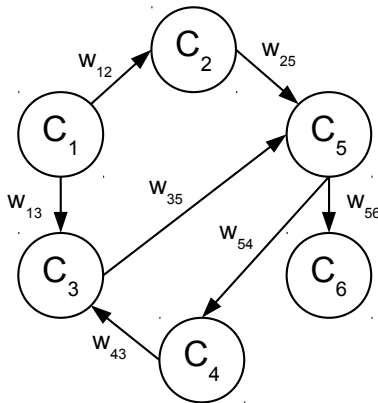


Figure 3: Fuzzy cognitive map – an example

The edges in the graph are directed and weighted. They express causal relationship between the concepts. An edge directed from concept C_i to concept C_j represents the knowledge that there is a causal link between C_i and C_j .

The weight of the edge going from C_i to C_j is denoted $w_{ij} \in [-1,1]$, and it specifies the strength of the causal link. If $w_{ij} > 0$, we can say that concept C_i causes C_j to some extent – it contributes positively to its activation value. If $w_{ij} < 0$, concept C_i has negative influence on the activation value of C_j . If $w_{ij} = 0$, there is no causal link at all (such edges are usually not drawn when the FCM is visualized).

At every time step the activation values of the concepts are updated. The update is synchronous. The update rule has several distinct forms. First of all there is the rule proposed in Kosko (1993) [the notation has been modified for the sake of consistency]:

$$A_i^{(k+1)} = f \left(\sum_{j=1}^N A_j^{(k)} w_{ji} \right), \quad (7)$$

where N is the number of concepts, $A_i^{(k)}$ is the activation value of concept C_i at time step k . f is the squashing function, which squashes the dot product $\sum_j A_j^{(k)} w_{ji}$ into some convenient interval.

Most often, f is either the sigmoid function, which squashes the dot product into interval $[0,1]$:

$$S(x) = \frac{1}{1 + e^{-x}}, \quad (8)$$

or the hyperbolic tangent, which yields the interval $[-1,1]$.

There are other forms of the rule. In some works, such as Groumpos and Stylios (2000) the feedback links from the concept to itself are removed:

$$A_i^{(k+1)} = f \left(\sum_{\substack{j=1 \\ j \neq i}}^N A_j^{(k)} w_{ji} \right). \quad (9)$$

In other versions, the feedback link is reintroduced, but the same weight is shared by all concepts (Groumpos and Stylios 2000):

$$A_i^{(k+1)} = f \left(k_1 \sum_{\substack{j=1 \\ j \neq i}}^N A_j^{(k)} w_{ji} + k_2 A_i^{(k)} \right), \quad (10)$$

where k_1 and k_2 are constants, such that $0 \leq k_1, k_2 \leq 1$.

Unless specified otherwise, we will adhere to the rule given in equation (7) in this work, because that is the most general one.

The weight matrix of the FCM is usually constructed by experts. There are several approaches which make the task easier and more reliable – for discussion of these, the reader may refer to Groumpos (2010), Stach, Kurgan, Pedrycz (2005a), or Stylios, Christova, and Groumpos (2002) for an instance.

It should also be noted that the FCM need not be acyclic. In the presence of cycles, the issue of stability naturally comes into mind. As mentioned in Dickerson, and Kosko (1993), the FCM will quickly settle down to a fixed point, to a limit cycle, or to a chaotic attractor (for illustration, see Figure 4).

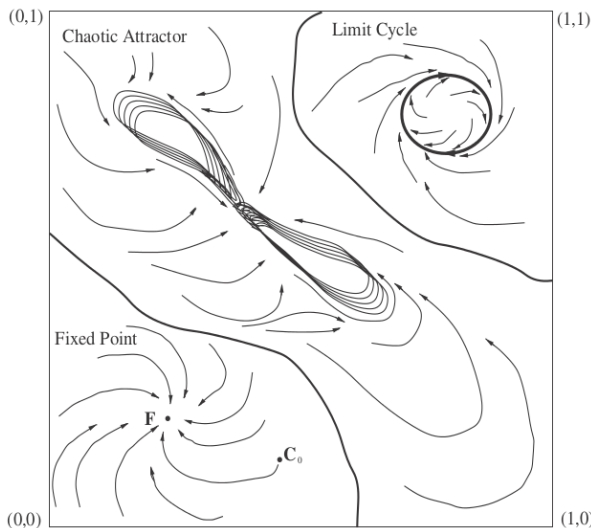


Figure 4: FCM attractors: fixed-point, limit-cycle, chaotic (Dickerson, and Kosko 1993)

3.1. The Relation between FCMs and Artificial Neural Networks

It is obvious that there is a close resemblance between the FCM model as described in equation (7), and the ANN model as shown in equation (1). More specifically, an FCM can be considered as a distinct type of a single-layer recurrent neural network with sigmoid squashing functions and synchronous activation of units.

The FCM can also be viewed as an extension of the concept of a Hopfield network to which its architecture bears several similarities. However, the analogy is not complete – there are several traits in which these differ. Most notably perhaps, the Hopfield network has been designed for binary (0 and 1) or bipolar (-1 and 1) activations, it uses the sign function as the squashing function, and its units are activated asynchronously. Also, the theory of learning developed for Hopfield is based on the concept of an energy function. The energy function derived for Hopfield networks requires that the weight matrix be symmetric (Krose and Smagt 1996), (Rojas 1996).

ANNs are notorious for their lack of interpretability. The knowledge they contain is implicit – it is sometimes called *procedural knowledge* for this reason.

In spite of their close relationship with ANNs, FCMs do not generally suffer from the same problem, because the knowledge they represent is modelled very explicitly. If the FCM is constructed by experts then it naturally follows that its dynamics are (by definition) well understood. Even in cases when one learning method or other is used to modify the weight matrix or to learn it from scratch, the inner workings of the resulting model typically remain transparent, due to the fact that every node is linked with a distinct concept.

Naturally, this feature is paid for by the fact that the FCM is not a universal approximator. To put this more precisely – if the concepts are linked by a more

complex relationship, which cannot be adequately represented using a single connection, the expert must explicitly provide all the auxiliary concepts required to express such relationship. In multi-layer artificial neural networks, neurons are not associated with particular concepts, and thus any of them is free to participate in modelling the relationship.

It may also be noted that – in contrast to ANNs (1), the FCM model (7) does not contain the threshold term. Thus, the absolute term of the linear relationship expressing the inner potential u is missing – if any given concept is to have some non-zero potential even though all of its input concepts have the activation value of zero, this is not possible to achieve unless an additional concept is added for that express purpose.

In any case, it should be obvious that there is a trade-off between the excellent interpretability of FCMs on one hand, and the ability of multi-layer ANNs to do universal approximation. Some work has been invested into creating hybrid models, which offer trade-off points closer to the conventional ANNs. Among these the fuzzy cognitive network of Kottas, Boutalis, and Christodolou (2007) can be mentioned, or the fuzzy neural network of Wang and Wang (2013) can be mentioned.

Furthermore, even though the concepts and weights of a conventional FCM are usually determined by experts, the close connection between the theory of FCMs and the theory of ANNs has been fuelling a promising line of research, which strives to bring some of the learning methods from the theory of ANNs to perform learning in FCMs. The next section covers some of the existing approaches.

3.2. Fuzzy Cognitive Maps and Learning

We have now covered some of the basic ideas and concepts associated with FCMs and their close relation to ANNs. In this section, we will consider the problem of learning the weight matrix of an FCM.

We note that there are two main classes of problems in the theory of FCMs, to which the existing learning methods apply: (a) *the regression problem*, that is to say how a fuzzy cognitive map can be trained as a regression model for a given dataset; (b) *the attractor problem*, that is to say given an initial fuzzy cognitive map, how can we shift a fixed-point attractor to a desired point, to encode a given limit-cycle, etc.

The most notable among the existing approaches inspired by the theory of ANNs are those based on Hebbian learning – to the description of these we now turn.

3.2.1. Differential Hebbian Learning

The first among the methods inspired by Hebbian learning is the so-called *differential Hebbian learning* (DHL) proposed by Dickerson and Kosko (1993). It introduces the following rule (notation modified for the sake of consistency):

$$\Delta w_{ij} = \begin{cases} c_t [\Delta A_i \Delta A_j - w_{ij}] & \text{if } \Delta A_i \neq 0 \\ 0 & \text{else} \end{cases}, \quad (11)$$

where $\Delta A_i(t) = A_i(t) - A_i(t-1)$, and c_t is the learning rate, which decreases in time. Dickerson and Kosko (1993) propose the following rule for c_t :

$$c_t(t_k) = 0.1 \left[1 - \frac{t_k}{1.1N} \right]. \quad (12)$$

A follow-up on this method can be found in Huerga (2002). The author shows that rule (11) has a considerable weakness in that it cannot encode some types of sequences correctly. If, for example, concept 4 should change its activation to 1 after concepts 1, 2, and 3 change their activations to 1, after learning is performed using DHL, concept 4 will react to any of the concepts, and not only to their simultaneous activation (Huerga 2002). The approach known as *balanced DHL*, is proposed instead in Huerga 2002.

Both of these approaches – DHL and balanced DHL – are able to encode attractors into the FCM. However, both of them also share a common disadvantage: the authors only consider encoding binary (or bipolar) attractors (as opposed to real-valued attractors). More importantly, even for such cases, the rules are unable to encode an arbitrary sequence.

3.2.2. Active Hebbian Learning

In Papageorgiou, Stylios, and Groumpos (2004b) the authors propose another learning method based on Hebbian learning – the *active Hebbian learning* (AHL) method.

AHL introduces the idea of the sequence of activation of the concepts. The expert specifies the sequence and manner (synchronous, asynchronous) in which the concepts are activated. The process starts from a concept which activates concepts linked to it, and thus the activation propagates until all the concepts have been activated at which point the simulation cycle stops and a new one starts.

Learning is based on the following rule:

$$w_{ji}(k) = (1 - \gamma) w_{ji}(k-1) + \eta A_j^{act}(k-1) A_i(k-1), \quad (13)$$

where γ , and η are tunable parameters, and A_j^{act} is the value of the activation concept. In addition to this Papageorgiou, Stylios, and Groumpos (2004b) also suggest normalization of the weight matrix to size 1 after every step, so as to prevent their growing indefinitely.

3.2.3. Nonlinear Hebbian Learning

Finally, there are several papers (e.g. Papageorgiou, Stylios, and Groumpos 2003; Papageorgiou, and Groumpos 2005a; Papageorgiou, Stylios, and Groumpos 2006; Stach, Kurgan, and Pedrycz 2008) discussing the so-called *nonlinear Hebbian learning*

(NHL). The learning rule used in this approach is based on the Oja rule, and it has the following form:

$$\Delta w_{ji} = \eta A_j (A_i - A_j w_{ji}). \quad (14)$$

In Papageorgiou, and Groumpos (2005a) the rule is further extended into the following:

$$w_{ji}^{(k)} = \gamma w_{ji}^{(k-1)} + \eta A_j^{(k-1)} \left(A_i^{(k-1)} - \text{sgn}(w_{ji}^{(k-1)}) A_j^{(k-1)} w_{ji}^{(k-1)} \right). \quad (15)$$

This introduces the weight decay parameter γ , and term $\text{sgn}(w_{ji}^{(k-1)})$, which is supposed to maintain the sign of the corresponding weight (thus keeping the physical meaning of the corresponding relationship between the concepts) (Papageorgiou, and Groumpos 2005a).

It should also be noted that the mode in which in these works NHL rule is coupled with the execution of the FCM is what makes the method quite distinct from the other learning methods discussed so far.

An initial FCM is constructed by the experts. This is run in the standard way using one of the equations (7), (9), (10). But in addition to this at every step, rule (14) or (15) is applied to the FCM using the values of concepts computed in that step. Thus the NHL method does not simply perform learning – it is used online to help drive the process, and to facilitate convergence to a target attractor. The method is not simply meant to train the FCM to perform a given task, or to encode a given attractor. Rather, it actively participates in the *execution* of the FCM – it adjusts the FCM cause-effect relationships and controls the system's output concepts (Papageorgiou, Stylios, and Groumpos 2006).

A more traditional application of the NHL rule is proposed by Stach, Kurgan, and Pedrycz (2008). In this case, NHL is used to make an FCM with a randomly initialized weight matrix learn the cause-effect relationships from historical data. In other words – the FCM learns to approximate a given data sequence. The authors use another randomly generated FCM to produce the data sequence, but the data could, naturally, come from the real system. The authors call this approach *data-driven NHL* (DD-NHL).

4. THE PROPOSED APPROACH

In this paper, we aim to approach the attractor problem using the concept of backpropagation through time. We refer to it as *BPTT-based attractor setting* (BAS). That is to say, given a specification of what the steady state should look like, and how quickly the model should converge to it, we use BPTT to encode this information into the FCM.

4.1. Using BPTT to Set the Attractor

Using BPTT we can train the FCM to give the desired response to a desired input. If we present it with an input, and run it for k steps, we can compare the real

output with the desired output, compute the error and backpropagate it through time in order to learn the weights.

Thus, if our intention is to set the attractor of the FCM, we may create an FCM with a randomly initialized weight matrix, run it for k steps from a number of randomly-generated initial states, and do backpropagation. The learning method should be able to generalize, and so when we run the FCM from an initial state for which it has not been trained, it should still end up in the same attractor.

In theory it should certainly be possible to encode limit cycles as well as fixed-point attractors, nevertheless in this paper we will focus on fixed-point attractors only. It is obvious that in addition to coming to the desired state after k steps, the FCM should also remain in that state, if it is supposed to be an attractor.

To ensure this, we propose to specify that the FCM should be in the desired state after k steps (*BPTT steps*), and should retain the same for m further steps (*stabilising steps*). If m is large enough, this should ensure that the FCM remains in the desired state indefinitely.

It should also be noted, that for the m steps, no BPTT needs to be done, because having the desired activation value of every concept, we can compute the error in every step precisely. BPTT is thus only done for the k steps.

However, backpropagation and BPTT could be useful in such cases, when the entire attractor is not specified, but rather only the values of certain concepts are available. In such case, we can use backpropagation and BPTT to compute errors for the missing concepts.

4.2. Vanishing/Exploding Gradients in FCMs

The vanishing/exploding gradient problem has been mentioned in connection with backpropagation learning in ANNs. Naturally the same problem may occur in FCMs. We conclude, however, that – probably owing to their limited size (according to Stach et al. (2005b) in practice FCMs are relatively small and most of them consist of 5-10 concepts), and also due to the fact that they are single-layer themselves – we did not find the gradient explosion/vanishing problem to hinder learning considerably.

The problem does occur in some cases (which is to be expected – especially when using naïve initialization methods), but these are not very frequent and it is possible to work around the problem by selecting a different initial point in the weight space and starting learning anew from there.

Furthermore, preliminary tests seem to indicate that if learning starts from an FCM constructed by the expert, the problem disappears altogether. Application of BPTT together with learning based on hessian-free optimization is nevertheless of considerable interest – especially if we are to encode chaotic attractors or limit cycles into the FCM (as opposed to simple fixed-point attractors), such more reliable learning methods may be called for.

5. SIMULATION EXPERIMENTS

In this section, we will present the results achieved using BPTT-based attractor setting. The first part will cover experiments starting from an FCM with a randomly-generated initial weight matrix, into which a randomly selected fixed-point attractor is encoded. The accuracy of the resulting model is reported. The second part provides a comparison with results reported for AHL and NHL in Papageorgiou, Stylios, and Groumpos (2006). There is also a third section, which offers some 2-dimensional visualizations.

5.1. Encoding Attractors into FCMs

In every experiment we do BPTT from a number of randomly selected initial points. It is obvious that this will make the process highly stochastic, and in consequence we can expect the results to have considerable variance. Therefore, unless otherwise specified, all experiments were carried out 100 times, and their results were averaged. The learning rate is set to 0.2 unless said otherwise.

For computing the attractor, 10 initial points are randomly selected, and the FCM is run for the maximum number of 1000 steps, or until the change of the activation values of the concepts from one step to another is less than $1E-30$ in terms of the mean squared error (MSE). Afterwards, we compare the real attractor of the FCM as computed with the target attractor (again using MSE).

In some cases the gradient explosion problem makes the weights grow indefinitely so that they become NaN (not-a-number). We detect these cases and report their number. Naturally, MSE cannot be computed in these cases and thus these runs are not included in the average. Gradient vanishing probably occurs in some cases as well, but we make no special effort to detect those cases. If we did exclude those cases from the MSE, the results might be somewhat improved.

5.1.1. Number of Initial Points

As mentioned, in every experiment, BPTT starts from a number of randomly generated initial points. The first collection of results shows the effect of that the number of said initial points has on the accuracy (in terms of MSE) and on the number of cases in which gradient explosion occurs.

Table 1: Number of gradient explosions, and the MSE for various numbers of stabilising steps

# of init points:	10	30	50	70
MSE	2.827 E-3	2.745 E-3	1.606 E-3	1.403 E-5
Grad. expl. #	2	4	8	14

The results are for an FCM with 5 concepts, the number of BPTT steps $k=5$, and $m=30$ stabilisation steps. 10 random initial vectors are used for training, and 5 training steps are applied for each.

It is obvious from Table 1 that with increasing the number of initial points, the MSE improves. This can be accounted for by the fact that the amount of training data increases. This should also improve generalization.

5.1.2. Number of Stabilising Steps

The following table shows the effect that the number m of stabilising steps has on accuracy and on the tendency of the algorithm to exhibit gradient explosion. The results are for an FCM with 5 concepts, the number of BPTT steps $k=5$, 10 random initial vectors are used for training, and 5 training steps are applied for each.

Table 2: Number of gradient explosions, and the MSE for various numbers of stabilising steps

m :	10	30	50
MSE	1.178 E-2	2.827 E-3	3.356 E-4
Grad. expl. #	0	2	4

As shown in Table 2, there is a correlation between the number of stabilising steps and the accuracy. Accuracy improves with increasing the number of stabilising steps, but the number of gradient explosions increases with it as well.

5.2. Visualization

Figures 5 and 6 show examples of randomly-generated attractor states encoded into an FCM. The FCM is run from a number of randomly chosen initial points to show how the FCM will eventually converge into the attractor state in every case.

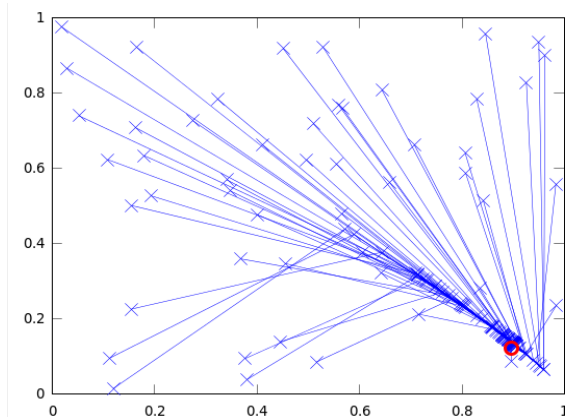


Figure 5: An example of a randomly generated attractor state encoded into an FCM; convergence to the state from randomly selected starting points shown

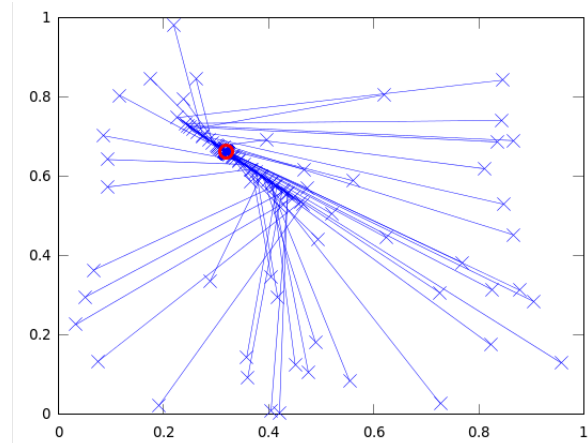


Figure 6: An example of a randomly generated attractor state encoded into an FCM; convergence to the state from randomly selected starting points shown

5.3. Comparison with Hebbian Learning

Let us now present a preliminary comparison with approaches based on Hebbian learning – in particular a cooperation with results achieved using AHL and NHL as reported in Papageorgiou, Stylios, and Groumpos (2006).

The authors present a FCM constructed by experts. Furthermore, the experts specify regions of acceptable values for selected concepts. If the experts specify that the activation value of concept C_j should fall in interval $[T_j^{min}, T_j^{max}]$, the learning goal is given by the following (Papageorgiou, Stylios, and Groumpos 2006):

$$T_j = \frac{T_j^{min} + T_j^{max}}{2}. \quad (16)$$

The results compared are those for the first case study. They follow in Table 3. In each case the steady-state difference from the target activation values (defined in terms of equation (16)) are computed, and the mean square error is reported.

The results reported for the BAS approach were achieved using the learning rate of 0.2, BPTT was started from 100 random initial positions, the number of steps after which the FCM should reach the attractor state was set to 5, and the additional number of steps for which was trained was set to 45. In this case, no gradient explosion problem occurred – having a weight matrix specified by experts clearly gives learning some advantage.

There are two columns in the table for the NHL method. This is because Papageorgiou, Stylios, and Groumpos (2006) report two results. The first one is for the steady-state starting from the initial weight matrix, and using NHL to modify weights, and control the process. NHL W refers to the steady-state reached when using the weight matrix learned using NHL without doing further learning. (There is no considerable difference between the errors though.)

Table 3: Comparison of results using AHL, NHL, and BPTT-based attractor setting (BAS)

	AHL	NHL	NHL W	BAS
MSE	3.394 E-04	1.312 E-3	1.405 E-3	1.322 E-12

It should be noted, that the comparison presented here is not in any sense definitive. The reason for this is that this paper does as of yet provide no tests for encoding attractors for which only the activation values of several concepts are specified. In this case we work around the problem by arbitrarily fixing the values of the other concepts to 0.5. It should, however, be possible to instead use backpropagation to propagate errors to the concepts with unspecified values. This issue remains for future investigation.

Also, we do not fix values of any of the weights – not even of the zero ones. All weights are allowed to change in this version of the algorithm. This may provide our approach with an unfair advantage in this case. This will also require further investigation, but existing research indicates that backpropagation can indeed work well even in cases when some or most of the weights are fixed – in fact this property is already being exploited by some types of ANNs, such as the echo state network.

We conclude that the error margin of the approach seems large enough to make the approach competitive even if the aforementioned restrictions were to hurt its performance to a certain extent.

6. FURTHER WORK

As a part of future work, the algorithm should be extended with the state-of-the-art learning methods based on Hessian-free optimization. This should effectively prevent the vanishing/exploding gradient problem, and make learning faster in general.

The algorithm should be tested with real models. It should be ascertained how well it can be used in scenarios where the training is only allowed to change some weights, while other remain fixed.

Backpropagation could be used to learn attractors in which only values of several concepts are specified. It should be investigated how such approach to work, and whether the values of the other concepts would stabilize as well, and also whether they would always stabilize at the same (though unspecified) values.

7. CONCLUSION

It has been shown in the past that the similarity between artificial neural networks allow for transfer of learning methods from one to another. Most notable among the related approaches have been those based on Hebbian learning.

In this paper we have contributed a new method for encoding attractors into fuzzy cognitive maps. The approach, as shown, is based on the notion of

backpropagation through time known from the theory of recurrent neural networks.

The application of the method has been presented and accompanied with simulation results. It has been shown that the method perform favourably, and preliminary comparisons show that its accuracy surpasses that of the approaches based on Hebbian learning. However, further work is necessary at this point.

It has been shown that increasing the number of stabilising steps has a positive influence on accuracy, but also increases the chance of gradient explosions. A similar relationship has been shown for the number of initial point from which BPTT learning is done.

Further study of some aspects of the approach is still to be carried out. It remains to be shown how well the method will be able to perform when target activation values are only known for certain concepts. It is also of much interest to investigate how well the method will perform when some of the weights will be fixed to their initial values. Also, some learning situations may require the introduction of more powerful optimization methods such as Hessian-free optimization.

REFERENCES

- Bengio, Y., Lamblin, P., Popovici, D., and Larochelle, H., 2007. Greedy layer-wise training of deep networks. *Advances in neural information processing systems* 19.
- Dickerson, J.A., and Kosko, B., 1993. Virtual worlds as fuzzy cognitive maps. *Virtual Reality Annual International Symposium*, 471–477.
- Groumpos, P.P., and Stylios, C.D., 2000. Modelling supervisory control systems using fuzzy cognitive maps. *Chaos, Solitons and Fractals* 11 (1), 329–336.
- Groumpos, P.P., 2010. Fuzzy cognitive maps: basic theories and their application to complex systems. In: Glykas, M., ed. *Fuzzy Cognitive Maps*. Berlin: Springer-Verlag, 1–22.
- Hinton, G.E., and Salakhutdinov, R.R., 2006. Reducing the dimensionality of data with neural networks. *Science* 313 (5786), 504–507.
- Huerga, A.V., 2002. A balanced differential learning algorithm in fuzzy cognitive maps. *Proceedings of the Sixteenth International Workshop on Qualitative Reasoning*, 10–12.
- Kottas, T.L., Boutalis, Y.S., and Christodoulou, M.A., 2007. Fuzzy cognitive network: A general framework. *Intelligent Decision Technologies* 1 (4), 183–196.
- Krose, B., and Smagt, P.V.D., 1996. *An Introduction to Neural Networks*. University of Amsterdam. Available from: http://www.cs.unibo.it/babaoglu/courses/cas/resources/tutorials/Neural_Nets.pdf [Accessed 10 May 2013].
- Martens, J., 2010. Deep learning via Hessian-free optimization. *Proceedings of the 27th International Conference on Machine Learning*.

- Martens, J., and Sutskever, I., 2011. Learning recurrent neural networks with Hessian-free optimization. *Proceedings of the 28th International Conference on Machine Learning* 46.
- Papageorgiou, E.I., Stylios, C.D., and Groumpos, P.P., 2003. Fuzzy cognitive map learning based on nonlinear Hebbian rule. *AI 2003: Advances in Artificial Intelligence*, 256–268.
- Papageorgiou, E.I., and Groumpos, P.P., 2004a. A new hybrid method using evolutionary algorithms to train fuzzy cognitive maps. *Applied Soft Computing* 5, 409–431.
- Papageorgiou, E.I., Stylios, C.D., and Groumpos, P.P., 2004b. Active Hebbian learning algorithm to train fuzzy cognitive maps. *International Journal of Approximate Reasoning*, 37 (3), 219–249.
- Papageorgiou, E.I., and Groumpos, P.P., 2005a. A weight adaptation method for fuzzy cognitive map learning. *Soft Computing*, 9 (11), 846–857.
- Papageorgiou, E.I., Parsopoulos, K. E., Stylios, C.S., Groumpos, P.P., and Vrahatis, M.N., 2005b. Fuzzy Cognitive Maps Learning Using Particle Swarm Optimization. *Journal of Intelligent Information Systems* 25 (1), 95–121.
- Papageorgiou, E.I., Stylios, C.D., and Groumpos, P.P., 2006. Unsupervised learning techniques for fine-tuning fuzzy cognitive map causal links. *International Journal of Human-Computer Studies* 64 (8), 727–743.
- Parsopoulos, K.E., Papageorgiou, E.I., Groumpos, P.P., and Vrahatis, M.N., 2003. A first study of fuzzy cognitive maps learning using particle swarm optimization. *The 2003 Congress on Evolutionary Computation, 2003. CEC'03*, 2, 1440–1447.
- Rojas, R., 1996. *Neural networks: a systematic introduction*. Berlin: Springer-Verlag.
- Stach, W., Kurgan, L., and Pedrycz, W., 2005a. A survey of fuzzy cognitive map learning methods. *Issues in soft computing: theory and applications*, 71–84.
- Stach, W., Kurgan, L., Pedrycz, W., and Reformat, M., 2005b. Genetic learning of fuzzy cognitive maps. *Fuzzy Sets and Systems*, 153 (3), 371–401.
- Stach, W., Kurgan, L., and Pedrycz, W., 2008. Data-driven nonlinear Hebbian learning method for fuzzy cognitive maps. *IEEE International Conference on Fuzzy Systems. FUZZ-IEEE 2008 (IEEE World Congress on Computational Intelligence)*, 1975–1981.
- Stylios, C.D., Christova, N., and Groumpos, P.P., 2002. A hierarchical modeling technique of industrial plants using multimodel approach. *Proceeding of 10th IEEE Mediterranean conference on Control and Automation, Lisbon, Portugal*.
- Sutskever, I., Martens, J., Hinton, G., 2011. Generating Text with Recurrent Neural Networks. *Proceedings of the 28th International Conference on Machine Learning*.
- Wang, H., and Wang, L., 2013. Application of Improved Fuzzy Cognitive Map Based on Fuzzy Neural Network in Intrusion Detection. *Journal of Information & Computational Science* 10 (1), 271–278.
- Werbos, P.J., 1990. Backpropagation through time: what it does and how to do it. *Proceedings of the IEEE* 78 (10), 1550–1560.

BOND-GRAPH BASED CONTROLLER DESIGN OF A TWO-INPUT TWO-OUTPUT FOUR-TANK SYSTEM

Nacusse, Matías A.^(a) and Junco, Sergio J.^(b)

LAC, Laboratorio de Automatización y Control, Departamento de Control, Facultad de Ciencias Exactas, Ingeniería y Agrimensura, Universidad Nacional de Rosario, Ríobamba 245 Bis – S2000EKE Rosario – Argentina.

^(a)nacusse@fceia.unr.edu.ar, ^(b)sjunco@fceia.unr.edu.ar

ABSTRACT

The quadruple-tank process has been proposed as a benchmark for multivariable control system design. This paper addresses the design in the bond graph domain of a robust controller having the volumetric flows of two pumps as manipulated variables and the level of the two lower tanks as the regulated outputs. The basic control objectives, expressed in terms of desired closed-loop energy and power-dissipation functions, are captured in the bond graph domain means a so-called Target Bond Graph, and the controller design is performed via Bond-Graph prototyping. The basic control law is further robustified against parameter uncertainties, measurement deviations and faults using the diagnostic bond graph concept, what leads to an additional loop consisting in a PI-law also being expressed with a physically meaningful bond graph subsystem. Some causal manipulations on the four-tank bond graph allow to extend to this multi-variable case the technique developed to solve the simpler monovisible two-tank control problem.

Keywords: quadruple-tank system, bond graph prototyping, robust fault-tolerant control, non-linear energy-based control.

1. INTRODUCTION

The quadruple-tank system proposed in (Johansson 2000) turned into a very popular benchmark allowing to test different control algorithms for multivariable processes. It is a Two-Input Two-Output or TITO nonlinear plant consisting of four interconnected water tanks fed by two pumps, whose linearized model has a multivariable zero, which can be made minimum or non-minimum phase by simply changing the position of two distribution valves. This system has been used to test and design several control schemes. In (Abdullah and Zribi 2012) a bibliographical review and three different control schemes are presented; gain scheduling, a linear parameter varying controller and input-output feedback linearization have been compared, measuring the pressure of the four tanks. In (Johnsen and Allgöwer 2007) an interconnection and damping assignment plus passivity based control (IDA-

PBC) algorithm for the minimum phase configuration of the four-tank system is presented showing simulation and experimental results. Limon, et al. 2010 present a robust model predictive control (MPC) algorithm for level tracking. In both cases the level of the four tanks are measured.

This paper addresses the design in the Bond Graph (BG) domain of an energy-based nonlinear control law which only measures the pressures of the two bottom tanks. The control system design objectives are to track the levels (or pressures) of the two bottom tanks, to reject disturbances originated in model uncertainties and measurement errors, and to be tolerant to some interconnection faults.

Fault tolerant control (FTC) can be classified in two main categories, Passive Fault Tolerant Control (PFTC) and Active Fault Tolerant Control (AFTC). Both approaches are usually complemented in the praxis to improve the performance and stability of the fault tolerant system (Blanke, et al. 2006). Refer to (Zhang and Jiang 2008) for a bibliographical and historical review on FTC. The passive approach defines a unique control law to achieve the control objectives even in the presence of a fault. Generally speaking, the passive approach ensures stability and confers robustness under faults to the control system, but there exists a trade-off between performance and robustness (Isermann 2006). Although this paper follows a PFTC-approach, some concepts commonly found in the design of AFTC controllers are used.

The active approach modifies the control law according to the faults occurred, so that in this approach a fault detection and isolation (FDI) phase is mandatory before making a decision on how to reconfigure the control law. Analytical redundancy relationships (ARR), which count among the many solutions used to generate residual signals for FDI, have been implemented in the BG domain via the Diagnostic Bond Graphs (DBG) technique presented in (Samantaray, et al. 2006). Using the plant inputs and plant measurements, residual signal are generated that depend on the model parameters and the real plant parameters.

Nacusse and Junco (2011) address the PFTC-problem of a two-tank system in the BG domain using

an energy and power shaping method (Junco 2004). This method first expresses the control system specifications in terms of desired closed-loop energy and power dissipation functions, proceeds further capturing both functions in a so called Target Bond Graph (TBG) that represents the desired closed-loop behaviour, and concludes constructing the controller via Bond Graph prototyping. This prototyping is such that the coupling of the resulting controller-BG and the plant-BG renders the whole equivalent to the TBG. In Nacusse and Junco (2011) the basic control law obtained in this way is robustified with additional terms derived considering a Diagnostic Bond Graph (DBG) of the closed-loop: the *nominal* control system represented by the TBG (originally proposed under ideal assumptions) is fed with the actual reference signals and measured plant outputs. Thus, the residual signal obtained from the closed loop DBG (CL-DBG) is a measure of the error between the desired and the actual dynamics of the control system. So, the control law aims at making the residual signal vanish in time, making the closed-loop system to behave asymptotically like the original TBG.

The rest of the paper is organized as follows. Section 2 reviews some background results and summarizes the main results presented in Nacusse and Junco (2011). Section 3, revisiting this previous result on the two-tank system, addresses some BG manipulations that simplifies the controller and, simultaneously, provides a way to extend the design method employed in the simpler system to the multivariable four-tank process which is shown in Section 4. Next, Section 5 presents some simulation responses that prove the good dynamic response of the control system and, finally, Section 6 addresses some conclusions.

2. BACKGROUND AND PREVIOUS RESULTS

This section briefly summarizes the main ideas on performing energy shaping and damping assignment directly in the BG domain through BG prototyping and recalls their application to solve a control problem on a two-tank system as presented in Nacusse and Junco (2011). This result will be revised in the next section as a prelude to the development of the main result in this paper, the design of a controller for the quadruple-tank benchmark process.

2.1. Energy- based control in the BG domain

The power and energy shaping control technique defines the control problem as a stabilization one, choosing desired closed-loop energy- and power-dissipation functions, and obtaining the control law through equations that match the control open-loop energy function (a kind of control Lyapunov function, see Sontag 1998) and the desired closed-loop functions. Passivity-based control on port-Hamiltonian models count among the most successful (Ortega, et al., 2002, Ortega, et al., 2008).

In the BG domain, the closed-loop specifications are expressed by a so-called Target Bond Graph (TBG) representing the equivalent closed-loop behavior. In order to obtain the control law, the controlled sources – which provide the manipulated variables in the BG model of the plant– are prototyped (meaning that their behavior is expressed means BG components) in such a way that their power-interconnection with the rest of the plant BG –which is called a Virtual BG (VBG)– matches the TBG. The control law is obtained from the VBG by simply reading the outputs of the prototyped sources with the help of the causal assignment in the VBG. This method is exemplarily performed below on a two-tank system. For more details refer to (Junco 2004).

2.2. Control via BG-prototyping: the 2-tank system

As shown in Figure 1, the tanks are located one above the other, the upper tank discharging into the lower tank. Both tanks are fed with a unique input flow splitted between them through a distribution valve whose parameter $\gamma \in [0,1]$ determinates how the input flow is distributed to the tanks as indicated by the BG in Figure 1.

The control objectives imposed on *Tank1* are:

- Tracking of constant reference levels
- Rejection of constant disturbances.
- Robustness regarding parametric uncertainties and faults.

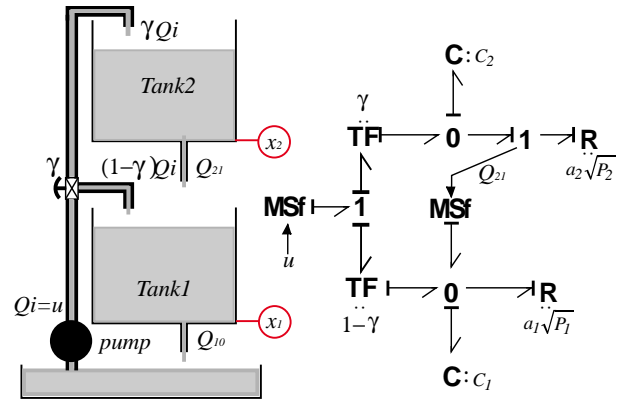


Figure 1: Two-tank system and its BG model. Measured plant outputs encircled in red.

The state equations can be read from the BG of Figure 1 using the standard procedure, giving as state variables the stored liquid volumes. Here the gauge pressures at the bottom of the tanks are chosen as state variables (instead the liquid levels used in Nacusse and Junco 2011) and presented in (1):

$$\begin{aligned} \dot{x}_1 &= -\frac{a_1\sqrt{x_1}}{c_1} + \frac{a_2\sqrt{x_2}}{c_1} + \frac{(1-\gamma)}{c_1}u \\ \dot{x}_2 &= -\frac{a_2\sqrt{x_2}}{c_2} + \frac{\gamma}{c_2}u \end{aligned} \quad (1)$$

Where, with $i=1,2$, x_i represents the gauge pressure at the bottom of *Tank* i ; C_i are the tanks hydraulic capacities and a_i are coefficients depending on the cross sections of the outlet holes of the tanks.

The proposed TBG for the closed loop system is shown in Figure 2 where the desired stored energy and power dissipation are expressed in terms of the tracking error state variable in (2) and (3).

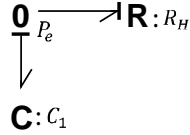


Figure 2: TBG for pressure control of lower tank.

$$V(x) = \frac{1}{2} C_1 x_e^2 \quad (2)$$

$$\dot{V}(x) = -\frac{1}{R_H} x_e^2 \quad (3)$$

The tracking error $x_e = x_1 - x_1^{ref}$ is the state variable of the TBG and x_1^{ref} is the *Tank1* reference pressure.

To enforce the desired closed-loop dynamics specified by the TGB, the Virtual BG (VBG) of Figure 3 is constructed. It shows how to proceed in order to obtain the control law. The left half of the figure is obtained prototyping the controlled power source **MSf** in such a way that access is gained to the chosen output, the pressure x_j , and an overall equivalent behavior to the TBG is achieved. The first objective is achieved via the exact compensation of the *Tank2* pressure on the pump over the distribution valve and of the discharge of *Tank2* on *Tank1*. The second objective is reached first adding the virtual elements with negative “gains” that cancel the own dynamics of *Tank1* and later building the incremental dynamics around the reference pressure P_1^{ref} for *Tank1* via the insertion of the virtual elements **C**: C_1 and **MSe** (shapes the closed-loop energy) and **R**: R_H (damping assignment).

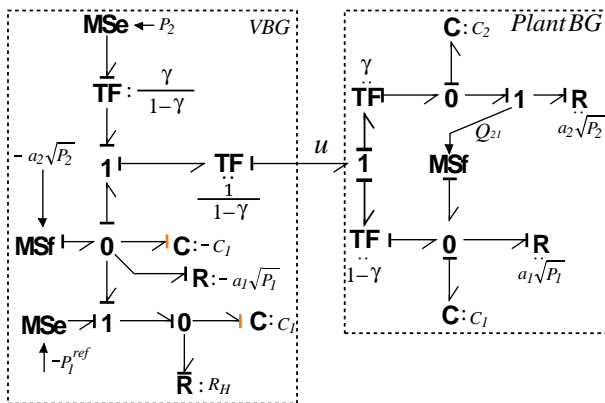


Figure 3: Virtual and plant BG.

Using the standard causality reading procedure the control law (12) can be read directly from the VBG as:

$$u = \left(\frac{1}{1-\gamma}\right) \left[a_1 \sqrt{x_1} - a_2 \sqrt{x_2} - \frac{1}{R_H} (x_1 - x_1^{ref}) + C_1 \dot{x}_1^{ref} \right] \quad (4)$$

Assuming exact model knowledge and perfect measurements, this control law yields a closed-loop behavior equivalent to the TBG of Figure 2, i.e., the closed-loop dynamics satisfies (3).

Remark: the rated control law (4) performs a *partial* energy shaping and damping assignment, since only the dynamics of *Tank1* is captured in the TBG. As no objectives are imposed on *Tank2* and its dynamics is hidden in closed-loop, its stability must be analyzed after the controller has been designed, property that can be easily verified in this case.

Perturbed closed-loop dynamics. Because of parameter dispersion, faults, modeling errors, sensor limited precision, noise, etc., neither the model nor the measurements are exact. To deal with this it is convenient to think the control input as composed by two terms as in (5), where u_r is the “rated” part of u , i.e., the control input part that performs the power and energy shaping under ideal plant and measurement conditions. In the same expression, δ_u is the unknown controller part due to modeling errors, parametric dispersion, faults, etc. The BG of Figure 4 reflects this situation.

$$u = u_r + \delta_u \quad (5)$$

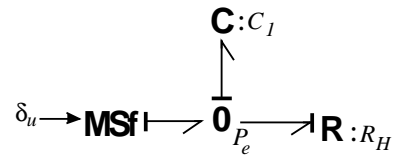


Figure 4: Perturbed TBG.

Under this situation the closed-loop dynamics no longer satisfies (3) but (6).

$$\dot{x}_e = -\frac{1}{C_1 R_H} x_e + \frac{1}{C_1} \delta_u \quad (6)$$

2.3. Robustifying the control law

The CL-DBG is defined injecting the pressure tracking error (as measured on the real control system) into the TBG through modulated sources and collecting a residual signal as shown in Figure 5.

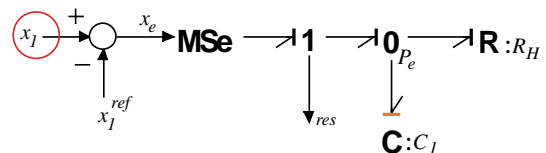


Figure 5: Proposed CL-DBG. Measurements to be fed encircled in red.

The CL-DBG yields to the new error dynamics in (7) which is driven by the residual signal *res*. The residual signal, which is the power co-variable of the error

injected into the CL-DBG, is a measure of the difference between the actual and the ideally expected closed-loop dynamics, i.e., when $res = 0$, x_e responds as previously defined in the TBG of Figure 2. This suggests that the control objectives could be reached extending the previously computed control law to a new one $u = u(x_1, x_2, x_1^{ref}, res)$ incorporating the residual signal in such a way that res tends to zero with growing time.

$$\dot{x}_e = -\frac{1}{c_1 R_H} x_e + \frac{res}{c_1} \quad (7)$$

The residual expression (8) obtained reading the CL-DBG clearly shows that choosing u as in (4) (rated control law) yields $res = 0$, in absence of faults and modeling errors.

$$res = -a_1 \sqrt{x_1} + a_2 \sqrt{x_2} + \frac{1}{R_H} (x_1 - x_1^{ref}) - C_1 \dot{x}_1^{ref} + (1 - \gamma)u \quad (8)$$

To improve the control system robustness, the extra term u_4 shown in (9) is added to the expression (4) for u .

$$u = \left(\frac{1}{1-\gamma}\right) \left[a_1 \sqrt{x_1} - a_2 \sqrt{x_2} - \frac{1}{R_H} (x_1 - x_1^{ref}) + C_1 \dot{x}_1^{ref} + u_4 \right] \quad (9)$$

Choosing $u_4 = -K \int res$ yields the residual dynamics (10):

$$res + K res = (1 - \gamma_n) \delta_u \quad (10)$$

Thus, with constant δ_u , res goes asymptotically to zero with time constant $1/K$. As already anticipated, this forces x_e to approach asymptotically the desired error dynamics defined in the TBG of Figure 2.

Representing u_4 in terms of $(x_1 - x_1^{ref})$ yields (11), expression showing that, in this case, the residual signal defined in the CL-DBG has a PI structure. Note however that this does not necessarily generalize, since the resulting structure depends on the TBG.

$$u_4 = -K C_1 (x_1 - x_1^{ref}) - \frac{K}{R_H} \int (x_1 - x_1^{ref}) \quad (11)$$

3. THE TWO-TANK PROBLEM REVISITED

In this Section the two-tank problem is revisited. First, a causal manipulation of the original system BG is shown which leads to a simplification of the control law and will be advantageously used in the process of deriving the control law for the quadruple-tank system. Second, a BG interpretation of the robustifying additional term is provided.

3.1. Causal manipulation and simplified control law

In Figure 1 the flow Q_{21} from Tank2 into Tank1 is computed by the R-element representing the discharge

orifice of the former. Putting in derivative causality the upper C-element (models the potential energy stored in the upper tank) yields the BG of Figure 6, where the discharging flow is computed as the sum of the incoming flow from the source and the output flow to the upper C element, i.e., $Q_{21} = \gamma u - Q_{c2}$. This new computation justifies the equivalent BG of Figure 7.

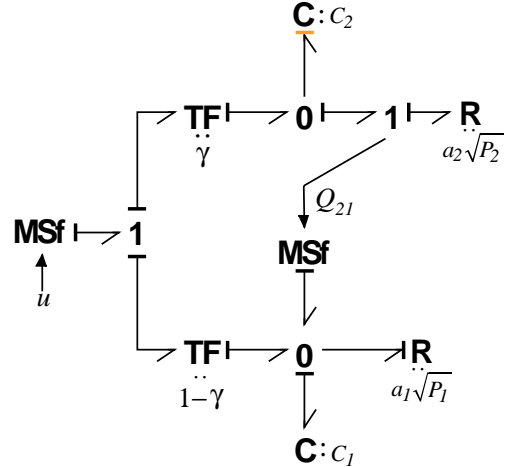


Figure 6: BG model of the two tanks system with the upper C in derivative causality.

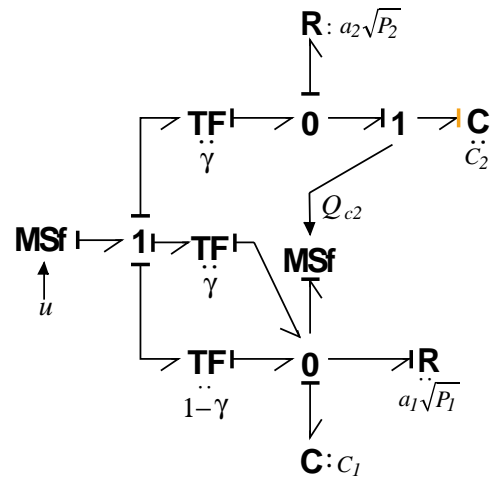


Figure 7: Equivalent plant model after manipulation of the original BG.

Furthermore, as the control objectives are placed only on Tank1, for control system design purposes the equivalent plant model shown in Figure 8 can be considered, where the effect of Tank2 enters as a disturbance.

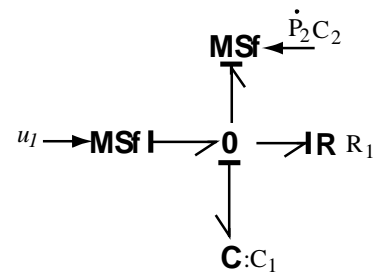


Figure 8: Equivalent control system design BG.

Following similar steps as those detailed in Section 2.2, the VBG of Figure 9 can be constructed to enforce the desired closed-loop dynamics specified by the TGB.

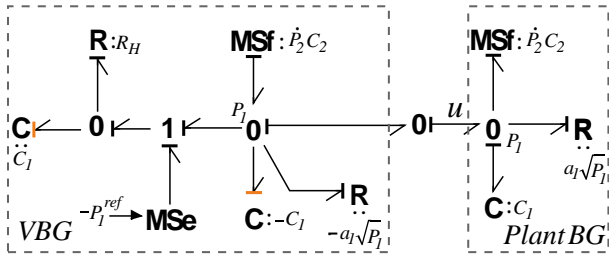


Figure 9: Virtual and plant BG.

The control law (12) can be read directly from the VBG using the standard causality reading procedure:

$$u = a_1 \sqrt{x_1} - \frac{1}{R_H} (x_1 - x_1^{ref}) + C_1 \dot{x}_1^{ref} + C_2 \dot{x}_2 \quad (12)$$

Remark: Equations (4) and (12) are fully equivalent and both show the need to measure not only the pressure of *Tank1* but also that of *Tank2* to implement the control law u . However, equation (12) – which results from the above manipulation performed on the BG– has the advantage of showing that its last term can be eliminated from the control law as it is an evanescent perturbation, i. e., it vanishes in steady state, and as such it does not affect the equilibrium point. Doing so yields the control law (13) which can be implemented with the sole measurement of x_1 . However, it must be realized that this simplification amounts to modifying the TGB as indicated in Figure 10.

$$u = a_1 \sqrt{x_1} - \frac{1}{R_H} (x_1 - x_1^{ref}) + C_1 \dot{x}_1^{ref} \quad (13)$$

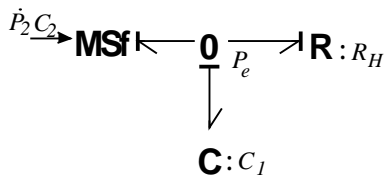


Figure 10: New TGB without measuring x_2 .

3.2. BG interpretation of the robustifying term

This subsection revisits the result of (Nacusse and Junco 2011) summarized in Section 2.3 of this paper in order to provide a BG implementation of the additional term u_4 of the control law given in (11).

The TGB defines the closed loop dynamics of the system. To robustify its behavior it is necessary to inject an additional control action. In order to analyze this problem in the BG domain a concise word BG version of Figure 9 is presented in Figure 11. Departing from Figure 11, Figure 12 shows the word BG of a power interconnection proposed as a means to provide the additional control action. There, the word BG block named *mDBG* must be capable of rejecting all of the above-mentioned disturbances.

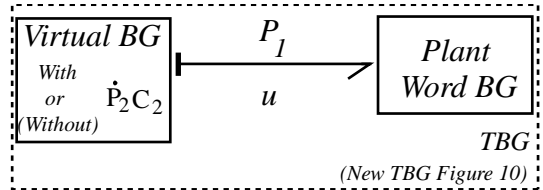


Figure 11: Power coupling between plant BG and VBG to obtain the TGB.

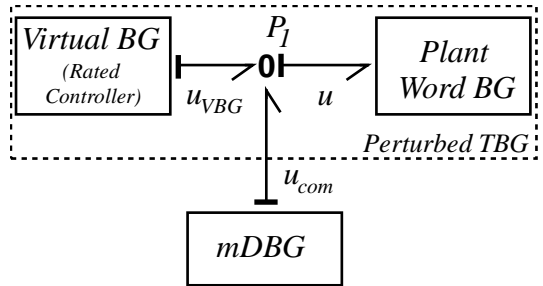


Figure 12: Proposed power interconnection

In the approach presented in Nacusse and Junco (2011) a residual signal is generated through a CL-DBG as indicated in Figure 13 (cf. Figure 5) (see Appendix B for a brief description of the DBG for FDI purposes). This residual measures the error between the PTBG and the TGB and is used to generate an additional control action forcing this error to vanish in steady-state (as well as the residual itself).

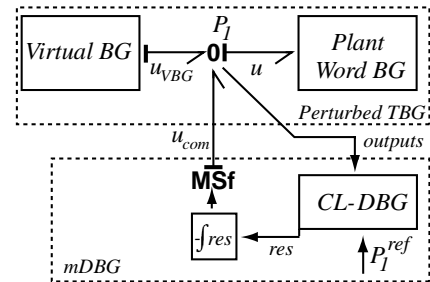


Figure 13: Signal coupling between PTBG and TGB through closed loop DBG.

The additional control action u_4 (a hydraulic flow) given in (11) in terms of the tracking error (a pressure) can be interpreted as produced by an effort-sharing set of a hydraulic resistance and inductance, i.e., an **I**- and a **R**-element. Figure 14 shows the resulting closed loop BG with power coupling between the PTBG and the *mDBG*, where $R_1 = 1/KC_1$ and $I_1 = R_H/K$.

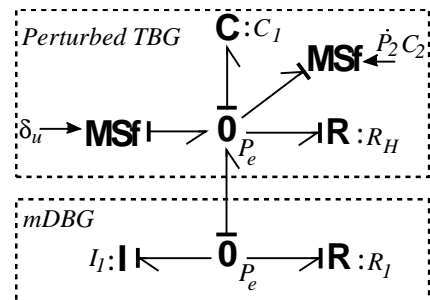


Figure 14: Power coupling between the PTBG and the *mDBG*.

Figure 15 shows the resulting closed loop BG, where the power interconnection among the plant BG, the VBG and the *mDBG* is highlighted in dotted squares. Notice that the redundancy in the MSf which injects the $-P_1^{ref}$ can be eliminated by shifting the *mDBG* into the VBG as it is shown in Figure 16.

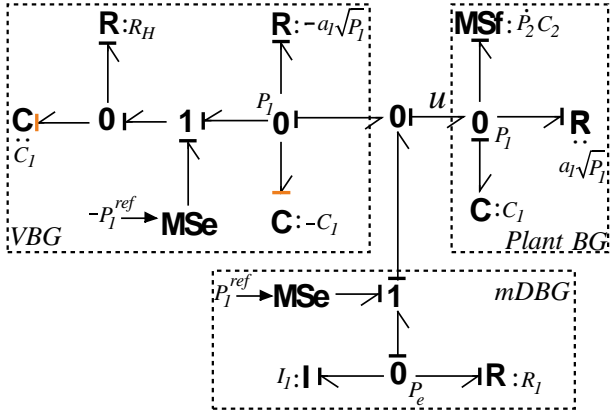


Figure 15: Resulting closed loop BG.

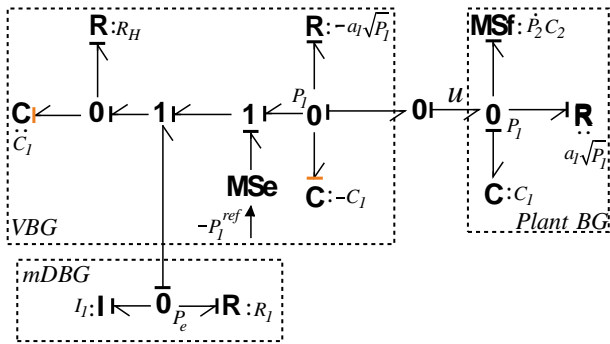


Figure 16: Closed loop BG with *mDBG* coupled into the VBG

Remark: As already anticipated, with constant δ_u , the tracking error x_e approaches zero asymptotically, as it can be easily verified through a causal and power analysis of the BG in Figure 14. Indeed, with constant disturbances at the outputs of both MSf, the I-element integrates its input effort P_e until it is driven to zero. At the same time, the I-element keeps at its output a constant flow-value which exactly cancels the sum of the MSf-flows and, thus, generates a zero-flow situation at the input of the C-element, which in turn keeps P_e in zero, which is precisely the control objective. The stability of this situation depends on the R elements being strictly dissipative (Junco 2001), which is of course ensured by design.

4. APPLICATION TO THE FOUR-TANK BENCHMARK PROBLEM

The four-tank system depicted in Figure 17 is a TITO nonlinear plant consisting of four interconnected water tanks fed by two pumps, whose linearized model has a multivariable zero, which can be made minimum or non-minimum phase by simply changing the position of two distribution valves.

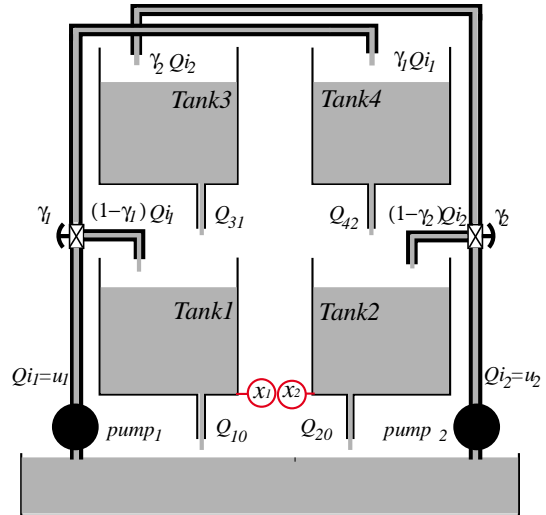


Figure 17: Four-tank system with measurements encircled in red.

4.1. Causal manipulation and controller design

In this subsection the control law for the four-tank system is designed. The control objectives are the same of that proposed for the two-tank system, in this case imposed on both of the bottom tanks.

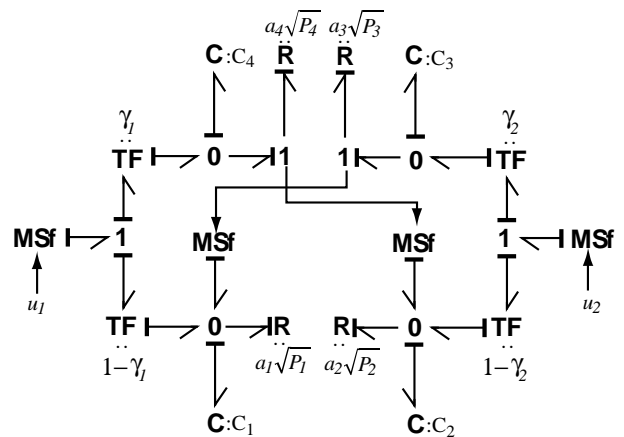


Figure 18: BG model of the four-tank system.

As the first step developing the multivariable control law, a causal manipulation is performed on the original BG of Figure 18 as shown in Figure 19. Similarly as in the two-tank case, again the discharge flows of the upper tanks are expressed not as computed by their associated R-elements but as the difference between the flows of the sources minus their net input flows ($\gamma_1 u_1 - C_3 \dot{P}_3$ and $\gamma_2 u_2 - C_4 \dot{P}_4$). This manipulation permits to construct the new BG given in Figure 20. This BG exhibits two internal variables u_1^* and u_2^* , which in the sequel are going to be treated as virtual control inputs. Seen from the bonds associated to these two auxiliary flow variables the quadruple-tank problem appears as two decoupled two-tank problems. Hence, the multivariable problem is strongly simplified, as the previously developed procedure can be first applied to each sub-problem and then the overall control law be recovered using the causal relationships relating the

auxiliary variables with the control inputs provided by the power-conserving structure.

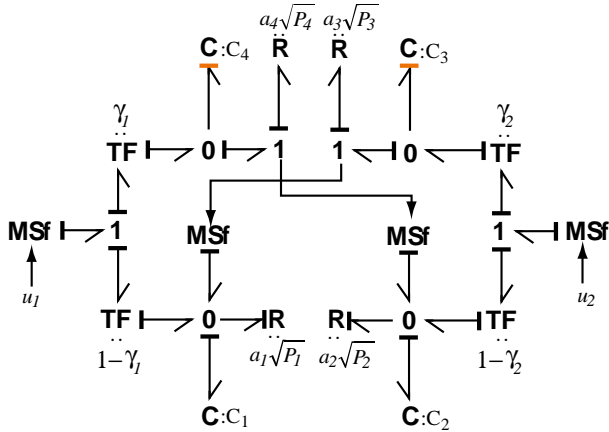


Figure 19: BG of the four tanks system with upper tanks in derivative causality.

The real and the virtual control inputs are related through a transformation matrix which is given in (14). Notice that when $\gamma_1 + \gamma_2 = 1$ the transformation matrix is singular. In this condition of the distribution valves the multivariable zeros (of the linearized system) are placed at the origin of the complex plane.

$$\begin{bmatrix} u_1^* \\ u_2^* \end{bmatrix} = \begin{bmatrix} (1 - \gamma_1) & \gamma_2 \\ \gamma_1 & (1 - \gamma_2) \end{bmatrix} \begin{bmatrix} u_1 \\ u_2 \end{bmatrix} \quad (14)$$

The virtual control laws, obtained following the same procedure as in the two-tank example ignoring the vanishing term, are given in (15).

$$\begin{aligned} u_1^* &= a_1 \sqrt{x_1} - \frac{1}{R_{H1}} (x_1 - x_1^{ref}) + C_1 \dot{x}_1^{ref} \\ u_2^* &= a_2 \sqrt{x_2} - \frac{1}{R_{H2}} (x_2 - x_2^{ref}) + C_2 \dot{x}_2^{ref} \end{aligned} \quad (15)$$

4.2. Robustifying the control law

The virtual control laws (15) are robustified, as in the two-tank example, via power coupling of the *mDBG* or by simply adding a term like (11) to each equation of (15). This yields the real control laws given in (16) and (17).

$$\begin{aligned} u_1 = -\frac{1}{\gamma_1 + \gamma_2 - 1} \left\{ (1 - \gamma_2) \left[a_1 \sqrt{x_1} - \frac{x_1 - x_1^{ref}}{R_{H1}} + C_1 \dot{x}_1^{ref} - K_1 C_1 (x_1 - x_1^{ref}) - \frac{K_1}{R_{H1}} \int (x_1 - x_1^{ref}) \right] - \gamma_2 \left[a_2 \sqrt{x_2} - \frac{x_2 - x_2^{ref}}{R_{H2}} + C_2 \dot{x}_2^{ref} - K_2 C_2 (x_2 - x_2^{ref}) - \frac{K_2}{R_{H2}} \int (x_2 - x_2^{ref}) \right] \right\} \end{aligned} \quad (16)$$

$$\begin{aligned} u_2 = -\frac{1}{\gamma_1 + \gamma_2 - 1} \left\{ (1 - \gamma_1) \left[a_2 \sqrt{x_2} - \frac{x_2 - x_2^{ref}}{R_{H2}} + C_2 \dot{x}_2^{ref} - K_2 C_2 (x_2 - x_2^{ref}) - \frac{K_2}{R_{H2}} \int (x_2 - x_2^{ref}) \right] - \gamma_1 \left[a_1 \sqrt{x_1} - \frac{x_1 - x_1^{ref}}{R_{H1}} + C_1 \dot{x}_1^{ref} - K_1 C_1 (x_1 - x_1^{ref}) - \frac{K_1}{R_{H1}} \int (x_1 - x_1^{ref}) \right] \right\} \end{aligned} \quad (17)$$

Using (16) and (17) the stability of the hidden closed-loop dynamics of *Tank_3* and *Tank_4* can be verified.

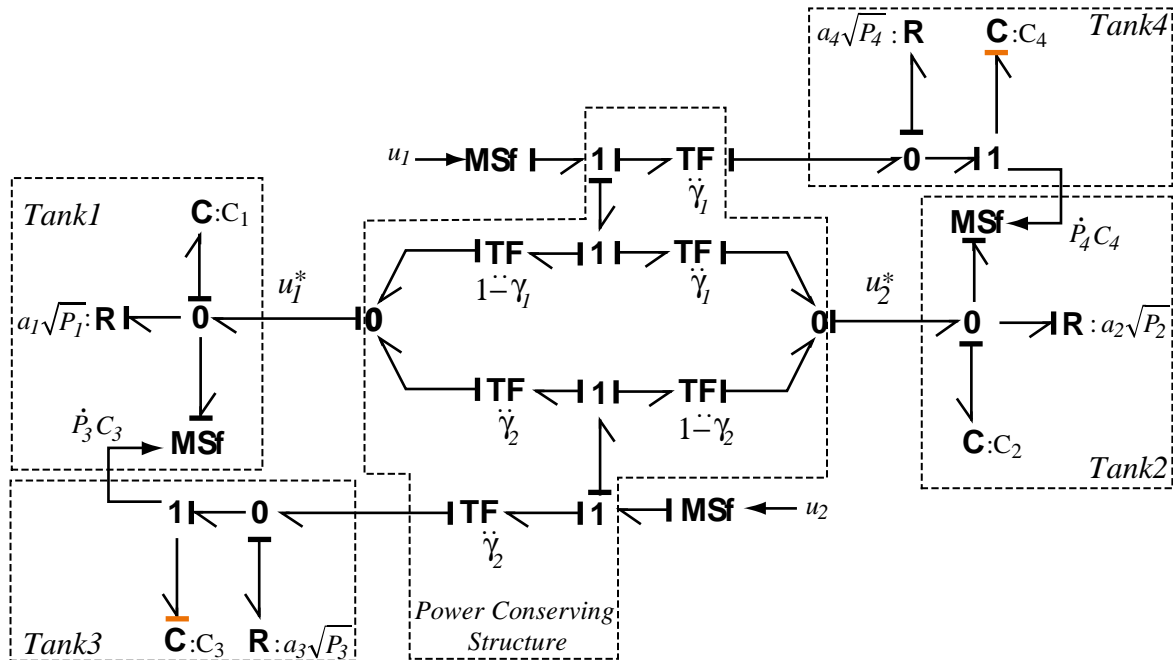


Figure 20: BG model after manipulation for controller design.

5. SIMULATION RESULTS.

The parameters used in the simulations, shown in Table I, were obtained from (Johansson 2000), where A_i are the cross section areas of the tanks, related to the tanks hydraulic capacities by the relation $C_i = A_i/\rho g$ where ρ is the liquid (water) density and g is the gravitational acceleration. The parameters of the *mDBG* are $R_{H1} = R_{H2} = 10$ and $K_1 = K_2 = 0.01$.

Table I. Simulation parameters

Parameter	Value
A_1, A_3	28 cm^2
A_2, A_4	32 cm^2
a_1, a_3	$0.071 \text{ cm}^2 \sqrt{\text{cm}^3/\text{gr}}$
a_2, a_4	$0.057 \text{ cm}^2 \sqrt{\text{cm}^3/\text{gr}}$

Using the control laws (16) and (17) with noisy measurements, with normal distribution and amplitude $n = 0.1 \text{ cm}$, of the bottom tanks pressures, the simulation scenarios involve abrupt faults in the system. To show the robustness of the control laws, the used parameters are -10% and +10% for those related with *Tank1* and *Tank2* respectively. For illustration purposes the simulations show tanks levels instead of tanks pressures.

The first simulation scenario, *Scenario_1*, consists of a minimum phase configuration with valves positions in $\gamma_{1r} = 0.3$ and $\gamma_{2r} = 0.2$. This are rated values used to parameterize the control laws. In this scenario two sequential faults occurred: at time $T = 2000\text{s}$ the value of the cross section area of outlet hole of *Tank2* is increased by 50% (forcing the same increment in a_2); and at time $T = 5000\text{s}$ the value of the valve position changes to $\gamma_1 = 0.6$.

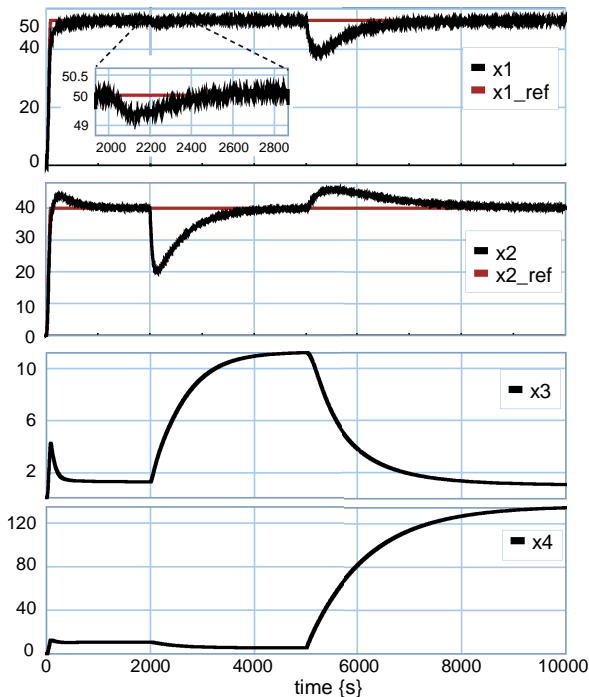


Figure 21: Tanks levels responses for sequential faults in *Scenario_1*.

The simulation responses for *Scenario_1* are shown in Figure 21 and Figure 22, which show that despite the faults occurrence the control system behaves as expected and the bottom tanks levels follow their references. For both cases, the control inputs, u_1 and u_2 , force to zero the residual signals in order to reject the faults.

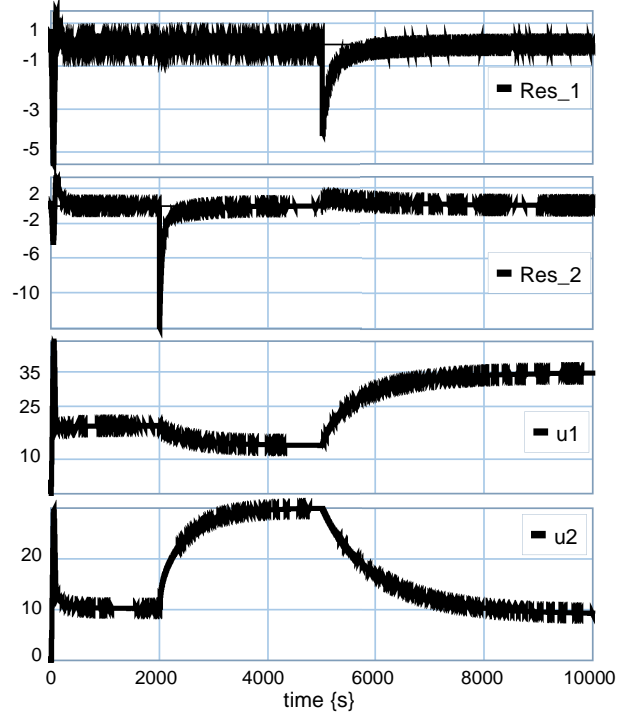


Figure 22: Residual signals and control inputs for sequential faults in simulation *Scenario_1*.

In simulation *Scenario_2* a non-minimum phase configuration is tested, where the valves position are placed at: $\gamma_{1r} = 0.7$, $\gamma_{2r} = 0.7$. Again two sequential faults occurred, the first, at time $T = 6000\text{s}$ where the value of the position valve changes to $\gamma_2 = 1$ which physically implies that *pump_2* injects all its flow to *Tank_3*; and the second, at time $T = 15000\text{s}$, where the value of the cross section area of outlet hole of *Tank1* (a_1) is increased by 50%.

In this scenario the bottom tank levels follow their references rejecting the disturbances originated by the faults occurrence as it is shown in

Figure 23. Figure 24 shows the associated residual signals and the control inputs. Here again, the control inputs force the residual signals to remain at zero to reject the faults.

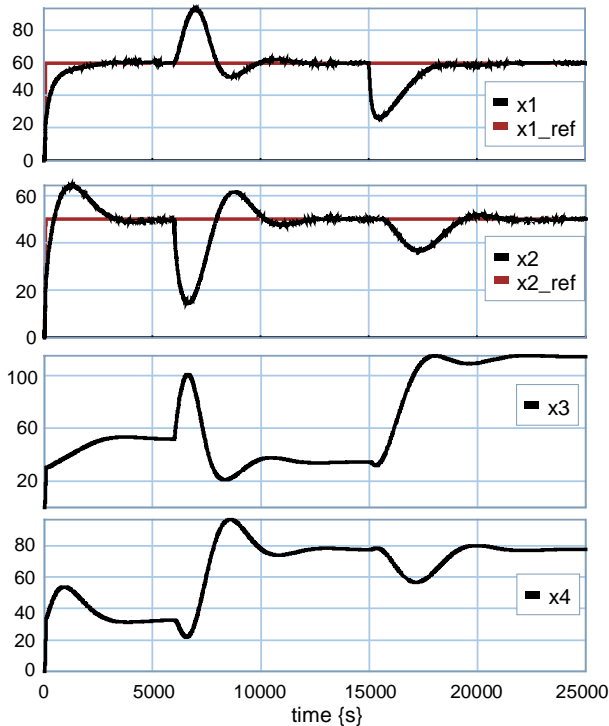


Figure 23: Tanks levels responses for sequential faults in *Scenario_2*.

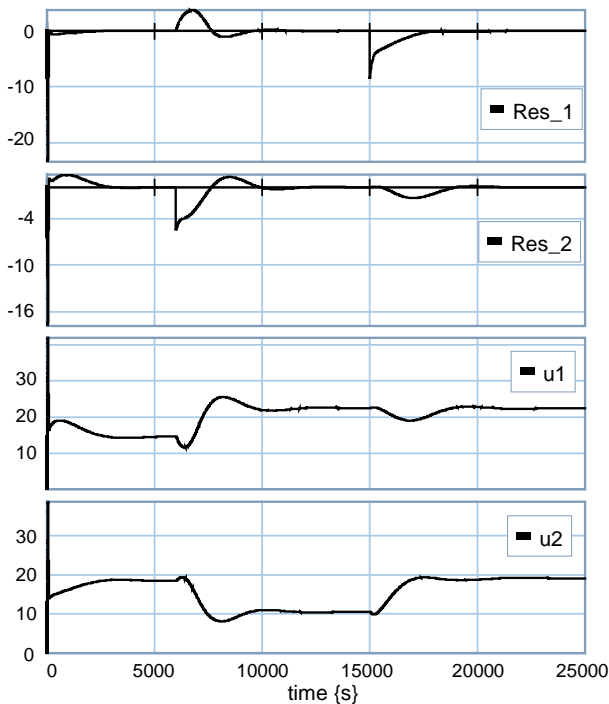


Figure 24: Residual signals and control inputs for sequential faults in simulation *Scenario_2*.

6. CONCLUSIONS

This work addressed the design of a robust controller for a multivariable four-tank system in three stages. A (partial) energy shaping and damping assignment control system design technique in the bond graph domain was first applied to obtain an almost-exact I/O-feedback linearizing controller for a simpler two-tank problem. The controller is just almost-exact because a

feedback term was ignored in the (otherwise exact) control law in order to spare a measurement. The second stage proceeded to robustify the previous controller to which aim a closed-loop diagnostic bond graph was introduced. Finally, a causal manipulation was performed on the BG of the quadruple-tank that permitted handling the associated multivariable problem as two monovariable decoupled problems, each for a simple two-tank system. Simulation results demonstrate the good response and the fault tolerance of the control system.

ACKNOWLEDGMENTS

The authors wish to thank SeCyT-UNR (the Secretary for Science and Technology of the National University of Rosario) for their financial support.

APPENDIX A: RESIDUAL SINKS

The residual sink component injects the necessary effort or flow in order to make vanish the power conjugated variable into the sink.

A residual sink element can be interpreted as an energy store where it parameter tend to zero. For example, an effort residual sink can be interpreted a C element in integral causality:

$$C\dot{e} = \Delta f$$

If the parameter C tends to zero, then \dot{e} is determined by the algebraic equation $\Delta f = 0$.

Figure 25 shows the graphical representation of the effort and flow residual sink used in (Borutzky 2009).



Figure 25: flow and effort residual sink.

APPENDIX B: DIAGNOSTIC BOND GRAPH

The Diagnostic Bond Graph was first presented by (Samantaray, et al. 2006) for numerical evaluation of analytical redundancy relationships (ARR). The ARRs are calculated to perform FDI in an AFTC frame.

Basically, the DBG is obtained from a BG model of the plant injecting the plant measurements and inputs through modulated sources. The residual signal is obtained by measuring the power co-variables of the modulated sources, see Figure 26.

Reading directly from the BG the residuals are:

$$\begin{aligned} res1 &= C_1\dot{x}_1 + a_1\sqrt{x_1} + a_2\sqrt{x_2} - (1 - \gamma)u \\ res2 &= C_2\dot{x}_2 + a_2\sqrt{x_2} - \gamma u \end{aligned} \quad (18)$$

As can be noted in (18), the residuals depend on system parameters. If the model represents perfectly the controlled system, then the residual signals are zero. The differential causality is an advantage in FDI, because no initial states are necessary to evaluate the residuals.

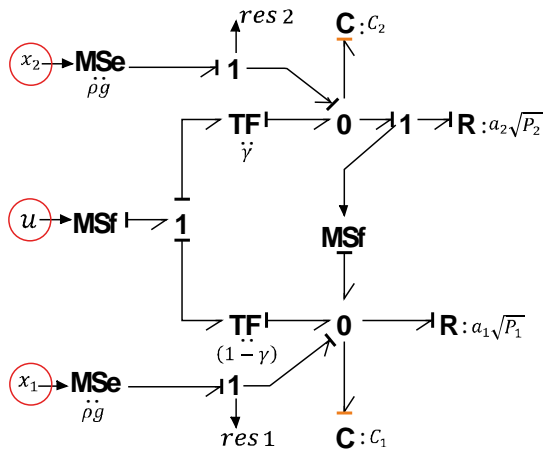


Figure 26: Diagnostic Bond Graph of the two tank system. Plant measurements to be fed into the DBG encircled in red.

REFERENCES

- Abdullah A., Zribi M., "Control Schemes for a Quadruple Tank Process". International Journal of Computers communications and control, ISSN 1841-9836, Volume:7(4):594-604, 2012.
- Blanke, M., Kinnaert, M., Lunze, J., Staroswiecki, M. "Diagnosis and Fault-Tolerant Control". Second Edition, Springer-Verlag.. 2006.
- Borutzky, W. "Bond graph model-based fault detection using residual sinks". Proceedings of the Institution of Mechanical Engineers, Part I: Journal of Systems and Control Engineering, Volume 223, 2009, pp. 337-352.
- Isermann, R. "Fault-Diagnosis Systems" Springer-Verlag. 2006.
- Junco, S. "Lyapunov Second Method and Feedback Stabilization Directly on Bond Graphs". Proc. ICBGM'2001, SCS-Simulation Series, 33:1, pp. 137-142.
- Junco, S. "Virtual Prototyping of Bond Graphs Models for Controller Synthesis through Energy and Power Shaping". Conference on Integrated Modeling and Analysis in Applied Control and Automation (IMAACA 2004).
- Johansson, K. "The Quadruple-Tank Process A multivariable laboratory process with an adjustable zero". IEEE Transactions on Control Systems Technology, 2000.
- Johnsen, Jøgen and Allgöwer, Frank. "Interconnection and Damping Assignment Passivity-Based Control of a Four-Tank System". Lecture Notes in Control and Information Sciences. Lagrangian and Hamiltonian Methods for Nonlinear Control 2006. Springer Berlin Heidelberg publisher. Vol. 366.2007, pages 111-122.
- Limon, D. Alvarado, I. Alamo, T. Camacho, E.F. "Robust tube-based MPC for tracking of constrained linear systems with additive disturbances." Journal of Process Control. . Vol 20.Nro 3. 2010. pages 248-260.
- Nacusse, M. Junco, S. "Passive Fault tolerant control: A bond graph approach". Conference on Integrated Modeling and Analysis in Applied Control and Automation (IMAACA 2011).
- Ortega, R. Van der Schaft, A., Castaños, F., Astolfi, A. "Control by Interconnection and Standard Passivity-Based Control of Port-Hamiltonian Systems". IEEE Transactions on Automatic Control, Vol. 53, No. 11. (December 2008), pp. 2527-2542, doi:10.1109/TAC.2008.2006930.
- Ortega, R., Van der Schaft, A., Maschke, B., Escobar, G. "Interconnection and damping assignment passivity-based control of port-controlled Hamiltonian systems". Automatica, Volume 38, Issue 4, April 2002, Pages 585-596.
- Samantaray, A. Medjaherb, K. Ould Bouamama, B. Staroswiecki, M. Dauphin-Tanguy, G. "Diagnostic bond graphs for online fault detection and isolation". Simulation Modelling Practice and Theory Volume 14, Issue 3, April 2006, pages 237-262.
- Sontag, E. "Mathematical Control Theory: Deterministic Finite Dimensional Systems". Second Edition, Springer, New York, 1998.
- Zhang, Y. Jiang. J. "Bibliographical review on reconfigurable fault-tolerant control systems" Annual Reviews in Control, Vol. 32, No. 2. (December 2008), pages 229-252.

OBSERVER-BASED ACTUATOR AND SENSOR FAULT ESTIMATION

Christophe Sueur

Ecole Centrale de Lille, LAGIS UMR CNRS 8219, BP 48, 59651, Villeneuve d'Ascq Cedex France

christophe.sueur@ec-lille.fr

ABSTRACT

A simple and straightforward unknown input observer with application to process fault estimation is presented. The observer information is devoted to the fault estimation for fault detection and isolation but it can be used to form an additional control input to accommodate the fault, since an estimated state vector is also obtained. An extension to fault sensor is discussed. The scheme is verified through simulation studies performed on the control of a vertical takeoff and landing aircraft in the vertical plane..

Keywords: actuator and sensor fault Estimation, unknown input observer, linear systems.

1. INTRODUCTION

Modern engineering systems need more reliable operating conditions because of increased productivity requirements. In order to improve reliability, an alarm occurs with a fault detection and isolation (FDI) scheme in the monitored system. The FDI problem is an attractive topic which has received considerable attention with different approaches.

Many FDI methods are observer based: the plant output is compared with an estimation provided by an observer, and a residual is calculated. The concept of unknown input observer (UIO) schemes were developed and in that case, the FDI scheme can detect, isolate and estimate faults. Some structural conditions are required (infinite zero structure and finite structure properties) on the model. The UIO problem can then be first studied and then applied on the particular FDI scheme.

Different approaches give solvability conditions and constructive solutions for the UIO problem. For LTI models, constructive solutions with reduced-order observers are first published with the geometric approach [15], [2], [1]. Constructive solutions based on generalized inverse matrices taking into account properties of invariant zeros are given in [21] and then in [22] and [17] with observability and detectability properties. Full order observers are then written in a similar way (based on generalized inverse matrices) in [8] and [7], but with some restriction on the infinite structure of the model. The algebraic approach is published in [29] and in [6] for continuous and discrete time systems, without restriction on the infinite structure of the model. New developments are now proposed with an observer based approach for some classes of nonlinear systems with a fuzzy approach [32], fuzzy systems with time delays [28] or with uncertain systems [4].

The structural invariants which play a fundamental role in this problem have been extensively studied in many papers and books [1], [23], [26], [19], [14], [20]. The knowledge

of zeros is often an important issue because zeros are directly related to some stability conditions of the controlled system and the infinite structure is often related to solvability conditions.

The FDI problem with a fault diagnosis observer based approach has been developed in many papers. [30] developed an FDI observer by directly using the result of [21]. A systematic investigation with new design principles are written in [12] with some examples. Other developments are proposed in [18], [10] [31], [25] and [35]. Two survey papers are proposed in [11] and [13].

The objective of this paper is the development of an UIO for linear systems when there are two kinds of inputs: measured and unmeasured inputs with application to observer-based fault estimation. This UIO is proposed in a previous work [33] for disturbance estimation and rejection. This work makes a contribution by using this UIO for sensor fault estimation. The second section gives the description of this observer and its properties. Particularly, since the state equations of this observer are exactly the same as the initial model with an added term, it is proved to be accurate for simulation and for an integrated design approach. This kind of observer is usually dedicated to actuator fault detection; an extension to sensor fault detection is proposed. In the third part, the new scheme is verified through simulation studies performed on the control of a vertical takeoff and landing aircraft in the vertical plane.

2. UNKNOWN INPUT OBSERVER

Consider the linear system (1). $x \in \mathfrak{X}^n$ is the state vector, $z \in \mathfrak{R}^p$ is the vector set of measured variables and $y \in \mathfrak{R}^{p_1}$ is the vector of output variables to be controlled. The input variables are divided into two sets. $u \in \mathfrak{R}^m$ represents the known input vector and $d(t) \in \mathfrak{R}^q$ is the unknown input vector (disturbance or additive actuator fault), with $p \geq q$. Matrices A , B , F and H are supposed to be full rank matrices.

$$\begin{cases} \dot{x}(t) = Ax(t) + Bu(t) + Fd(t) \\ z(t) = Hx(t) \\ y(t) = Cx(t) \end{cases} \quad (1)$$

2.1 Preliminaries

Some assumptions are required for the state space model $\Sigma(H, A, F)$. The first one is non restrictive in a physical approach. These properties are developed in section 2.3.

Assumption 1. It is supposed that system $\Sigma(H, A, F)$ defined in (1) is controllable/observable and that the state matrix A is invertible.

Assumption 1 is not a restrictive condition for systems modeled with a physical approach, for example with a bond graph approach, because in that case, state variables are energy variables and except for particular cases, the eigenvalues of the state matrix are different from 0, and the state matrix is thus invertible. In a same way, the state model is controllable and observable. If the state matrix is non-invertible, a simple extension could be proposed.

Assumption 2. Matrix HF is a full column rank matrix.

If $p > q$, matrix HF is not a square matrix and matrix H is written as $H = [H_1^t H_2^t]^t$ with a reordering of measured output variables in order to have a full rank square matrix $H_1 F$. If several choices are possible, the reordering will depend on the studied problem: actuator or sensor fault estimation. Similarly, if matrix HF is not a full column rank matrix, a reduced-order state estimation can be proposed.

Assumption 3. The invariant zeros s of system $\Sigma(H, A, F)$ in (1) satisfy $Re(s) < 0$.

Necessary condition in assumption 2 for the existence of observers is often required (see [21]; [8]) and is called *observer matching condition*. It is also defined as an infinite structure requirement.

The condition on invariant zeros in assumption 3, or equivalently the strong detectability property defined in [16] corresponds to the minimum-phase condition, directly related to the zeros of system $\Sigma(H, A, F)$ (finite structure) defined as to be the values of $s \in \mathcal{C}$ (the complex plane) for which (2) is verified.

$$\text{rank} \begin{pmatrix} sI - A & -F \\ H & 0 \end{pmatrix} < n + \text{rank} \begin{pmatrix} -F \\ 0 \end{pmatrix} \quad (2)$$

2.2. Unknown Input Observer

The state equation (1) without output variable $y(t)$ is now rewritten as (3).

$$\begin{cases} \dot{x}(t) = A^{-1}\dot{\hat{x}}(t) - A^{-1}Bu(t) - A^{-1}Fd(t) \\ z_1(t) = H_1 A^{-1}\dot{\hat{x}}(t) - H_1 A^{-1}Bu(t) - H_1 A^{-1}Fd(t) \\ z_2(t) = H_2 A^{-1}\dot{\hat{x}}(t) - H_2 A^{-1}Bu(t) - H_2 A^{-1}Fd(t) \end{cases} \quad (3)$$

If matrix $H_1 A^{-1} F$ is invertible (Model $\Sigma(H_1, A, F)$ has no null invariant zero), vector $d(t)$ can be written as in equation (4) and then the estimation of the disturbance variable can be written as in equation (5). The extension to models with a non-invertible matrix $H_1 A^{-1} F$ is not proposed in this paper.

$$d(t) = -(H_1 A^{-1} F)^{-1} [z_1(t) - H_1 A^{-1} \dot{\hat{x}}(t) + H_1 A^{-1} Bu(t)] \quad (4)$$

$$\hat{d}(t) = -(H_1 A^{-1} F)^{-1} [z_1(t) - H_1 A^{-1} \dot{\hat{x}}(t) + H_1 A^{-1} Bu(t)] \quad (5)$$

Since equation (6) is satisfied for the state vector, a new estimation is proposed for the state vector, defined in equation (7).

$$\hat{x}(t) = A^{-1}\dot{\hat{x}}(t) - A^{-1}Bu(t) - A^{-1}Fd(t) \quad (6)$$

$$\hat{x}(t) = A^{-1}\dot{\hat{x}}(t) - A^{-1}Bu(t) - A^{-1}F\hat{d}(t) + K(\dot{z}(t) - \dot{\hat{z}}(t)) \quad (7)$$

The state estimation equation deduced from (7) can also be written as (8), which is similar to a classical estimation, but with a difference in the last term. It needs the derivation of the measured variables. By Comparison with numerous existing UIO methods proposed in the literature, the advantage of this new approach is that the model of the observer (apart the derivative of the measurement) is exactly the model of the physical system. Note that it is not the case for other methods. It is a main advantage for example in an integrated design approach with physical considerations. Some discussions on the influence of noise measurement are proposed in the following. Note that in some often cited papers, [6], a r^{th} derivative (infinite zero order of the output variable) is needed for the output variable ($(r-1)^{th}$ for the input control variable) and that in [7], only state estimation with pseudo-inverse matrices is proposed. Note that if variables in vector $d(t)$ are associated to actuators faults, a FDI procedure with accommodation can be designed.

$$\dot{\hat{x}}(t) = A\hat{x}(t) + Bu(t) + F\hat{d}(t) - AK(\dot{z}(t) - \dot{\hat{z}}(t)) \quad (8)$$

2.3. Properties of the observer

The convergence of the disturbance variables can be verified with equation (9), obtained from (4) and (5).

$$d(t) - \hat{d}(t) = (H_1 A^{-1} F)^{-1} H_1 A^{-1} (\dot{x}(t) - \dot{\hat{x}}(t)) \quad (9)$$

The estimation of the disturbance variables converges to the disturbance variable only if $(\dot{x}(t) - \dot{\hat{x}}(t))$ converges asymptotically.

In order to simplify notations, new matrices N_{BO} and N_{BF} are introduced in (10).

$$\begin{cases} N_{BO} = A^{-1} - A^{-1}F(H_1 A^{-1}F)^{-1}H_1 A^{-1} \\ N_{BF} = A^{-1} - A^{-1}F(H_1 A^{-1}F)^{-1}H_1 A^{-1} - KH \end{cases} \quad (10)$$

From (6) and (7), with $e(t) = x(t) - \hat{x}(t)$ it comes (11).

$$e(t) = N_{BF}\dot{e}(t) \quad (11)$$

Convergence of the state estimation must be proved with the study of the observer fixed poles. In equation (11), conditions for pole placement with matrix K are studied. If matrix N_{BF} is invertible, a classical pole placement is studied, and the error variable $e(t) = x(t) - \hat{x}(t)$ does not depend on the disturbance variable. The conditions for (8) to be an asymptotic state observer of $x(t)$ is that N_{BF} must be a Hurwitz matrix, i.e., has all its eigenvalues in the left-hand side of the complex plane.

Some properties of the observer are now explained. The proofs are in Appendix A. It is proved that this new observer must verify the matching condition defined in some well known approaches [16], [7] and that in that case, fixed poles

of the estimation error are all the invariant zeros of system $\Sigma(H, A, F)$.

A necessary condition for the existence of the state estimator is proposed in proposition 1.

Property 1: A necessary condition for matrix N_{BF} defined in (10) to be invertible is that $\text{rank}(HF) = q$.

Condition defined in proposition 1 means that all the infinite zero orders of system $\Sigma(H, A, F)$ are equal to 1. This set of global infinite zero orders contains q integers.

It is now supposed that the condition $\text{rank}(HF) = q$ is satisfied. Two properties are proposed and proved in appendix.

Property 2: Matrix N_{BO} has q eigenvalues equal to 0.

Property 3: The fixed poles of the state estimation error defined in (11) are the invariant zeros of model $\Sigma(H, A, F)$

This property is proved with the study of the observability property of model $\Sigma(H, N_{BO})$.

2.4. Unknown Output observer

The method can be extended to the sensor observation or the sensor fault case with an augmented model. The system under consideration is written as (12), [9] and [35].

$$\begin{cases} \dot{x}(t) = Ax(t) + Bu(t) \\ z(t) = Hx(t) + Df_s(t) \end{cases} \quad (12)$$

$f_s(t)$ represents the sensors fault vector and D is a full column rank matrix. Consider a new state vector $x_s(t) \in \mathfrak{R}^p$ and a new state equation (13).

$$\dot{x}_s(t) = -A_s x_s(t) + A_s H x(t) + A_s D f_s(t) \quad (13)$$

With a new state vector $\bar{x}(t) = (x^t(t) \ x_s^t(t))^t$, the augmented system can be expressed as (14).

$$\begin{cases} \dot{\bar{x}}(t) = \bar{A}\bar{x}(t) + \bar{B}u(t) + \bar{F}f_s(t) \\ \bar{z}(t) = \bar{H}\bar{x}(t) \end{cases} \quad (14)$$

The new matrices \bar{A} , \bar{B} , \bar{H} and \bar{F} are defined as follows:

$$\bar{A} = \begin{pmatrix} A & 0 \\ A_s H & -A_s \end{pmatrix}, \quad \bar{B} = \begin{pmatrix} B \\ 0 \end{pmatrix}, \quad \bar{F} = \begin{pmatrix} 0 \\ A_s D \end{pmatrix}$$

$$\bar{H} = (0 \quad I_p)$$

From the above augmented system, sensor fault may be treated as an actuator fault problem studied with an observer based approach and the properties of the new model can be easily pointed out. Remark that matrix D can be equal to the identity matrix (this choice is possible for physical systems).

Suppose first that only one observer is used for all sensors fault detection. In that case, A_s is chosen as a Hurwitz matrix with a good response time for variables x_s defined in equation (13), and $D = I_p$. Since $\bar{H}\bar{F}$ is a square invertible matrix, matrix \bar{H} is not rewritten with two submatrices. In that case, some simple results are obtained:

$$\bar{A}^{-1} = \begin{pmatrix} A^{-1} & 0 \\ HA^{-1} & -A_s^{-1} \end{pmatrix}, \quad -(\bar{H}\bar{A}^{-1}\bar{F}) = I_p$$

$$N_{BO} = \begin{pmatrix} A^{-1} & 0 \\ 0 & 0 \end{pmatrix}, \quad N_{BF} = \begin{pmatrix} A^{-1} & K_1 \\ 0 & K_2 \end{pmatrix}$$

In that case, the set of invariant zeros is equal to the set of system poles (eigenvalues of the state matrix), which is also the set of fixed poles for the estimation error equation (11) for the extended system (14), because matrix N_{BF} is a block-diagonal matrix with one block equal to matrix A^{-1} . Due to time convergence of the estimation error compared with the system one, this observer must be modified in order to have appropriate fixed modes. Using one observer (or one sensor) is thus not successful in fault isolation problem.

A bank of observers is often proposed in the literature for actuator fault detection or isolation [5] and sensor fault isolation in presence of unknown disturbance or model uncertainties [3], [34].

New output vectors z_j and z^j can be defined with new output equations, equation (15)

$$\begin{cases} z^j(t) = H^j \bar{x}(t) + f_s^j(t) \\ z_j(t) = h_j \bar{x}(t) + f_{sj}(t) \end{cases} \quad (15)$$

h_j is the j^{th} row of matrix H , H^j is obtained from matrix H by deleting the j^{th} row h_j . z_j is the j^{th} component of vector z and z^j is obtained from vector z by deleting the j^{th} variable z_j . The extended model (14) can be rewritten as equation (16). \bar{F}_j is the j^{th} column of matrix \bar{F} and $f_{sj}(t)$ is the j^{th} fault variable associated to the j^{th} sensor.

$$\begin{cases} \dot{\bar{x}}(t) = \bar{A}\bar{x}(t) + \bar{B}u(t) + \sum \bar{F}_j f_{sj}(t) \\ \bar{z}^j(t) = \bar{H}^j \bar{x}(t) \\ \bar{z}_j(t) = \bar{h}_j \bar{x}(t) \end{cases} \quad (16)$$

It is supposed that each subsystem has only one faulty sensor, in that case, p UIO can be constructed from the augmented system defined in equation (16) and only matrix \bar{F}_j is used for the j^{th} observer. Equations defined in (3) are written with $z_1(t) = \bar{z}_j(t)$ and $z_2(t) = \bar{z}^j(t)$. The state vector estimates $\hat{\bar{x}}$ and the p unknown variables $f_{sj}(t)$ are calculated from equations (8) and (5) from the new state equations (16).

If one sensor is faulty and if the system keeps on at least two other sensors, it is possible to accommodate a new observer with safe sensors by a simple modification in vector $z_2(t) = \bar{z}^j(t)$. In that case new estimates must be defined with new matrices for pole placement. This problem is not treated in this paper. It is also possible to use this new observer for actuator and sensor fault detection and isolation at the same time, but with some more conditions.

3. EXAMPLE

A VTOL (vertical takeoff and landing) aircraft in the vertical plane was studied by [24] and [27]. Its linearized dynamics are given in the state space formulation as (1), where

$$x = \begin{bmatrix} v_h - \text{horizontal velocity} \\ v_v - \text{vertical velocity} \\ q - \text{pitch rate (deg/s)} \\ \theta - \text{pitch angle (deg)} \end{bmatrix}$$

$$u = \begin{bmatrix} \delta_c - \text{collective pitch control} \\ \delta_l - \text{longitudinal cyclic pitch control} \end{bmatrix}.$$

The two inputs are used to control the vertical motion and horizontal velocity of the aircraft, respectively. An unknown input (an actuator fault) is implemented in the system. The model parameters are given as follows

$$A = \begin{bmatrix} -9.9477 & -0.7476 & 0.2632 & 5.0337 \\ 52.1659 & 2.7452 & 5.5532 & -24.4221 \\ 26.0922 & 2.6361 & -4.1975 & -19.2774 \\ 0 & 0 & 1 & 0 \end{bmatrix}$$

$$B = F = \begin{bmatrix} 0.4422 & 0.1761 \\ 3.5446 & -7.5922 \\ 5.52 & 4.49 \\ 0 & 0 \end{bmatrix} \quad H = \begin{bmatrix} 1 & 0 & 0 & 0 \\ 0 & 1 & 0 & 0 \\ 0 & 0 & 0 & 1 \end{bmatrix}$$

The system poles are located at $\{-6.8271, -2.5506\}$ and $\{-1.0112 \pm 1.5146j\}$, and there is no invariant zero in system $\Sigma(H, A, F)$.

In this paper, we do not consider measurement noises. A first order filter is used before the derivative of the measurement variable. Simulations (not proposed in this paper) can prove the robustness of the approach with some kind of noises. Theoretical developments for the study of the influence of noises on the convergence and on the applicability of the proposal for industry-sized examples will be proposed in an extended paper.

3.1. Actuator fault

The known input $u = [1 \ 1]^T$ is implemented to the system with an initial condition of state variable $x_0 = [0.01 \ 0 \ 0 \ 0]$ and initial conditions equal to zero for the observer variables. Since a fault actuator study is proposed, matrices B and F are equal and the unknown input is $d(t) = f(t)$ and $f(t) = [f_1(t) \ f_2(t)]^T$ is chosen as (17).

$$f_1(t) = \begin{cases} 0 & 0 \leq t \leq 2 \\ 0.3 & 2 < t \leq 3 \end{cases} \quad f_2(t) = 0. \quad (17)$$

The existence conditions of an UIO are satisfied. Matrix HF is a full rank matrix and $\Sigma(H, A, F)$ has no invariant zero. Since matrix HF is not a square matrix, matrix H_1 in this example contains only the two first rows of matrix H , and H_1F is a square full rank matrix. In the state estimation equation defined in (8), matrix $K = [k_{ij}]$, $i = 1, \dots, 4$, $j = 1, \dots, 3$ is used for pole placement. All the poles can be chosen, because fixed poles for the estimation problem are the invariant zeros. The four poles of matrix N_{BF}^{-1} defined in the state estimation error equation (11) are chosen as $s_1 = -20$, $s_2 = -25$, $s_3 = -\frac{100}{3}$ and $s_4 = -50$, compared with system's poles.

To validate the new results, different time responses of system variables are shown. A comparison between variables and their estimates is proposed. The estimated output variables $\{\hat{z}_1, \hat{z}_2, \hat{z}_3\}$ and the estimated unknown variables (actuators faults) $\{\hat{f}_1, \hat{f}_2\}$ are very close to the real variables, Fig. 1 and Fig. 2. With Fig. 3 it is proved that the estimation errors for the state variables converge rapidly to zero. From the above simulations, it can be concluded that asymptotic convergence of fault estimation can be achieved.

The robustness of this new observer is also proved with a time varying fault. In Fig. 4, a time varying fault is

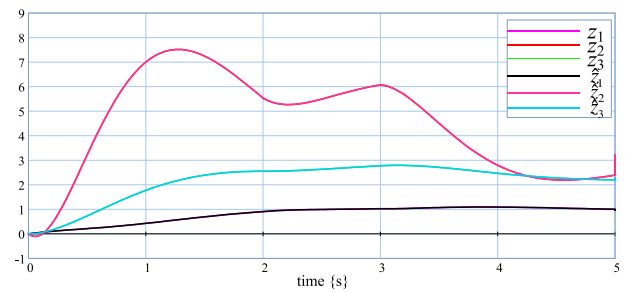


Figure 1: Output variable $z(t)$ and their estimates \hat{z}

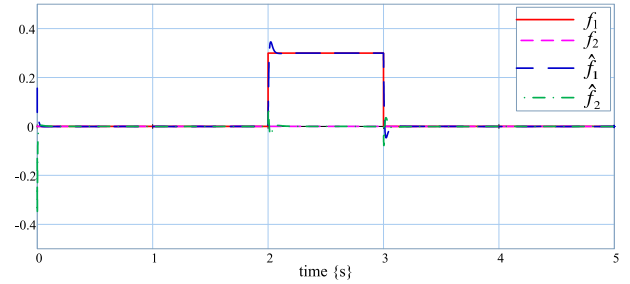


Figure 2: Fault variables $f(t)$ and their estimates \hat{f}

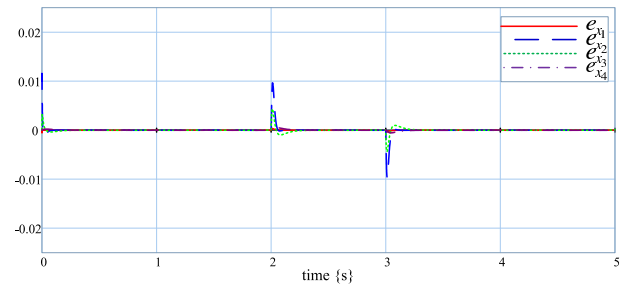


Figure3: Trajectories $e_i = x_i - \hat{x}_i, i = 1, \dots, 4$ with UIO in (8)

considered with a rather high frequency. The asymptotic convergence property and the good performance of the observer is proved in that case. It is also proved in case of a system with not well known parameters (not drawn here).

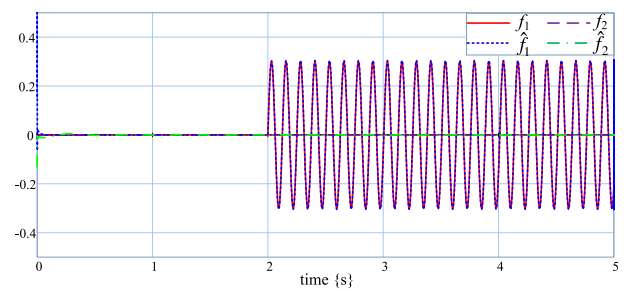


Figure 4: Fault variables $f(t)$ and their estimates \hat{f} : time varying fault

3.2. Sensor fault

The sensor fault analysis is now proposed on this example. It is supposed that the first sensor can be faulty. The new matrices are written in Appendix B. The extended model defined in (14) is now a 5th order model. The new 5th state variable

is x_s and the new state matrix is chosen as $-A_s = -25$. The five poles of matrix N_{BF}^{-1} defined in the state estimation error equation (11) are located at $\{-30, -40, -40, -50, -50\}$. It can be shown that the extended model $\Sigma(\bar{H}, \bar{A}, \bar{F})$ has no invariant zero, and thus for this new estimation problem, there is not any fixed mode.

With a simple pole placement for matrix N_{BF} , it comes:

$$K = \begin{bmatrix} 0 & -0.0267 & -0.4457 \\ 0 & -0.6815 & 3.1666 \\ 0 & 0.0008 & 0.9954 \\ 0 & -0.0605 & -0.3685 \\ 0.0250 & 0 & 0 \end{bmatrix}$$

It is supposed that the faulty sensor is defined as a disturbance $d(t) = f_{s1}(t)$ which is a pulse signal with start time 1s, end time 2s and amplitude 1. Variable $d(t)$ and its estimated are shown in Fig. 5.

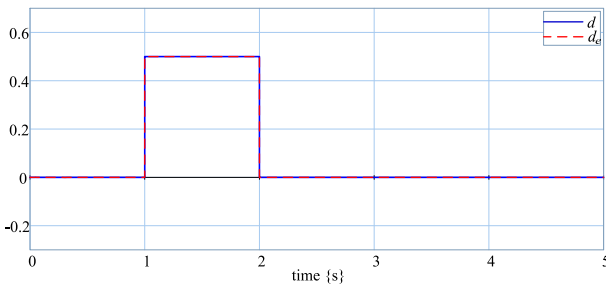


Figure 5: Fault variable $f_{s1}(t)$ and its estimates $\hat{f}_{s1}(t)$

Three variables are depicted in Fig. 6. The object is to compare the information given by the faulty sensor, its estimate and the "true" value of the system variable (horizontal velocity) obtained from the state estimation. In Fig. 6, time responses of variable $z_1(t)$ and its estimate \hat{z}_1 are very close. The third time response x_{1e} is the estimate of the first state variable and is the time response which should be obtained with a non faulty sensor. From these time responses, it is concluded that sensor fault is well solved and that fault accommodation is possible because a good estimate of the measured variable with a faulty sensor is obtained. Robustness issues could also be included, but due to lack of space, they are not proposed in this paper. By changing the plant model (parameters), it is shown by simulation that a good performance is obtained, and compared with some other well-known techniques, it is proved that this UIO is as well as other one.

Two other problems could be studied for this physical example: the case with one actuator fault and one sensor fault in the same model and secondly two sensors fault. The first situation is simple, the model must just be rewritten with the two kinds of fault. The second problem is simple if the two sensor faults don't occur simultaneously. Otherwise, only one sensor is no more sufficient for sensor fault estimation and accommodation.

4. CONCLUSION

An unknown input observer is proposed in this paper with application to the actuator and sensor fault detection and

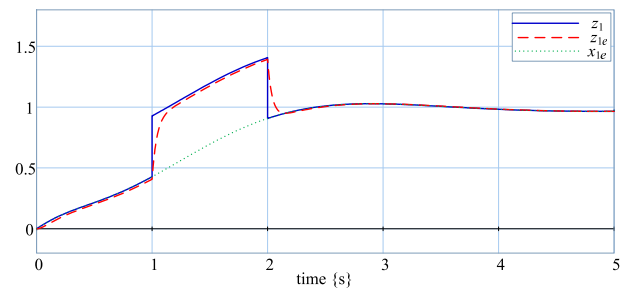


Fig. 6. Sensor time response $z_1(t)$, its estimate $\hat{z}_1(t)$ and state variable estimate $\hat{x}_{1e}(t)$

isolation problem. This observer is proved to be accurate with classical restrictive conditions based on the infinite structure and finite structure requirements. The application of this new scheme to a vertical takeoff and landing aircraft system shows that actuators and sensors faults can be estimated with satisfactory rapidity and accuracy. Theoretical developments for the study of the influence of noises on the convergence and on the applicability of the proposal for industry-sized examples will be proposed in an extended paper.

REFERENCES

1. G. Basile and G. Marro. A new characterization of some structural properties of linear systems: Unknown-input observability, invertibility and functional controllability. *International Journal of Control*, 17(5):931943, 1973.
2. S.P. Bhattacharyya. Observer design for linear systems with unknown inputs. *IEEE Transactions on Automatic Control*, 23:1483–484, 1978.
3. J. Chen and R. J. Patton. *Robust model-based fault diagnosis for dynamic systems*. Massachusetts: Kluwer Academic Publishers, 1999.
4. W. Chen, A.Q. Khan, M. Abid, and S.X. Ding. Integrated design of observer based fault detection for a class of uncertain nonlinear systems. *Int. J. of Applied Mathematics and Computer Sciences*, 21 (3):423–430, 2011.
5. C. Commault, J. M. Dion, O. Sename, and R. Moteyeian. Observer-based fault detection and isolation for structured systems. *IEEE Transactions on Automatic control*, 47 (12):2074–2079, 2002.
6. J. Daafouz, M. Fliess, and G. Millerioux. Une approche intrinsèque des observateurs linéaires à entrées inconnues. *CIFA 2006, Bordeaux*, 2006.
7. M. Darouach. Complements to full order observer design for linear systems with unknown inputs. *Applied Mathematics Letters*, 22:1107–1111, 2009.
8. M. Darouach, M. Zasadzinski, and S.J. Xu. Full-order observers for linear systems with unknown inputs. *IEEE Transactions on Automatic Control*, 39:606–609, 1994.
9. C. Edwards. A comparison of sliding mode and unknown input observers for fault reconstruction. *Proc. of the 43rd IEEE Conference on Decision and Control*, pages 5279–5284, 2004.
10. P. M. Frank. Enhancement of robustness in observer based fault detection. *Inter. J. Control*, 59:955–981, 1994.
11. P. M. Frank and X. Ding. Survey of robust residual generation and evaluation methods in observer-based fault detection systems. *J. Process Control*, 7:403424, 1997.
12. P. M. Frank and J. Wunnenberg. Robust fault diagnosis using unknown input observer schemes. in *Patton, R.J., Frank, P.M., and Clark, R.N. (Eds.): Fault diagnosis in dynamical systems: theory and applications in Prentice Hall, New York*, pages 47–98, 1989.
13. E. A. Garcia and P. M. Frank. Deterministic nonlinear observer-based approaches to fault diagnosis: a survey. *Control Eng. Pract.*, 5:663–670, 1997.
14. E. G. Gilbert. The decoupling of multivariable systems by state feedback. *SIAM Journal of Control and Optimization*, 7:50–63, 1969.
15. R. Guidorzi and G. Marro. On wonham stabilizability condition in the synthesis of observers for unknown-input systems. *IEEE Trans. Automat. Control*, 16:499–500, 1971.

16. M. L. J. Hautus. Strong detectability and observers. *Linear Algebra and its Applications*, 50:353–368, 1983.
17. M. Hou and P.C. Muller. Design of observers for linear systems with unknown inputs. *IEEE Trans. Automat. Control*, 37:871–875, 1992.
18. M. Hou and P.C. Muller. Fault detection and isolation observers. *Int. J. Control*, 60(5):827–846, 1994.
19. T. Kailath. *Linear Systems*. Prentice Hall, Englewood-Cliff, N.J., 1980.
20. R. E. Kalman, P. L. Falb, and M. A. Arbib. *Topics in Mathematical System Theory*. McGraw-Hill, New York, 1969.
21. P. Kudva, N. Viswanadham, and A. Ramakrishna. Observers for linear systems with unknown inputs. *IEEE Trans. Automat. Control*, 25:113–115, 1980.
22. B.J. Miller and R. Mukunden. On designing reduced-order observers for linear time-invariant systems subject to unknown inputs. *Internat. J. Control*, 35:183–188, 1982.
23. A. S. Morse. Structural invariants of linear multivariable systems. *SIAM J. Control*, 11:446–465, 1973.
24. K.S. Narendra and S.S. Tripathi. Identification and optimization of aircraft dynamics. Technical report, DTIC Document, 1972.
25. T. G. Park and K.S. Lee. Process fault isolation for linear systems with unknown inputs. *IEE Proc. Control Theory Appl.*, 151(6):720–726, 2004.
26. H.H. Rosenbrock. *State space and multivariable theory*. Nelson, London, England, 1970.
27. M. Saif and Y. Guan. A new approach to robust fault detection and identification. *IEEE Transactions on Aerospace and Electronic Systems*, 29(3):685–695, 1993.
28. S. Tong and G. Yang. Observer-based fault-tolerant control against sensor failures for fuzzy systems with time delays. *Int. J. of Applied Mathematics and Computer Sciences*, 21 (4):617–628, 2011.
29. H. L. Trentelman, A. A. Stoorvogel, and M. Hautus. *Control theory for linear systems*. London, UK: Springer, 2001.
30. N. Viswanadham and R. Srichander. Fault detection using unknown input observers. *Control Theory Adv. Technol.*, 3:91–101, 1987.
31. H. Wang and S. Daley. Actuator fault diagnosis: an adaptative observer-based technique. *IEEE Transactions on Automatic Control*, 41(7):1073–1078, 1996.
32. D. Xu, B. Jiang, and P. Shi. Nonlinear actuator fault estimation observer: an inverse system approach via a t-s fuzzy model. *Int. J. of Applied Mathematics and Computer Sciences*, 22 (1):183–196, 2012.
33. D. Yang and C. Sueur. Unknown input observer: a physical approach. *IMAACA 2012, September 19-21, Vienna, Austria*, 2012.
34. J. Zarei and J. Poshtan. Sensor fault detection and diagnosis of a process using unknown input observer. *Mathematical and Computational Applications*, 16(1):31–42, 2011.
35. K. Zhang, B. Jiang, and V. Cocquemot. Adaptive observer-based fast fault estimation. *International Journal of Control, Automation, and Systems*, 6(3):320–326, 2008.

APPENDIX

Appendix A: Properties of the observer

Proof proposition 1

Matrix $N_{BF}F$ is equal to $[A^{-1} - A^{-1}F(H_1A^{-1}F)^{-1}H_1A^{-1} - KH]F$, thus $N_{BF}F = A^{-1}F - A^{-1}F(H_1A^{-1}F)^{-1}H_1A^{-1}F - KHF = KHF$. If the rank condition $\text{rank}(HF) = q$ is not satisfied, the Kernel of matrix N_{BF} is not empty, which means that matrix N_{BF} is not invertible and that this matrix contains at least one null mode, thus pole placement is not possible (all its eigenvalues are not in the left-hand side of the complex plane). \square

Proof proposition 2

Since $H_1N_{BO} = H_1A^{-1} - H_1A^{-1}F(H_1A^{-1}F)^{-1}H_1A^{-1}$, it comes $H_1N_{BO} = 0$. Since vector H_1^t is orthogonal to matrix N_{BO} , matrix N_{BO} contains at least q null eigenvalues.

Proof proposition 3

First, the observability property of model $\Sigma(H, N_{BO})$ is studied. The non observable poles are the roots of the invariant polynomials obtained from the Smith form of matrix $N(s)$ defined in (18). With matrix H_1 , only the q null modes of matrix N_{BO} can be assigned. The goal is to emphasize the number of modes which can be assigned with matrix H_2 .

$$N(s) = \begin{pmatrix} sI - N_{BO} \\ H_1 \\ H_2 \end{pmatrix} \quad (18)$$

The fixed poles of the state estimation error defined in (11) are thus the non observable poles of model $\Sigma(H, N_{BO})$. Now, some equivalent transformations are proposed for the Smith matrix $S(s)$ of system $\Sigma(H, A, F)$ defined in (19).

$$S(s) = \begin{pmatrix} sI - A & -F \\ H_1 & 0 \\ H_2 & 0 \end{pmatrix} \quad (19)$$

$$S(s) \sim \begin{pmatrix} sA^{-1} - I & -A^{-1}F \\ H_1 & 0 \\ H_2 & 0 \end{pmatrix} \quad (20)$$

$$\sim \begin{pmatrix} sA^{-1} - I & -A^{-1}F \\ H_1 + sH_1A^{-1} - H_1 & -H_1A^{-1}F \\ H_2 & 0 \end{pmatrix} \quad (21)$$

$$\sim \begin{pmatrix} sA^{-1} - I & A^{-1}F(H_1A^{-1}F)^{-1} \\ sH_1A^{-1} & I \\ H_2 & 0 \end{pmatrix} \quad (22)$$

$$\sim \begin{pmatrix} sA^{-1} - I - A^{-1}F(H_1A^{-1}F)^{-1} - sH_1A^{-1} & 0 \\ sH_1A^{-1} & I \\ H_2 & 0 \end{pmatrix} \quad (23)$$

$$\sim \begin{pmatrix} sN_{BO} - I & 0 \\ 0 & I \\ H_2 & 0 \end{pmatrix} \sim \begin{pmatrix} sN_{BO} - I & 0 \\ H_2 & 0 \\ 0 & I \end{pmatrix} \quad (24)$$

The non observable modes are thus all the inverse of the invariant zeros of system $\Sigma(H, A, F)$. They are the fixed modes of the state estimation error equation.

Appendix B: Sensor fault model

$$\bar{A} = \begin{bmatrix} -9.9477 & -0.7476 & 0.2632 & 5.0337 & 0 \\ 52.1659 & 2.7452 & 5.5532 & -24.4221 & 0 \\ 26.0922 & 2.6361 & -4.1975 & -19.2774 & 0 \\ 0 & 0 & 1 & 0 & 0 \\ 25 & 0 & 0 & 0 & -25 \end{bmatrix}$$

$$\bar{B} = \begin{bmatrix} 0.4422 & 0.1761 \\ 3.5446 & -7.5922 \\ 5.52 & 4.49 \\ 0 & 0 \\ 0 & 0 \end{bmatrix} \quad \bar{F} = \begin{bmatrix} 0 \\ 0 \\ 0 \\ 0 \\ 25 \end{bmatrix}$$

$$\bar{H} = \begin{bmatrix} 0 & 0 & 0 & 0 & 1 \\ 0 & 1 & 0 & 0 & 0 \\ 0 & 0 & 0 & 1 & 0 \end{bmatrix}$$

$$\bar{H}_1 = [0 \ 0 \ 0 \ 0 \ 1] \quad \bar{H}_2 = \begin{bmatrix} 0 & 1 & 0 & 0 & 0 \\ 0 & 0 & 0 & 1 & 0 \end{bmatrix}$$

Author's Index

Abdelkrim, 52
Arvani, 70
Bouamama, 37, 52
Butt, 70
Da Cruz, 22
Dauphin-Tanguy, 52
Delatore, 22
El Harabi, 52
Fallahi, 70
Gahlouz, 37
Gregor, 78
Groumpos, 78
Gühmann, 44
Gupta, 15
Han, 1
Huang, 44
Ibrahim, 61
Ilinca, 61
Joyram, 61
Junco, 87
Kaddissi, 6
Kenné, 6
Knoblich, 44
Kohda, 28
Leonardi, 22
Nacusse, 87
Novazzi, 22
Nowoisky, 44
Paradis, 61
Polotski, 6
Ramdenée, 61
Rastogi, 15
Rideout, 70
Saoudi, 52
Sato, 28
Shaer, 6
Sueur, 37, 97
Suzuki, 28
Tanaka, 28
Tarasov, 37
Tsukamoto, 28